Cryopreservation of retinal organoids and applications of RPE cells for disease modelling in retinitis pigmentosa

Maria Georgiou

A thesis submitted to Newcastle University for the degree of Doctor of Philosophy (PhD)

Biosciences Institute

Faculty of Medical Sciences

Newcastle University

October 2021

Abstract

Generation of retinal cells from human induced pluripotent stem cells (hiPSCs) provides great opportunities for research and therapeutics. In this study, we generated hiPSC-derived retinal cells to evaluate their ability to be cryopreserved, shipped at room temperature (RT), and assess their application in disease modelling by studying the mechanisms causing Retinitis Pigmentosa (RP).

To develop an effective cryopreservation protocol for the long-term storage of retinal organoids (ROs), previously published cryopreservation methods were used. The structure and presence of retinal cells in cryopreserved ROs were assessed by immunofluorescence analysis. The 'Master Liver Supercooling' protocol was the most promising among all in preserving the overall retinal structure. However, success was limited, and only PRs survived.

To assess whether hiPSC-derived ROs can be shipped at RT, ROs were kept at RT for 5 days or shipped internationally for 3 days using a commercial container. The structure, morphology and function of ROs were assessed by immunofluorescence, transmission electron microscopy and electrophysiology, indicating no differences between control, RT incubated and shipped organoids. This study provides an effective shipping method to facilitate the transportation of ROs at RT.

To identify the disease mechanisms of RP associated with *PRPF31* mutations (known as RP11), proteomic analyses of hiPSCs-retinal pigmented epithelium (RPE) cells from control and RP11-patients were conducted. These showed that RNA splicing, retinoid metabolism and visual perception, and protein folding pathways were affected. RP11-RPE cells were characterised by reduced functional PRPF31 protein and the presence of insoluble aggregates containing mutant PRPF31, misfolded and ubiquitin-conjugated proteins. The waste disposal mechanisms were impaired exacerbating aggregate formation which was associated with cell death activation. Treatment of RP11-RPE cells with rapamycin (autophagy activator) reduced cytoplasmic aggregates and improved cell survival.

This thesis highlights the applications of hiPSC-derived retinal cells and provides more insights in cryopreservation, transportation and potential therapeutics for RP.

“Not everything that can be counted counts, and not everything that counts can be counted”.

- Albert Einstein

Acknowledgements

I would like to express my special appreciation and gratitude to my supervisor Professor Majlinda Lako for her invaluable supervision during my PhD. This PhD thesis would not have been possible without her advice, continued support, guidance and help. I am very grateful to Professor Lako for supporting me in my transition from technician to PhD student. Also, I would like to thank her for believing in my abilities and for giving me the opportunity to publish research articles and get involved in many more projects beyond the scope of my PhD thesis. Additionally, I would like to thank my second supervisor, Dr Valeria Chichagova, for her time, insights, help and support during my PhD along with the useful comments and suggestions for my thesis. I would also like to thank my thesis committee, Professor David Steel and Professor David Elliot, for their time and expertise.

Thank you to Dr Birthe Dorgau for all her knowledge, help, support and expertise on retinal organoids and for her help with the electrophysiology experiments. I would also like to thank Robert Atkinson and Edvinas Cerniauskas for teaching me all the necessary techniques required for the RPE project and Dr Marzena Kurzawa-Akanbi for her knowledge and expertise on the field. Special thanks to our collaborators, Peter Kilbride (Asymptote, Cytiva) for his expertise, help, advice and assistance with the cryopreservation experiments, Dr Sina Mozzafari-Jovin (Max-Planck Institute of Biophysical Chemistry, Göttingen, Germany) for running the proteomic analysis and his contribution to the project, and Tracey Davey (Newcastle University Electron Microscopy Facility) for her help with the Transmission electron microscopy.

I would like to thank my PhD friends, Robert Atkinson and Avril Watson for being very helpful and supportive creating a collaborative environment and a friendly community that extended beyond the lab. Also, I would like to thank all of the members in the stem cell group for all their help during this time. It has been a privilege to be a member of this cell group during my PhD.

I am thankful to my mum, dad and my sister for all their support throughout my PhD studies by always being next to me, encouraging and motivating me to continue the hard work. Thank you! I would not be where I am today without you. Special thanks to my boyfriend Gregory for his continued support, patience and understanding, and for being always next to me, encouraging and motivating me.

Table of Contents

List of Figures

List of Tables

List of Abbreviations

AD	Alzheimer disease
adRP	Autosomal dominant retinitis pigmentosa
ALS	Amyotrophic lateral sclerosis
AMD	Age-related Macular Degeneration
arRP	Autosomal recessive retinitis pigmentosa
ATF6	Activating transcription factor 6
bb	Basal body
CC	Connecting cilium
CMA	Chaperone-mediated autophagy
CNOT3	CCR4-NOT transcription complex subunit 3
CO_2	Carbon dioxide
CPAs	Cryoprotectants
CRALBP (RLBP1)	Cellular retinaldehyde-binding protein
DE	Differentially expressed
DHA	Docosahexaenoic acid
DMSO	Dimethyl sulfoxide
ECM	Extracellular matrix
EG	Ethylene glycol
eIF2a	Eukaryotic translation initiation factor 2A
ER	Endoplasmic reticulum
ERAD	Endoplasmic reticulum-associated degradation
ESCs	Embryonic stem cell
FBS	Foetal bovine serum
FGF	Fibroblast growth factors
GCL	Ganglion cell layer
GO	Gene ontology
GOBP	Gene ontology biological process
GPCR	G-protein coupled receptor
HD	Huntington's disease
HDFs	Human dermal fibroblast cells
HEPEs	4-(2-hydroxyethyl)-1piperazineethanesulfonic acid
hESCs	Human embryonic stem cell

hiPSCs	Human-induced pluripotent stem cells
hMSCs	Human mesenchymal stem cells
HPC	Hematopoietic progenitor cells
HSPs	Heat shock proteins
ICM	Inner cell mass
IF	Immunofluorescence
IGF-I	Insulin-like growth factor 1
INL	Inner nuclear layer
INZ	Inner nuclear zone
IPL	Inner plexiform layer
IRD	Inherited retinal diseases
IRE1α	Inositol-requiring protein-1α
ISs	Inner segments
LAMP1	Lysosomal-associated membrane protein 1
LCA	Leber congenital amaurosis
MEM-NEA	MEM-Eagle with non-essential amino acids
MIP	Maximum intensity projection
MITF	Microphthalmia-associated transcription factor
mM	millimollar
mRNA	Messenger RNA
MSR1	Minisatellite repeat element
mt	Mitochondria
MT	Material transfer
MVBs	Multivesicular bodies
NDs	Neurodegenerative diseases
NRPCs	Neuroretinal progenitor cells
NSCs	Neural stem cells
ONL	Outer nuclear layer
ONZ	Outer nuclear zone
OPL	Outer plexiform layer
OS	Outer segment
OVs	Optic vesicles
Pax6	Paired box 6
PCW	Post-conception week

PD	Parkinson disease
PDGF	Platelet-derived growth factor
PEG	Polyethylene glycol
PERK	Protein kinase RNA (PKR)-like ER kinase
PFA	Paraformaldehyde
PHO	Rhodopsin
PRPF31	Pre-mRNA processing factor 31
PRPFs	Pre-mRNA processing factors
PRs	Photoreceptors
POSs	Photoreceptor outer segments
PVDF	Polyvinylidene difluoride
RA	Retinoic acid
RDH	Retinol dehydrogenases
RLBP1	Retinaldehyde binding protein 1
ROs	Retinal organoids
RP	Retinitis pigmentosa
RPCs	Retinal progenitor cells
RPE	Retinal pigmented epithelium
snRNP	Small nuclear ribonucleic proteins
TBS-T	Tris-buffered saline with tween
TGF-3	Transforming growth factor-3
UPR	Unfolded protein response
UPS	Ubiquitin proteasome pathway
UV	Ultraviolet light
VEGF	Vascular endothelial cell growth factor
WB	Western blot
µl	Microliter

Chapter 1

Chapter 1. Introduction

1.1. The human retina

1.1.1. Structure and function of the human retina

The human eye is a specialized sensory organ responsible for perceiving vision, including motion, colour, shape, and variable light intensities (Sung and Chuang, 2010). The light enters through the cornea, the transparent outer layer of the eye, and passes through the lens, which transmits and focuses the light to the posterior part of the eye, the retina (**Figure 1-1**).

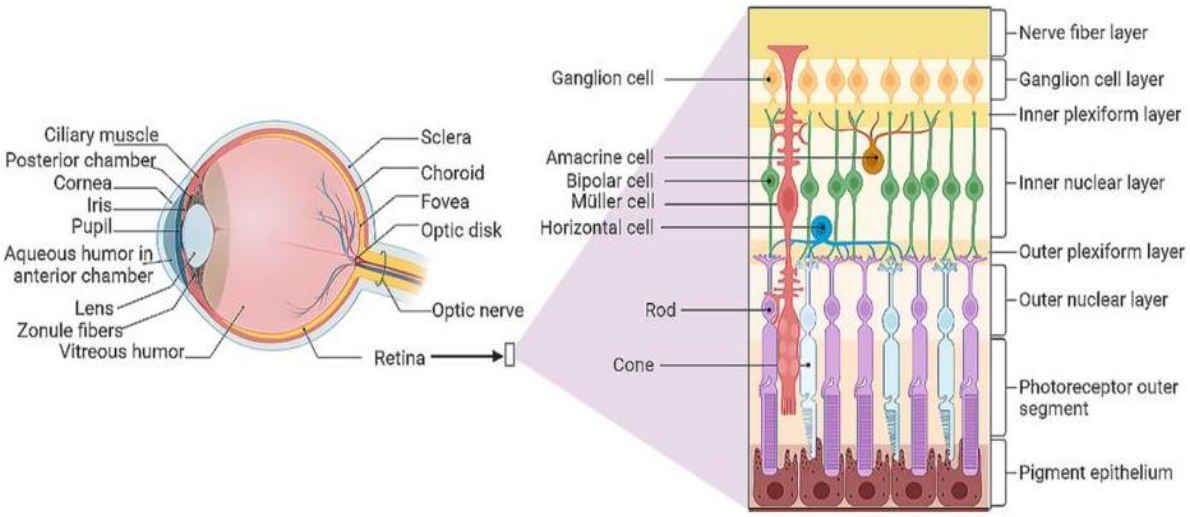

Figure 1-1: Diagram of the human retina. The human retina is a complex organized structure located at the back of the eye. It is composed of three main layers, the outer nuclear layer, the inner nuclear layer, and ganglion cell layer and contains five major neuronal cell types; light-sensitive photoreceptors, horizontal, bipolar, amacrine and ganglion cells (You et al., 2021). It is responsible for the absorption of light and transmission of this signal to the brain. Müller glial cells are also present in the retina and extend their processes throughout the retina, providing homeostatic and metabolic support.

The retina is an extension of the central nervous system and functions as a light-sensitive tissue to collect and transform light energy into a neural signal that is transmitted to the brain through the optic nerve (Mannu, 2014). It is the innermost layer of the wall of the eye (approximately 0.2 mm thick) which lies between the vitreal cavity on the inner side and RPE and choroid on the outermost side (Sung and Chuang, 2010). It is a compact, organized structure composed of five types of neuronal sensory cells that are perfectly ordered into three main layers (Sung and Chuang, 2010). These layers are comprised of the light-sensitive photoreceptors (PRs) located in the outer nuclear layer (ONL); horizontal, bipolar and amacrine cells that are found in the inner nuclear layer (INL); and ganglion cells which are located in the ganglion cell layer (GCL) (Nag and Wadhwa, 2006b) (**Figure 1-1**). The dendrites and axons of these neurons extend into

the outer and inner plexiform layers enabling retinal cells to synapse and form a signalling network. In addition to these cells, Müller glia, with their cell bodies located in the INL, have dendrites that span the full length of the retina (**Figure 1-1**). Müller glial cells are not involved in neuronal signal transduction but support the retina by providing structure and support. Additionally, Müller glial cells provide homeostatic and metabolic support as they control the transport of ions, water, and bicarbonate in the extracellular space (Reichenbach and Bringmann, 2013).

The photosensitive cells of the retina are known as the PR cells. They convert light energy into electrical signals through a biochemical pathway known as phototransduction.

PRs are classified into two types; rods which are active in dim light and cones which are responsible for colour vision and are activated in bright light (Kefalov et al., 2003). PRs are composed of several parts including the outer segment (OS), which contains the visual pigment. The visual pigment molecule comprises an 11-*cis* retinal chromophore covalently bound to an opsin G-protein coupled receptor (GPCR), known as opsin. It is activated by a photon of light. Activation of the opsin molecule induces isomerization and dissociation of the visual pigment resulting in the sequential activation of proteins which convert 11-*cis* retinal to all-*trans* retinal in the PRs (Tsin et al., 2018). However, for the continued function and survival of the PRs, all-*trans* retinal is converted back to 11-*cis* retinal to regenerate the photosensitive visual pigment. This process occurs through a series of enzymatic steps known as the visual cycle (**Figure 1-2**) (Sung and Chuang, 2010).

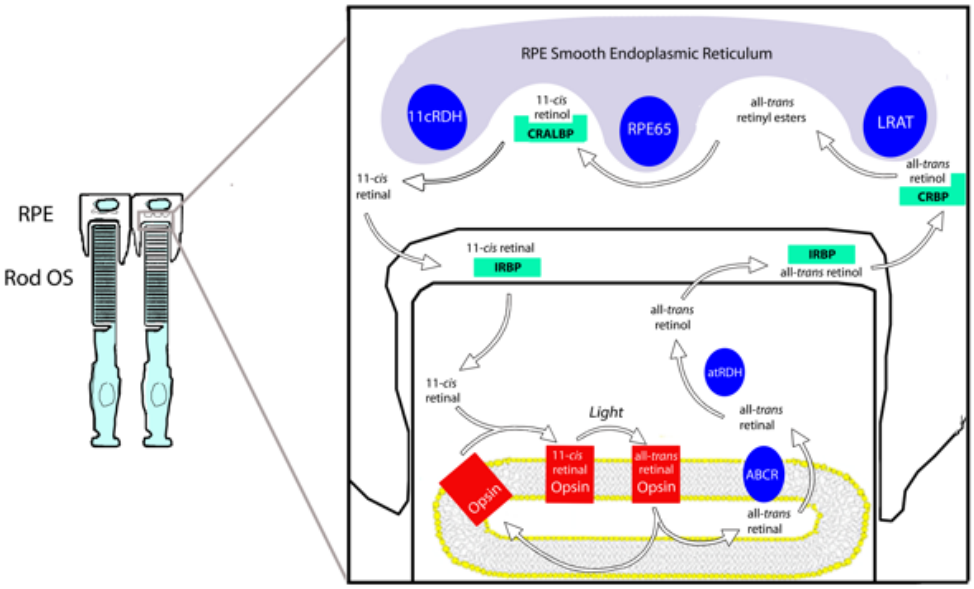

Figure 1-2: The visual cycle: Schematic representation of the biochemical reactions involved in the regeneration of 11-*cis* retinal in PR and RPE cells.

PR OSs are in close contact with RPE cells (Sung and Chuang, 2010) (**Figure 1-1**). RPE is a monolayer of pigmented, hexagonal, cuboidal, post-mitotic cells located between the PR cells on the inner side and Bruch's membrane (BrM) and the choroid on the external side (Strauss, 2005). Although RPE cells are not part of the neural retina, they are essential for the viability and functionality of PR cells (Kolb H, 1995). Specifically, RPE cells act as a selective barrier by regulating the transport of nutrients, ions and waste products to and from the retina. Through phagocytosis, RPE cells are also responsible for the clearance of OSs that are shed by PRs diurnally (**Figure 1-3**). RPE cells contain a high number of melanin granules which protect the PR layer from absorbing excessive high energy light. Additionally, RPE cells secrete a wide variety of growth factors including fibroblast growth factors (FGF), transforming growth factor-3 (TGF-3), insulin-like growth factor-I (IGF-I), platelet-derived growth factor (PDGF) and vascular endothelial cell growth factor (VEGF), that control the metabolic activity and the synthesis of retinoids, which are crucial for phototransduction (**Figure 1-3**) (Boulton and Dayhaw-Barker, 2001). Finally, BrM, which is a five-layered structure located between the RPE and the choroidal capillaries of the eye, is essential not only for the transportation of fluids, biomolecules, and oxygen between the blood and the retina, but it is also responsible for cellular migration, communication, and differentiation (Strauss, 2005).

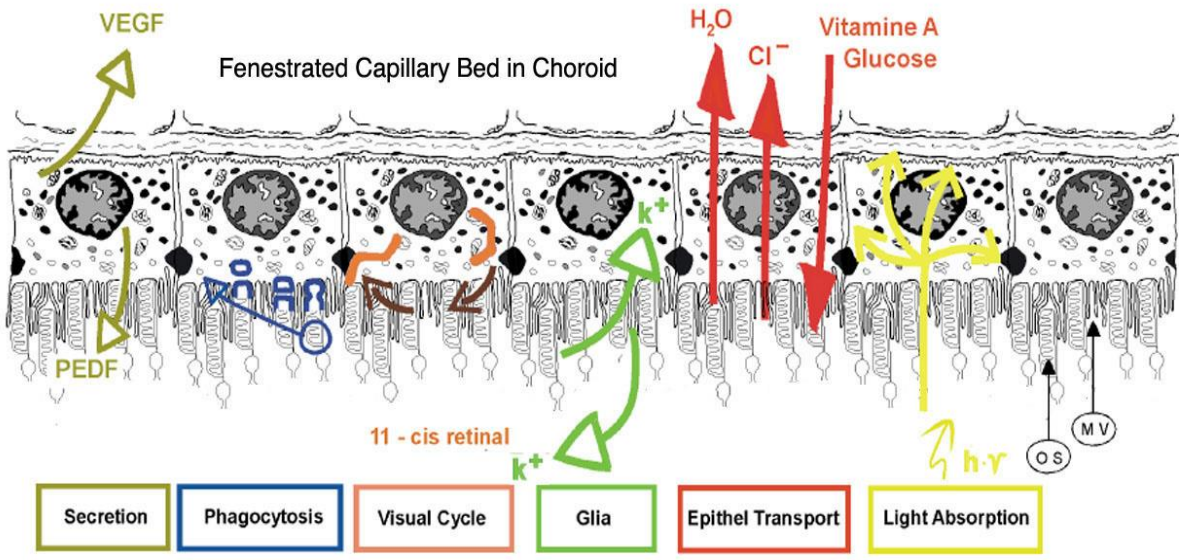

Figure 1-3: Diagram illustrating the major functions of RPE cells. Figure obtained from the retinal pigment epithelium in visual function (Strauss, 2005).

1.2. Mammalian eye development and formation of retinal cells

In humans, the eye is derived from three embryonic tissues; the neural ectoderm, the surface ectoderm, and the periocular mesenchyme (Heavner and Pevny, 2012). The neural ectoderm gives rise to the retina, RPE, optic nerve, ciliary body and iris, whereas the neural crest gives rise to the sclera and cornea. Specifically, the neural crest gives rise to the corneal stroma and cornea endothelium but not to the corneal epithelium as it derives from the surface ectoderm. Also, the vitreous humour and blood vessels derive from mesoderm (Heavner and Pevny, 2012). Development of the eye begins at around day 22 of embryonic development with the appearance of *optic sulci* (optic primordium), otherwise known as the eye field. Consequently, the evagination of optic sulci commences forming optic vesicles (OVs). The OVs then enlarge and invaginate to create the optic cup by embryonic day 32 (**Figure 1-4**) (O'Rahilly and Gardner, 1975). The optic cup formation is regulated by several signalling pathways, such as Notch, IGF-1 and Wnt, which regulate local gene expression before neurogenesis. Once the optic vesicles have invaginated, the surface ectoderm becomes thicker and forms the lens vesicle behind the surface ectoderm, which later forms the lens (Kwan et al., 2012). At the beginning of the 7th foetal week (FW), the inner layer of the optic cup proliferates and differentiates to form a multilayered neural retina, whereas the outer layer remains a single layer giving rise to the RPE (Quinn and Wijnholds, 2019).

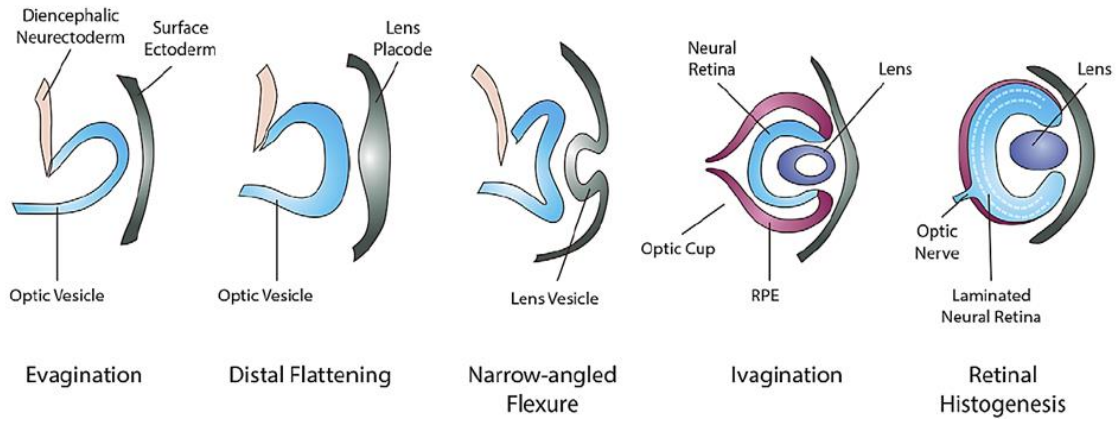

Figure 1-4: Schematic diagram of embryonic eye development. The surface ectoderm thickens and together with the neuroepithelium of the optic vesicle (OV), invaginates. The inner layer of the optic cup gives rise to the neural retina, whereas the outer layer becomes RPE. The mature retina comprises of three main layers containing the photoreceptors, the interneurons and the ganglion cells (Mellough et al., 2014).

The generation of different retinal cells is a regulated procedure that occurs at different time points during development and is regulated by intrinsic and extrinsic factors that differentiate common retinal progenitors into different retinal cell types (**Table 1-1**) (Osakada et al., 2008).

Several studies have identified and reported important markers of differentiation from different stages of retinogenesis. A common marker expressed in the optic vesicles and optic cup is retinal homeobox protein (RX/Rax) but as the development proceeds, Rx is limited to the neural retina. Additionally, paired box 6 (Pax6) is expressed throughout the optic cup but its expression is restricted to ganglion and amacrine cells as development continues (Meyer et al., 2009). Another critical marker is the Microphthalmia-associated transcription factor (MITF), which is expressed in all cells that will become either RPE cells or neural retina. However, repression of MITF by VSX2 expression gives rise to neural retina and upregulation of MITF gives rise to RPE cells (Meyer et al., 2009).

Table 1-1: Intrinsic and extrinsic factors regulating retinal cell differentiation.

Cell Type	Intrinsic factors	Extrinsic factors
	Transcription factors	**Soluble factor**
Photoreceptor cells	Crx / Otx2	(+) Retinoic acid (+) Taurine (+) Thyroid hormone (+) Shh (+) FGF (+) CNTF
Horizontal cells	Pax6 / Six3 / Prox1	
Bipolar Cells	Chx10	(+) CNTF
Amacrine cells	Pax6 / Six3	
Ganglion cells	Pax6	(-) Shh
Müller glia	Rx	(-) Retinoic acid (-) FGF

Differentiation of retina begins by forming the inner neuroblastic zone at post-conception week (PCW) 7. At early stages in the process (4.6 until 7.2 PCW), retinal progenitors proliferate, RPE emerges in the external layer of the optic cup, and the lenses begin to form (Mellough et al., 2019a). At 7.7-10 PCW, RGCs are generated in the internal layer, followed by the initiation of transcriptional programmes that give rise to horizontal and amacrine cells, and cone PRs (Mellough et al., 2019b). Specifically, cone PRs are differentiated from the outer rows of the outer nuclear zone (ONZ), followed by the differentiation of rod PRs at 12 PCW (Hendrickson and Zhang, 2019, Mellough et al., 2019b). Mainly, PCW 12-18 is characterized by the sequential development of cone PRs, rod PRs, bipolar cells and Müller glial cells (Mellough et al., 2019a). A small projection arises from the apical end of inner segments (ISs) in cone and rod PRs, known as the connecting cilium (CC), between 12 and 18 PCW (Mellough et al.,

2019a). The majority of retinal neurons are differentiated centrally and then migrate peripherally by 20 PCW. By that time, the axons of GCs are partially connected to the visual centres. All retinal layers and neurons are fully mature before birth, with the exception of PRs located in the fovea (a small central region in the macula responsible for chromatic and high acuity vision) where they continue to develop up to 5 months after birth. Retina size also continues to increase until the 6th postnatal year (Nag and Wadhwa, 2006a).

In addition to the human retinal development, mouse retinal development has also been well studied. Many differences have been reported between the two species in regard to retinal structure, morphogenesis, and the number, ratio and distribution of retinal cells. For example, the human retina is characterized by a significant amount (5%) of trichromatic cone PRs (red, green, and blue for long-wavelength (LW), middle wavelength (MW), and short-wavelength (SW), respectively) and all the PRs are generated prenatally (Sung and Chuang, 2010). However, as mice are nocturnal animals, their retinal physiology is adapted to that and so mouse retina contains fewer cone PRs (3%) and only two types; M and S cones, are expressed (Fu and Yau, 2007).

In addition to this, human retina features a section called the fovea, which is absent in mouse retina, and whilst all PRs are generated prenatally in human retina, mice can continue to develop PRs postnatally (**Figure 1-5**) (Swaroop et al., 2010). Due to the differences between these species, murine models are considered an imperfect model to study human retinogenesis. Therefore, there is a need for more physiologically relevant models to study the human retina.

There are additional limitations with the use of animal models in general. In some instances of disease modelling, the human disease phenotype is not correctly recapitulated in the animal model. Another disadvantage of using animal models like mice is their short life span. This precludes the development of age-related disease phenotypes and thereby hinders our understanding of age-related diseases. As a result of these shortcomings, many researchers across the globe have worked to generate a more physiological and biologically relevant model. By understanding the basic principles of retinal development and combining this knowledge with pluripotent stem cell applications, it is now possible to generate and study the human retina in a dish using three-dimensional (3D) culture systems.

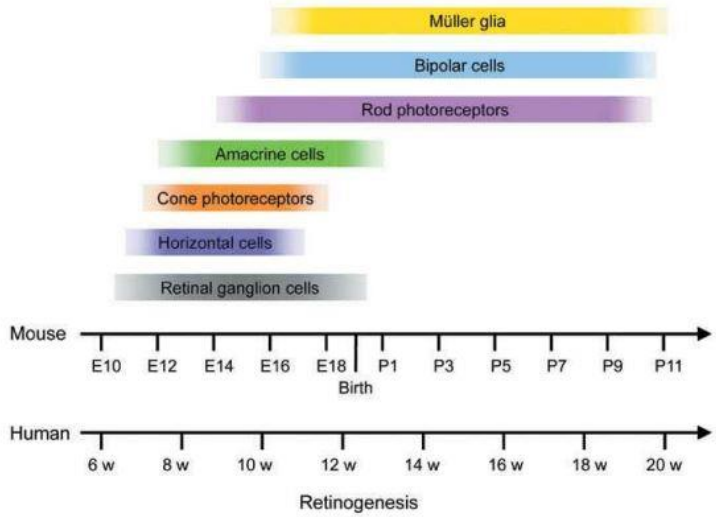

Figure 1-5: Neurogenesis of retinal cell types in mice and human. The sequence of retinal cell development is conserved between species, initiating with retinal ganglion cells, horizontal cells followed by cone PRs, amacrine cells, rod PRs, bipolar cells, and Müller glial cells with an overlap in the appearance of the cells (Osakada et al., 2008).

1.3. Stem cells

Stem cells are found in all multicellular organisms and are characterized by infinite self-renewal and the ability to differentiate into multiple specialized cell types of the body (Yamashita et al., 2010). Different types of stem cells exist and vary based on their potency to differentiate into specialized cell types. They are classified as either totipotent, pluripotent, multipotent, or unipotent (Bindu A and B, 2011).

- *Totipotent stem cells* can give rise to any cell type found in an organism, including extra-embryonic structures such as the placenta. An example of a totipotent stem cell is the zygote, which can reproduce the whole organism by cell division in the uterus.
- *Pluripotent stem cells*, which are located in the inner cell mass (ICM) of the blastocyst, are capable of differentiating into all cell types of an organism except the placenta. An example of pluripotent stem cells are human embryonic stem cells (hESCs), which can form all three embryonic germ layers (mesoderm, endoderm, and ectoderm).
- *Multipotent stem cells* differentiate into lineages that could give rise to more than one type of cell in the body. An example of multipotent stem cells is the hemopoietic stem cells which can be differentiated into all blood cells in the body, including white blood cells, red blood cells, and platelets.
- *Unipotent stem cells* can give rise only to one cell type, such as epidermal stem cells that produce skin cells.

1.3.1. Characteristics of stem cells

- *Self-renewal and asymmetric division.* This is one of the most important characteristics of stem cells, as their constant production is fundamental for the functionality and homeostasis of the tissue throughout the lifetime of an organism. When asymmetric cell division occurs two daughter cells are formed. One daughter cell inherits the mother stem cell properties, and the other daughter cell is differentiated into a specialized cell. The daughter cells committed to differentiation undergo mitosis and DNA synthesis. This is followed by post-mitosis, where the cells are no longer capable of proliferating further and thus mature into terminally differentiated cells (Terskikh et al., 2009).
- *Give rise to specialised cells.* Although stem cells are undifferentiated cells, they can give rise to differentiated cells through a process called differentiation. Several steps are involved in the process of differentiation. These steps include internal signalling cascades, that are controlled by genes encoding for cellular structures and functions, and external signals, such as cell-cell adhesion, and chemical and molecular secretion into the microenvironment by other cells.
- *High proliferative potential.* In a steady-state condition, the rates of proliferation in stem cells are very low. However, in the case of cell replacement and/or injury, the proliferative rate is increased to meet the needs of the tissue.

1.3.2. Pluripotent stem cells

There are two classes of pluripotent stem cells (PSCs), the ESCs, and human-induced pluripotent stem cells (hiPSCs), capable of self-renewing and differentiating into any specialised cell types of the human body, holding thus a great therapeutic potential. Both ESCs and hiPSCs share similarities in the expression of pluripotency markers and differentiation ability; however, they differ in their origin and derivation ways (Robinton and Daley, 2012).

1.3.2.1. Embryonic stem cells (ESCs)

Embryonic stem cells (ESCs) are derived from embryos after *in vitro* fertilization of an oocyte with a spermatozoon (Thomson et al., 1998). The generated zygote forms a morula and then a blastocyst, after multiple cell divisions. The blastocyst stage, which is formed three to five days after egg fertilization, consists of approximately 50 to 150 cells that form an outer layer of cells known as the trophoblast, and an ICM (**Figure 1-6**). The ICM found inside the blastocyst is

destined to give rise to the embryo is the source of ESCs (Pera et al., 2000). ESCs are characterized by their origin, the ability to maintain a normal karyotype *in vitro*, divide indefinitely without losing their primitive embryonic state, and spontaneously differentiate into cells representative of the three embryonic germ layers, giving rise to any cell type in the human body (**Figure 1-6**) (Pera et al., 2000).

Once cells from the ICM are isolated, they can be cultured in tissue culture plates or flasks coated with a feeder layer (mitotically-inactive mouse embryonic fibroblasts) in the presence of a culture medium that contains specific nutrients. Once ESCs attach to the surface, the feeder cells release nutrients to assist in the maintenance of ESC pluripotency. Secreted molecules subsequently activate numerous signalling pathways that help the cells to divide and expand, generating unlimited numbers of ESCs. Under the appropriate culture conditions, the differentiation of ESCs to specific lineages can be directed with future clinical potentials, which can be used to replace cells in disease states (Thomson et al., 1998).

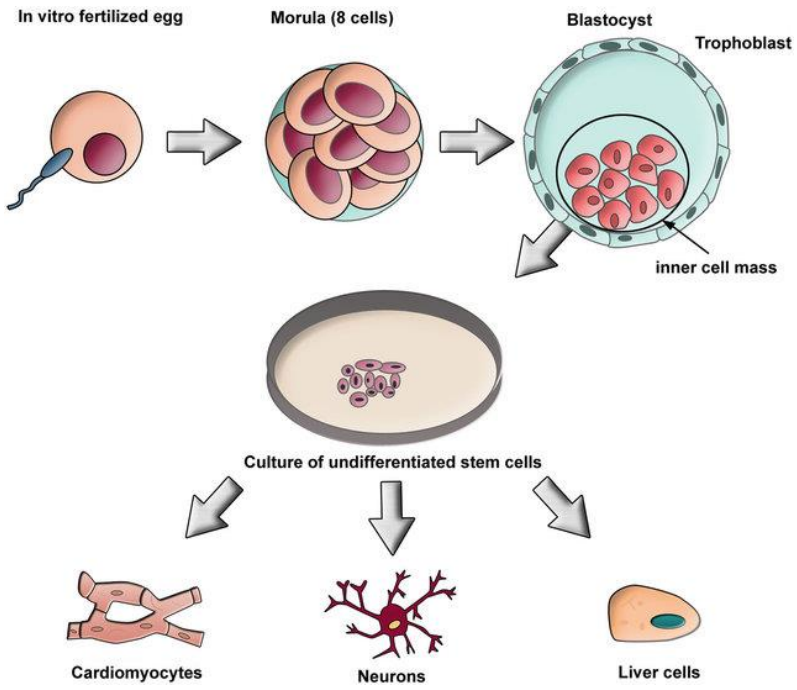

Figure 1-6: The origin of human embryonic stem cells. Once an oocyte is fertilised by a spermatozoon, the fertilised egg is developed into a blastocyst that contains the trophoblast and the inner cell mass (ICM). Pluripotent stem cells in the ICM are isolated and are cultured with growth factors to give rise to different specialised cells (Thomson et al., 1998).

The first mouse ESCs were derived approximately 40 years ago from the blastocyst of a normal preimplantation mouse embryo. Martin and colleagues reported the successful isolation of ESCs and their differentiation into various cell types. This was performed by isolating the ICM

that gave rise to ESCs after culturing them with ESC-conditioned medium (Kleinsmith and Pierce, 1964, Martin, 1981).

Current clinical trials have used hESCs for the treatment of multiple diseases. In the context of retina, a phase 1 clinical trial run by Liu and colleagues focused on the safety and therapeutic effect of transplanted hESCs-derived RPE cells in three wet age-related macular degeneration (wet-AMD) patients. Preliminary data has shown the safety profile and efficacy of the transplantation of RPE cells in AMD patients and no adverse effects in the first 12 months after transplantation were recorded. However, although they reported that a new RPE-like cell layer developed in the damaged area, visual and physiological tests revealed that functional improvements were limited and varied between the patients (Liu et al., 2018c).

Another clinical study reported the delivery of hESC-derived RPE monolayer patches into the subretinal space of AMD patients. The results indicated the feasibility of manufacturing an hESC-RPE monolayer on a synthetic basement membrane and the tolerability of transplanted patches into the subretinal space of the patients. This clinical study provides a potential treatment for AMD patients suggesting efficacy, stability, and tolerability using an RPE patch for approximately 12 months (da Cruz et al., 2018).

Although ESCs have significant therapeutic potential in producing multiple different lineages, and they have been used in several clinical trials providing promising results, there are some remaining concerns related to immunogenicity and potential tissue rejection that is always a possibility after transplantation. In addition to this, there are ethical issues regarding the use of ESCs due to their derivation from human embryos (Leist et al., 2008).

1.3.2.2. Human induced pluripotent stem cells (hiPSCs)

A hallmark discovery in stem cell research was the successful reprogramming of somatic cells into ESC-like cells with pluripotent properties, designated as hiPSCs (**Figure 1-7**). Specifically, Takahashi and Yamanaka in 2006 demonstrated the induction of pluripotent stem cells from mouse fibroblasts by inducing the expression of four key factors (Oct3/4, Sox2, c-Myc, and Klf4) simultaneously in the nucleus of the cell (Takahashi and Yamanaka, 2006). The generated iPSCs exhibited the same morphology, growth characteristics, and gene expression as in ESCs. A year later, Takahashi and colleagues successfully reprogrammed adult human dermal fibroblasts into hiPSCs using the same four key factors as before. The generated hiPSCs shared the same morphology, proliferation, gene expression, surface antigens, telomerase activity, and

epigenetic status of pluripotent cell-specific genes with hESCs (Takahashi et al., 2007). On the same day, another group, Thomson and colleagues, also reported the reprogramming of somatic cells into hiPSCs, which exhibit similar characteristics to hESCs. Their method utilised a combination of four different factors (OCT4, SOX2, NANOG, and LIN28) (Yu et al., 2007). Following on from this discovery, it was noted that several other factors can be introduced in combination to somatic cells for the generation of hiPSCs.

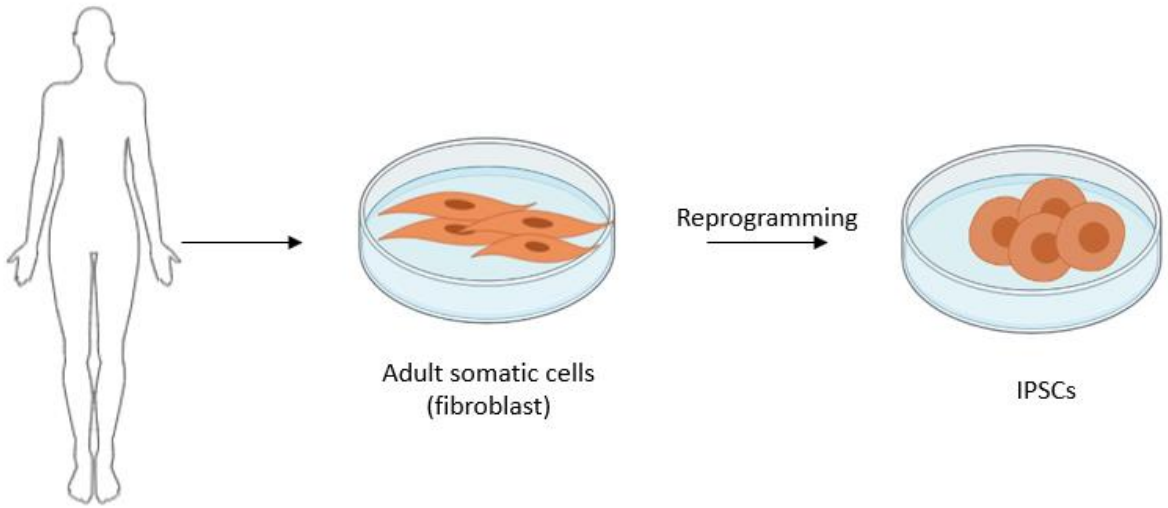

Figure 1-7: Reprogramming of adult somatic cells to hiPSCs. The generation of hiPSCs is achieved by reprogramming adult somatic cells using key transcription factors that reset the transcriptional profile of somatic cells and reverts them back to their embryonic state.

For the reprogramming of hiPSCs into any cell type, several methods utilising delivery vectors were used. Early studies used DNA-integrating viral vectors such as retroviruses and lentiviruses (**Table 1-2**), to insert transgenes into the genome. Yamanaka's reprogramming method to generate hiPSCs was performed using retroviral vectors to express each reprogramming factor in the genome (Takahashi and Yamanaka, 2006). However, integration of reprogramming factors in the genome of generated hiPSCs can induce insertional mutagenesis. Also, residues of reprogramming factors could remain in hiPSCs and hence transmitted to their derivatives (Kang et al., 2015). As a result, subsequent studies have used non-integrating viral vectors which are capable of generating hiPSCs without inducing permanent genetic modifications (**Table 1-2**) (Han and Yoon, 2011). Non–integrating viral vectors, such as adenovirus, can deliver transcription factors directly without causing DNA-related complications (Robinton and Daley, 2012). Although non-integrating viral vectors could be used to reprogram hiPSCs, low delivery efficiency and high cost are some of their disadvantages. However, in contrast to adenoviruses, the Sendai virus, another non-integrating

viral delivery method, has demonstrated significant improvements in efficacy over other viral delivery methods (Oh et al., 2012). Examples of delivery vectors and their efficiencies are mentioned in the table below (**Table 1-2**).

Table 1-2: Methods for generating hiPSCs for clinical applications. Integrating and non-integrating vectors are the main strategies to reprogram somatic cells into hiPSCs using variable gene delivery systems. Pig (P); rat (R); rhesus monkey (Rh); mouse (M); human (H) (Yamanaka, 2012).

Vector Type	Subtypes	Methods	Species	Efficiency (%)
Integrating		Retroviral vectors	P, R, Rh, M, H	0.01∼0.5
		Lentiviral vectors	M, H	0.1∼1
		Induced lentiviral vectors	P, M, H	0.1∼1
Non-integrating		Adenoviral vectors	*M*, *H*	∼0.001
		Sendai viral vectors	H	0.001∼1
		Plasmids	*M*, *H*	∼0.001
		Plasmids + Nanoparticles	M	0.001∼0.003
		oriP/EBNA-1 episomal vectors	*H*	∼0.0003
		Cre/loxP recombination systems	H	0.1∼1
		Minicircle DNA episomal vectors	H	∼0.005
	DNA Free	Proteins	M, H	∼0.001
		RNAs	H	∼1
	Chemical induction	Factors + Small molecules	M, H	∼2.05
	Excisible	Piggybac transposon/transposase system	M, H	∼0.1

1.3.2.3. The use of hiPSCs in disease modelling

A key advantage of generating hiPSCs from somatic cells from any genetic background, is the ability to generate cell lines possessing disease-causing mutations (Singh et al., 2015). Patient-derived hiPSCs could serve as a platform for disease modelling studies. This application has provided new avenues for drug development and to study the pathogenesis of various degenerative diseases, including retinitis pigmentosa (RP) (**Figure 1-8**) (Achberger et al., 2019).

hiPSCs have been used by several stem cell research groups to study retinal diseases. For example, Yoshida and colleagues generated hiPSCs from a RP patient harbouring Rhodopsin mutation (E181K). Following correction of the patient-derived hiPSCs using an adenoviral vector, corrected and mutated hiPSCs were subjected to differentiation, which showed that PR cells harbouring the mutation had reduced survival rate compared to the corrected cells. These results were also associated with an increase in the expression of endoplasmic reticulum (ER) markers; BIP, CHOP, and apoptotic markers; NOXA, BID. After that, Yoshida and colleagues demonstrated that treatment of patient-derived hiPSCs with Salubrinal, an inhibitor of eIF2α, increased the survival of mutant rod PR cells and reduced the levels of ER stress and apoptotic markers in Salubrinal-treated cells (Yoshida et al., 2014).

Usher syndrome is a hereditary disease that involves deafness and RP - usually due to mutations in the *USH2A* gene. To model this disease *in vitro* and determine the pathophysiological mechanism of *USH2A* mutation, Tucker and colleagues generated eye-cup-like structures from hiPSCs harbouring *USH2A* mutation. These structures expressed PR-specific markers such as Recoverin and Rhodopsin and exhibited the structural characteristics of photoreceptor outer segments (POSs). Analysis of the PR cells revealed an increase in the expression of GRP78 and GRP94 when compared to the control cells, indicating protein misfolding and subsequent ER stress. Following this, Tucker and colleagues transplanted patient-specific PR precursor cells in dystrophic mice and demonstrated the ability of PR cells to integrate and develop into mature PR cells in the retina (Tucker et al., 2013).

All of the above are examples of hiPSCs used in disease modelling to mimic retinal degeneration. Thereby, highlighting the utility of hiPSCs in understanding the mechanisms and pathogenesis of various human diseases.

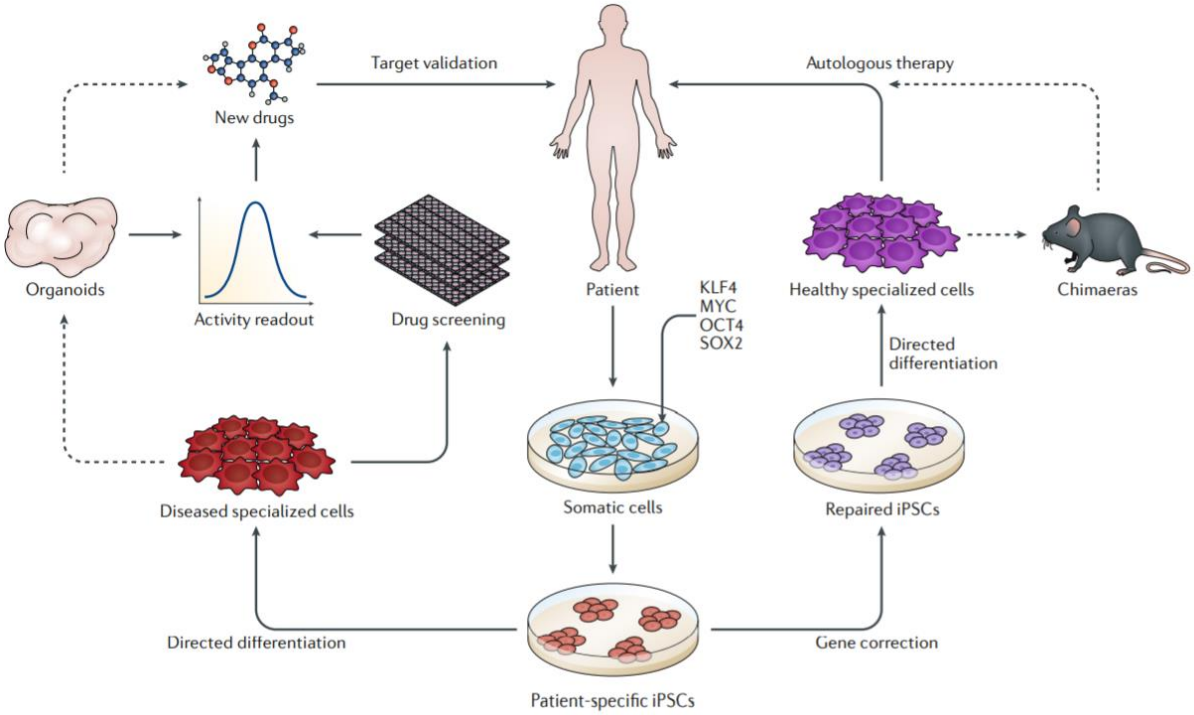

Figure 1-8: Diagram of generating hiPSCs and their applications. Differentiating hiPSCs to specialised cells could be used as a platform for drug screening, validation studies, and generation of hiPSC-derived organoids to model and study diseases and cell therapies (Rowe and Daley, 2019).

1.3.2.4. The use of hiPSCs and ESCs, and generation of retinal organoids

Initially, hiPSCs and ESCs were differentiated as 2D monolayers and were used to study the molecular mechanisms underlying disease phenotype (Liu et al., 2018a). However, this technology cannot recapitulate the architecture of complex tissues and organ functions (Liu et al., 2018a) as they do not mimic cell-cell communication, cell-matrix mechanisms, and the unique *in vivo* niche environment (Brafman, 2013).

In the last few decades, a major breakthrough occurred in stem cell research with the generation of three dimensional (3D) 'organoid' models. These organoids can recapitulate the structures and functions of the organs or tissues they represent (Eiraku et al., 2008). 3D modelling technology is essential for creating *in vitro* disease models to understand disease pathology and develop therapeutic drugs (Dutta et al., 2017). The development of organoids is achieved by inducing the differentiation of stem cells to develop cells of a specific lineage and generate 3D structures with tissue-specific properties using *in vitro* cell culture techniques (Liu et al., 2018a).

Several studies have reported that differentiation of ESCs into retinal organoids (ROs) using a 3D culture system could recapitulate retinal development. In 2011, Eiraku and Sasai generated a fully laminated 3D neural retina from mouse ESCs, which contained all the major neuronal cell types, including rod and cone PRs (**Table 1-3**) (Eiraku et al., 2011).

Later in 2012, Nakano and colleagues reported the generation of a 3D optic cup from hESCs that allowed the formation of a three-layered neural retina with RPE and a high number of PRs, as well as other retinal neurons and Müller glial cells. The study reported the generation and advanced maturation of PRs, facilitated by notch inhibitor, DAPT. However, the formation of OSs was not clearly observed (**Table 1-3**) (Nakano et al., 2012).

In another group, Zhong and colleagues generated 3D retinal cups from hiPSCs by enriching the culture media with retinoic acid (RA), which promotes differentiation of PR precursors to rods. This study reported the development of fully laminated 3D retinal organoids expressing all major cell types. The PR cells also displayed a level of photosensitivity, although a limited amount of PRs (2 out of 13 randomly chosen cells) responded to a light flash (Zhong et al., 2014) (**Table 1-3**). This is likely due to the rarity of PR OSs which also required further developmental maturation, including the formation of OS discs. One limitation of this technology is the time-consuming nature of the method. Maturation of retinal organoids requires more than 200 days and loss of central ganglion cells and amacrine cells is observed after day 100 of differentiation.

Several other groups (Phillips et al., 2014), including ours (Mellough et al., 2015, Hallam et al., 2018b) (**Table 1-3**), are using the 3D approach to generate retinal organoids that contain all major retinal cell subtypes with distinct layering to reflect the structural, morphological, and functional properties as seen in *in vivo* development (Chichagova et al., 2020). Therefore, the development of retinal organoids from hiPSCs serves as a biologically and physiologically relevant platform to study retinal development (Siller et al., 2013). Recently, Hallam and colleagues used hiPSCs to generate retinal organoids, which respond to light in a similar way to neonatal mouse. However, variability in organoid efficiency was observed and was reported to be a consequence of nutrient availability. This suggests a link between the availability of nutrients with the process of cell development in retinal organoids (**Table 1-3**) (Hallam et al., 2018a).

Table 1-3: Summary of key differentiation protocols of hiPSCs or ESCs into 3D retinal organoids.

Publication	Cell source	Retinal organoids formation method	Differentiation methods				Protocol Length	Features/ Characteristics
			Plates	Medium				
(Eiraku et al., 2011)	Mouse ES cells	Serum-free floating embryonic bodies (SFEB)	**Day 0 - Day 7:** 96-well low-cell-adhesion plates (lipidure coat) **Day 7 – Day 24** 6-well plates (2% matrigel)	**Day 0 – Day 7** G-MEM 1.5% KOSR 0.1 mM MEM-NEAA 1 mM pyruvate, 1 mM β-mercaptoethanol	**Day 7 – Day 24** DMEM/F12 P/S, N2, (foetal bovine serum) FBS	**Day 10 – Day 24** 0.5 retinoic Acid (R.A) 1mM Taurine	24 days	• Formation of 3D optic cups and 3D organoids with further differentiated into retinal progenitors. • RPE and fully stratified neuroepithelium (NR). • Expression of NR cells PRs, BCs, GCs, HCs, ACs, MGCs. • Lamination including ONL, INL, GCL • Apical-basal polarity, inner portion invaginated with the apical site.
(Nakano et al., 2012)	hESCs 3D SFEBq	Floating SFEBq-cultured hESC aggregates Balance of RPE and NR differentiation lead to OC formation	**Day 0- Day 12** 96-well low-cell-adhesion plates (lipidure coat) **Day 12** 10 cm Petri dishes	**Day 0 - Day 18** DMEM/F12, N2, NEAA, 1% P/S 1% antimycotic, 20% KOSR, RI, IWR1e **Day 12 – Day 18** Add FBS **Day 15 - Day 18** Add Chir99021, SAG	**Day 18 - Day 24** DMEM/F12, 1% GlutaMax, N2, 1% P/S, 1% Fungizone	**Day 24 - collection day** DMEM/F12 , GlutaMax, N2, 10% FBS, 0.5 µM R.A	126 days	• Formation of 3D optic cups and 3D organoids with further differentiated into retinal progenitors. • Multi-layered neural retina with RPE and fully stratified NR. • Expression of PR-specific markers, rods and cones, GC, and interneuron precursors. • Increase PR (Cones and Rods) number and maturation. • Presence of IS and connecting cilium (CC).
(Zhong et al., 2014)	hiPSC	Combination of 2- & 3-dimensional RO formation	**Day 0 - Day 7** Suspension **Day 7-28** Adherent culture of hiPSCs aggregates **Day 28** Suspension	**Day 0 – Day 16** DMEM/F12, 1% N2, NEAA, 2µg/ml Heparin **At day 7** DMEM/F12, 2% B27, 1% MEM-NEAA, 1% P/S, 1% Fungiozone	**Day 16 - collection day** DMEM/F12, 2% B27, 1% MEM-NEAA, 1% P/S, 1% Fungizone,	**At day 42** 10% FBS, 100 µM Taurine, 2mM GlutaMAX **At day 63** 0.5 µM R.A	Retinal cup: 30-35 days PRs: 21 weeks	• Formation of 3D optic cups. • Lamination including ONL, INL and GCL. • Expression of PR-specific markers (Rods, cones), GC, HC, AC, BC, and MGCs. • Presence of OLM, IS, cc, and OS with disc membranes. • Phototransduction and photosensitivity.

Publication	Cell source	Retinal organoids formation method	Differentiation methods				Protocol Length	Features/ Characteristics
			Plates	Medium				
(Phillips et al., 2014)	Blood derived hiPSCs	hiPSC-OV RPE	**Day 0 - Day 6** Suspension **Day 6 - Day 20** Adherent culture of hiPSCs aggregates **Day 28** Suspension	**Day 0 - Day 4** DMEM/F12, 20% KOSR, 1% MEM-NEAA, 1 mM L-glutamine, and 0.1 mM β-mercaptoethanol	**Day 4 - Day 16** DMEM/F12, 1% N2, 1% MEM – NEAA 2µg /mL heparin	**Day 16 – collection day** DMEM/F12 , MEM-NEAA 2% B27 supplement 1% P/S	OV: 20 days RPE 40-50 days	• Some degree of lamination, with RGC-like cells in an inner most layer and recoverin positive PR-like cells in an outer layer. • Formation of optic vesicle-like structures. • Homogenous population of proliferative neuroretinal progenitor cells (NRPCs).
(Mellough et al., 2015)	hESC H9 hiPSCs	Outgrowth of RO positive spheres	SFEB culture	**Day 0 - Day 37** DMEM/F12, 1% N2, MEM-NEAA 2 µg/mL heparin IGF-1 (5 ng/ml)	**Day 37 - Day 90** N2, G-MEM, 5% KOSR, 0.1 mM MEM-NEAA, 1 mM pyruvate, 0.1 mM β-mercaptoethanol, 1 µM R.A 100 µM taurine, N2 P/S 10 ng/ml IGF-1		90 days	• Formation of 3D optic-cups which undergo further differentiation into multi-layered neural retina with RPE and fully stratified NR. • Synapses (inner and outer plexiform layer, indicative of synaptic zones that connect PRs with bipolar and ganglion cells). • Enhance optic cup differentiation. • Acceleration of PRC maturation. • Multilayer optic vesicle-like structures comprising multiple retinal cell types and displaying the ability to form retinal laminae.
(Hallam et al., 2018a)	hiPSC	Floating SFEBq-cultured hESC aggregates	**Day 0 - Day 17:** 96-well lipidure-coated U-bottom plate **Day 18:** Pooled in 6-well plates	**Day 0 - Day 18:** 45% IMDM 45% HAM's F12, 10% KOSR, 1% GlutaMAX 1% CDLC, 450 µM 1-thioglycerol M6145 **At Day 6:** 1.5 nM BMP-4	**Day 18 - Day 24:** DMEM/F12, 10% FBS, 1% GlutaMAX 1% N2, 1% Pen/Strep DMEM/F12, 3 µM CHIR99021 5µM SU5402	**Day 24:** Same as day 18 without CHIR99021 and SU5402	150 days	• 3D optic-cup with RPE and fully stratified NR. • PR-specific markers PR (rods and cones), GC, HC, AC, BC, and MGCs. • Lamination including ONL, INL and GCL. • Presence of IS, cc, and OS-like structures with disc membranes. • Formation of synapses. • Phototransduction and photosensitivity.

1.3.2.5. The use of hiPSCs and ESCs in the generation of human RPE cells

In addition to the generation of retinal organoids, other human eye cells, including RPE cells, have been generated from hiPSCs or ESCs to study inherited retinal diseases (IRDs) and to identify common mechanisms between retina and RPE cells.

The RPE is a monolayer of pigmented hexagonal cells that lie between the PRs and the choriocapillaris of the retina. It is fundamental for the normal function of the retina (Kolb H, 1995). Several studies have reported the generation of RPE cells using different protocols (**Table 1-4**) (Hallam et al., 2017, Regent et al., 2019, Chichagova et al., 2017). Studies have reported differentiation of hiPSCs into RPE cells using RPE inducers such as activin A (Regent et al., 2019), nicotinamide (Ferrer et al., 2014, Regent et al., 2019) and retinal inducing factors such as noggin (Ferrer et al., 2014). Also, Wnt inhibitors (DKK1 and FGF2) (Osakada et al., 2008, Klimanskaya et al., 2004, Buchholz et al., 2009) and Nodal signalling inhibitors (Lefty-A) (Osakada et al., 2008), inhibiting specific signalling pathways, such as the WNT signalling pathway, have been used to direct PSCs towards a range of retinal fates (**Table 1-4**) (Lund et al., 2006, Osakada et al., 2008).

PSC-derived RPE cells are considered a potential therapy for some retinal degenerative diseases as in animal models, transplantation of hiPSCs-derived RPE cells has shown promising results (Carr et al., 2009). However, transplantation of hiPSC-derived RPE cells in humans in the past revealed some safety concerns. Specifically, in 2013, the first clinical trial using hiPSC-RPEs was initiated by Takahashi and colleagues who transplanted an autologous hiPSC-derived RPE sheet to treat patients with AMD (Mandai et al., 2017). Although no adverse effects were observed in the first patient, genetic abnormalities were detected in the hiPSCs intended for the second patient. The clinical trial was subsequently cancelled due to safety concerns that associated hiPSC instability with tumorigenicity (Yoshihara et al., 2017). Later in 2017, the study was continued using allogeneic hiPSC-derived RPE cells that were safer for administration. Recently, the NIH team initiated phase I/IIa clinical trials to test the safety of autologous transplantation of the iPSC-derived RPE cells in dry-AMD patients (NCT04339764, 2020). This clinical trial opens the door to other scaffold-supported transplant approaches using iPSC-derived cells (Ikelle et al., 2020).

The generation of hiPSCs-derived RPE cells and organoids has provided a great advantage in drug and toxicological studies, since access to physiologically relevant cells and tissues is one of the main issues in pharmacological studies. However, differentiation of hiPSCs-derived RPE or organoids is a very lengthy and time-consuming procedure, and thus immediate availability

is not possible at the time of the demand. As a result, there is an emerging need to produce, expand and store complex tissues that are well characterized and could be used for such purposes. This requires the development of cryopreservation methodologies that could preserve the biological and physical functions of the cells at low temperatures and provide on-demand supply.

Table 1-4: Summary of published protocols to differentiate hiPSCs or hESCs into RPE cells

Publication	Cell source	Differentiation methods				Key factors	Collection method	Protocol Length	Features/ Characteristics
		Matrix of PSCs	Type of differentiation	Initiation	Differentiation				
(Klimanskaya et al., 2004)	hESCs	MEF, Gelatin; Feeder-free; EB	Spontaneous differentiation	DMEM, 500 u/mL P/S, 1% MEM-NEAA, 2mM of GlutaMAX-I, Carlsbad, CA 0.1 mM, β-mercaptoethanol, 8% KOSR, bFGF 10 ng/mL human LIF, 8% Plasmanate	DMEM, 500 u/mL P/S, 1% MEM-NEAA, 2mM GlutaMAX, 0.1 mM β-mercaptoethanol, 8% of KOSR	FGF2, LIF	Pigmented cells were isolated manually and re-plated	6-9 months	• Pigmentation. • Between week 4-8 less than 1% of Retinal organoids had pigmented islands. • At 6-9 months 100% of Retinal organoids had pigmented cells. • RPE-specific proteins express RPE65, CRALBP, PEDF, Bestrophin.
(Lund et al., 2006)	hESCs	MEF, Gelatin	Monolayer/Spontaneous differentiation	DMEM, 500 g/mL P/S, 1% MEM-NEAA, 2 mM GlutaMAX I, 0.1 mM -β-mercaptoethanol, 4 ng/mL bFGF, 1-ng/mL human LIF, 8% of KOSR, and 8% Plasmanate	DMEM, 15% KOSR, 500 /ml P/S, 1% MEM-NEAA, 2 mM GlutaMAX, 0.1 mM -β-mercaptoethanol, 4 ng/mL bFGF, 10 ng/mL human LIF	FGF2, LIF	Pigmented cells were isolated manually and re-plated	6-8 weeks	• RPE clusters appeared in adherent cultures and retinal organoids. • At 6-8 weeks first pigmented clusters were observed. • RPE-specific proteins express RPE65, CRALBP, PEDF and Bestrophin markers.
(Osakada et al., 2008)	hESCs hiPSCs	SFEB, Poly-D-Lysine-Laminin-Fibronectin	Directed differentiation	**ES differentiation medium:** DMEM/F-12, 0.1 mM β-mercaptoethanol, 0.1 mM MEM-NEAA, 2 mM L-glutamine, 20% KSR, 4 ng/ml bFGF	**Day 0 - Day 2** ES differentiation medium without bGFGF **Day 2 - Day 6** 20% KOSR, G-MEM, 0.1 mM MEM-NEAA, 1 mM pyruvate and 0.1 mM, β-mercaptoethanol **Day 6 - Day 14** ES differentiation medium + 15% KOSR **Day 14 - Day 20**	FGF2, Dkk1, Lefty-A	Pigmented cells were isolated manually and re-plated	120-200 days	• RPE cells have squamous and hexagonal morphology. • By day 120, RPE cells formed tight junctions. • Pigmented cells have microvilli, a basal membrane, melanin granules, adherent junctions

Publication	Cell source	Differentiation methods				Key factors	Collection method	Protocol Length	Features/ Characteristics
		Matrix of PSCs	Type of differentiation	Initiation	Differentiation				
(Osakada et al., 2008)					ES differentiation medium + 10% KOSR **Day 20 – Day 40** Dkk-1 (100 ng/ml), Lefty-A (500ng/ml)				and tight junctions.
(Buchholz et al., 2009)	hESC hiPSC	Gelatin	Monolayer/ spontaneous differentiation	**Day 0 - Day 20** DMEM/F12, 2 mM GlutaMAX-I, 10% KOSR, 0.1 mM MEM-NEAA, 0.1 mM β-mercaptoethanol	**Day 20 - Day 35** DMEM/F12, 7% KOSR, 0.1 mM MEM-NEAA, 2 mM GlutaMAX, 0.1 mM β-mercaptoethanol, 5% FBS, 10 ng/ml bFGF	FGF2 and its removal	Pigmented cells were manually isolated and re-plated onto gelatin-coated plates	60-90 days	• Pigmentation was observed at day 20-35. • RPE cells express Tyrosinase, Tyrp1, Tyrp2, and SILVER, genes involved in pigment synthesis. • RPE cells are polarised. • RPE cells express PEDF, EMMPRIN, Bestrophin, and RPE65 markers.
(Ferrer et al., 2014)	hiPSCs	Matrigel	Monolayer/ spontaneous differentiation	**Day 2- Day 5** **KOSR medium:** KOSR, 500 ng/ml Noggin, 10 μM SB431542 **Day 5 – Day 35** KOSR medium + 1 mM Nicotinamide, 150 ng/ml Activin A	PRE re-plated and cultured in taurine, hydrocortisone, THT medium until highly enriched RPE monolayer	Noggin, SB431542, Nicotinamide, Taurine	Pigmented cells were manually isolated and replated on T25 flasks and grown of RPE-THT medium	35 days	• RPE cells have ‘’cobblestone” morphology. • Pigmentation appeared at early stage (days 25–35). • RPE express differentiation genes such as TYROSINASE, RPE65, RDH5, TRPM1, CSPG5, and BEST1. • RPE cells expressed EZRIN, DCT, CLCN2, SLC16A1.

Publication	Cell source	Differentiation methods				Key factors	Collection method	Protocol Length	Features/ Characteristics
		Matrix of PSCs	Type of differentiation	Initiation	Differentiation				
(Hallam et al., 2017)	hiPSCs	Matrigel	Monolayer/ spontaneous differentiation	**Day 0 - Day 16** Differentiation medium: B-27 Supplement 10% KOSR, 1% 100X GlutaMAX, 1% P/S	**Day 16 – Day 21** Differentiation medium + 2 µM Purmorphamine	Purmorphamine	Pigmented cells were manually isolated and re-plated onto laminin coated TWs	3-4 months	• RPE cells are pigmented and have hexagonal morphology. • Express RPE markers (ZO-1, CRALBP, and BEST1). • RPE phagocytose bovine rod OS. • RPE cells secrete pigment epithelium-derived factor serpin F1, like adult RPE cells.
(Regent et al., 2019)	hiPSCs hESCs	Matrigel	Monolayer/ Directed differentiation	**Day 0 - Day 7** Differentiation medium: MEM (High Glucose), 50 µM β-mercaptoethanol 1% MEM-NEAA, 20% KOSR, 10 mM Nicotinamide	**Day 7- Day 14** Differentiation medium + 100 ng/ml Activin A **Day 14 - Day 42** Differentiation medium + 3 µM CHIR99021 **Day 42 – Collection Day** Differentiation medium + 4% KOSR	Nicotinamide, Activin A, CHIR99021	Pigmented cells were manually isolated and re-plated onto Matrigel coated dishes	8 to 12 weeks	• By day 21, RPE precursors express MITF and PAX6. • RPE cells are positive for EZRIN, BEST, ZO-1 and MERTK. • By day 42, Pigmented RPE cells were confluent.

1.4. Cryopreservation

Cryopreservation is the process that preserves living biological samples, such as organelles, cells, and tissues, at low temperatures by slowing down chemical reactions, physical intracellular and extracellular activities, and other biological processes (Jang et al., 2017).

In ancient times, around 2000 BC, maintenance and storage of perishable food was achieved using icehouses (Love, 2009). By the 20th century, the need for long-term storage of food was increasing. This long-term storage necessity required low/sub-zero temperatures and led to the development of cryogenic technologies. Luyet initially introduced the concept of cryopreservation in 1940 with the publication 'Life and Death at Low Temperature' (Luyet and Gehenio, 1940). Soon after, Polge's group discovered the effects of glycerol as a cryoprotectant agent (CPA) to maintain spermatozoa from fowl (POLGE et al., 1949). Since then, the effects of other molecules as CPAs – DMSO and ethylene glycol, were discovered and are routinely used in modern cryobiology for the cryopreservation of cells and tissues (Coriell et al., 1964).

Later, came a breakthrough hypothesis that associated the survival of cells in a solution with the rate of cooling. This hypothesis was introduced by Mazur in 1965 (Mazur, 1965) and provided the foundations to understand the mechanisms behind the cryopreservation procedure. Subsequently, in the 1980s, researchers demonstrated the importance of cooling and thawing rate in the survival of cells during cryopreservation (Chesne and Guillouzo, 1988).

Nowadays, cryopreservation offers major advantages in several sectors, including the storage and maintenance of food, and drug testing, as well as numerous medical and industrial applications. The latter application includes processes such as bone marrow transplantation, blood transfusion (Jang et al., 2017), *in vitro* fertilization, and long-term preservation of samples for general research use, in addition to the transportation of these samples between research centres (Bojic et al., 2021). Another advantage of cryopreservation, that can provide unique benefits, is the banking of mammalian cells and tissues, which can be used in clinical fields such as regenerative medicine and medical applications (Bahari et al., 2018).

Up until now, several cryopreservation protocols have been established by many research centres. These centres routinely use standard cryopreservation methods to successfully and effectively freeze a variety of different cell types, including PSCs, and yield high survival rates in doing so (Cohen et al., 2014). However, such protocols have not retained high survival and recovery rates in complex structures such as 3D organoids, tissues, or organs.

1.4.1. Methodology of cryopreservation

Generally, the main steps of the cryopreservation workflow include the collection of the samples (cells, tissues) and their transfer to the cryovessels (cryovial, plate, straw), where they will be frozen. Subsequently, tissues or cells are mixed with CPAs before freezing to protect the cells against ice crystal formation. This is known as pre-freezing treatment (**Figure 1-9**). Thereafter, samples are frozen at specific temperatures at predefined cooling rates, and later stored in the appropriate location. Usually, for long-term storage, cells are kept in liquid nitrogen vapour. Upon removal from storage, the samples are warmed and gradually thawed at certain temperatures. The samples are then washed to remove residual CPAs (**Figure 1-9**) and are then cultured as normal. From then on, the samples are maintained in a sterile incubator at 37°C with 5% CO_2, allowing them to recover (**Figure 1-9**). Each step of the cryopreservation process is crucial and needs optimisation for each specific tissue, to ensure the best survival rates are achieved.

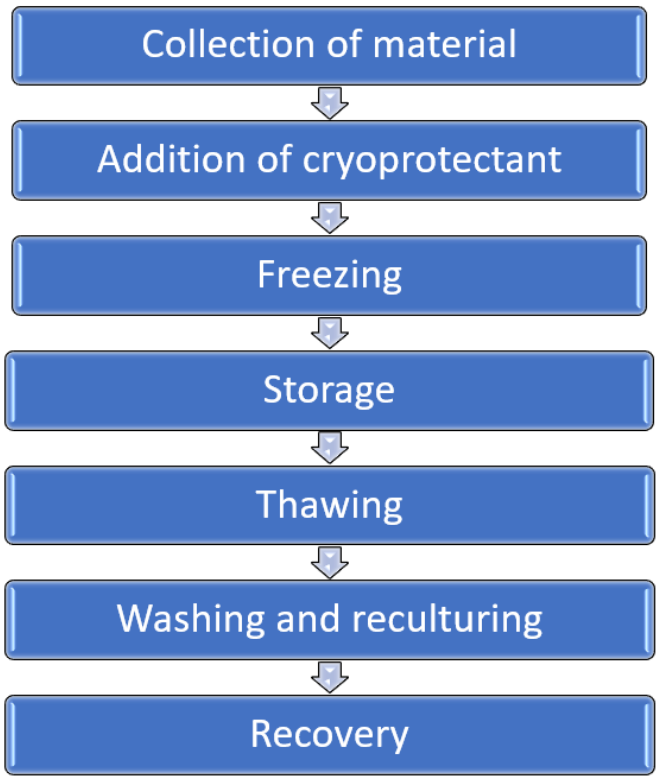

Figure 1-9: Schematic representation of cryopreservation steps.

1.4.2. Cryoprotective agents

CPAs are used in cryopreservation media to reduce freezing injury during the cryopreservation process. There are two main categories of CPAs which are defined by their ability to penetrate the cell membrane. These are permeable and non-permeable CPAs. Permeable CPAs can diffuse across the cell membrane via concentration gradients and subsequently replace the fluids inside the cell. Thereby, they function intracellularly to protect the cells from freezing injury. Dimethyl Sulfoxide (DMSO), ethylene glycol and glycerol are examples of penetrating CPAs. In contrast to this, non-penetrating CPAs cannot enter the cell. Examples of these include various sugars like sucrose or dextran (**Table 1-5)** (Jang et al., 2017). As a result of this, these CPAs can only provide extracellular protection from freezing injury. There are alternatives to CPAs that have been used for cryopreservation. These alternatives include antioxidants such as Trolox, trehalose (de Vries et al., 2019), glutathione, resveratol (Len et al., 2019) and other compounds to inhibit ice crystal formation, and subsequently reduce freeze/thaw-associated cell death (Jang et al., 2017). Typically, penetrating CPAs are used in combination with non-penetrating CPAs and antioxidants to provide both intra- and extracellular protection. However, the concentration of CPAs used along with the necessary incubation times needs to be optimised for the specific cell or tissue of interest, to minimize any possible cytotoxic effects.

Table 1-5: Common cryoprotective agents and their uses.

Compound	Source	Formulation	Permeability	Use	Toxicity
Glycerol	Fat and animal or vegetable oil	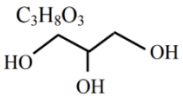	Yes	Antifreeze counteract dehydration prevent cell lysis	Metabolic acidosis
Ethylene glycol (EG)	Reaction of ethylene oxide with water	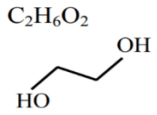	Yes	Coolant antifreeze	If converted to oxalate
Polyethylene glycol	Made from ethylene glycol and derives from petroleum	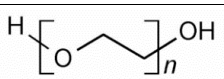	No	Increase the viscosity of the medium at low temperature to inhibit ice crystal growth	if converted to oxalate
Propylene glycol	Hydration of propylene oxide	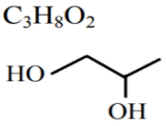	Yes	Solvent emulsifier humectant	Cell acidosis
Sulfoxides dimethyl sulfoxide (DMSO)	Wood pulp	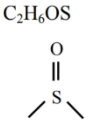	Yes	Solvent antioxidant permeability of cell membrane	Allows toxic agents to enter into the cell due to an increase in cell membrane permeability
Polyvinyl alcohol (PVA)	Synthetic resin obtained from hydrolysis of polyvinyl acetate	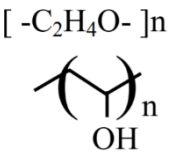	Yes	Anticoagulant	Non-toxic
Sucrose	Plants	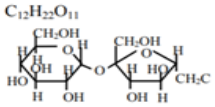	No	Protects cell membranes against chilling and freezing binding to the phospholipid head groups and forming a gel phase as cells dehydrate	Non-toxic
Trehalose	Fungi, plants, invertebrate animals	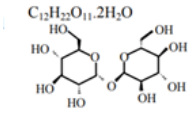	No	Similar to sucrose but with higher stability and less solubility	Non-toxic

1.4.3. Freezing methods

1.4.3.1. Existing strategies for cryopreservation

The appropriate CPA and working concentration depend on the cryopreservation method to be implemented. Currently, two conventional cryopreservation methods exist; slow-rate freezing and vitrification.

Slow freezing involves the freezing of samples with CPAs at relatively slow cooling rates with the aim of reducing the possibility of intracellular ice formation, which is the main risk associated with the cryopreservation procedure (Paynter, 2008). During slow freezing, there is an increase in water diffusion from the intracellular to the extracellular space via osmosis and the cytoplasmic water is replaced with CPAs, which prevent the formation of ice crystals inside the cell and thus minimise freezing-related cell damage (**Figure 1-10**) (Jang et al., 2017).

When using faster cooling rates, the flow of water to the extracellular space via osmosis is reduced. Hence, intracellular water remains in the cells and crystallises upon freezing, thereby causing cell death (**Figure 1-10**). In most cryopreservation protocols, the typical cooling rate is 1°C per minute but the rate should be adjusted for each sample (Jang et al., 2017) as different cell types have distinct optimal cooling rates. Particularly between different cryopreservation protocols, optimisation of the cooling rate is critical (**Figure 1-10**).

The slow freezing method was the first technique to be widely implemented following the successful cryopreservation of semen samples in 1950. Later, in 1983, the successful cryopreservation of early cleavage-stage human embryos was reported. Since then, cryopreservation of embryos and oocytes has become a well-established and commonplace technique and more than 500,000 births have been achieved from cryopreserved human embryos. This strategy utilises both 1,2-propanediol and sucrose, and has been used worldwide for the cryopreservation of zygotes and early cleavage-stage embryos (Son and Tan, 2009).

There has been increasing interest over the last few years, with regards to the vitrification method of cryopreservation to preserve cellular and structural viability (Fahy et al., 1984). Vitrification refers to the transition of a cell suspension from the aqueous phase to a ‘glass state’, where crystal formation is inhibited. This is achieved via the exposure of cells to high concentrations of non-penetrating CPAs, which interact very strongly with water molecules preventing ice formation. The cell suspension is then rapidly cooled to cryogenic temperatures which prevents ice formation, giving the cells a glassy appearance which is referred to as the ‘glass state’ (**Figure 1-10**) (Fahy and Wowk, 2021).

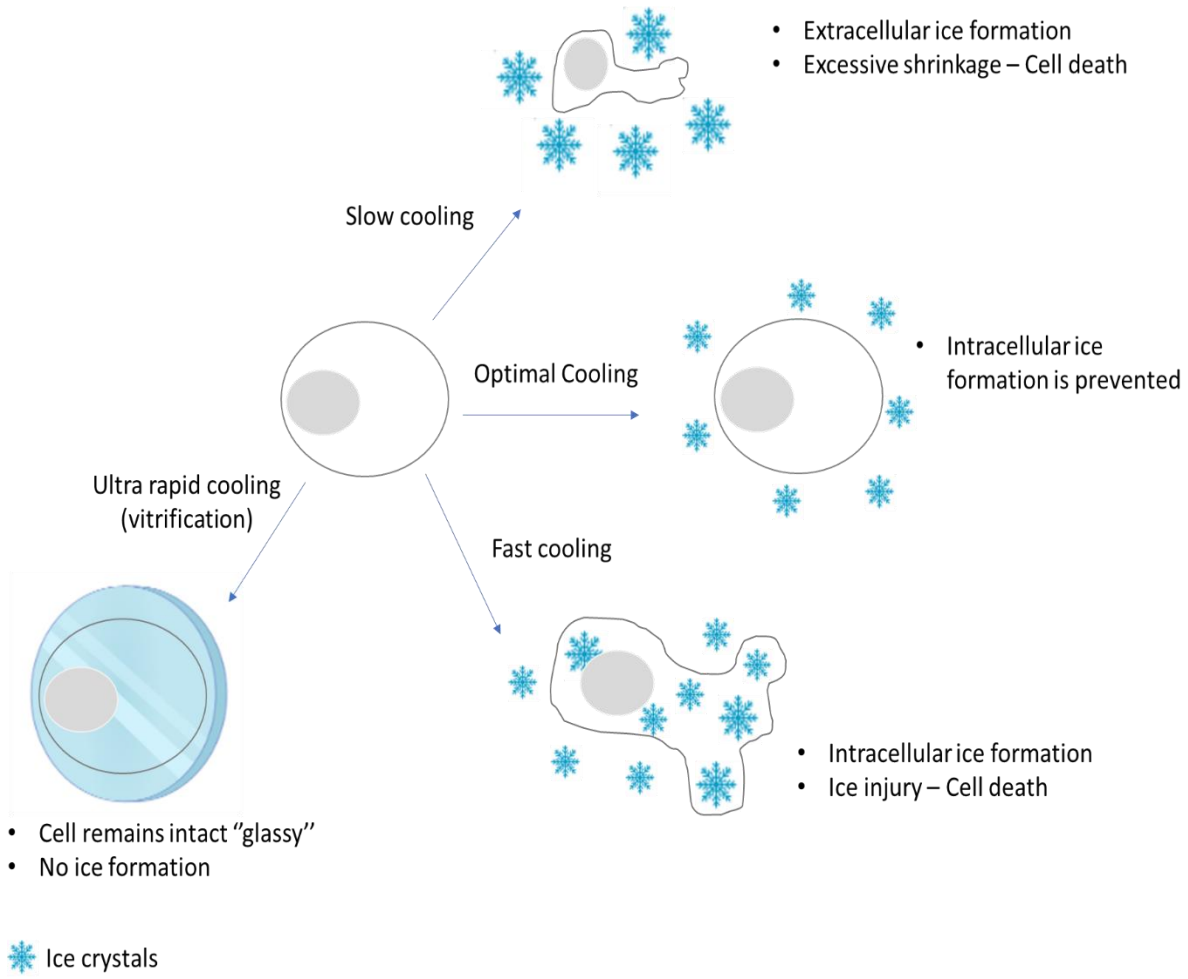

Figure 1-10: Schematic diagram of the physical events during freezing. During freezing, when the temperature drops to about -5°C, ice crystals are formed extracellularly, and hence water flows out of the cells. Subsequent cooling rates have a pivotal role in the survival of cells. If cooling rates are fast, then not all intracellular water flows out of the cell, and hence ice crystals are formed intracellularly. If cooling rates are very slow, water flows out of the cells, the cells dehydrate, and the organelles and membranes shrink. Upon ultra-rapid cooling (vitrification), cells turn into a glass state, and no icy crystals are formed. Optimal cooling rates are considered fast enough to prevent cryoinjury as a result of shrinkage and slow enough to avoid intracellular ice formation.

Multi-agent vitrification solutions have been used in several studies with promising results (**Table 1-6**). In one such study, Pichugin and colleagues reported the successful preservation of mature, organised, and complex neural networks (hippocampal slices) using vitrification solutions, namely VEG and VM3. These solutions contained DMSO, formamide and ethylene glycol (Pichugin et al., 2006) (**Table 1-6**). In another study, Nakano and colleagues reported the successful preservation of stratified neural retina, derived from hESCs. With the use of en bloc cryopreservation method of vitrification, they maintained the expression of several retina-specific markers, including progenitor marker Chx10, ganglion cell marker Pax6 and PR marker

Blimp1 (**Table 1-6**) (Nakano et al., 2012). Their method offers a new approach to cryopreserve stratified neural retina of human origin.

In addition to these applications, the vitrification method is considered a promising and effective approach for the cryopreservation of embryos. However, the scaling up of vitrification protocols to effectively cryopreserve larger tissues/structures has not been achieved, impeding their application to the clinical realm.

Table 1-6: Summary of vitrification experiments.

Publication	Cell type	CPA	Freezing	Thawing	Viability
(Valdez et al., 1992)	Mouse blastocysts	20% Ethylene Glycol (EG), 20% Me2SO 10% 1,3-butanediol	Equilibrated for 3 minutes at RT in 25% CPA. Followed by storage in liquid nitrogen.	20°C (water bath in straws)	96.2% developmental rate after 24 hours.
(Reubinoff et al., 2001)	Human ESCs	20% Me2SO, 20% EG, 0.5M Sucrose	liquid nitrogen (using straw)	37°C	All clumps recovered.
(Fujioka et al., 2004)	Human ESCs	2M Me2SO, 1M Acetamide, 3M PG	liquid nitrogen	37°C	12.2% normal morphology and karyotype.
(Kuleshova et al., 2004)	Hepatocytes	40% EG, 0.6 M Sucrose	cooling: 400°C/minute	650°C/minute	Almost 100% retention of cell function.
(Pichugin et al., 2006)	Hippocampal slices	50% w/v VEG 61% w/v VM3	liquid nitrogen	−10°C	Structure and Viability are well preserved.
(Wang et al., 2007)	Articular cartilage	72% Me2SO	liquidus tracking (−170°C)	−5°C	Functionality 60%
(Kuleshova et al., 2009)	Mouse neural stem cells (NSCs)	40% EG, 0.6M Sucrose	liquid nitrogen	38°C (water bath in straws)	>99% viability
(Nakano et al., 2012)	Neural retina (NR) derived from hESCs	2 M DMSO, 1 M acetamide, and 3 M PG, 10% DMSO, 5% EG, and 10% sucrose	liquid nitrogen	Addition of warmed medium directly to the freezing tube	NR integrity was preserved Expression of Chx10 (progenitors) Pax6 (GCs), Blimp1 (PR precursors).

Despite the many advantages vitrification offers, the high concentrations of CPAs required is a major disadvantage (Fahy et al., 2004). During vitrification, cells are exposed to a high concentration of CPAs which enter the cells, occupy the space and thus decrease the volume of intracellular water compared to the physiological levels. High concentration usage of these CPAs may induce cell damage and cytotoxicity as a consequence of abrupt osmotic changes (Pegg, 2007). In addition to this, the removal of CPAs during thawing can be hazardous for the

cells. This is due to the exposure of cells at a lower concentration of permeable CPAs, resulting in osmotic uptake and cellular swelling (Jang et al., 2017). At diluted concentrations, permeable CPAs begin to leave the cell, and are replaced by water via osmosis. Following this step, the cells should be returned to their typical physiological volume (Pegg, 2007). The degree of shrinkage and swelling of cells after the addition of permeable CPAs largely depends on the concentration of CPAs used and the membrane's permeability to CPAs and water. Therefore, for the best chance of cell survival, a balance among the sample volume, cooling and thawing rate, and the concentration of CPAs should be maintained (Pegg, 2007) (Zhang et al., 2011). In cases where there is no balance between these factors, the cells are subjected to a range of thermal, chemical, and mechanical forces that can affect the cells' viability and functionality, leading to cryoinjuries.

1.4.4. Cryopreservation Injuries

Cryoinjury is defined as the damage of cells caused by changes in water states either intracellularly or extracellularly at low temperatures. Specifically, biophysical and physicochemical reactions are affected by different parameters such as cooling and thawing rate, and CPAs concentration. Additionally, fluctuations in temperature during cooling can damage cells due to intracellular water loss or intracellular ice formation, causing deformation of the cells. Examples of cryopreservation injuries include intracellular ice formation and cellular dehydration (Jang et al., 2017). The phenomenon of ice formation corresponds to the solidification process, which is defined as the transformation of solutions from a liquid phase towards a solid-state. This process depends on the aggregation speed and is proportional to the changes in cytoplasmic temperature and the dehydration of intracellular compartments. Ice formation, either intracellularly or extracellularly, is detrimental to cell samples. The process of crystallization generates mechanical stress on the cell membrane and modifies the chemical environment leading to decreased cell viability post-thaw (Bakhach, 2009).

1.4.4.1. Cellular dehydration

Extracellular ice formation increases the ion concentration of the extracellular space. This results in the efflux of intracellular water and the influx of solutes into the intracellular space. The loss of cytoplasmic water results in cellular dehydration and consequentially, cellular lesions, of which mechanical stress and thermal shock are the two main forms (Bakhach, 2009).

1.4.4.1.1. Mechanical stress

Mechanical stress is caused by extracellular ice formation which deforms the cell. This occurs as a result of growing masses of ice that squeeze the cells into narrow channels of unfrozen solutes. Specifically, the formed ice crystals separate the cells into small channels filled with residual water, necessary for cell function (Mazur et al., 1981). As the temperature falls, the cell volume decreases and progressively shrinks and deforms the cells. Rapid efflux of water decreases the volume of cells to approximately 50%, resulting in structural distortion of the cells (Bakhach, 2009).

1.4.4.1.2. Thermal shock

Thermal shock is caused by rapid changes in temperature during the cooling of cells. This can occur in the absence of ice formation and typically between the temperatures of +15°C and 37°C. However, shock can also occur between 0°C and −80°C. Contractions of the cellular components of the cell can induce the formation of lesions. This process is affected by changes in anion composition, especially chloride, acetate and sulphate anions (Bakhach, 2009). The addition of CPAs works to reduce thermal shock when used in combination with slow cooling (Pegg et al., 2006).

1.4.4.1.3. Intracellular crystallisation

Intracellular ice formation is often due to rapid cooling. During fast cooling, the diffusion of water is relatively slow, and the water remains in the cell. This residual water freezes and forms intracellular ice crystals, disrupting the integrity of the cell. This finding was noted following the observation of low cell viability after fast cooling experiments (Mazur, 1960). Cell density is another important factor to consider in the freezing process. For example, in multicellular structures, such as spheroids or confluent monolayers where there is close cell-cell contact, cellular dehydration is more complicated. Water exits the cell sequentially from the centre of the structure to the periphery (Ehrhart et al., 2009).

1.4.4.1.4. Cryoinjury associated with storage period

In addition to the harmful effects of ice formation, storage is another important parameter essential for the viability of cells. Cold storage (4°C) is typically used for storage purposes in the transportation of cells, but also it can be used for short-term storage of organs where cryopreservation is not appropriate. At temperatures between 0°C and −25°C, the main challenge is related to cellular activity, which is reduced but not completely inactivated. This has a negative effect on the cell as it can cause cellular swelling, membrane leakage, and tissue degeneration (Baertschiger et al., 2008). During cryopreservation, tissues must inevitably transverse from this temperature window twice; during freezing and thawing, and each time cells need to overcome obstacles such as extracellular and intercellular ice formation, dehydration, and osmotic effects and oxidative stress, which can cause cell damage. At temperatures below −40°C, the physicochemical changes are dramatically reduced, yet the cells remain viable. Therefore, for longer preservation of cells, it is recommended to freeze the cells below −130°C. This is known as the vapour phase of liquid nitrogen, where biological and chemical reactions are completely inhibited, and therefore no tissue degeneration can occur (Gast et al., 2018).

Despite the progress in cryopreservation methodologies in recent years, cryopreservation of cell types such as hepatocytes, and tissues like blood vessels, skin or even reproductive organs (testes and ovaries) remains difficult (Taylor et al., 2019). The cryopreservation of organs and complex tissues are limited to several hours of viability before they are no longer suitable for use, and this is one of the major concerns in transplantation today. This fact alone highlights the importance and necessity of effective cryopreservation methodologies to efficiently cryopreserve tissue and organs, and enhance their storage and banking capabilities. In addition to this, effective cryopreservation will benefit pharmacological companies by facilitating the generation of a supply of complex tissues that will be readily available at the time of demand for drug discovery and development. An increase of tissue availability will also strengthen collaboration between research centres and hospitals, as with the use of efficient transportation methods, biological and functional properties of precious organs and tissue samples will be preserved.

1.5. Shipment of hiPSC retinal organoids

The transportation of efficiently cryopreserved samples has the potential to forge strong collaborative networks between research centres, pharmaceutical companies, and medical centres. However, the method of transportation and the conditions of delivery must be executed in a way that will ensure the viability of the tissue.

One way this could be facilitated is the use of special containers that maintain the temperature at a certain range optimal for the tissue in question (Prendini et al., 2002). This is an important consideration as shipping conditions, such as temperature control and timing, are critical for tissue viability. Therefore to ensure that samples remain intact, they must be shipped immediately using the shortest possible route and under conditions that are permissive for maintaining cellular structure and physiological functions (Prendini et al., 2002). The transportation of tissue is mainly dependent on three parameters; the shipment method, the nature of the samples and the state of samples i.e. whether they are preserved or live. Therefore, limiting temperature fluctuations is very important for the survival and functionality of the sample. This is because exposure of tissues to high or low temperatures could affect their biological and mechanical activity, inducing cellular lesions and intracellular degeneration.

A common method used for shipping biological samples is to use dry ice, which keeps samples stable at approximately -80°C. Another option is to use cryogenic storage boxes with frozen cool packs to keep samples at approximately -20°C. Although these methods can keep the samples at the temperatures needed to remain viable, there is a high risk for coolants to thaw and dry ice to evaporate, particularly if there are delays in the shipments.

Several studies have reported that cryopreservation and subsequent thawing could have a negative impact on the viability of cells or tissues. In addition to this, most pharmacological companies or clinical end-users prefer the supply of samples to be ready to use without the need for thawing (Mathew et al., 2004). This suggests that shipment of samples at cold temperatures (2–8°C) might be more appropriate. However, it appears that temperature is not the only concern in this process. A few studies have also shown that vibrations throughout the shipment process could cause detrimental effects and reduce cell viability during transportation (Tirkkonen et al., 2011). Indeed, Nikolaev and colleagues have shown that the viability of hMSCs, when subjected to vibrations to recapitulate movement from vehicular transport, was reduced when compared to control cells. However, in this case, it is likely that the damaging effects observed on hMSCs are due to a combination of both mechanical and hypothermic effects induced by vibration and cold storage, respectively (Nikolaev et al., 2012).

An alternative transportation method for samples is to ship at room temperature (RT) (18–24°C). This method is considered to be one of the most commonly used approaches based on a research survey for therapeutic product transportation (Pamphilon et al., 2010). Several studies have attempted to ship biological samples at RT. Hori and colleagues have demonstrated the usage of a new technology to ship RPE tissues at RT. This technology utilises a heat-insulating container to minimise exposure of the cells to physical and chemical stresses (Hori et al., 2019).

In addition to the protection of samples from cryoinjury, transportation of samples at RT provides benefits both financially and logistically.

- *Financial advantages:* Whilst there are benefits to freezing tissue samples, there are also significant drawbacks, especially if the specimens are not appropriately frozen. An alternative approach is to ship at RT, which is cheaper and requires less storage space during shipment. There are typically significant costs associated with the shipment of frozen samples as they require special packaging with dry ice. The shipment is therefore hazardous, and its transport is more heavily regulated (Lou et al., 2014). In addition to this, any delays with the shipment of frozen samples pose the risk of thawing and thus damaging of the tissue.
- *Sample protections:* Shipment at RT does not require the transport of tissues in these special temperature-regulated containers (Lou et al., 2014). This provides a great benefit over cold shipment and storage, as it negates the risks associated with unforeseen events that would affect only a temperature-sensitive shipment, such as power failure.
- *Logistical advantages:* Shipment at RT does not require specialized labour or handling (Lou et al., 2014). This allows the recipient of the parcel to process the specimen without any specialized instructions for the thawing and recovery process.

Despite the numerous advantages of this shipment method, several studies have reported detrimental effects of storing and transporting cells at ambient temperature. One such study reported that the storage and transport of hematopoietic progenitor cells (HPCs) at RT significantly reduced the viability of HPCs, compared to HPCs cells stored at cooled temperatures (Antonenas et al., 2006). Nevertheless, shipping at RT may be more beneficial for larger tissues such as organoids or human tissues where cryopreservation is not appropriate.

Shipping or transportation is a viable solution to overcome the difficulties associated with the limited availability of transplant grafts worldwide. Although high-performance preservation systems have been conceptualised and tested to extend the preservation of organs (liver or heart)

for transplantation purposes, these methods are costly and have been specifically optimised to handle 3D organs and not regenerative transplantable tissues (Giwa et al., 2017).

Also, the generation of tissue-engineered cell sheets requires well-trained specialists to guarantee the quality, safety, and validity of the cells. These engineered tissues are often generated off-site in a laboratory environment away from hospitals, where they are required for use in patients. This highlights the need for effective transport protocols of tissues between institutions that ensures safe delivery of the tissues at an appropriate cost. The shipment of hESC/hiPSC-derived transplantable cells or tissues minimises the costs of unnecessary equipment and facilitates the widespread use of engineered cell sheets (Hori et al., 2019). Several clinical studies have already developed transplants using hESCs or hiPSCs to treat patients suffering from retinal disorders such as AMD. Mandai and colleagues performed the first autotransplantation of hiPSC-derived RPE cells in an AMD patient in 2013 (Mandai et al., 2017).

The development of 3D retina has been established to provide patient-specific disease models to better understand human retinal diseases. These models help to reveal unknown mechanisms of pathogenesis and provide new pathways for drug screening (Hallam et al., 2017). However, this technology is highly demanding and time-consuming and requires specialist techniques to grow and mature them. As a result of this, the technology is not available in many laboratories. Therefore, transportation of 3D retinal structures is essential to increase accessibility and availability globally.

To facilitate the transportation of retinal organoids in pharmacological centres for drug discovery and cell therapy-based studies, it is important to validate the most optimal transport conditions that will retain the structural and functional characteristics of retinal organoids. Recently, a new protocol for shipping retinal organoids at 37°C was developed using a battery-driven portable shipping container to maintain the temperature. This study has shown that retinal organoids can remain viable over large distances, facilitating the transportation of retinal tissues worldwide. A downside to this transportation method is that battery-based containers may be heavy and therefore less cost-effective for shipping purposes. Also, battery failure during transportation may delay results up to 5-7 months, which is the time required to generate and mature retinal organoids (Singh et al., 2020). Therefore, to avoid any variables influencing the widespread transportation of retinal organoids, shipping of retinal organoids at ambient temperature could facilitate substantial savings in time and money. This shipping method does not require sample freezing, and hence any possible damaging or cytotoxic effects caused during cryopreservation are prevented. Also, this method provides a product ready to be used.

ESC and/or hiPSCs-derived 3D models serve as a powerful tool in regenerative medicine as a robust platform for cell-based therapies. Global shipment of these models increases accessibility to this niche technology and yields substantial potential in the drug discovery and disease modelling field, particularly for cases of inherited retinal disease (IRD) pathogenesis. This increased availability of human tissue will ultimately facilitate collaborative networks between research centres, pharmaceutical companies, and medical centres.

1.6. Inherited Retinal Diseases

Inherited Retinal Diseases (IRDs) are a large and diverse group of clinically and genetically heterogeneous disorders that are characterized by progressive degeneration of retinal cells and/or RPE cells, leading to visual field loss and eventually blindness (Cremers et al., 2018). It is estimated that approximately 36 million individuals are blind, and 253 million people have moderate to severe visual impairment worldwide (Motta et al., 2018). The total incidence of IRDs is estimated to be 1:3000 individuals worldwide, with family history and mutations in disease-causing genes being the main risk factors. To date, more than 300 genes have been discovered and implicated in the development of IRDs (Wright et al., 2010). The spectrum of IRDs is broadly classified based on the disease progression and the retinal cell types that are primarily involved. Some common IRDs are Stargardt disease (STGD1), Leber congenital amaurosis (LCA) and achromatopsia, but the most common is RP (Cremers et al., 2018).

1.6.1. Retinitis Pigmentosa

1.6.1.1. Definition

RP is a group of genetic retinal diseases characterized by progressive loss of peripheral retinal cells (PRs and RPE cells) that subsequently damage inner retinal cells leading to atrophy of the retinal tissue (Hamel, 2006). Specifically, rod PRs degenerate gradually and eventually die, inducing various symptoms (Jones et al., 2012). Initially, visual impairment manifests as night blindness followed by peripheral vision loss where the visual field is constricted. Later in life, central vision can be affected, causing partial or complete blindness, depending on the severity of the disease (Hartong et al., 2006). Throughout the years, multiple different terms have been used to describe RP, including pigmentary retinopathy or primary pigmentary retinal degeneration referring to the pigment deposits.

1.6.1.2. Epidemiology

The prevalence of RP is 1:4,000 globally, with approximately 1.5 million affected individuals. However, the prevalence of RP varies from 1:750 to 1:9,000 depending on the geographic region. In the USA and Switzerland, the prevalence is about 1:5,200 and 1:6,000, respectively. The highest frequency of occurrence with 1:1,875 individuals affected is in India (Gregory-Evans et al., 2013).

1.6.1.3. Classification

RP is classified as systemic, syndromic, or non-syndromic, based on whether the disease is associated with dysfunction in other organs or not. Systemic RP is associated with systemic abnormalities affecting multiple organs, whereas syndromic RP is associated with other neurosensory systems. Non-syndromic RP is an isolated disorder that is not associated with other organs and affects only the sight. Although most RP cases are classified as non-syndromic, 20-30% of RP patients are associated with non-ocular abnormalities, such as Usher syndrome where both sight and hearing are affected (Verbakel et al., 2018). Non-syndromic RP can be inherited via all the three Mendelian modes of inheritance (Ferrari et al., 2011).

1.6.1.4. Inheritance

Approximately 30-40% of RP cases are diagnosed with autosomal dominant inheritance (**Figure 1-11**), meaning that the disease can be inherited in the presence of a single mutated allele. Autosomal dominant RP (adRP) is the mildest inheritance form, and patients have the best long-term prognosis concerning retaining central vision (Verbakel et al., 2018). Approximately 25% of adRP cases are caused by mutations in the *RHO* gene, which encodes rhodopsin protein, a key component of the visual cycle. This is the most common mutation. The second most common cause of adRP accounts for approximately 5-10% of cases and is caused by mutations in Peripherin genes, followed by mutations in the pre-mRNA splicing factor 31 (*PRPF31)* that account the 8-10% of adRP cases (Brydon et al., 2019, Wheway et al., 2020).

Autosomal recessive RP (arRP) accounts for approximately 50-60% of all RP cases (**Figure 1-11**), which are caused by the inheritance of two mutated alleles of a gene. The most common cause of arRP are mutations in the *USH2A* gene that accounts for 10-15% of all arRP cases. However, approximately 35 other genes are associated with the disease (Bernal et al., 2003).

X-Linked RP accounts for 5-15% of all cases (**Figure 1-11**), of which 70-80% are caused by mutations in RP GTPase regulator (*RPGR*). At present, 5 genes are associated with the disease, indicating that the rest of the cases (7-10%) are caused by mutations in *RP2*, *RP6*, *RP23*, and *RP24* genes. X-linked RP is inherited more likely in men since the mutation is located on the X chromosome (Hartong et al., 2006).

Non-mendelian inheritance patterns are present for RP also. A small percentage of RP cases are classified as digenic or mitochondrial inheritance (**Figure 1-11**) caused by mutations in *PRPH2* and *ROM1* genes (Dryja et al., 1997).

Although RP is well categorised in different modes of inheritance, classification of RP in a specific group is very challenging. This is because RP comprises a class of complex diseases where mutations from different genes can cause the same phenotype. Also, different phenotypes can be caused by mutations in the same gene as a result of allelic heterogeneity (Nash et al., 2015). For example, mutations in *Rhodopsin* could cause adRP but also arRP. In addition to this, the disease phenotype and the severity of the disorder often vary between patients who share the same mutation due to other genetic and/or environmental factors (Daiger et al., 2007).

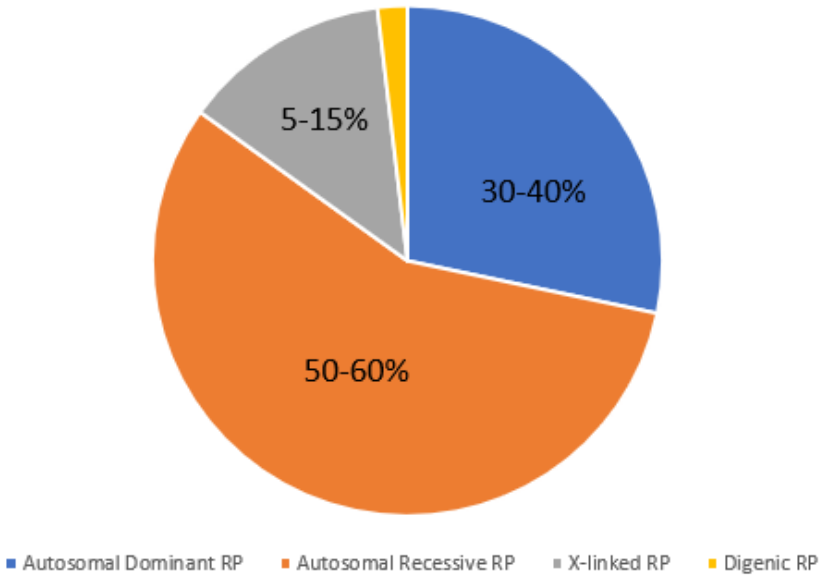

Figure 1-11: Estimated percentage of RP cases by modes of inheritance. Orange represents autosomal recessive RP (50-60%), blue represents autosomal dominant RP (30-40%), grey represents X-Linked RP (5-15%), and yellow represents Digenic RP (30-40%).

1.6.1.5. Clinical features

The clinical features of non-syndromic RP begin with night blindness. In the first or second decade of their life, RP patients experience difficulties with vision at night. This is referred to as nyctalopia (Gregory-Evans et al., 2013). In the early stages of disease, the quality of vision

is often not affected. Some RP patients do exhibit a narrowing of the visual field in the dark, but it is not often recognized as the loss is very gradual (**Figure 1-12**). The second hallmark feature of RP is progressive or gradual loss of the peripheral vision. As the disease develops, patients begin to lose vision from their far mid-peripheral field and eventually develop constricted vision known as 'tunnel vision' (**Figure 1-12**). Usually, visual field loss is symmetric between both eyes as the disease advances (Hamel, 2006).

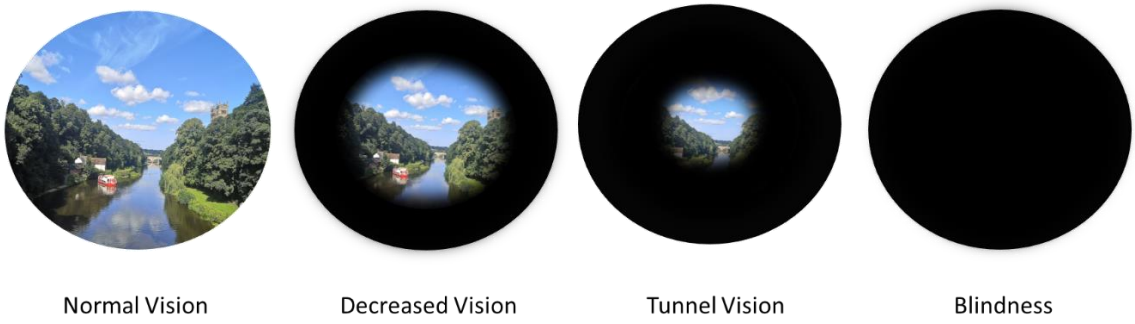

Figure 1-12: Stages of progressive visual loss in RP. Image of a normal visual field (left image). The death of PRs and accumulation of pigment decreases the visual field (second image from the left) characterized by visual field constriction. This is followed by tunnel vision (second image from the right) which is characterized by loss of peripheral vision, and central vision is still preserved at this stage. Subsequently, central vision is lost, leading to complete blindness (right image).

Central visual loss usually remains intact and preserved until the peripheral vision is lost. However, in some cases, central vision (specifically central cone function) is lost, leading to a reduction in visual acuity (**Figure 1-12**). This statement is supported by several research studies that reported the degeneration of cone PRs immediately after the loss of rod PRs (Hamel, 2006). Lin and colleagues support the finding that mutations in the rod-specific phosphodiesterase gene induces the degeneration of rod PRs in *rd1* mouse, a murine model for human RP. The degeneration of PRs subsequently affects the structural remodelling of neuroretina cells such as bipolar and horizontal cells (Lin et al., 2009).

Clinically, RP patients are characterized by pigmentary deposits of melanin that migrate from disintegrated RPE cells in the periphery and accumulate in the interstitial spaces (**Figure 1-13**). The loss of pigmentation from RPE cells results in fundus pallor leading to the retina's desaturated appearance, which is related to attenuation of retinal vessels and arteriolar narrowing. In advanced cases, atrophy of RPE cells and the choriocapillaris results in fundus pallor and pallor of the optic nerve. Fundus topography and electroretinogram could be used to diagnose the disease (Gregory-Evans et al., 2013).

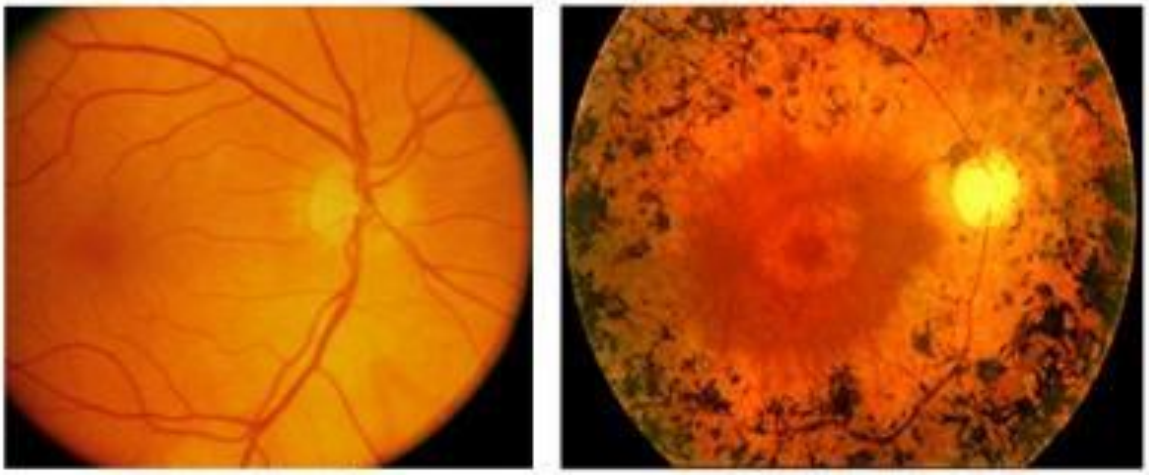

Figure 1-13: Photos of the healthy retina (left) and a RP retina (right). Fundus appearance is illustrated in the RP retina, characterised by attenuated retinal vessels, bone spicule intraretinal pigmentation and optic nerve head pallor (Gregory-Evans et al., 2013).

1.6.1.6. Pathophysiology

RP pathophysiology is caused by defects in retinal molecular pathways leading to the degeneration of PR cells and subsequently the RPE cells (Jones et al., 2012). The first histological change detected in individuals with RP is the shortening of POSs, followed by the loss of PRs. Consequently, the loss of PRs leads to a non-uniformly distributed pattern where the PR cells are displaced, leading to peripheral vision loss and night blindness (**Figure 1-14**) (Marc et al., 2003). As the disease progresses, the ONL containing the rod and cone PRs collapses and is converted into a debris layer found between the RPE layer and the INL (**Figure 1-14**) (Yang et al., 2012). Loss of the ONL induces retinal remodelling, leading to substantial changes in cell populations and connectivity between the cells (Jones et al., 2003). These include differentiation of bipolar and horizontal cells and retraction of their dendrites (**Figure 1-14**) (Marc et al., 2003). Following ablation of the sensory neuronal cells, a dense fibrotic layer is formed in the subretinal space due to an increased synthesis of filament from Müller glial cells (Marc et al., 2003). These changes lead to the hypertrophy of Müller glial cells and the migration of neuronal cells to ectopic sites, leading to complete blindness. Followed by degeneration of the ONL, pigments from the disintegration of RPE cells migrate in the inner layers of the retina, creating clumps of melanin described as bone spicules (Marc et al., 2003).

Several genes have been implicated in approximately 50% of non-syndromic forms of RP (Hartong et al., 2006). Currently, mutations in more than 80 genes have been associated with RP (Verbakel et al., 2018). These genes are involved in several cellular pathways such as the

phototransduction pathway, structural and cytoskeletal support, signalling and trafficking of intracellular proteins, splicing and synaptic interactions, and the visual cycle. Therefore, mutations in genes expressed in PR cells could affect almost every aspect of their function (Wright et al., 2010).

The diversity of genetic defects associated with this disease explains the high heterogeneity seen in RP patients. In the early 90s, the identification of the first gene involved in adRP, known as *Rhodopsin* (*RHO*), was reported (Dryja et al., 1990). Since then, and every year thereafter, new genes associated with non-syndromic RP have been included in the list. Most causative genes are retina-specific, meaning that they have a distinct role and/or expression in the retinal cells (Ferrari et al., 2011). However, several ubiquitously expressed genes have also been implicated in RP and display an isolated retinal phenotype only. These include pre-mRNA processing factors (PRPFs) such as PRPF3, PRPF8, PRPF31, PAP1 and SNRN200 (Farkas et al., 2014). These are all splicing-related genes as they are core components of the U4/U6.U5 tri-snRNP complex, a major constituent of the spliceosome (Utz et al., 2013).

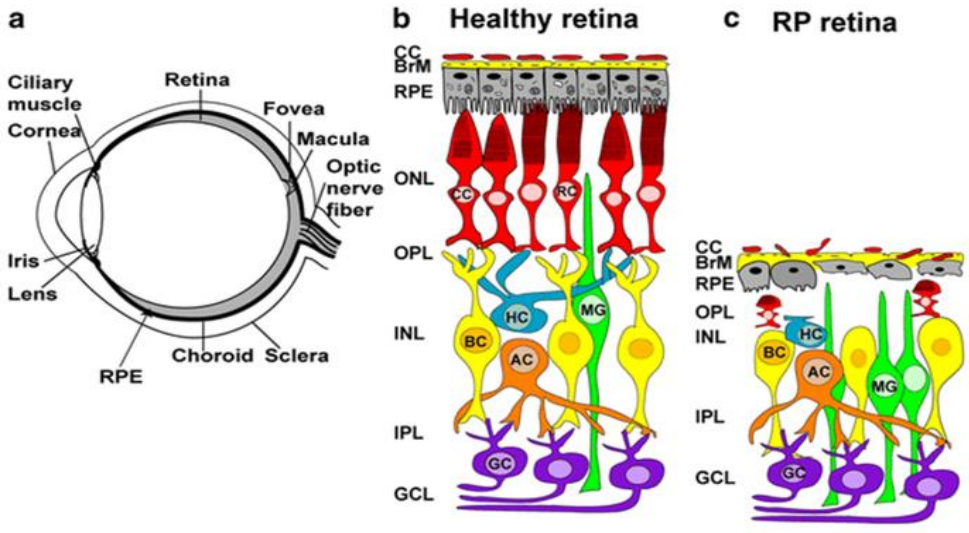

Figure 1-14: Schematic diagram of healthy and RP retinal circuit. Left panel (a) illustrates the location of the retinal, middle panel (b) represents a schematic diagram of healthy retinal circuits and right panel (c) illustrates a schematic diagram of the structure and organization of retina in RP (RP retinal circuit). The RP retina is thinner because of PR cell death. This induces subsequent dramatic changes in the structure of horizontal, bipolar and amacrine cells. cc=choriocapillaris, BrM=Bruch's membrane, RPE=retinal pigmented epithelium, ONL=outer nuclear layer, OPL=outer plexiform layer, INL=inner nuclear layer, IPL=inner plexiform layer,

GCL=ganglion cell layer CC=cone cells, RC=rod cells, BC=bipolar cells, HC=horizontal cells, AC=amacrine cells, GC=ganglion cells, MC= Müller glial cells (Singh et al., 2018).

1.7. Splicing and the Spliceosome

1.7.1. Pre-mRNA splicing

Pre-mRNA splicing is a process that takes place in the nucleus of the cell where non-coding sequences of genes, known as introns, are removed from pre-mRNA and the protein-coding sequence, known as exons, are joined together to form a mature messenger RNA (mRNA) (Růžičková and Staněk, 2017). Excision or splicing of introns and ligation of exons is performed by a large ribonucleotide protein complex called the spliceosome, which generates a mature mRNA that will subsequently be translated to form a protein.

1.7.2. The spliceosome

The spliceosome is a large, complex macromolecular machine composed of five small nuclear ribonucleoproteins U1, U2, U4/U6 and U5, known as snRNPs. In addition to this, there are accessory proteins, which together facilitate the splicing of introns from pre-mRNA in a stepwise process to produce a mature mRNA (Wahl et al., 2009). Spliceosome assembly involves the binding of U1 and U2 initially to the 5' and 3' splicing ends of the intron, respectively, to define the splicing ends of the intron. This is known as complex A (**Figure 1-15**). Subsequently, U4/U6 and U5 assemble together to form the U4/U6.U5 tri-snRNP, an important component for spliceosome activation. This is known as complex B (**Figure 1-15**). Subsequently, the tris-snRNA binds to the spliceosome complex and causes conformational changes that induce the dissociation of U1 and U4 from the complex. As a result, the intron is excised and the exons are joined together to form a mature, spliced mRNA (**Figure 1-15**). For the correct assembly of the tri-snRNA and successive splicing of pre-mRNA, the presence of all five snRNPs and PRPFs, in addition to other splicing factors, is essential (Utz et al., 2013).

PRPFs are widely expressed in all tissues of the human body. However, defects in these genes have been associated with retinal-specific phenotypes (Tanackovic et al., 2011). Approximately 10% of adRP cases are caused by defects in *pre-mRNA processing factor 31* (*PRPF31),* an essential component of the splicing machinery (Waseem et al., 2007).

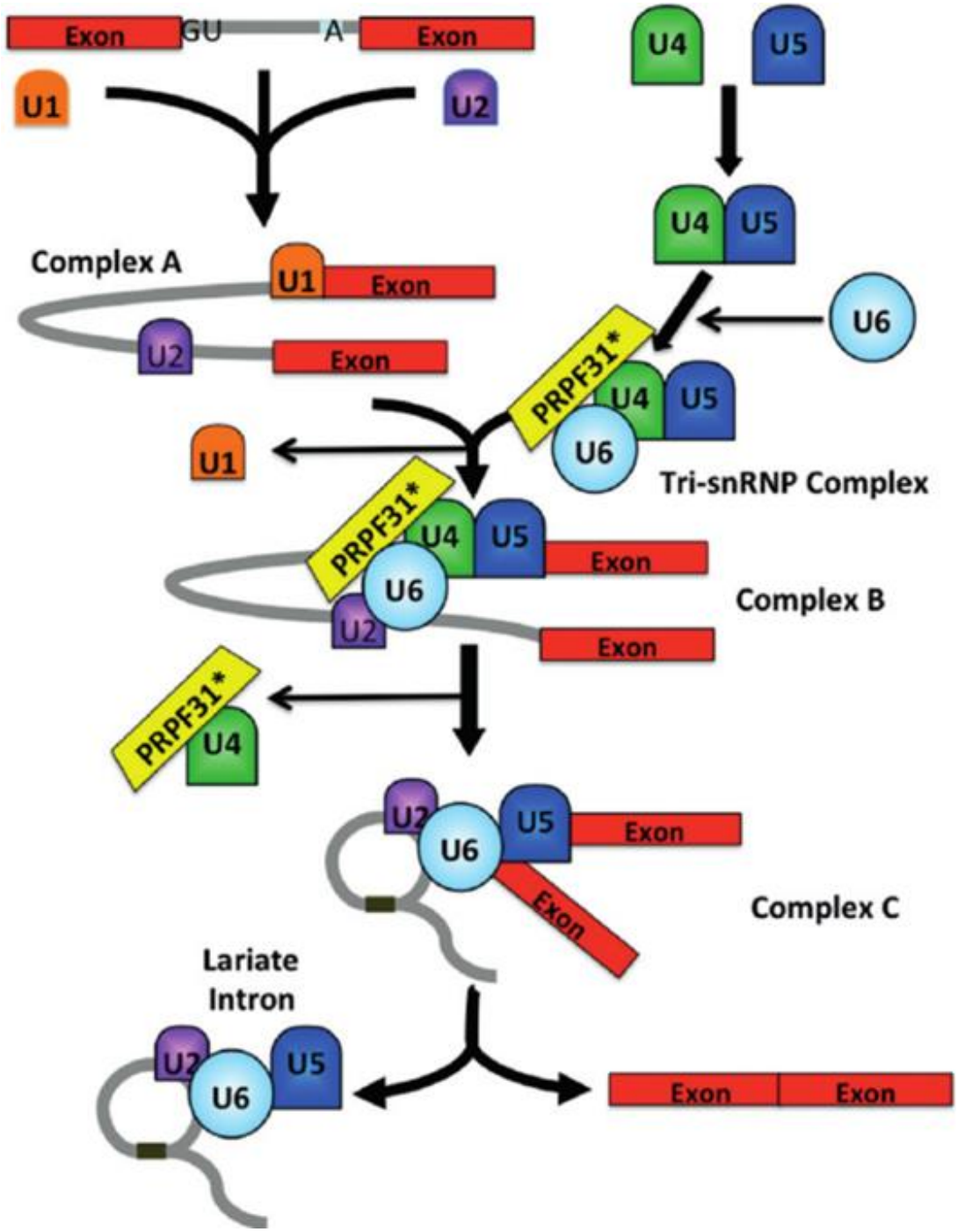

Figure 1-15: Schematic diagram of the spliceosome assembly and the excision of introns. The spliceosome assembly. The U1snRNP interact with the conserved sequences at the 5' splice site (GU) and the U2snRNP at the 3' splice site, forming the pre-spliceosome. Then, the U4/U6 snRNP is associated with the U5snRNP to form the U4/U6.U5 tri-snRNP. For the formation of the U4/U6.U5 tri-snRNP, PRPF8, PRPF3 and PRPF31, in addition to other splicing factors, are required. Once the U4/U6.U5 tri-snRNP integrate into the spliceosome, U1 and U4 are displaced from the 5' splice site and from U4/U6 snRNP, respectively, forming the Complex B. Therefore, U6 interacts with the 5' splice site and with the U2snRNP, leading to the formation of Complex C. Subsequently, the splice sites are aligned, followed by two sequential trans-esterification reactions, that result in the removal of the intron. (Obtained from Autosomal Dominant Retinitis Pigmentosa Secondary to Pre-mRNA Splicing-Factor Gene PRPF31 (RP11): Review of Disease Mechanism and Report of a Family with a Novel 3-Base Pair Insertion (Utz et al., 2013).

1.7.3. PRPF31

Mutations in *PRPF31*, which cause RP11, have been defined as the second most common cause of adRP (Hartong et al., 2006). The *PRPF31* gene is located on chromosome 19 at the position 19q13.42 (**Figure 1-16**) (Vithana et al., 2003). It is composed of 14 exons encoding a 61 kDa protein which consists of 499 amino acids (Utz et al., 2013). PRPF31 is part of the U4 small nuclear RNP, which binds to U5 to form the U4/U6.U5 tri-snRNP complex. Therefore, PRPF31 plays an important role in the assembly and stability of the U4/U6.U5 tri-snRNP complex (Tanackovic and Rivolta, 2009). However, mutations in *PRPF31* destabilize PRPF31 mRNA, leading to reduced functional PRPF31 protein, which subsequently inactivates spliceosome assembly leading to RP (Rivolta et al., 2006). The reduced concentration of functional PRPF31 and its association with RP has been confirmed in mice (Farkas et al., 2014), Drosophila (Ray et al., 2010) and zebrafish (Linder et al., 2011).

To date, the Human Genome Mutation Database (HGMD) has recorded more than 60 mutations in the *PRPF31* gene caused either by deletions, frameshifts, or mutations that inhibit splicing, induce exon skipping or generate premature stop codons (Růžičková and Staněk, 2017). All types of mutations have been shown to deregulate *PRPF31*, ultimately reducing the levels of functional protein. Different mutations in the *PRPF31* gene cause variability in clinical phenotype, age of onset, and disease severity (Audo et al., 2010). Interestingly, this degree of variability is also present within families which share the same mutations.

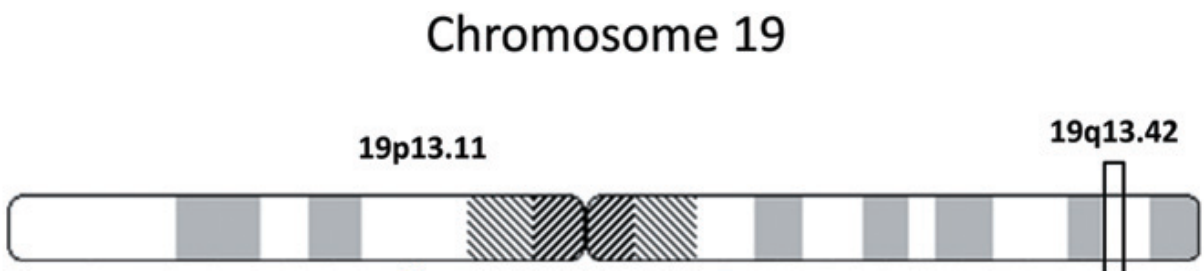

Figure 1-16: The location of the PRPF31 gene. PRPF31 gene is located on chromosome 19, in the short arm, and it is composed of 14 exons that encode a protein that consists of 499 amino acids (Nobusawa et al., 2012).

1.7.4. Impact of PRPF31 mutations on splicing

Mutations in *PRPFs* in mammalian cells have been associated with retinal degenerative diseases, although these genes are ubiquitously expressed (Farkas et al., 2014). Specifically, PRPF31 plays an essential role in the assembly and stability of the spliceosome. However,

mutations in the *PRPF31* gene have been associated only with retinal diseases causing degeneration of both RPE and PRs (Villanueva et al., 2014).

Two main hypotheses have been devised to explain how mutations in splicing factors affect only retinal cells. The first hypothesis suggests that defects in splicing factors cause splicing deficiency in all tissues. However, only retinal cells are affected due to the high levels of mRNA required in retinal cells. This hypothesis is based on haploinsufficiency. In the human retina, there are approximately 10 million rod PRs and renewal of the whole rod POSs takes approximately 10 days (Boesze-Battaglia and Goldberg, 2002). This highlights that there is an increased production of mRNA levels in the retina compared to the number of mRNA levels produced in other tissues. If only one functional copy of PRPF31 exists in retinal cells, then a reduced number of proteins are generated causing an overall deficiency in active spliceosome complexes. In this scenario, the levels of active spliceosome are inadequate for the functional splicing of genes in rod PRs (Baehr and Chen, 2001). This hypothesis was supported by previous studies indicating that defects in PRPF31 cause the translocation of PRPF31 protein from the nucleus to the cytoplasm in mammalian cells (COS-7 cells) (Wilkie et al., 2006), leading to reduced functional protein and hence insufficient splicing. Since retina and RPE cells are highly metabolic tissues requiring high splicing levels, this explains why these are the only affected cells (Wilkie et al., 2006).

A second hypothesis suggests that mutations in *PRPFs* cause retinal specific degeneration probably because PRs are more susceptible to stress caused by mutations and from splicing stress during the renewal of POSs in rod PRs (Deery et al., 2002). Another study has reported that mouse PRs display a specific slicing program with higher inclusion levels of exons that are not found in extraretinal tissues, indicating that alternative splicing can be tissue specific (Murphy et al., 2016). For example, it was previously reported that genes implicated in ciliopathies have retinal-specific isoforms (Murphy et al., 2016).

Although several hypotheses have been proposed to explain retinal-specific degeneration, the exact mechanisms correlating mutations in PRPFs and retinal cells are not well understood yet. To address this, Lako's group differentiated hiPSCs from patients harbouring *PRPF31* mutation to patient-specific RPE and retinal organoids to investigate the pathogenesis of the PRPF31 form of RP (Buskin et al., 2018). The most significantly mis-spliced genes identified from our study were present in RPE and retinal organoids and were involved in pre-mRNA and alternative mRNA splicing. This indicates that impaired splicing of pre-mRNA due to RP11 is restricted to retinal and RPE cells only (Buskin et al., 2018). Specifically, our study has shown that *PRPF31* mutations cause splicing defects in splicing-related genes leading to global

spliceosome dysregulation. As a result, a plethora of genes were mis-spliced and these were associated with phenotypical defects in PRPF31-RPE patient-derived cells and retinal organoids, including defective ciliogenesis, disrupted apical and basal polarity in RPE cells, reduced phagocytic capacity and decreased transepithelial resistance (barrier function) (Buskin et al., 2018). Alongside these results, TEM ultrastructural studies revealed the presence of large deposits located on the basal side in the PRPF31 patient derived RPE cells. Based on the study's findings, it is believed that altered pre-mRNA splicing is the initial pathogenic defect and probably subsequent pathologies arise from splicing deficiencies (Buskin et al., 2018).

In agreement with our previous findings, other studies reported that the knockdown of pre-mRNA splicing factors, including PRPF31, has a significant impact on ciliogenesis (Wheway et al., 2015, Kim et al., 2016). Further studies using PRPF31 hiPSC-derived RPE cells reported cellular deficiencies associated with the PRPF31 pathology, including reduced phagocytic capacity, defects in ciliogenesis, reduced barrier function, and defective cell structure. However, treatment of PRPF31 hiPSC-derived RPE cells using AAV-PRPF31 has shown partial structure and barrier function restoration and rescue of ciliogenesis (Brydon et al., 2019).

Recently, another study has used a mouse model with the p.A216P mutation in *PRPF31* to study the effects of mutated PRPF31 protein in RPE cells. This study showed that mutation in *PRPF31* causes aberrant splicing of genes and aggregation of mutated PRPF31 protein in the cytoplasm of RPE cells. Depletion of PRPF31 protein from the nucleus results in a splicing deficiency, which is probably the primary cause of RP in this case (Valdés-Sánchez et al., 2019). Since the nuclear levels of PRPF31 are below the normal threshold, the splicing machinery is affected, inducing overproduction of PRPF31 to meet the normal levels of PRPF31 in the nucleus. This aberrant expression of PRPF31, which is prone to aggregation, reinforces the negative effect (Valdés-Sánchez et al., 2019). These results were confirmed by other studies showing that proteins in patients expressing mutations in PRPFs such as *PRPF31* have reduced solubility and could lead to the formation of large protein aggregates (Wheway et al., 2020).

1.8. Aggregate formation

The presence of large deposits in cells, or the phenomenon when misfolded proteins clump together forming insoluble aggregates, is known as protein aggregation and is a common hallmark event in multiple neurodegenerative diseases such as Alzheimer disease (AD), Parkinson disease (PD), Huntington's disease (HD), amyotrophic lateral sclerosis (ALS) and

age-related macular degeneration (AMD) (Hyttinen et al., 2014). Although protein aggregates associated with neurodegenerative disorders are often harmful and could be lethal for the cells (Chung et al., 2001), sometimes they have protective effects in the cells by storing harmful proteins in insoluble clumps (Shiarli et al., 2006).

Under normal circumstances, newly synthesized proteins which are merely chains of amino acids, undergo folding to form functional proteins (Shamsi et al., 2017). The biosynthesis, assembly and correct folding of most proteins occur in a vital organelle known as the endoplasmic reticulum (ER). Proteins are synthesized by ER-bound ribosomes and then undergo modification and folding by foldases and molecular chaperones in the ER lumen to form distinct three-dimensional (3D) conformations (Wang and Kaufman, 2012). Correctly folded proteins exit the ER and translocate to other organelles or the extracellular space (Guo et al., 2019).

The folding mechanism of the newly synthesized proteins is a crucial stage in the regulation of their biological activity and it is predominantly dependent on the intrinsic properties of the primary amino acid sequence, which is driven by the formation of hydrophilic, hydrophobic, and electrostatic interactions, as well as from other influences present in the cellular environment (Schröder and Kaufman, 2005). Other factors such as mutations, transcriptional or translational errors, errors in protein trafficking, and structural alterations from environmental changes could cause misfolding of the proteins leading to the generation of dysfunctional structures (Shamsi et al., 2017). Under normal conditions, misfolded proteins are retained in the ER and are handled by chaperones to restore their folding, or if appropriate they are directed for degradation by the ER-associated protein degradation pathway (ERAD) (Wang and Kaufman, 2012). However, disturbances in ER could cause ER stress (Sano and Reed, 2013). As a response to ER stress, a highly conserved signalling pathway known as unfolded protein response (UPR) is activated to restore protein homeostasis and hence, cell survival (Sano and Reed, 2013). The UPR is characterized by three sensor proteins named IRE1α (inositol-requiring protein-1α), PERK (protein kinase RNA (PKR)-like ER kinase) and ATF6 (activating transcription factor 6), which are activated upon the accumulation of misfolded proteins (**Figure 1-17**) (Wang and Kaufman, 2012). In response to UPR, the translation of most mRNAs is downregulated to prevent further accumulation of misfolded proteins. At the same time, expression of chaperones is upregulated to improve protein folding. Misfolded proteins are transported from the ER to the cytosol for ubiquitination and degradation by the ERAD system, which is frequently referred to as the proteasome (**Figure 1-17**).

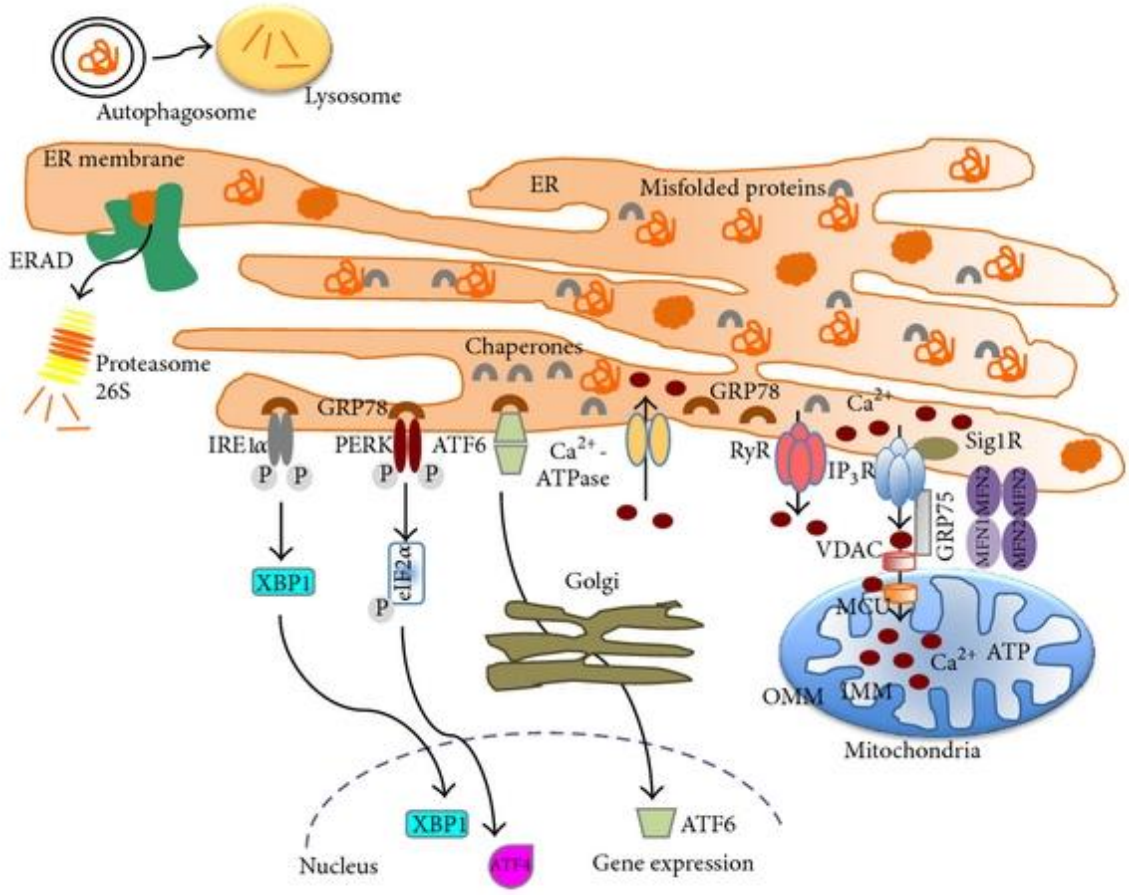

Figure 1-17: The Unfolded Protein Response (UPR). Under normal conditions, the UPR transducers (ATF6, IRE1α, and PERK) are associated with GRP78 chaperone. However, upon accumulation of misfolded proteins in the ER lumen, the three UPR transducers are released and activated. Each transducer uses different mechanisms of signal transduction. Specifically, ATF6 regulates proteolysis, PERK induces translational control by reducing protein synthesis and translation, and IRE1 controls mRNA splicing by degradation of ER-bound mRNAs. Figure adapted from Crosstalk between Endoplasmic Reticulum Stress and Protein Misfolding in Neurodegenerative Diseases (Santos and Ferreira, 2018).

1.8.1. Molecular chaperones

Molecular chaperones such as heat shock proteins (HSPs) act as an initial defence mechanism against damaged, misfolded, and aggregated proteins, and facilitate the re-folding of denatured proteins to restore their normal conformation, providing protein homeostasis and cell protection. The HSPs are classified into different categories, including HSP40, HSP60, HSP70 and HSP90. These categories are based on their molecular size, cellular localization and also based on their function. For example, an increase in the expression of HSP90 and HSP27 (HSPB1) has been observed in drusen (Decanini et al., 2007). However, HSP70 was upregulated in lysosomal fractions of RPE cells (Ryhanen et al., 2009) and was also highly

expressed in the form of cytoplasmic aggregates in Prpf31$^{p.A216P/+}$ mouse model (Valdés-Sánchez et al., 2019). Members of the HSP70 family bind to unfolded regions of the polypeptide chains to stabilize them during translation. Then, chaperones from the HSP60 family are recruited to facilitate the folding of the proteins. Re-folding of the proteins reduces the probability of aggregate formation. However, proteins that are unable to reassemble correctly are targeted for degradation by the proteolytic degradation machinery.

The major protein degradation pathways in eukaryotic cells are the Ubiquitin-Proteasome Pathway (UPS) and the autophagy pathway. The UPS pathway degrades most proteins (80-90%), whereas the autophagy pathway is responsible for the degradation of 10-20% of proteins, which are usually aggregated proteins or cellular organelles. Both pathways are crucial to maintaining cellular homeostasis, and disruption of either could induce variable diseases (Lilienbaum, 2013).

1.8.2. UPS pathway

The UPS pathway is the most important cellular system to eliminate damaged proteins in response to oxidative stress. The UPS includes two main steps; the conjugation step where multiple ubiquitin molecules tag the misfolded proteins, and the degradation step where misfolded proteins are degraded by the 26S proteasome, composed of the 20S and 19S complexes (**Figure 1-18**).

The ubiquitin-26 proteasome is a cellular defence mechanism that is activated in response to the accumulation of misfolded proteins (Lilienbaum, 2013). To target proteins for proteasomal degradation, polyubiquitin chains composed of small proteins known as ubiquitin (Ub) are covalently tagged on proteins to mark them for degradation by the 26S proteasome (Hyttinen et al., 2014). The 26S proteasome is a multi-component enzymatic complex composed of two major particles; a 20S catalytic core (known as the 20S proteasome), which is composed of seven alpha and seven beta subunits forming a ring, and two regulatory complexes known as 19S, which are composed of the lid and the base compartments (Wolf and Hilt, 2004). Although the 20S core is comprised of many subunits, only three subunits are responsible for catalytic activities. These are the caspase-like activity, β1 subunit (PSMB6), trypsin-like activity, β2 subunit (PSMB7), and chymotrypsin-like activity, β5 subunit (PSMB5). However, alpha subunits are important to activate the 20S proteasome, allowing the entry of ubiquitously tagged proteins to the proteasome for degradation (Tanaka, 2009) (**Figure 1-18**). Specifically, the lid recognizes ubiquitinated proteins and transfers them to the central proteolytic chamber, the 20S,

for catalysis. The end products are small peptides that are further degraded by peptidases into single amino acids, which can be recycled in the cell (**Figure 1-18**) (Lilienbaum, 2013). However, large insoluble aggregated proteins that cannot fit in the 20S chamber remain undigested in the cytoplasm (Hyttinen et al., 2014).

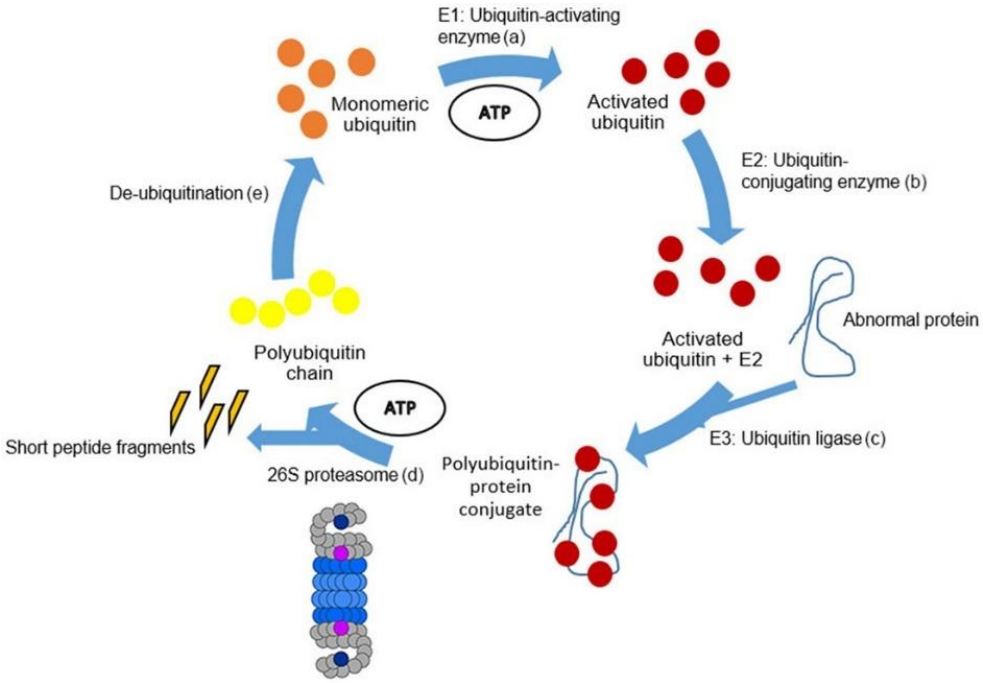

Figure 1-18: The UPS pathway. Ubiquitinating enzymes E1, E2 and E3, recognize polyubiquitinated protein and transfer them to the 26S proteasome complex for degradation. Degradation of the proteins is facilitated upon transfer of the protein by the 19S regulatory cap in the 20S proteasome core particle (Gentier and van Leeuwen, 2015).

1.8.3. Autophagy

When UPR malfunctions, an intrinsic apoptotic pathway (autophagy) is activated as a secondary response to degrade the undigested or accumulated cytoplasmic aggregates (Sano and Reed, 2013). The autophagy pathway is a self-degradative mechanism (Kroemer et al., 2010). Under stress conditions, autophagy aids with the removal and clearance of misfolded cytoplasmic proteins, cellular macromolecules and unwanted organelles by encapsulating them within double-membrane structures, which are then fused with lysosomes for degradation (Mizushima and Komatsu, 2011). Autophagy includes four main steps known as initiation, elongation, maturation, and fusion. In the first step, a membrane structure known as a phagophore is formed in the cytoplasm, which accumulates additional membranes and extends to engulf intracellular cargos such as protein aggregates. This is known as the elongation

procedure (**Figure 1-19**). The cytoplasmic cargos are then enclosed in a double membrane structure known as autophagosomes. Then autophagosomes mature and fuse with lysosomes, the site where engulfed proteins are degraded (**Figure 1-19**) (Eskelinen and Saftig, 2009). The formation of autophagosomes is regulated by the mammalian target of rapamycin (mTOR) complex 1, inhibition of which activates autophagy (**Figure 1-19**) (Sano and Reed, 2013). However, dysregulation of autophagy often leads to protein aggregation diseases (Hyttinen et al., 2014).

Autophagy was first described in 1963 by Christian De Duve as a lysosomal degradation process. It is a degradation system of intracellular damaged organelles, proteins, and debris. There are three major forms of autophagy: macroautophagy, microautophagy and chaperone-mediated autophagy (CMA). In CMA, chaperones such as HSP70 recognize specific proteins that contain the Lys-Phe-Glu-Arg-Gln sequence of the peptide, which then binds to the lysosome-associated membrane protein type 2A (LAMP-2A). Microautophagy takes place during lipid degradation and nutrient recycling. In microautophagy, the lysosomal membrane invaginates to trap all the cargo, regulates the lysosomal membrane composition and delivery of glycogen to lysosomes. However, macroautophagy consists of a double membrane that wraps around damaged organelles and proteins and further extends to become an autophagosome.

Failure of aggregation-prone proteins to be degraded by any known proteolytic mechanisms (UPS and autophagy) leads to the accumulation and growth of larger aggregated proteins. Several studies have reported that NDs such as HD, AD, PD, and ALS are characterised by the continuous accumulation of mutant aggregated proteins resistant to degradation, inducing cytotoxicity and neuronal cell death. It is still to be revealed whether cytoplasmic proteins resistance to degradation stems from an impairment of degradation pathways or failure of protein quality control systems to initiate in association with molecular chaperon sequestration to remove misfolded proteins.

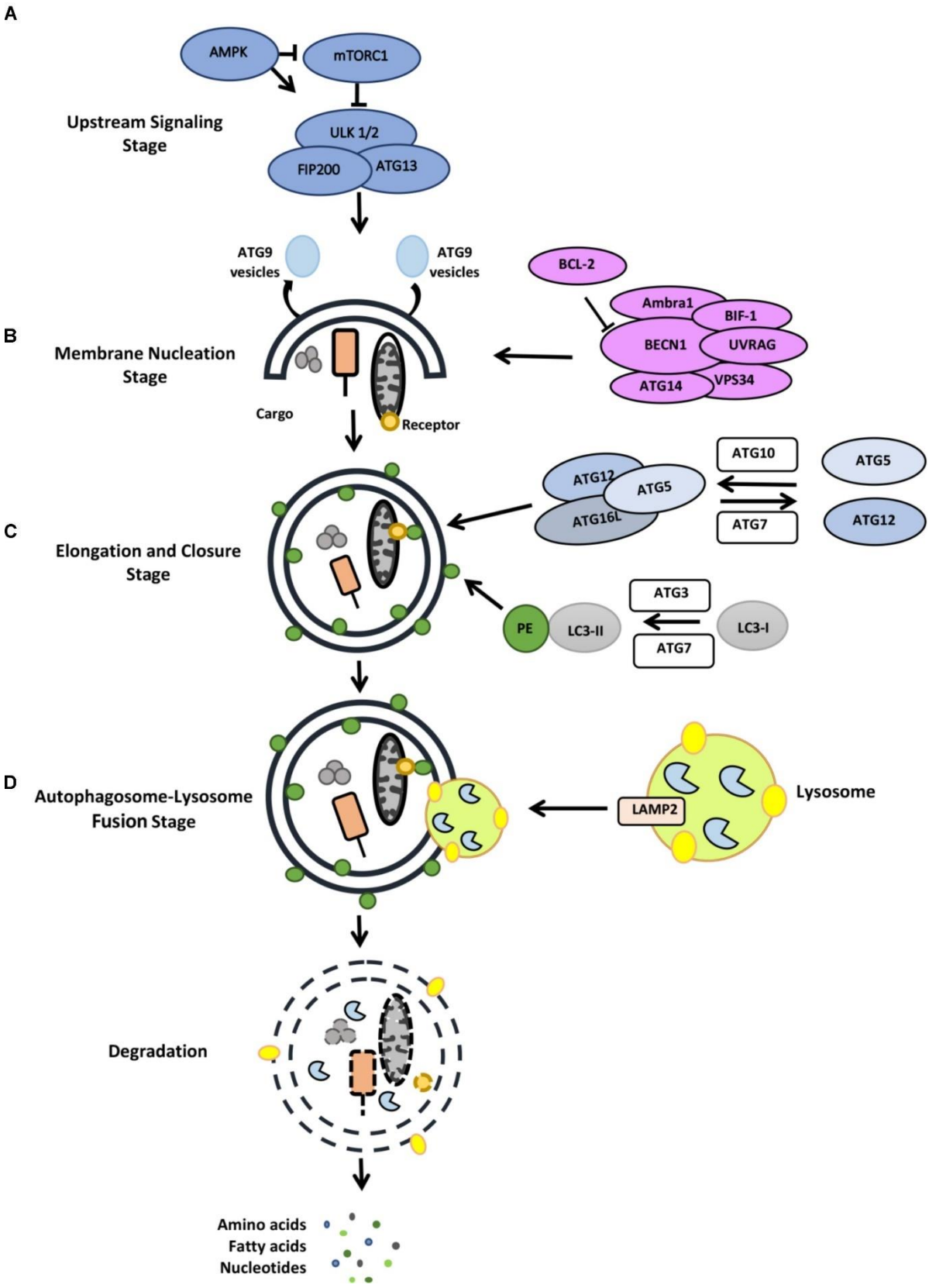

Figure 1-19: The autophagy pathway. The main steps in the autophagy pathway include the nucleation of the membrane, elongation, and closure of the membrane to form an autophagosome, and fusion of the autophagosome with the lysosome to degrade cargos (Kocaturk and Gozuacik, 2018).

1.9. Treatments

Currently, no available treatments exist to inhibit the progression of pigmentary retinopathies or restore vision. However, various approaches have been tried and tested including drug treatments, nutritional supplements, transplantation of cells (retinal cells of stem cells) and gene therapy.

1.9.1. Pharmacological therapies

Today, the pharmacological agents aiming to restore vision or to prevent disease deterioration are neurodegenerative agents and food supplements. In addition to this, drugs which target misfolded proteins, which is a hallmark of NDs, has shown promising results.

Usually, during translation or under cellular stress, many cellular proteins become misfolded. These abnormally folded proteins can either regain their normal conformation by HPSs or be removed effectively through the degradation pathways; UPS, CMA, and macroautophagy. However, mutant proteins are commonly resistant to degradation by the proteolytic mechanisms by forming β-sheet-enriched folds that are difficult to refold by molecular chaperones. These misfolded proteins are not fully unfolded and therefore may stick in the proteasome cylinder or on components of CMA, thereby preventing their degradation.

One strategy to enhance the degradation of denatured proteins is to increase the levels of molecular chaperones. These are the molecules to become activated in response to misfolded proteins (Gentier and van Leeuwen, 2015). Several studies have reported the protective role of HSP27 (HSPB1) against the formation of fibrils such as α-synuclein (α-syn), which is a hallmark characteristic of PD (Cox et al., 2018). Also, one of the most well-known examples of pharmacological drug which has completed phase II clinical trial (Benatar et al., 2018) and has been used to increase the activity of HSPs showing neuroprotective role in ALS (Kieran et al., 2004) and RP (Parfitt et al., 2014) is Arimoclomol.

An alternative strategy to attenuate aggregation of misfolded cytoplasmic proteins is activating the UPR, which comprises three arms and regulates proteostasis in the ER. To date, targeting any of the three arms that activate the UPR has shown very encouraging results (Eisele et al., 2015). Salubrinal, which targets the PERK branch and is an inhibitor of eIF2a phosphatase, has improved the survival of PRs cells in the adRP model (Eisele et al., 2015). Additionally, STF-083010 that selectively inhibits IRE1α, another arm of UPR, has been shown to inhibit

apoptosis effectively. In this context, apoptosis is caused by prolonged UPR, which is stimulated by ER stress (Liu et al., 2018b).

Another strategy to remove misfolded proteins is to target the autophagy pathway. Many small molecules have been developed to activate autophagy and induce clearance of pathogenic proteins. Some of these molecules activate autophagy by specifically inhibiting mTORC1 like Rapamycin. Studies have shown that Rapamycin can effectively reduce cytoplasmic mutant proteins such as α-synuclein (Webb et al., 2003), huntingtin (Sarkar and Rubinsztein, 2008) or tau proteins (Rodriguez-Navarro and Cuervo, 2010) from the brain of transgenic mouse models, and consequentially ameliorating neurodegeneration effectively.

1.9.2. Nutritional supplements

In addition to pharmacological treatments targeting specifically misfolded proteins, several studies have reported that nutritional supplements such as Vitamin A and E could be beneficial in treating RP. Research studies have proposed that vitamin therapy could protect the PRs' function via trophic and antioxidant effects (Parmeggiani et al., 2011). However, findings from several clinical trials argue that nutritional supplements do not reduce the progression of RP based on clinical measurements such as visual acuity, which showed no improvement following treatment (Hoffman et al., 2004). Additionally, lutein supplements, a natural carotenoid, was used as a therapeutic approach to protect eyes from oxidative stress and blue light showing positive effect on the visual field of RP patients, based on clinical study findings (Bahrami et al., 2006). Some clinical studies have reported advantages of using vitamin supplements in the treatment of RP. However, some other studies reported no positive changes (Berson et al., 2010, Dagnelie et al., 2000). Although these nutritional supplements are being used, no definitive conclusions on their impact in slowing or stopping RP progression were reached.

Docosahexaenoic acid (DHA), an abundant lipid in rod PRs, is reduced in RP patients. Therefore, two independent studies have tested the effects of oral DHA supplements in RP individuals but no clear benefits were observed. However, a slowed decrease in visual acuity was correlated with individuals expressing high DHA concentrations in red blood cells (RBC) (Berson et al., 2004b, Berson et al., 2004a).

1.9.3. Gene therapy

Although pharmacological treatments or nutritional supplements have been used to cure retinal diseases, gene-therapy approaches to identify and replace mutated disease-causing genes are under investigation. Gene therapy strategies are based on the type of mutation. In arRP cases, abnormalities lead to overall loss of protein function. Therefore, to correct the genetic defects, delivery of genes to the affected cells is required. Specifically, a functional copy of the gene is introduced in the diseased cells, often the PR cells, through a recombinant adenovirus vector to restore protein function. In AD-inherited diseases, where variant proteins are encoded with different amino acid sequences, the introduction of genes that silence the mutant gene using specific antisense oligonucleotides can prevent abnormal production of proteins (**Figure 1-20**) (Verbakel et al., 2018).

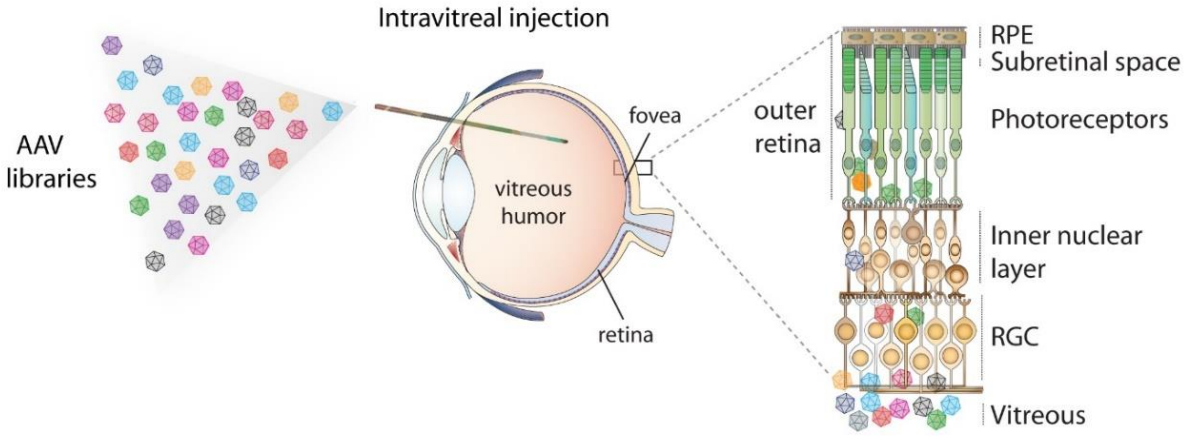

Figure 1-20: Schematic representation of gene therapy process. Adeno-associated viruses were engineered and injected intravitreally into an adult eye targeting the retina-specific cells (Dejneka et al., 2004).

A clinical study using animal models (Swedish Briard dog) with mutations in the *RPE65* gene has shown improvements in retinal function and vision restoration after administration of AAV vectors with RPE65 cDNA via subretinal injection (Acland et al., 2001). Additional clinical studies using mice and dogs were performed using adenovirus vectors with the *RPE65* gene, showing vision restoration (Dejneka et al., 2004, Narfström et al., 2003). However, in 2013 a clinical study that involved patients with Leber congenital amaurosis (LCA), a severe inherited retinopathy that results in the dysfunction and degeneration of PR cells, has displayed results consistent with improved vision short term and increased stability of vision long term but progressive retinal degeneration persists (Cideciyan et al., 2013). Although gene replacement strategies have shown visual restoration and improvements in retinal function in animal models,

questions related to the degree of efficacy, safety, and complications with the vectors used are still unresolved.

Despite the challenges, in 2017, the first gene therapy (Luxturna) was approved by FDA for the treatment of Leber congenital amaurosis (LCA) type-2 caused by *RPE65* mutations (LCA2; NCT00999609). The drug Luxturna is delivered subretinally to supplement RPE cells with a functional copy of *RPE65* to restore their ability to produce all-*trans* retinyl ester isomerase, an important enzyme for the visual cycle (Russell et al., 2017).

Additionally, the drug Sepofarsen (QR-110) is currently in phase-II/III of a clinical trial for treating LCA type 10 (LCA10) caused by mutations in gene *CEP20*. The gene *CEP20* is important for the generation of CEP290 protein, essential for forming light-sensitive POSs. QR-110 is an antisense oligonucleotide that targets specifically a point mutation in the *CEP290* gene, silencing the effects of this mutation and thus producing a functional CEP290 protein (clinicaltrials.gov identifier NCT03913143).

1.9.4. Cell therapy for the replacement of PRs

One of the most promising strategies to replace degenerated or lost retinal cells is cell therapy. A landmark achievement in the field was performed by MacLaren and colleagues who successfully isolated post-mitotic rod precursors from a transgenic mouse and transplanted them into the subretinal space of a recipient mouse. This study revealed that postnatal mouse-derived cells migrated into the ONL of the host retina, integrated, and differentiated into rod PRs, forming synaptic connections (MacLaren et al., 2006). The findings of this study have provided promising results supporting that transplantation of PR precursors cells can be a viable therapeutic strategy to restore visual function. In agreement with this study, Lakowski and colleagues have reported the transplantation of CRX positive cells from transgenic mice into degenerating retina of a Leber congenital amaurosis mouse model and showed that post-mitotic PR precursor cells differentiated into rod PRs, whereas prenatal cells integrated in the ONL of the recipient mouse and were developed into cone PRs (Lakowski et al., 2010). Taken together, the above studies highlight that successful transplantation of cells at the correct retinal layer is dependent on the stage of maturity (MacLaren et al., 2006, Lakowski et al., 2010).

Later, landmark studies have reported that the integration of donor cells in the host retina is probably a result of material exchange between donor and host PRs, a process known as material transfer (MT). Specifically, Pearson and colleagues have shown that host cells received

GFP labelling from GFP+ donor PR cells through the transfer of fluorescent reporters without nuclear translocation or transfer of nucleic acid. This suggests that there is an intracellular material exchange between donor and host PRs (Pearson et al., 2016). In agreement with this study, Santos-Ferreira and colleagues reported that donor PRs are present in the subretinal space rather than having integrated within the retinal tissue, suggesting the exchange of cellular components between the host and donor PR cells. This study further indicates that MT between the donor and host PRs could be used as a therapeutic strategy to treat retinal disorders (Santos-Ferreira et al., 2016).

A different source of cells that has been used for cell replacement therapies is the transplantation of retinal stem cells (RSCs). A research study has used RSCs from adult mouse retina to restore light responses in PR-deficient *rd7* mutant mice, a PR-deficient RP model (Li et al., 2013). This study reported that RSCs integrated into the retina, differentiated, and developed into mature PR cells following transplantation in the subretinal space of *rd7* mutant mice. Morphologically, retinal stem cells-derived PR cells resemble endogenous PRs, forming synaptic connections with the host's retinal neurons (Li et al., 2013).

In addition to the promising results from RSCs, another promising cell replacement therapy is the transplantation of foetal-derived retinal progenitor cells (RPCs). Scientists have isolated RPCs from the human foetal retina and have used them as donor cells to treat retinal diseases. Specifically, Seller and Aramant have shown that transplanted foetal-derived RPCs improved visual acuity in animals and humans (Seiler and Aramant, 2012). Foetal tissue-derived RPCs have been used in phase I/II clinical trials and approved by the FDA (clinicaltrials.gov identifier NCT03073733, NCT02464436) and hold a great promise in the clinical treatment of retinal diseases. However, low efficiency and availability of foetal donor tissue are the main limitations associated with the use of this technology.

hESCs or hiPSC-derived PR precursors present an additional source for cell replacement therapies. Previous studies demonstrated that ESC-derived rod precursor cells could be transplanted in the subretinal space of completely dysregulated ONL in *rd1* mice. The results indicated the development and maturation of transplanted cells in the host niche with light-sensitive OSs, and the formation of synaptic structures with downstream neurons, supporting that precursors cells can reform an anatomical polarized ONL. These results are encouraging, suggesting that the responses are not a result of pre-existing rescued cells from the host. This serves as an argument for stem cell therapy to be used to re-establish a light-sensitive cell layer and restore structurally damaged cells (Singh et al., 2013).

However, a recent study from our group where hiPSC-derived cone precursor cells were transplanted into mice with an autosomal recessive form of RP (Pde6brd1) showed that the transplanted cells were engrafted and integrated into the ONL of the host retina without any evidence of MT between the donor and host PRs. Our study has shown that transplanted cells differentiated into cone PRs, formed functional synaptic connections with bipolar cells and responded to light after transplantation, which suggests successful engraftment of pluripotent stem cell-derived cone precursors with the host retina and novel synapse formation (Zerti et al., 2021). Our study provides a promising therapeutic strategy that could be useful in clinical applications. In support of this, another study reported that transplanted purified hiPSC-derived cone PRs in the rd1 mouse model of end-stage retinal degeneration matured *in vivo*, formed functional synapses with recipient retina cells and observed light responses, suggesting the restoration of retinal responses. This study provides a promising strategy to rescue cone-mediated visual function (Ribeiro et al., 2021).

1.10. Aims of the study

This project aimed to:

- Develop effective cryopreservation methodologies for hiPSC-derived retinal organoids (ROs) that can be used for research, therapeutic and/or pharmacological applications. Integrated approaches based on previously published studies were tested, and the morphology and survival of post-thaw organoids was assessed by bright-field images and immunofluorescence (IF) analysis (Chapter 2).

- Assess room temperature (RT) shipment of hiPSC-derived ROs. The survival, structure, and function of shipped ROs were assessed using IF analysis, transmission electron microscopy (TEM), and electrophysiology (Chapter 3).

- Understand PRPF31 disease pathomechanism. Differentiate hiPSCs from patients with *PRPF31* mutations and unaffected controls towards RPE cells, and investigate the impact of *PRPF31* mutations on the proteome of RPE cells using mass spectrometry. Validate the expression and location of key candidates using WB analysis, IF analysis and transmission electron microscopy (TEM) in order to identify the disease mechanisms causing Retinitis Pigmentosa (RP) (Chapter 4).

Chapter 2

Chapter 2. Establishing cryopreservation of hiPSC-derived retinal organoids

2.1. Introduction

The generation of mouse iPSCs in 2006 and hiPSCs in 2007 by Shinya Yamanaka and his colleagues has opened up new avenues towards regenerative medicine, disease modelling, drug discovery, and toxicity assessments (Takahashi and Yamanaka, 2006, Takahashi et al., 2007). These applications are based on the characteristics of iPSCs to differentiate into any cell type of the human body (Takahashi and Yamanaka, 2006). Differentiation of ESCs and hiPSCs provides an essential and great advantage in research to study human development and disease in the dish by generating three-dimensional (3D) culture systems, such as retinal organoids (Shi et al., 2017). Specifically, over the last 10 years, several studies have reported the generation of eye field, neural tissue, retinal progenitor cells as well as differentiated cells derived from ESCs or hiPSCs using established protocols (Nakano et al., 2012, Zhong et al., 2014, Meyer et al., 2009, Lowe et al., 2016). Generated hiPSC-derived retinal organoids contain all retinal-related cells seen *in vivo*, recapitulating the major molecular and cellular events of human retinogenesis (Zhong et al., 2014, Llonch et al., 2018, Gonzalez-Cordero et al., 2017, Meyer et al., 2011, Mellough et al., 2015, Nakano et al., 2012, Völkner et al., 2016, Eiraku et al., 2011). Due to these advantages, this technology holds great promise in the research field.

The development of 3D organoids has provided a plethora of information in the biomedical research field, and therefore continuous generation of 3D organoids is required (Llonch et al., 2018). However, developing 3D organoids derived from hiPSCs or ESCs is a lengthy and time-consuming procedure (Huang et al., 2019). Hence, banking or storage of organoids using cryopreservation methods would solve the need for constant production.

Cryopreservation is referred to the freezing of living cells and tissues at very low temperatures using cryoprotectant solutes (Jang et al., 2017). A standard freezing media, containing 5%-20% Foetal Bovine Serum (FBS) and 10% of Dimethyl sulfoxide (DMSO) supplemented in a culture medium, is widely used for the prolonged storage of many different mammalian cells. This protocol is well established for the cryopreservation of single cells (Hunt, 2019). However, effective cryopreservation procedures for the storage of 3D organoids or tissues are yet to be established.

Alternative changes to the traditional cryopreservation protocol which is used for the cryopreservation of single cells have been reported. These alternative methodologies include the use of different cryoprotectants (CPAs) to DMSO that can provide intracellular or

extracellular protection to the cells and therefore protect them against cryoinjuries. This is achieved by using permeating CPAs such as glycerol, which can penetrate the cellular membrane and protect the cells intracellularly, in combination with non-permeating CPAs such as trehalose or polymers that provide only extracellular protection. The main important function of CPAs is to increase the concentration of solutes intracellularly and extracellularly and hence inhibit intracellular ice formation (Jang et al., 2017). However, although CPAs play an important role in the cryopreservation procedure, additional parameters such as the storage temperature, the cooling and thawing rate, and the sample volume should be optimised based on the different cell types and tissues. Importantly, the rate of freezing plays an important role in the survival of cryoprotected cells or tissues. Specifically, slow freezing is suggested for the best survival rate of cells. In theory, during slow freezing, the intracellular water is effluxed, substituted with CPAs, and hence, intracellular ice formation is inhibited. Usually, the cooling rate during slow freezing is about 1°C/minute (relatively slow) to permit adequate cellular dehydration (Miyazaki and Suemori, 2016). However, the cooling rate should be optimised depending on the type of cells or the tissue.

An alternative cryopreservation method is the vitrification technique. Vitrification is a novel cryopreservation strategy that has been proposed to prevent ice crystal formation. This new strategy aims to fast freeze living cells by directly transforming the cells or tissues to a glass state (Jeong et al., 2020). The vitrification process requires a high concentration of CPAs and fast cooling to cryogenic temperatures to prevent mechanical injury caused by the formation of ice crystals (Yavin and Arav, 2007). Although vitrification is usually performed at a very fast cooling rate, other parameters such as warming rate, sample viscosity, or the volume of the sample should be optimised based on the tissue type (Yavin and Arav, 2007). This strategy was initially proposed in the 1980s with the successful vitrification of human embryos, oocytes (Herrero et al., 2011) and thereafter in liver spheroids (Wu et al., 2007).

Since 1949, when cryobiology was born, and the cryoprotective properties of glycerol were discovered by Polge for the preservation of sperm (POLGE et al., 1949), a great interest in the cryopreservation of human cells and tissues was generated. Over the years, scientists have proposed different cryopreservation and vitrification protocols in the effort to achieve an optimised protocol that will effectively ensure the survival of cells maintaining their physiological functions and abilities. These protocols differ from one another in the type of CPAs, the cooling and warming rates, the storage method and the storage temperature. Nowadays, successful optimal conditions have been reported for the cryopreservation of homogenous cell populations, including hiPSCs (Hunt, 2011), or one cell-layer tissue, assuring

a high recovery rate after thawing (Bakhach, 2009). However, long-term preservation of 3D structures or larger tissues or organs has been one of the major problems in transplantation. So far, cryopreservation of whole organs including kidneys (Fahy and Ali, 1997), liver (Alexandre et al., 2002), heart (Amir et al., 2004), lung (Lee and Bastacky, 1995), embryos (Donnez et al., 2006), trachea (Yokomise et al., 1996) and parathyroid glands (Walgenbach et al., 1999) has been performed; however, results have remained experimental. An optimal protocol for the preservation of these tissues has not been established yet, and more work is required for the successful recovery of the tissues.

Additionally, cryopreservation protocols have been designed to preserve different types of organoids and evaluate organoids' survival after thawing. To assess the efficiency of cryopreservation protocols, studies compare the functional and physiological properties of cryopreserved organoids with freshly derived organoids. Cryopreservation of retinal organoids was attempted in the past. Nakano and colleagues have reported the successful cryopreservation of hESC-derived stratified retinal tissue using a vitrification method (Nakano et al., 2012), but other groups, including ours, have not been able to reproduce their findings. Another study has reported that hiPSC-derived retinal organoids (at early stages, before day 50) and dissociated retinal cells were preserved after thawing, maintaining their phenotypic characteristics (Reichman et al., 2017). Although these studies have reported the ability to cryopreserve and store retinal neuroepithelial cells and retinal organoids, no optimal protocols that cryopreserve whole retinal organoids at later developmental time points have been reported.

The development of 3D organoids and their application in research and therapy could benefit from the development of an effective cryopreservation method that would assure the availability of viable and functional stocks of organoids. The discovery of an efficient cryopreservation protocol that will efficiently preserve the structure and function of the organoids will support the development of an organoid biobank. This will reduce the batch-to-batch variability and minimise laborious and time-consuming culture systems for laboratories that are interested in their application (Huang et al., 2019). Also, cryopreservation of 3D organoids derived from patient cells will facilitate donor cells' direct and faster availability in potential clinical applications and will support their long-term storage (Kim et al., 2020).

2.2. Aims

The main aim of this chapter was to develop a cryopreservation protocol that will ensure the survival and preservation of the physiological functions of fully developed retinal organoids derived from hiPSCs. This will allow the cryo-storage of a large number of retinal organoids that can be used for pharmacological purposes, toxicological assessments, and clinical applications. Cryopreserved retinal organoids were assessed by bright-field images and IF analysis using cell type-specific retinal markers.

2.3. Materials and Methods

2.3.1. Cell lines

Adult human dermal fibroblast cells (HDFs) were collected from healthy volunteers for the generation of control hiPSCs. Two hiPSC lines, WT2 (AD3, Male, aged 68) and WT3 (AD4 CC-2511 Female, 84-year-old), were derived and characterised in Lako's group as described in our previous studies (Melguizo-Sanchis et al., 2018, Buskin et al., 2018).

2.3.2. Human-induced Pluripotent Stem Cell (hiPSC) Culture

The culture of hiPSCs was performed in a Class II biosafety cabinet laminar airflow tissue culture hood, on a hot plate, under a dissection microscope. All the hiPSCs were cultured and expanded in mTeSR™1 (Stem Cells Technologies, 05851) media supplemented with 1% Penicillin/Streptomycin (P/S, Life Technologies, 15140130) on a low adhesion 6-well plate pre-coated with reduced growth-factor Matrigel (BD, 354230). Media changes were performed daily. The cells were maintained in a humidified environment at 37°C, with 5% CO_2. Approximately after 4-5 days, when hiPSCs reached a confluency of about 80%, hiPSCs were passaged using 1 ml of Versene EDTA 0.02% (Lonza BE17-711E) per well of a 6-well plate for approximately 3 minutes. Once the hiPSC colonies were dissociated, Versene EDTA was removed and replaced by a fresh culture medium. The cells were passaged at a ratio 1:3-1:6 to a new Matrigel-coated 6-well plate that was kept in a humidified environment at 37°C, with 5% CO_2. Freezing and storage of hiPSCs were performed using freezing media containing 90% FBS (Gibco, 10270–106), 10% DMSO (Sigma, D2650), and 10μM ROCK inhibitor (Y-27632, Chemdea, CD0141). The ROCK inhibitor was used to prevent apoptosis of single cells. The cell suspension was transferred into a 15 ml falcon tube and centrifuged for 300 g for 5 minutes. The supernatant was aspirated, and the pellet was re-suspended in 500μl of freezing media. Then, the cell suspension was transferred in cryovials which were then placed into a Mr. Frosty (freezing container, Nalgene) and stored at -80°C for 24 hours. For long-term storage, the cryovials were transferred to liquid nitrogen.

2.3.3. Human-induced Pluripotent Stem Cells differentiation to retinal organoids

Retinal organoids were generated from two different hiPSC lines (WT2 and WT3). Differentiation of hiPSCs into retinal organoids was performed in low-cell adhesion 96-well

plates with round-bottomed conical wells (Helena, 92697T). The 96-well plates were manually coated one day before starting differentiation with 50µl of Lipidure solution (AMSbio, AMS.52000011GB1G) per well (1g/200 ml 100% ethanol) to provide a low adhesion surface. The plates were maintained under the hood overnight to let Lipidure evaporate. Then, the plates were sterilised using ultraviolet (UV) light. Briefly, when hiPSCs reached a confluency of about 80%, a washed with 1 ml of Phosphate Buffered Saline (PBS, Sigma, P4417-100TAB) was performed, followed by the addition of Accutase (Gibco, A1110501) for 3 minutes, to dissociate hiPSCs into single cells. The cells were transferred in mTeSR™1 medium supplemented with 10 µM of ROCK inhibitor to reduce the apoptosis of single cells and enhance cell aggregation. The hiPSCs were seeded at a density of 7,000 cells/well in a total volume of 100µl, followed by incubation of the plates at 37°C, with 5% CO_2 for 48 hours. This was defined as day -2 of differentiation (**Figure 2-1**). At day 0 of differentiation, 200µl of differentiation medium (**Table 2-1**) was added per well. Half media changes were performed every 2 days from day 2 to day 6 by removing 100µl of media and replacing it with 100µl of fresh media. On day 6 of differentiation, 2.25 nM of BMP4 (R&D, 314-BP) was added to the media, and medium changes were carried out every 3 days thereafter (**Figure 2-1)**. From day 18 until day 24 of differentiation, the media was changed to reversal medium **(Figure 2-1)** (**Table 2-1**). Medium changes were performed every 2 days. Further modifications performed at day 24 of differentiation, where the medium was replaced with maintenance medium (**Figure 2-1**) (**Table 2-1**). Media changes were performed every 3-4 days.

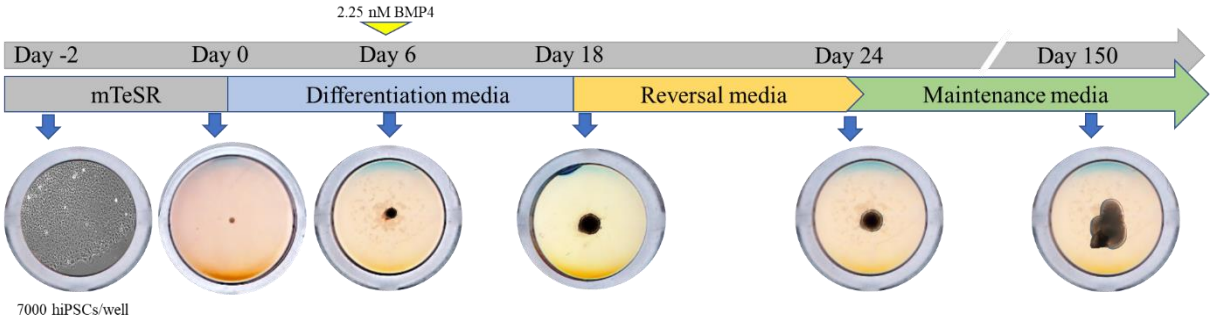

Figure 2-1: Differentiation of hiPSCs into retinal organoids. Schematic diagram illustrating the differentiation procedure of hiPSCs to retinal organoids showing representative bright-field images of organoids at each step of the differentiation procedure.

Table 2-1: Composition of the differentiation, reversal and maintenance medium.

Reagents	Concentration	Supplier	Catalogue Number
Differentiation Medium - Day 0-18			
IMDM	41%	Gibco	12440–053
HAM's F12	41%	Gibco	31765–029
KOSR	15%	Gibco	10828–028
GlutaMAX	1%	Gibco	35050–038
Chemically defined lipid concentrate	1%	ThermoFisher Scientific	11905031
Pen/Strep	1%	Gibco	15140–122
1-Thioglycerol	225 µM	Sigma	M6145
Reversal Medium - Day 18-24			
DMEM/F12	97%	Gibco	31330—038
GlutaMax	1%	Gibco	35050–038
N2	1%	Thermo	A1370701
CHIR99021	0.25 µM	Sigma Aldrich	SML1046
SU5402	0.1 mM	Tocris	3300
Pen/Strep	1%	Gibco	15140–122
Maintenance Medium - Day 24 onwards			
DMEM/F12	92%	Gibco	31330–038
FBS	5%	ThermoFisher Scientific	A2720801
GlutaMax	1%	Gibco	35050–038
N2	1%	Thermo	A1370701
Retinoic acid	0.25 µM	Sigma	R2625
Taurine	0.1 mM	Sigma	T8691
Pen/Strep	1%	Gibco	15140–122
Fungiozone	0.25 µg/ml	Gibco	15290–02

2.3.4. Cryopreservation of retinal organoids

Cryopreservation of organoids was performed either using 96-well plates or cryovials. CPAs were mixed with organoids before freezing to enhance their penetration into the cells and subsequently to prevent intracellular freezing. Thereafter, organoids were cooled down at low temperatures at specific cooling rates using the VIA Freeze™ (Asymptote), in which organoids were stored for 24 hours. This was defined as 'day 0' of the cryopreservation experiments (**Figure 2-2**). Then, organoids were thawed using a water bath, followed by washing to remove the CPAs. This was defined as 'day 1' of the cryopreservation experiments (**Figure 2-2**). In cases where cryopreservation of organoids was performed in cryovials, after thawing, the organoids were transferred back in the 96-well plates to recover before their collection for immunofluorescence (IF) analysis. Media changes were performed three times per week. The recovery of organoids was evaluated by bright-field images taken before cryopreservation, immediately after thawing (Day 1), 7 days post-thaw (Day 7), and 14 days post-thaw (Day 14)

(**Figure 2-2**). The above procedure is a general protocol used for the cryopreservation of organoids.

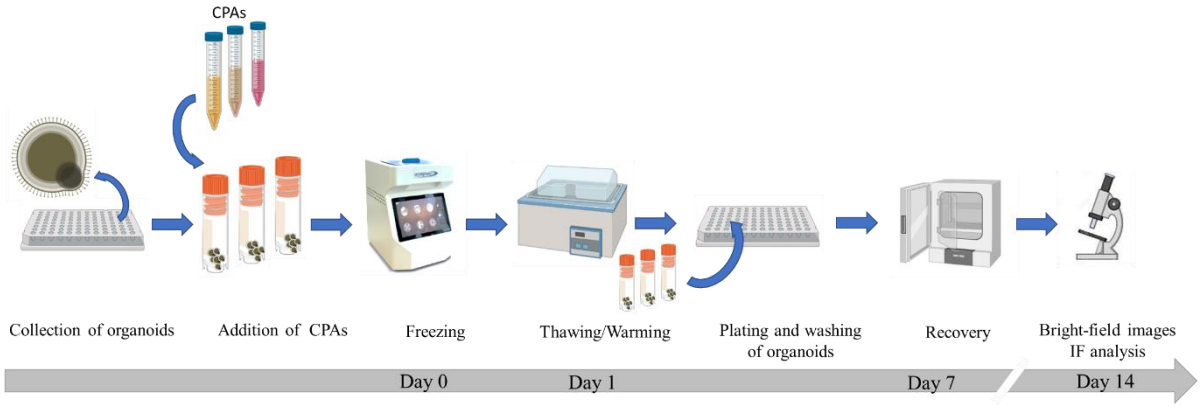

Figure 2-2: Schematic diagram showing a general procedure for the cryopreservation of retinal organoids.

2.3.4.1. Cryopreservation of retinal organoids using VEG vitrification protocol

VEG vitrification protocol was obtained from a research study in which rat hippocampal slices remained viable after vitrification at -100°C (Pichugin et al., 2006). The cryopreservation protocol was modified and adapted according to the aims of our study following internal and external discussions with our collaborator Dr Peter Kilbride (Asymptote, Cytiva), who is a cryopreservation specialist. Modifications were made on the freezing rate, the concentration of CPAs, and the composition of carrier solution. Vitrification of day 80 WT3 retinal organoids was performed using a single stirling engine powered system VIA Freeze™ (Asymptote). Initially, all the vitrification solutions were freshly prepared and maintained in the fridge (4°C). The vitrification solution was prepared using 16.84% ethylene glycol (EG), 13.96% formamide, 50% DMSO, and 0.8 mM Vitamin C, diluted in the carrier solution (**Table 2-2**). The maintenance media, used as a carrier solution, was employed to dilute the CPAs. Initially, 200µl of 1.6% VEG solution was added per well of the 96-well plate. The 96-well plate was cooled at 4°C for 5 minutes. Following half media changes, the organoids were vitrified consecutively with pre-cooled 6.55%, 13.11%, 24.59%, and 50% VEG vitrification solutions followed by 5 minutes incubation at 4°C for each concentration (**Figure 2-3 A**). Thereafter, the organoids were cooled and maintained at -10°C for 10 minutes (**Figure 2-3 B**). Then, retinal organoids were gradually cooled (decreasing the temperature gradually at a specific rate) to -100°C at -1°C/minute (**Figure 2-3 iC**). Retinal organoids were stored in the VIA Freeze™ at -100°C for 24 hours (**Figure 2-3 D**). Following vitrification, retinal organoids were thawed and maintained

at -10°C for 10 minutes (**Figure 2-3 E and F**). Warming of the organoids was performed at 4°C followed by consecutive washes with 24.59%, 13.11%, 6.55%, 3.28%, and 1.6% VEG thawing solution (**Figure 2-3 G**) (**Table 2-2**). The organoids were incubated for 5 minutes at 4°C for each washing step. Therefore, the organoids were transferred to the incubator to recover for 14 days before their collection for IF analysis (**Figure 2-3 H**).

To identify whether modifications in the freezing rate can improve the survival of retinal organoids, the VEG vitrification experiment was repeated, but rather than cooling the organoids gradually (-1°C/minute) to -100°C, the retinal organoids were fast cooled by transferring them immediately to -100°C (**Figure 2-3 iiC**). This was defined as direct freezing (**Figure 2-3 iiC**). All the other steps were performed as mentioned above.

Table 2-2: Composition of solutions for the VEG vitrification protocol.

Reagents	Concentration	Supplier	Catalogue Number
VEG Vitrification Solution			
DMSO	24.2%	Sigma Aldrich	D2650
Formamide	13.96%	Sigma Aldrich	F9037
Ethylene glycol	16.84%	Sigma Aldrich	324558
Vitamin C	0.8 mM	Sigma Aldrich	A5960
VEG Thawing Solution			
DMSO	24.2%	Sigma Aldrich	D2650
Formamide	13.96%	Sigma Aldrich	F9037
Ethylene glycol	16.84%	Sigma Aldrich	324558
Vitamin C	0.8 mM	Sigma Aldrich	A5960
Mannitol	300 mM	Sigma Aldrich	M4125
Carrier Solution			
Maintenance Media	section 2.3.3		
Glucose	90 mM	Sigma Aldrich	50-99-7
Mannitol	45 mM	Sigma Aldrich	M4125

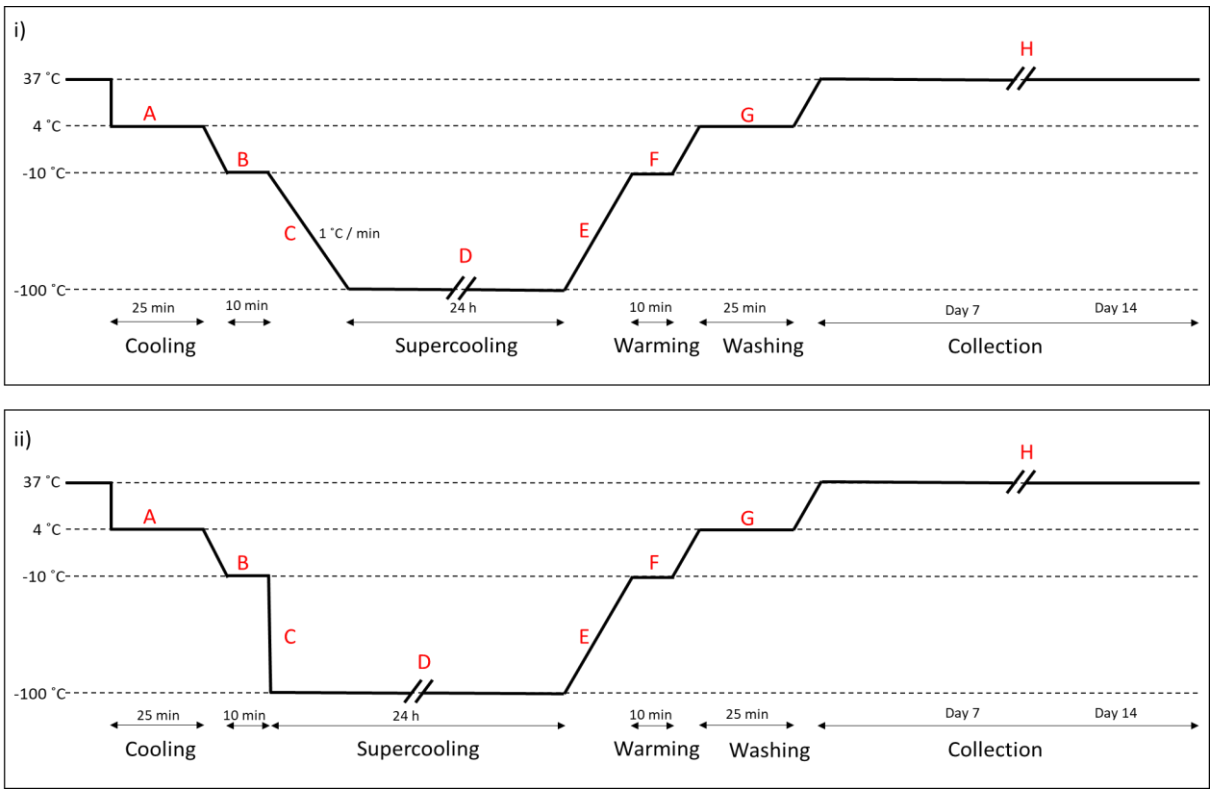

Figure 2-3: Schematic outline of VEG vitrification protocol. The overall protocol entails 8 steps (A-H). A) Cooling to 4°C with 5 minutes successive incubations, per concentration, with 1.6%, 3.28%, 6.55%, 13.11%, 24.59% VEG vitrification solution. B) Further cooling to -10°C for 10 minutes with 100µl 50% VEG. C) i) Gradual cooling to a rate of -1°C/minute, ii) Direct cooling to -100°C. D) Storage of ROs in VIA Freeze at -100°C for 24 hours. E) Warming to -10°C and F) incubation of organoids at -10°C for 10 minutes. G) Successive washes for 5 minutes with 24.59%, 13.11%, 6.55%, 3.28%, and 1.6% VEG thawing solution supplemented in the carrier solution, at 4°C. H) Storage of organoids in the incubator at 37°C, for 14 days. Media changes were performed three times a week. Organoids were collected on day 14 for IF analysis.

2.3.4.2. Cryopreservation of retinal organoids using VM3 vitrification solution

In addition to the VEG vitrification solution used for the cryopreservation of hippocampal slices, another vitrification solution that is more stable and more advanced, known as VM3 vitrification solution, was tested on WT3 day 98 retinal organoids. This vitrification solution was successfully used for the vitrification of rat hippocampal slices, mouse ova and renal cortical slices. (Pichugin et al., 2006). Therefore, the VM3 vitrification solution was modified and adapted to assess whether it could be used for the cryopreservation of retinal organoids. Modifications included the incubation time of organoids with freezing and thawing solutions, the concentration of CPAs, and the composition of carrier solution. Initially, all the vitrification solutions were freshly prepared and maintained in the fridge (4°C). The VM3 vitrification solution was prepared by supplementing the carrier solution (maintenance media) with 22.3% DMSO, 12.86% formamide, 16.84% EG, 7% polyvinylpyrrolidone K12, 1% "Supercool X-1000" ice blocker, and 1% "Supercool Z-1000" ice blocker (**Table 2-3**). Briefly, 200µl of 2% pre-cooled VM3 solution was added per well of the 96-well plate. Then, retinal organoids were cooled to 4°C for 5 minutes. Following half media changes, the organoids were vitrified consecutively with pre-cooled 4%, 8%, 16%, and 30% of VM3 solutions followed by 5 minutes incubation at 4°C after each concentration (**Figure 2-4 A**). Thereafter, the organoids were vitrified with 61% pre-cooled VM3 solution, followed by cooling the organoids at -10°C for 10 minutes (**Figure 2-4 B**). Subsequently, retinal organoids were cooled slowly (decreasing the temperature gradually at a specific rate) to -100°C at -1°C/minute (**Figure 2-4 iC**). Thereafter, retinal organoids were stored in the Via Freeze machine at -100°C for 24 hours (**Figure 2-4 D**). Following vitrification, retinal organoids were thawed to -10°C, and CPAs were washed using 31% VM3 thawing solution. The organoids were maintained at -10°C for 10 minutes (**Figure 2-4 E and F**). Then, the organoids were warmed to 4°C and washed successively using 16%, 8%, 4%, 2%, and 1% VM3 thawing solutions (**Figure 2-4 G**) (**Table 2-3**). The organoids were incubated for 5 minutes at 4°C for each washout step. Therefore, the organoids were transferred to the incubator at 37°C with 5% CO_2 to recover for 14 days before their collection for IF analysis (**Figure 2-4 H**).

The VM3 vitrification experiment was repeated, but instead of cooling the organoids slowly (at -1°C/minute), retinal organoids were cooled at a fast cooling rate. Specifically, after cooling the organoids at -10°C, retinal organoids were transferred directly to -100°C (**Figure 2-4 iiC**) where they were stored for 24 hours. All the other steps were performed as mentioned above.

Table 2-3: Composition of solutions for the VM3 vitrification protocol.

Reagents	Concentration	Supplier	Catalogue Number
VM3 Vitrification Solution			
DMSO	22.3%	Sigma Aldrich	D2650
Formamide	12.86%	Sigma Aldrich	F9037
Ethylene Glycol	16.84%	Sigma Aldrich	324558
Polyvinylpyrrolidone K12	7%	Sigma Aldrich	PVP12
Supercool X-1000	1%	21st Century Medicine	N/A
Supercool Z-1000	1%	21st Century Medicine	N/A
VM3 Thawing Solution			
DMSO	22.3%	Sigma Aldrich	D2650
Formamide	12.86%	Sigma Aldrich	F9037
Ethylene Glycol	16.84%	Sigma Aldrich	324558
Polyvinylpyrrolidone K12	7%	Sigma Aldrich	PVP12
Supercool X-1000	1%	21st Century Medicine	N/A
Supercool Z-1000	1%	21st Century Medicine	N/A
Mannitol	300 mM	Sigma Aldrich	M4125
Carrier Solution			
Maintenance Media	Section 2.3.3		
Glucose	90 mM	Sigma Aldrich	50-99-7
Mannitol	45 mM	Sigma Aldrich	M4125

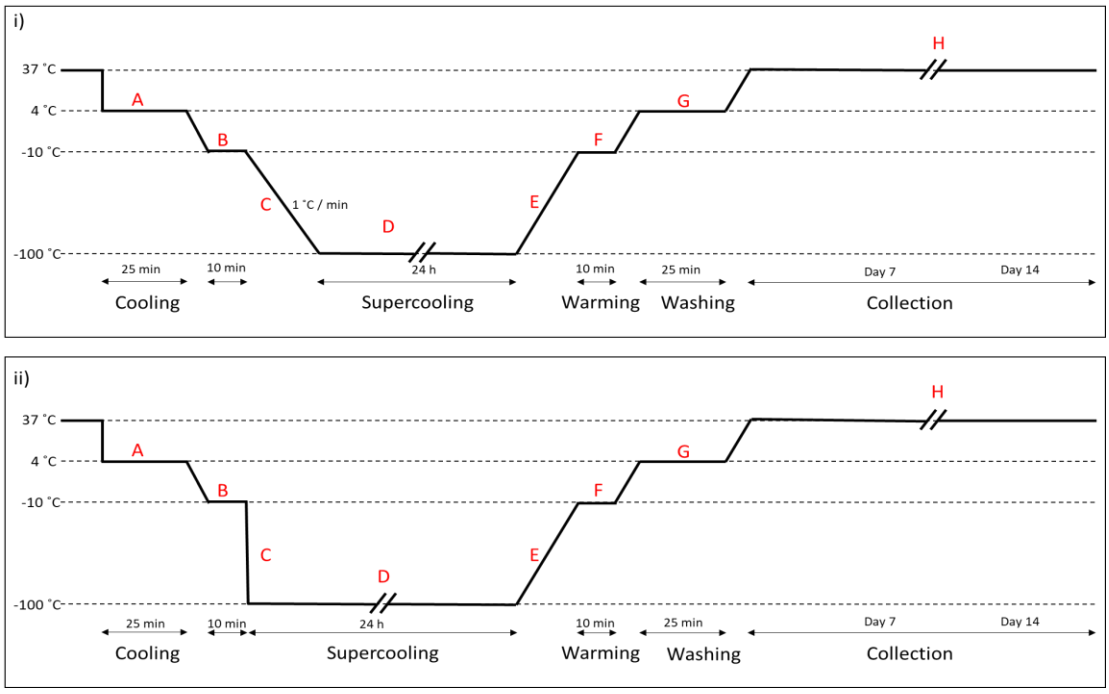

Figure 2-4: Schematic outline of VM3 vitrification protocol. The overall protocol entails 8 steps (A-H). A) Cooling to 4°C with 5 minutes successive incubations, per concentration, with 2%, 4%, 8%, 16% and 30% of VM3 vitrification solution. B) Further cooling to -10°C for 10 minutes with 61% VM3. C) i) Gradual cooling to a rate of -1°C/minute, ii) direct cooling to -100°C. D) Storage of ROs in VIA Freeze at -100°C for 24 hours. E) Warming to -10°C. F) Washing with 31% VM3 thawing solution at -10°C for 10 minutes to remove CPAs. G) Further successive washes for 5 minutes with 16%, 8%, 4%, 2% and 1% VM3 thawing solution supplemented in a carrier solution, at 4°C. H) Storage in the incubator (37°C) for 14 days. Media changes were performed three times a week. Organoids were collected on day 14 post-thaw for IF analysis.

2.3.4.3. Cryopreservation of retinal organoids using ES-HEPES vitrification protocol

The ES-HEPES vitrification protocol has been shown to successfully cryopreserve hESCs (Richards et al., 2004). Therefore, this protocol was assessed for the cryopreservation of WT3 retinal organoids on day 91 of differentiation. Initially, the VIA Freeze machine was cooled to -100°C. Thereafter, ES-HEPES vitrification solution consisting of 78% DMEM/F12, 20% heat-treated FBS, and 2% (1M) HEPES (**Table 2-4**) was freshly prepared and maintained at 37°C. Briefly, 100µl of HEPES vitrification solution was added per well of the 96-well plate, followed by incubation of the organoids for 2 minutes at 37°C. Then, the media was replaced by 100µl of 10% vitrification solution (80% ES-HEPES Solution, 10% EG, and 10% DMSO) (**Table 2-4**) followed by 2 minutes incubation at 37°C. Thereafter, the media was replaced with 100µl of 20% vitrification solution (30% ES-HEPES Solution, 30% (1M) Sucrose Stock, 20% EG and 20% DMSO), followed by 50 seconds incubation at 37°C (**Figure 2-5 A**) (**Table 2-4**). Then, 50µl of fresh 20% vitrification solution was added per well of the 96-well plate followed by cooling of the organoids directly to -100°C (**Figure 2-5 B**). Following overnight storage (**Figure 2-5 C**), retinal organoids were warmed to 37°C (approximately 10 minutes) (**Figure 2-5 D**) and washed from cryoprotective agents using 100µl of 0.2 M sucrose solution (80% ES-HEPES Solution, 20% (1M) sucrose stock) per well of the 96-well plate (**Table 2-4**). The organoids were maintained at 37°C for 3 minutes. Thereafter, the organoids were washed with 100µl of 0.1 M sucrose solution (90% ES-HEPES solution and 10% (1M) sucrose stock) (**Table 2-4**), following incubation of the organoids for 5 minutes at 37°C. Subsequently, retinal organoids were washed twice with 100µl 1M sucrose stock solution for 5 minutes at 37°C (**Figure 2-5 E**). Then, retinal organoids were incubated with warm culture media and transferred to the incubator. The organoids were maintained in the incubator for 14 days to recover before their collected for IF analysis (**Figure 2-5 F**).

Table 2-4: Composition of solutions for the ES-HEPES vitrification protocol.

Reagents	Concentration	Supplier	Catalogue Number
ES-HEPES Solution			
DMEM Knockout	78%	ThermoFisher Scientific	12660012
FBS	20%	ThermoFisher Scientific	A2720801
1M HEPES	2%	Sigma Aldrich	7365-45-9
10% Vitrification Solution 1			
ES-HEPES	80%	Sigma Aldrich	7365-45-9
DMSO	10%	Sigma Aldrich	D2650
Ethylene Glycol	10%	Sigma Aldrich	107-21-1
20% Vitrification Solution 2			
ES-HEPES	30%	Sigma Aldrich	7365-45-9
1M Sucrose Stock	30%	Sigma Aldrich	57-50-1
Ethylene Glycol	20%	Sigma Aldrich	324558
DMSO	20%	Sigma Aldrich	D2650
1M Sucrose Stock			
Sucrose	624.5 mM	Sigma Aldrich	57-50-1
ES-HEPES Solution	87.5%	Sigma Aldrich	7365-45-9
FBS	12.5%	ThermoFisher Scientific	A2720801
0.2M sucrose solution:			
1M Sucrose Stock	20%	Sigma Aldrich	57-50-1
ES-HEPES Solution	80%	Sigma Aldrich	7365-45-9
0.1M sucrose solution:			
1M Sucrose Stock	10%	Sigma Aldrich	57-50-1
ES-HEPES Solution	90%	Sigma Aldrich	7365-45-9

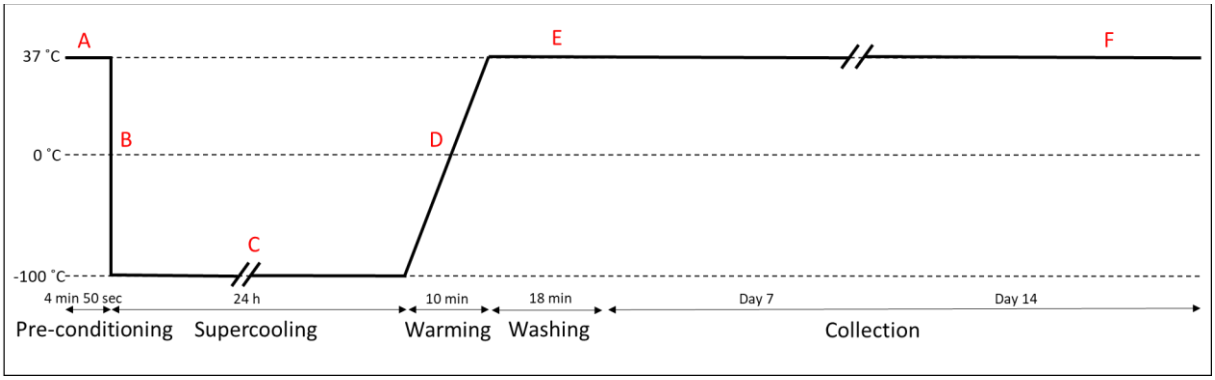

Figure 2-5: Schematic outline of ES-HEPES vitrification protocol. The overall protocol entails 6 steps (A-F). A) Incubation with ES-HEPES solution with 10% and 20% vitrification solutions at 37°C for 4 minutes and 50 sec. B) Direct cooling to -100°C, and C) storage ROs in VIA Freeze at -100°C for 24 hours. D) Warming at 37°C. E) Washing for 3 minutes with 0.2M sucrose solution followed by another wash with 0.1 M sucrose solution for 5 minutes and two subsequent washes with ES-HEPES solution for 5 minutes each. F) Storage of ROs in the incubator (37°C) for 14 days before their collection for further analysis. Media changes were performed three times a week. Organoids were collected on day 14 post-thaw for IF analysis.

2.3.4.4. Cryopreservation of retinal organoids using the 'Mouse retinal' protocol

The following protocol was obtained from a research study that has successfully cryopreserved mouse testicular tissue (Fayomi et al., 2019). The protocol was modified for the cryopreservation of retinal organoids. Modifications included the storage temperature and the assessment of two additional thawing solutions. Briefly, 20 WT3 day 105 retinal organoids were transferred in cryovials. The organoids were incubated with 300µl pre-cooled freezing media (90% Alpha Modification media (MEMα), (M4526, Sigma) supplemented with 5% FBS, and 5% DMSO) (**Table 2-5**) at 4°C for 30 minutes (**Figure 2-6 A**). Thereafter, the organoids were cooled to 0°C at a rate of -1°C/minute (**Figure 2-6 B**) and maintained at 0°C for 5 minutes (**Figure 2-6 C**). Subsequently, retinal organoids were cooled to -8°C and then to -40°C at 0.5°C/minute (**Figure 2-6 D**) where they were kept at -40°C for 10 minutes (**Figure 2-6 E**). Therefore, at a rate of -1.5°C/minute, retinal organoids were cooled to -80°C (**Figure 2-6 F**). Then, the cryopreserved organoids were transferred and stored in liquid nitrogen for 24 hours (**Figure 2-6 G and H**). Thawing was performed at 37°C by incubating the organoids in a water bath until the ice was thawed (**Figure 2-6 I**). Washing of the organoids to remove CPAs was performed using three different thawing solutions; A) washing with 100% Hank's Balanced Salt Solution (HBSS) for 5 minutes followed by a wash with maintenance media (**Table 2-5**). B) Consecutive washes with 95%, 97%, 99% and 100% HBSS supplemented with 5%, 2%, 1% and 0% of DMSO respectively, for 5 minutes each. Then, the organoids were incubated with maintenance media and transferred to the incubator (**Table 2-5**). C) Successive washes with 95%, 97% and 99% maintenance media supplemented with 5%, 2% and 1% of DMSO, respectively, for 5 minutes for each concentration, followed by 5 minutes incubation with 100% HBSS (**Table 2-5**). Therefore, the organoids were washed with maintenance media (**Figure 2-6 J**) and kept in the incubator at 37°C, with 5% CO_2. Media changes were performed three times a week before their collection on day 14 post-thaw for further analysis (**Figure 2-6 K**).

Table 2-5: Composition of freezing and thawing solutions for the 'mouse retinal' protocol

Reagents	Concentration	Supplier	Catalogue Number
Freezing media			
MEMa	90%	Sigma Aldrich	M4526
FBS	5%	ThermoFisher Scientific	A2720801
DMSO	5%	Sigma Aldrich	D2650
Thawing media A			
HBSS	100%	Life Technologies	14175129
Maintenance media	100%	Section 2.3.3	
Thawing media B			
HBSS	95%, 97%, 99%	Life Technologies	14175129
DMSO	5%, 2%, 1%	Sigma Aldrich	D2650
Maintenance Media	100%	Section 2.3.3	
Thawing media C			
Maintenance Media	95%, 97%, 99%	Section 2.3.3	
DMSO	5%, 2%, 1%	Sigma Aldrich	D2650
HBSS	100%	Life Technologies	14175129

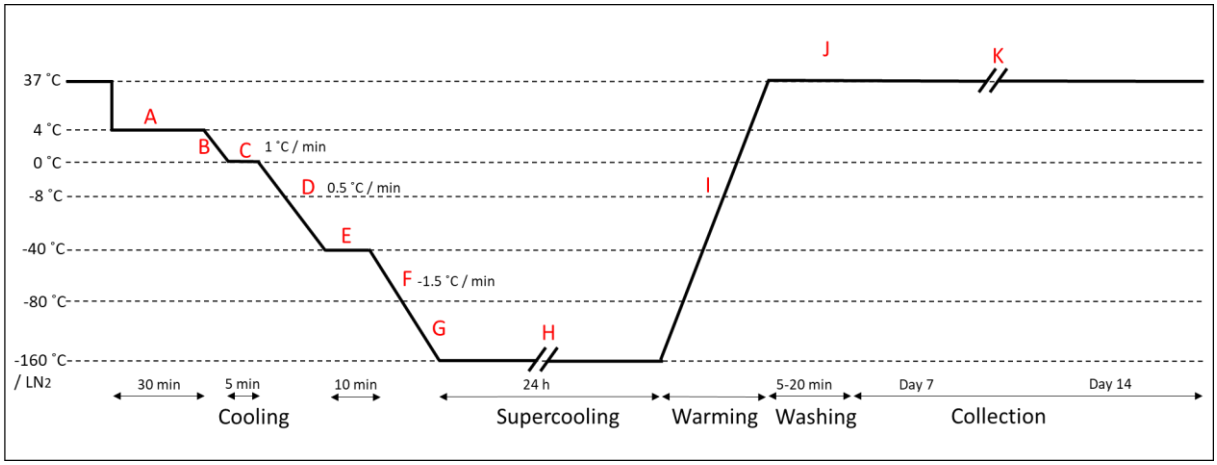

Figure 2-6: Schematic outline of the 'Mouse retinal' protocol. The overall protocol entails 11 steps (A-K). A) Cooling of the organoids to 4°C for 30 minutes. B) Further cooling to 0°C at -1°C/minute, C) incubation at 0°C for 5 minutes. D) Cooling to -8°C and then to -40°C at -0.5°C/minute. E) Maintenance of organoids at -40°C for 10 minutes. F) Further cooling to -80°C at -1.5°C per minute. G) Storage of cryovials in liquid nitrogen for 24 hours. I) Thawing at 37°C, and J) washing using three different thawing solutions; A) HBSS, B) HBSS supplemented with culture media, and C) HBSS supplemented with DMSO. K) Organoids were transferred in the incubator at 37°C for 14 days, and media changes were performed three times a week. Organoids were collected on day 14 post-thaw for IF analysis.

2.3.4.5. Excision of optic vesicles (OVs) and cryopreservation

This protocol is based on our previous 'Mouse retinal' protocol in combination with previously published studies that have shown that excising optic vesicles (OVs) from whole organoids can improve retinal differentiation (Eiraku and Sasai, 2011). Therefore, we hypothesised that possibly excision of OVs could enhance the preservation of the overall structure and expression of retinal cells after cryopreservation. Initially, OVs were excised using a dissection tool. Then OVs were maintained in the incubator (at 37°C) for four days to recover. Cryopreservation of OVs was performed in a 96-well plate. Briefly, 100µl of freezing solution (90% DMEM/F12, 5% FBS, and 5% DMSO) (**Table 2-6**) was added per well of the 96-well plate followed by incubation of the organoids at 4°C for 30 minutes (**Figure 2-7 A**). At a rate of 1°C/minute, OVs were cooled to 0°C and maintained at this temperature for 5 minutes (**Figure 2-7 B and C**). Subsequently, OVs were cooled to -8°C and then to -40°C at a rate of 0.5°C/minute (**Figure 2-7 D**) followed by maintenance of the OVs at -40°C for 10 minutes (**Figure 2-7 D and E**). Then, cooling of the OVs to -80°C at 0.5°C/minute was performed (**Figure 2-7 F**) followed by further cooling to -100°C at 1.5°C/minute (**Figure 2-7 G**). Storage and maintenance of the OVs was performed at -100°C for 24 hours (**Figure 2-7 H**). For the thawing procedure, retinal organoids were warmed to 37°C (**Figure 2-7 I**), and CPAs were washed with 100µl of 100% HBSS for 10 minutes. Subsequent washes with 100µl of culture media were performed (**Figure 2-7 J**) (**Table 2-6**). The OVs were maintained in the incubator at 37°C to recover for 14 days, and media changes were performed three times a week before their collection for IF analysis (**Figure 2-7 K**).

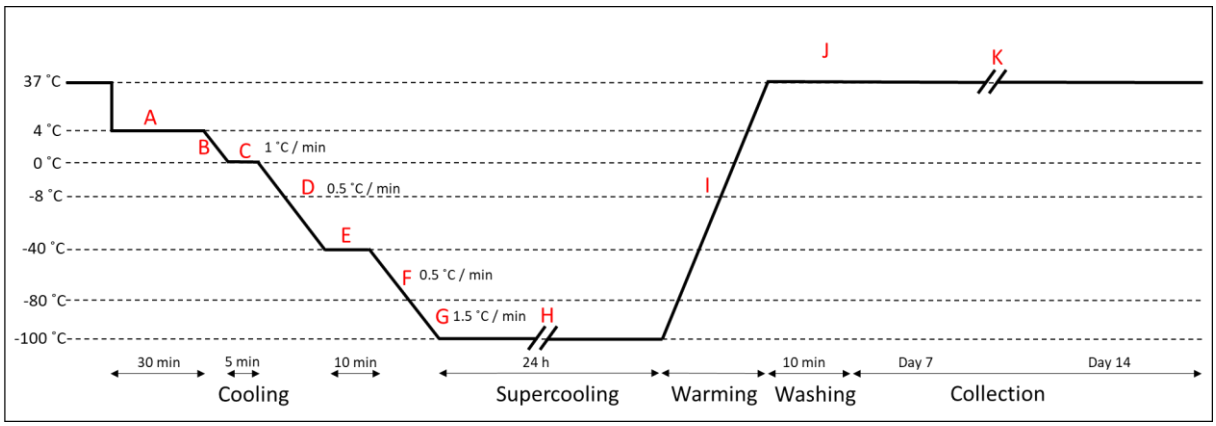

Figure 2-7: Schematic outline of the cryopreservation protocol after excision of OVs. The overall protocol entails 11 steps (A-K). A) Cooling to 4°C for 30 minutes. B) Further cooling to 0°C at -1°C/minute. C) Storage of OVs at 0°C for 5 minutes, D) cooling to -8°C and -40°C at -0.5°C/minute. E) Incubation of OVs at -40°C for 10 minutes. F) Supercooling to -80°C at a rate of -0.5°C/minute, and further to -100°C at a rate of -1.5°C/minute. H) Storage of ROs in Via Freeze at -100°C for 24 hours. I) Warming at 37°C gradually, J) wash with HBSS for 5 minutes, and then wash with culture media for another 5 minutes. K) OVs were transferred in the incubator at 37°C for 14 days. Media changes were performed three times a week. OVs were collected on day 14 post-thaw for IF analysis.

Table 2-6:Composition of solutions for the cryopreservation protocol after excision of OVs.

Reagents	Concentration	Supplier	Catalogue Number
Freezing Solution			
FBS	5%	ThermoFisher Scientific	A2720801
DMEM F12	90%	ThermoFisher Scientific	3133009
DMSO	5%	Sigma Aldrich	D2650
Thawing Solution			
HBSS	100%	Life Technologies	14175129
Maintenance Media	100%	Section 2.3.3	

2.3.4.6. Cooling Experiment

2.3.4.6.1. Cooling of retinal organoids (-10°C) followed by immediate thawing

For the cooling experiment, a basic thawing medium consisting of 98% DMEM/F12, 31.9 mM glucose, 1% Glutamine, and 1% P/S, (**Table 2-7**) was prepared and kept in the incubator overnight in a T75 flask with a pore lid in an upright position to oxygenate. The following day, a complete thawing medium was prepared using 5% of the basic thawing medium, 25% HBSS, and 25% FBS (**Table 2-7**). For the cooling experiment, WT3 retinal organoids at day 169 of differentiation were transferred to cryovials containing 270µl (90%) of cooled (4°C) FBS. Thereafter, retinal organoids were cooled at 4°C and stored at this temperature for 5 minutes

(**Figure 2-8 A and B**). Then, 30µl (10%) of DMSO was added slowly in the cryovials and mixed with FBS. Thereafter, retinal organoids were cooled gradually to -10°C at a rate of -1°C/minute (**Figure 2-8 C**). Once the temperature reached -10°C, retinal organoids were thawed, using a pre-warmed (37°C) thawing medium (**Table 2-7**) (**Figure 2-8 C**), were washed with a fresh complete thawing medium (**Table 2-7**), and were incubated for 24 hours at 37°C (**Figure 2-8 D**). Media changes were performed three times a week. The retinal organoids were collected on day 14 post-thaw for further analysis (**Figure 2-8 E**).

Table 2-7: Composition of solutions for the cooling protocol.

Reagents	Concentration	Supplier	Catalogue Number
Basic thawing Medium			
P/S	1%	ThermoFisher Scientific	15140122
Glutamine	1%	Sigma Aldrich	56-85-9
Glucose	31.9 mM	Sigma Aldrich	50-99-7
DMEM F12	98%	ThermoFisher Scientific	31330095
Freezing Medium			
FBS	90%	ThermoFisher Scientific	A2720801
DMSO	10%	Sigma Aldrich	D2650
Complete thawing medium			
FBS	25%	ThermoFisher Scientific	A2720801
HBSS	25%	Life Technologies	14175129
Basic Medium	50%	Section 2.3.3	

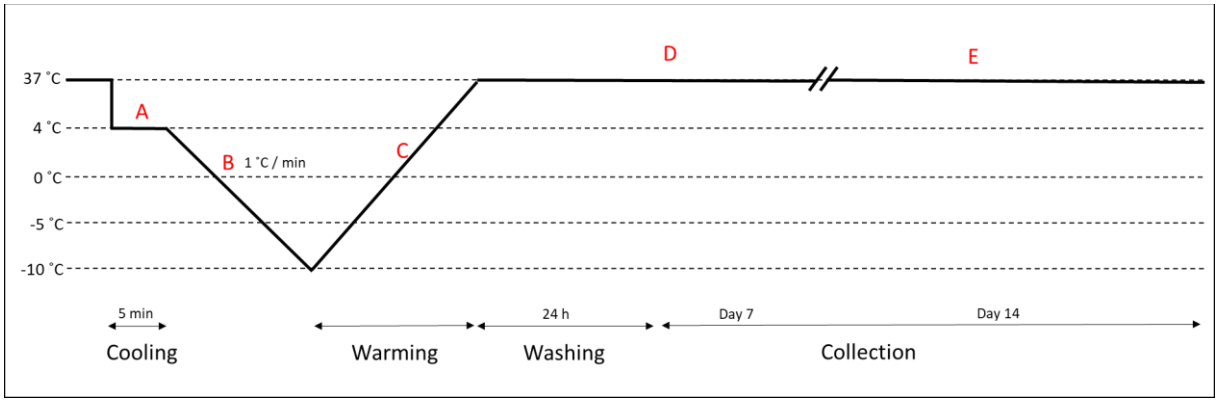

Figure 2-8: Schematic outline of cooling protocol at –10°C. The overall protocol entails 5 steps (A-E). A) Cooling to 4°C for 5 minutes followed by B) gradual cooling to -10°C at -1°C/minute. C) Warming as soon as the temperature reached -10°C. D) Washing with complete thawing medium and then with fresh complete thawing medium. Storage of retinal organoids in the incubator at 37°C, for 24 hours. E) Media changes were performed three times a week. Organoids were collected on day 14 post-thaw for IF analysis.

2.3.4.6.2. Cooling of retinal organoids (-10°C) followed by overnight incubation (24 hours)

To assess whether retinal organoids can survive following overnight incubation at -10°C, the same cooling protocol (section 2.3.4.6.1) was used with some additional modifications. Particularly, following preconditioning with protective agents (**Figure 2-9 A and B**), retinal organoids were maintained at -10°C for 24 hours (**Figure 2-9 C**). After cooling, the organoids were thawed at 37°C, and subsequent steps were performed as mentioned above (section 2.3.4.6.1).

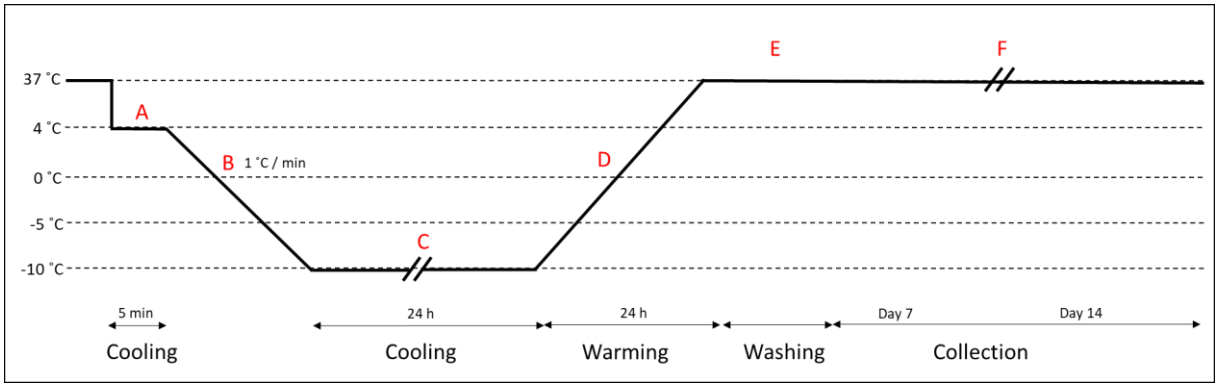

Figure 2-9: Schematic outline of cooling protocol at –10°C for 24 hours. The overall protocol entails 6 steps (A-F). A) Cooling to 4°C for 5 minutes and B) gradual cooling to -10°C at -1°C/minute. C) Storage ROs in VIA Freeze at -10°C, for 24 hours. D) Thawing at 37°C, E) washing with complete thawing medium and then with fresh complete thawing medium. Storage of ROs in the incubator at 37°C. F) Media changes were carried out three times a week. Organoids were collected at day 14 post-thaw for IF analysis.

2.3.4.6.3. Cooling of retinal organoids (-10°C) followed by overnight incubation with the addition of ROCK inhibitor in the thawing solution

To improve further the survival of retinal organoids, the cooling experiment at -10°C with overnight incubation mentioned above (section 2.3.4.6.2) was repeated alongside additional modifications. Modifications included the addition of 10µM of ROCK inhibitor in the complete thawing medium to improve the survival of retinal organoids. Therefore, retinal organoids were processed as mentioned previously (section 2.3.4.6.2).

2.3.4.6.4. Cooling of retinal organoids at -20°C followed by overnight incubation with the addition of ROCK inhibitor in the thawing solution

To identify the appropriate cooling temperature for long-term storage of retinal organoids, the above experiment (section 2.3.4.6.3) assessing the effects of retinal organoids with and without ROCK inhibitor was repeated with final freezing temperature -20°C, instead of -10°C (**Figure**

2-10 C). Retinal organoids were cooled and maintained at -20°C for 24 hours (**Figure 2-10 C**). Then, retinal organoids were washed with a fresh complete thawing medium (**Table 2-7**) and maintained in the incubator at 37°C. All the other steps were performed as described above.

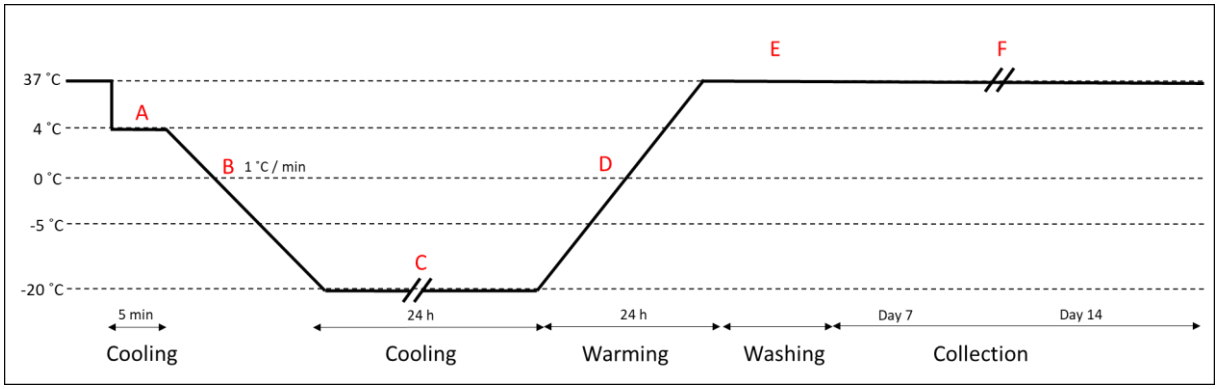

Figure 2-10: Schematic outline of cooling protocol at –20°C for 24 hours. The overall protocol entails 6 steps (A-F). A) Cooling to 4°C for 5 minutes and B) gradual cooling to -20°C at -1°C/minute. C) Storage ROs in the Via Freeze machine at -20°C, for 24 hours. D) Thawing of retinal organoids at 37°C. E) Washing with fresh complete thawing medium. Storage in the incubator at 37°C. F) Media changes were carried out three times a week. Organoids were collected on day 14 post-thaw for IF analysis.

2.3.4.7. Supercooling of retinal organoids using the 'Liver Supercooling' (-4°C) protocol

The following protocol was modified and adapted from a published research study in which human liver organs were successfully viable after supercooling to -4°C (de Vries et al., 2019). Modifications included the incubation time of organoids with freezing and thawing solutions, the addition and exclusion of CPAs in the freezing and thawing solutions, and the concentration of CPAs. Briefly, WT3 day 160 retinal organoids were transferred in cryovials followed by the addition of 300µl of pre-supercooling recovery solution consisting of 92.2% maintenance media, 0.8% P/S, 100 mM Polyethylene glycol, and 100 mM 3-O-methyl-D-glucose (**Table 2-8**). After 20 minutes of incubation at RT (21°C) (**Figure 2-11 A**), pre-supercooling recovery solution was removed and replaced with loading solution 1 consisting of 100 mM Polyethylene Glycol, 5% glycerol, 100 mM D-(+)-trehalose dihydrate, 3 mM glutathione, 100 mM lactobionic acid and 30 mM Raffinose (**Table 2-8**). Subsequently, the organoids were cooled to 4°C, at 1°C per minute, followed by incubation for 10 minutes (**Figure 2-11 B and C**). Later, loading solution 1 was replaced with pre-cooled loading solution 2 (100 mM Polyethylene Glycol, 10% glycerol, 100 mM D-(+)-trehalose, 3 mM glutathione, 100 mM lactobionic acid, and 30 mM raffinose) (**Table 2-8**), followed by incubation of retinal organoids at 4°C for another 10 minutes (**Figure 2-12 C**). Following pre-conditioning with the protective agents, retinal organoids were cooled to -4°C at 1°C per minute, followed by overnight incubation

(**Figure 2-11 D and E**). The next day retinal organoids were thawed to 4°C (**Figure 2-12 F**). Then, washing of the organoids at 4°C for 10 minutes was performed using pre-cooled unloading solution (0.8% P/S, 100 mM Polyethylene Glycol, 2 mM Trolox, 5% Glycerol, 100 mM D-(+)-trehalose dihydrate) (**Table 2-8**), (**Figure 2-11 G**). Thereafter, retinal organoids were further warmed to 37°C (**Figure 2-11 H**) and incubated for 20 minutes in a post-supercooling recovery solution (0.8% P/S, 2 mM Trolox and 100 mM Polyethylene Glycol) (**Table 2-8**) (**Figure 2-11 I**). Retinal organoids were rinsed with maintenance media and transferred in the incubator for 14 days to recover before collection for IF analysis (**Figure 2-11 J**).

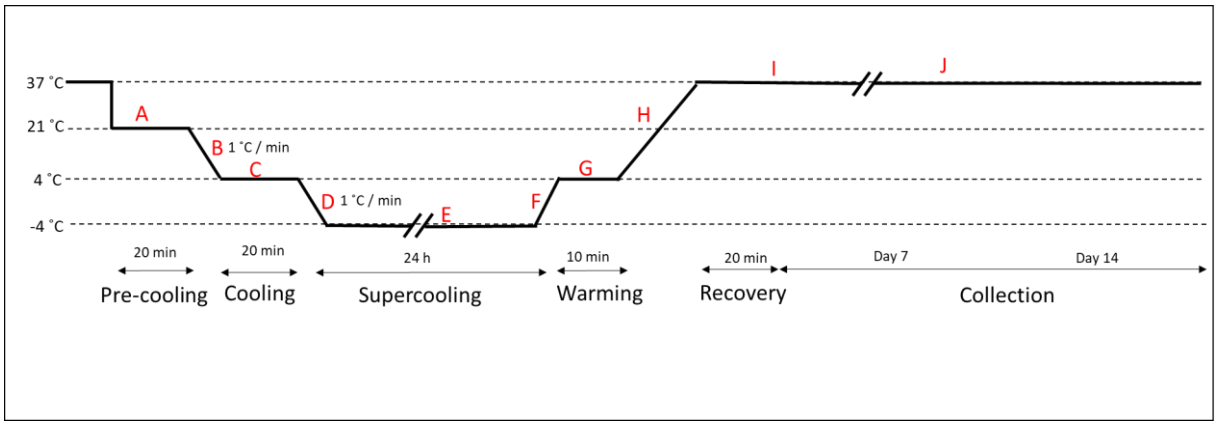

Figure 2-11: Schematic outline of the 'Liver Supercooling' protocol (-4°C). The overall protocol entails 10 steps (A-J). A) Pre-cooling with pre-supercooling recovery solution at 21°C for 20 minutes. B) Further cooling to 4°C at -1°C/minute using loading solution 1. C) Incubation with loading solution 1 at 4°C for 10 minutes followed by further incubation with loading solution 2 for another 10 minutes. D) Cooling to -4°C at 1°C/minute. E) Storage of ROs in VIA Freeze at -4°C for 24 hours. F) Thawing to 4°C followed by G) washing of retinal organoids using unloading solution for 5 minutes at 4°C. H) Thawing of retinal organoids gradually to 37°C, and I) incubation with post-supercooling recovery solution for 20 minutes. K) Transfer of retinal organoids in the incubator at 37°C for 14 days. Media changes were performed three times a week. Organoids were collected on day 14 post-thaw for IF analysis.

2.3.4.8. Master Liver Supercooling (-60°C)

To identify the ideal temperature to freeze retinal organoids, the 'Liver Supercooling' protocol was repeated as mentioned above (section 2.3.4.7), but this time, the organoids were supercooled at a lower temperature, at -60°C. This protocol is referred to as the 'Master Liver Supercooling' protocol. Initially, retinal organoids were transferred in cryovials. Then, 300µl of pre-cooling recovery solution was added per cryovial, and the organoids were incubated for 20 minutes at RT. Thereafter, the 'pre-supercooling recovery solution' was replaced with 300µl of loading solution 1 (**Figure 2-12 A**). Subsequently, retinal organoids were cooled at 1°C per

minute and maintained at 4°C for 10 minutes (**Figure 2-12 B**). Then, 'loading solution 1' was replaced with pre-cooled 'loading solution 2' (**Table 2-8**) following incubation of retinal organoids at 4°C for another 10 minutes (**Figure 2-12 C**). Then the organoids were cooled to -4°C at 1°C per minute and incubated for 10 minutes (**Figure 2-12 D and E**). Following cooling to -10°C at 1°C per minute (**Figure 2-12 F**), the organoids were maintained at -10°C for 20 minutes (**Figure 2-12 G**), and then they were further cooled to -60°C (**Figure 2-12 H**). The organoids were maintained at -60°C for 24 hours (**Figure 2-12 I**). The organoids were warmed to 4°C (**Figure 2-12 J**) followed by washing of the organoids with pre-cooled 'unloading solution' for 10 minutes to remove the protective agents (**Figure 2-12 K**). Subsequently, retinal organoids were warmed to 37°C (**Figure 2-12 L**) and incubated with a 'post-supercooling recovery solution' for 20 minutes (**Table 2-8**) (**Figure 2-12 M**). Then, retinal organoids were rinsed with maintenance media and transferred in the incubator for 14 days to recover before their collection for IF analysis (**Figure 2-12 N**).

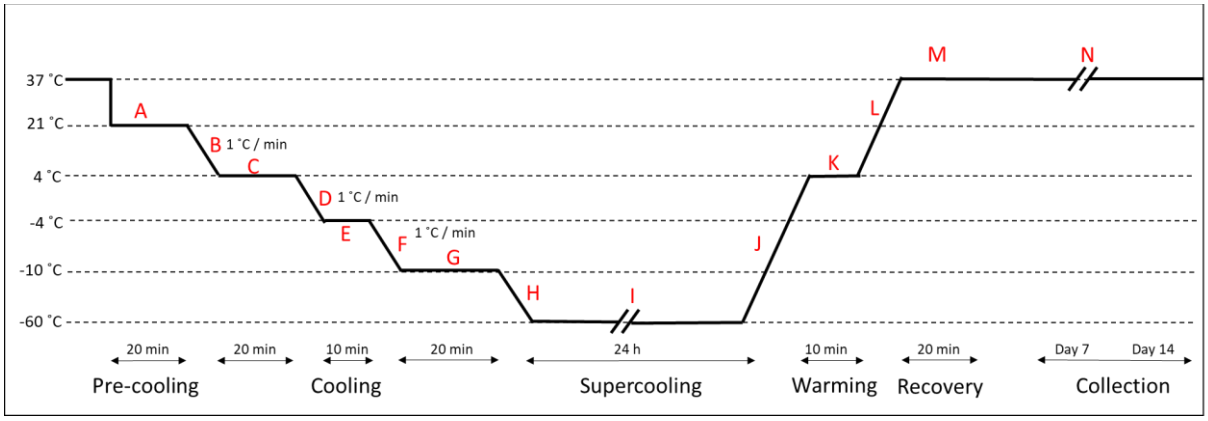

Figure 2-12: Schematic outline of the 'Master Liver Supercooling' protocol (-60°C). The overall protocol entails 14 steps (A-N). A) Pre-cooling with pre-supercooling recovery solution at 21°C for 20 minutes, B) further cooling to 4°C at -1°C/minute using 'loading solution 1'. C) Incubation of ROs with 'loading solution 1' at 4°C for 10 minutes and then with 'loading solution 2' for another 10 minutes followed by D) cooling to -4°C at 1°C/minute. E) Maintenance of ROs at -4°C for 10 minutes, F) cooling to -10°C at 1°C/minute and G) incubation of the organoids at -10°C for 20 minutes. H) Cooling to -60°C at 1°C/minute. I) Storage of ROs in VIA Freeze at -60°C for 24 hours. J) Warming at 4°C, K) washing with unloading solution for 10 minutes at 4°C. L) Warming gradually to 37°C and M) incubation of ROs with post-supercooling recovery solution for 20 minutes. N) Transfer of ROs in the incubator at 37°C for 14 days. Media changes were performed three times a week. Organoids were collected on day 14 post-thaw for IF analysis.

Table 2-8: Composition of solutions for the 'Liver Supercooling' and the 'Master Liver Superocooling' protocol.

Reagents	Concentration	Supplier	Catalogue Number
Pre - supercooling recovery solution			
P/S	0.8%	Thermo Fisher Scientific	15140122
Polyethylene Glycol	100 mM	Sigma Aldrich	25322-68-3
3-O-Methyl-D-glucose	100 mM	Sigma Aldrich	13224-94-7
Maintenance media	92.2%	Section 2.3.3	
Loading Solution 1			
Polyethylene Glycol	100 mM	Sigma Aldrich	25322-68-3
Glycerol	5%	Sigma Aldrich	56-81-5
D-(+)-Trehalose dihydrate	100 mM	Sigma Aldrich	6138-23-4
Glutathione	3 mM	Sigma Aldrich	70-18-8
Lactobionic Acid	100 mM	Sigma Aldrich	96-82-2
Raffinose	30 mM	Sigma Aldrich	17629-30-0
Loading solution 2			
Polyethylene Glycol	100 mM	Sigma Aldrich	25322-68-3
Glycerol	10%	Sigma Aldrich	56-81-5
D-(+)-Trehalose dihydrate	100 mM	Sigma Aldrich	6138-23-4
Glutathione	3 mM	Sigma Aldrich	70-18-8
Lactobionic Acid	100 mM	Sigma Aldrich	96-82-2
Raffinose	30 mM	Sigma Aldrich	17629-30-0
Unloading Solution			
P/S	0.8%	Thermo Fisher Scientific	15140122
Polyethylene glycol	100 mM	Sigma Aldrich	25322-68-3
Trolox	2 mM	Sigma Aldrich	53188-07-1
Glycerol	5%	Sigma Aldrich	56-81-5
D-(+)-Trehalose dihydrate	100 mM	Sigma Aldrich	6138-23-4
Post-supercooling recovery solution			
P/S	0.8%	Thermo Fisher Scientific	15140122
Trolox	2 mM	Sigma Aldrich	53188-07-1
Polyethylene Glycol	100 mM	Sigma Aldrich	25322-68-3
Rinsing media			
Culture maintenance media	5 ml	Section 2.3.3	

2.3.4.8.1. 'Master Liver Supercooling' protocol in combination with enriched loading and thawing solutions

Additional modifications to the 'Master Liver Supercooling' protocol were performed to improve the survival of retinal cells by enhancing the loading and thawing solutions. The 'Master Liver Supercooling' protocol was repeated in combination with additional conditions, which tested individually alongside the original protocol. These conditions included:

Condition 1: Addition of 10 µM ROCK inhibitor and 3 mM Glutathione in the rinsing media **(Table 2-9)**.

Condition 2: Addition of 2.5% and 5% of DMSO in 'loading solution 1' and 'loading solution 2', respectively **(Table 2-9)**.

Condition 3: Combination of condition 1 (addition of 10 µM ROCK inhibitor and 3 mM Glutathione in the rinsing media) and condition 2 (addition of 2.5% and 5% of

DMSO in ‘loading solution 1’ and ‘loading solution 2’, respectively) **(Table 2-9)**. All the steps were performed as mentioned previously (section 2.3.4.8).

Table 2-9: Composition of solutions for the ‘Master Liver Supercooling’ protocol with enriched loading and thawing solutions.

Reagents	Concentration	Supplier	Catalogue Number
Pre - supercooling recovery solution			
P/S	0.8%	Thermo Fisher Scientific	15140122
Polyethylene Glycol	100 mM	Sigma Aldrich	25322-68-3
3-O-Methyl-D-glucose	100 mM	Sigma Aldrich	13224-94-7
Maintenance media	92.2%	Section 2.3.3	
Loading Solution 1			
Polyethylene Glycol	100 mM	Sigma Aldrich	25322-68-3
Glycerol	5%	Sigma Aldrich	56-81-5
D-(+)-Trehalose dihydrate	100 mM	Sigma Aldrich	6138-23-4
Glutathione	3 mM	Sigma Aldrich	70-18-8
Lactobionic Acid	100 mM	Sigma Aldrich	96-82-2
Raffinose	30 mM	Sigma Aldrich	17629-30-0
DMSO	2.5%	Sigma Aldrich	D2650
Loading solution 2			
Polyethylene Glycol	100 mM	Sigma Aldrich	25322-68-3
Glycerol	10%	Sigma Aldrich	56-81-5
D-(+)-Trehalose dihydrate	100 mM	Sigma Aldrich	6138-23-4
Glutathione	3 mM	Sigma Aldrich	70-18-8
Lactobionic Acid	100 mM	Sigma Aldrich	96-82-2
Raffinose	30 mM	Sigma Aldrich	17629-30-0
DMSO	5%	Sigma Aldrich	D2650
Unloading Solution			
P/S	0.8%	Thermo Fisher Scientific	15140122
Polyethylene glycol	100 mM	Sigma Aldrich	25322-68-3
Trolox	2 mM	Sigma Aldrich	53188-07-1
Glycerol	5%	Sigma Aldrich	56-81-5
D-(+)-Trehalose dihydrate	100 mM	Sigma Aldrich	6138-23-4
Post-supercooling recovery solution			
P/S	0.8%	Thermo Fisher Scientific	15140122
Trolox	2 mM	Sigma Aldrich	53188-07-1
Polyethylene Glycol	100 mM	Sigma Aldrich	25322-68-3
Rinsing media			
Culture media	5 ml	Section 2.3.3	
ROCK inhibitor	10 µM	Chemdea	CD0141
Glutathione	3 mM	Sigma Aldrich	70-18-8

2.3.4.8.2. 'Master Liver Supercooling' protocol in combination with enriched RPE condition medium and ECM in loading and thawing solutions for the cryopreservation of retinal organoids

To improve the survival of retinal organoids after cryopreservation, additional conditions were tested individually in combination with the unmodified 'Master Liver Supercooling' experiment. Modifications included:

Condition A: Incubation of organoids with RPE condition medium (CM) during the recovery period. RPE cells were collected from mature RPE monolayers (**Table 2-10**).

Condition B: Supplementation of culture medium used during the recovery period with extracellular matrix (ECM). ECM was collected from adult bovine neural retina as described in our previous study (Dorgau et al., 2019).

Condition C: Incubation of organoids with both RPE CM and ECM during the recovery period.

Condition D: Addition of RPE CM and ECM 7 days prior to supercooling and during the recovery period.

All other steps were performed as mentioned previously (section 2.3.4.8).

Table 2-10: Composition of RPE condition media and ECM for the 'Master Liver Supercooling' protocol.

Reagents	Concentration	Supplier	Catalogue Number
Complete RPE condition medium			
FBS	10%	ThermoFisher Scientific	A2720801
RPE condition medium from H9 RPE cells	42.5%	collected from mature RPE monolayers derived from hESCs – stored in the freezer	
RPE condition medium from AD3 RPE cells	42.5%	collected from mature RPE monolayers derived from hiPSCs – stored in the freezer	
N2 supplement	4.5%	ThermoFisher Scientific	A1370701
Taurine	0.5%	Sigma	T8691
ECM			
ECM	8mg/ml	adult bovine neural retina (decel NR)	
Maintenance Media	100%	Section 2.3.3	

2.3.4.8.3. 'Master Liver Supercooling' protocol with extended pre-cooling incubation times

Additional modifications were tested individually in combination with the original protocol to ensure that CPAs enter intracellularly and inhibit intracellular freezing. Modifications included:

1) Extension of the cooling period from 20 minutes to 2 hours. Incubation of 'loading solution 1' for 1 hour, followed by incubation with 'loading solution 2' for another 1 hour (**Figure 2-13 iC**). All the other steps were performed as mentioned in section 2.3.4.8.

2) Extension of the cooling period from 20 minutes to 3 hours. Incubation of 'loading solution 1' for 1.5 hours, followed by incubation with 'loading solution 2' for another 1.5 hours (**Figure 2-13 iiC**). All the other steps were performed as mentioned previously (section 2.3.4.8).

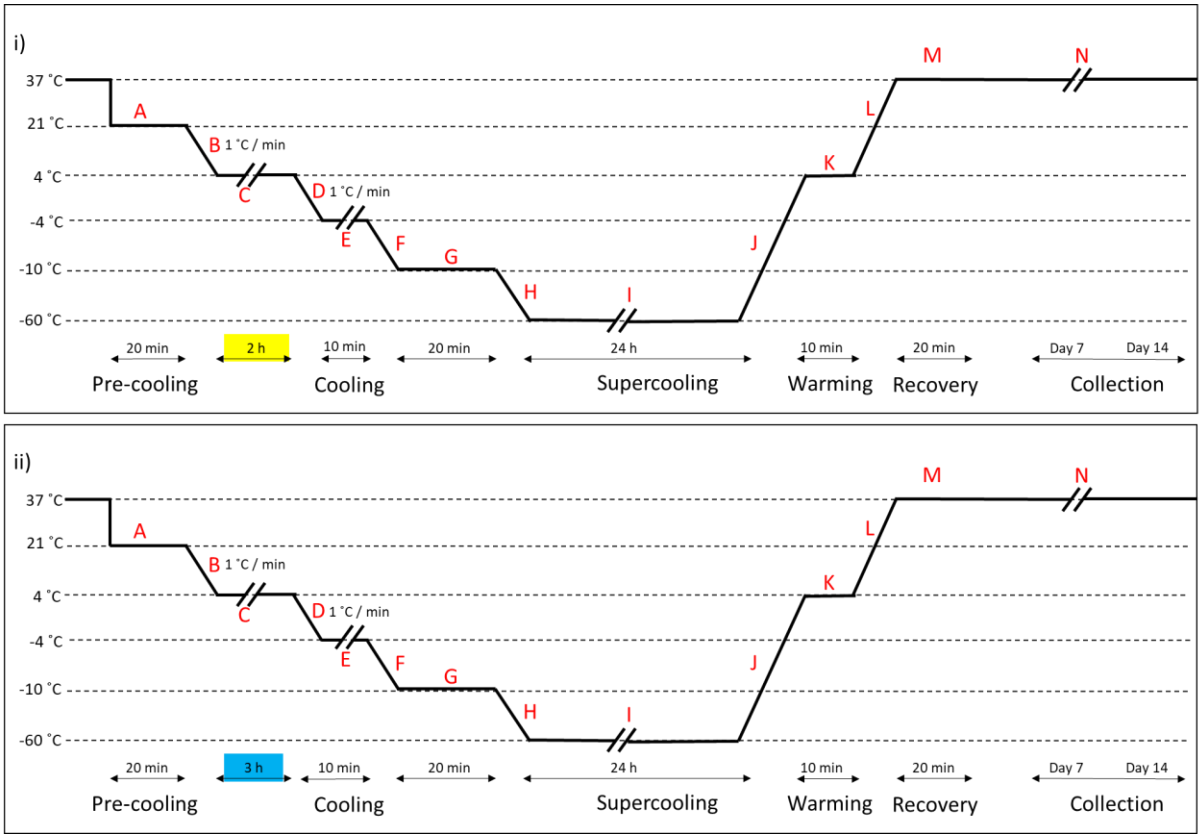

Figure 2-13: Schematic outline of modified 'Master Liver Supercooling' protocol with extended pre-cooling incubation times. The overall protocol entails 14 steps (A-N). A) Pre-cooling with pre-supercooling recovery solution at 21°C for 20 minutes, B) further cooling to 4°C at -1°C/minute using loading solution 1. C) Incubation with loading solution 1 at 4°C for i) 1 hour or ii) 1.5 hours. Incubation with loading solution 2 for another i) 1 hour or ii) 1.5 hours. D) Cooling to -4°C at 1°C/minute. E) Maintenance at -4°C for 10 minutes, F) cooling to -10°C at 1°C/minute. G) Incubation of the organoids at -10°C for 20 minutes. H) Cooling to -60°C at 1°C/minute. I) Storage of ROs in Via Freeze at -60°C for 24 hours. J) Warming of ROs at 4°C and K) washing with unloading solution for 10 minutes at 4°C. L) Warming gradually to 37°C followed by M) incubation of the ROs with post-supercooling recovery solution for 20 minutes. N) Transfer of ROs in the incubator at 37°C, for 14 days. Media changes were performed three times a week. Organoids were collected on day 14 post-thaw for IF analysis. h= hour

2.3.4.8.4. 'Master Liver Supercooling' protocol in combination with matrigel-enriched rinsing media for the cryopreservation of retinal organoids

To enhance the survival of retinal organoids after cryopreservation, additional modifications to the 'Master liver supercooling' protocol were performed. These modifications were focused on the enrichment of the rinsing media to assess whether recovery of retinal organoids could be improved. In combination with the unmodified 'Master Liver Supercooling' protocol, the addition of matrigel in the rising media was tested in parallel (**Table 2-11**). For this experiment, WT3 retinal organoids, as well as WT2 retinal organoids, were used. All the other steps were performed as mentioned previously (section 2.3.4.8).

Table 2-11: Composition of the rinsing solution enriched with matrigel for the 'Master Liver Supercooling' protocol.

Reagents	Concentration	Supplier	Catalogue Number
Rinsing solution			
Matrigel	2mg (300µl)	BD	354230
Maintenance Media	300µl	Section 2.3.3	

2.3.4.8.5. 'Master Liver Supercooling' protocol with the addition of glycerol in the pre-conditioning stage for the cryopreservation of retinal organoids

Some studies have reported that several chemicals are too large to penetrate through the cell membrane, and therefore protection of cells against ice formation is inhibited (Best, 2015). Therefore, pre-incubation of the tissues with CPAs or addition of permeable CPAs could be used to solve this problem. In this experiment, retinal organoids were pre-incubated for 30 minutes at 37°C with 2.5% glycerol supplemented in maintenance media (**Figure 2-14**) (**Table 2-12**). All the following steps were processed as mentioned previously (section 2.3.4.8). In parallel with the modified experiment, the unmodified 'Master Liver Supercooling' protocol was performed.

Table 2-12: Composition of pre-conditioning media with glycerol for the 'Master Liver Supercooling' protocol.

Reagents	Concentration	Supplier	Catalogue Number
Pre-conditioning media			
Glycerol	2.5%	Sigma Aldrich	56-81-5
Maintenance Media	5 ml	Section 2.3.3	

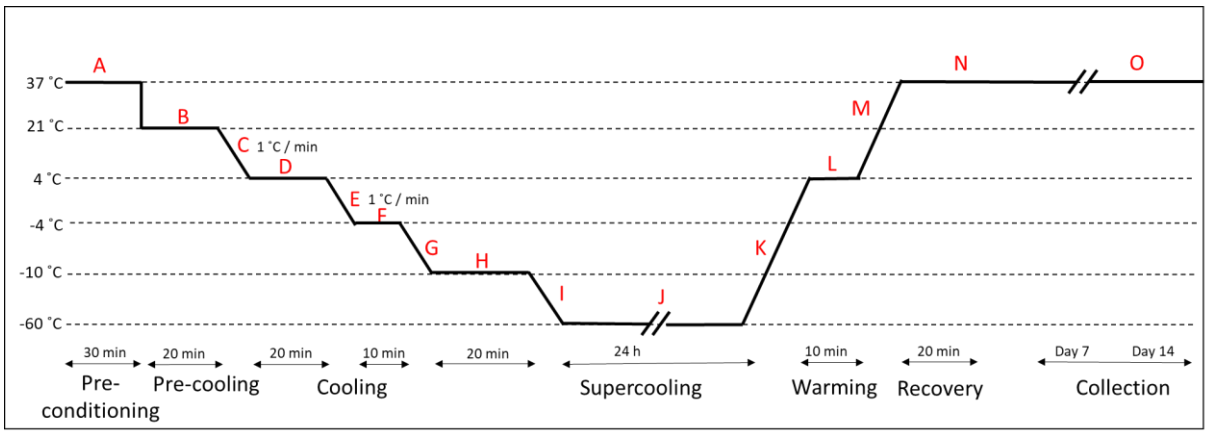

Figure 2-14: Schematic outline of the 'Master Liver Supercooling' protocol with pre-conditioning of ROs with glycerol. The overall protocol entails 15 steps (A-O). A) Pre-conditioning with glycerol at 37°C for 30 minutes. B) Pre-cooling with pre-supercooling recovery solution at 21°C for 20 minutes, C) further cooling to 4°C at -1°C/minute using loading solution 1. D) Incubation with loading solution 1 at 4°C for 10 minutes and then with loading solution 2 for another 10 minutes. E) Cooling to -4°C at 1°C/minute. F) Maintenance at -4°C for 10 minutes, G) cooling to -10°C at 1°C/minute and H) incubation of the organoids at -10°C for 20 minutes. I) Cooling of ROs to -60°C at 1°C/minute. J) Storage of ROs in Via Freeze at -60°C for 24 hours. K) Warming further at 4°C, L) washing with unloading solution for 10 minutes at 4°C. M) Warming gradually to 37°C, N) incubation of ROs with post-supercooling recovery solution for 20 minutes. O) ROs were transferred in the incubator at 37°C for 14 days. Media changes were performed three times a week. Organoids were collected on day 14 for IF analysis.

2.3.5. Processing of cryopreserved organoids

2.3.5.1. Sectioning of organoids

Before sectioning, retinal organoids were collected and fixed in 4% paraformaldehyde (PFA) for 15 minutes (Santa Cruz, 30525-89-4) at RT, followed by three washes with PBS for 5 minutes each. Dehydration of retinal organoids was achieved by incubating organoids in 1 ml of 30% sucrose for 24 hours at 4°C. Then, retinal organoids were embedded in moulds (Tebu-Bio, UK 18985-1) using optimum cutting temperature (OCT) medium (CellPath (KMA-0100-00A). The sample blocks were sectioned into slices of 10 µm thickness using a cryostat (Leica, CM1860) and placed by order on glass slides (SuperFrost, Menzel) (**Figure 2-15**). The slides were then stored at -20°C until further use.

2.3.5.2. Immunofluorescence (IF) analysis

Retinal organoid sections were separated using ImmEdge pen (VectorLabs, H-4000) and air-dried for 20 minutes at RT, followed by three washes with PBS for 5 minutes to remove OCT

from the tissue. Sections were incubated with a blocking solution (5% goat/donkey serum, 0.3% Triton-X in PBS) for 1 hour at RT. Then the organoids were incubated overnight at 4°C with primary polyclonal non-conjugated antibodies (**Table 2-13**) diluted in antibody diluent (1% bovine serum albumin (BSA, Sigma, A9418), 0.3% Triton-X in PBS). Therefore, the sections were washed thrice with PBS for 15 minutes each, and secondary conjugated to fluorophores antibodies (**Table 2-14**) (**Figure 2-15**) were diluted in antibody diluent and added to the sections for 1 hour at RT. To remove unspecific binding, sections were washed three times with PBS for 10 minutes each. Sections of retinal organoids were covered by Hoechst nuclear stain (Sigma, B2261) diluted in Vectashield at 1:2000 (VectorLabs, H-1000), followed by sealing of the slides by a coverslip.

Table 2-13: List of primary antibodies.

Antibody	Conjugate/Tissue	Host	Source	Cat. No.	Dilution
Ap2α	Amacrine cells	Mouse	Santa Cruz	sc-12726	1:200
ARL13B	Connecting cilium	Rabbit	Abcam	ab83879	1:250
Arrestin 3	Cone photoreceptors	Rabbit	Novus Biological	NBP2-41249	1:100
RLBP1	RPE and Müller glial cells	Mouse	Abcam	ab15051	1:100
Crx	postmitotic photoreceptors	Mouse	Abnova	H00001406-M02	1:200
HuC/D	Amacrine and retinal Ganglion Cells	Mouse	Invitrogen	A21271	1:200
Opsin Blue	S cone photoreceptors	Rabbit	Abcam	AB5407	1:200
Opsin red/green	L/M cone photoreceptors	Rabbit	Millipore	AB5405	1:200
Prox 1	Horizontal and Amacrine cells	Rabbit	Millipore	AB5475	1:1000
Recoverin	photoreceptors and midget OFF bipolar cells	Rabbit	Millipore	AB5585	1:1000
RetP1 (Rhodopsin)	Rod photoreceptors	Mouse	Sigma	O4886	1:200
SNCG	Retinal ganglion cells	Mouse	Abnova	H00006623-M01A	1:500

Table 2-14: List of secondary antibodies used for IF on retinal organoids. r=rabbit, m= mouse, gt=goat.

Antibody	Host	Source	Cat. No.	Dilution
Gt a-r Alexa (546)	Jackson ImmunoResearch	Goat	111545144	1:800
Gt a-m Cy3	Jackson ImmunoResearch	Goat	115165003	1:800
Gt a-m Alexa (488)	Jackson ImmunoResearch	Goat	115-545-146-JIR	1:800

2.3.5.3. Microscopy and image analysis

The images were analyzed using the Axio Imager upright microscope with Apotome structured illumination fluorescence (Zeiss, Germany). Fluorescent filters such as Hoechst, Cy3 and Alexa 488 and Alexa 546 were used to cover multiple dyes. Images were taken at 20 x objective (**Figure 2-15**). Approximately 8-10 organoids were analyzed per condition. Images were analyzed and presented as a maximum intensity projection (MIP) using Ziss Zen blue software, and brightness and contrast were adjusted using Adobe Photoshop (Adobe Systems).

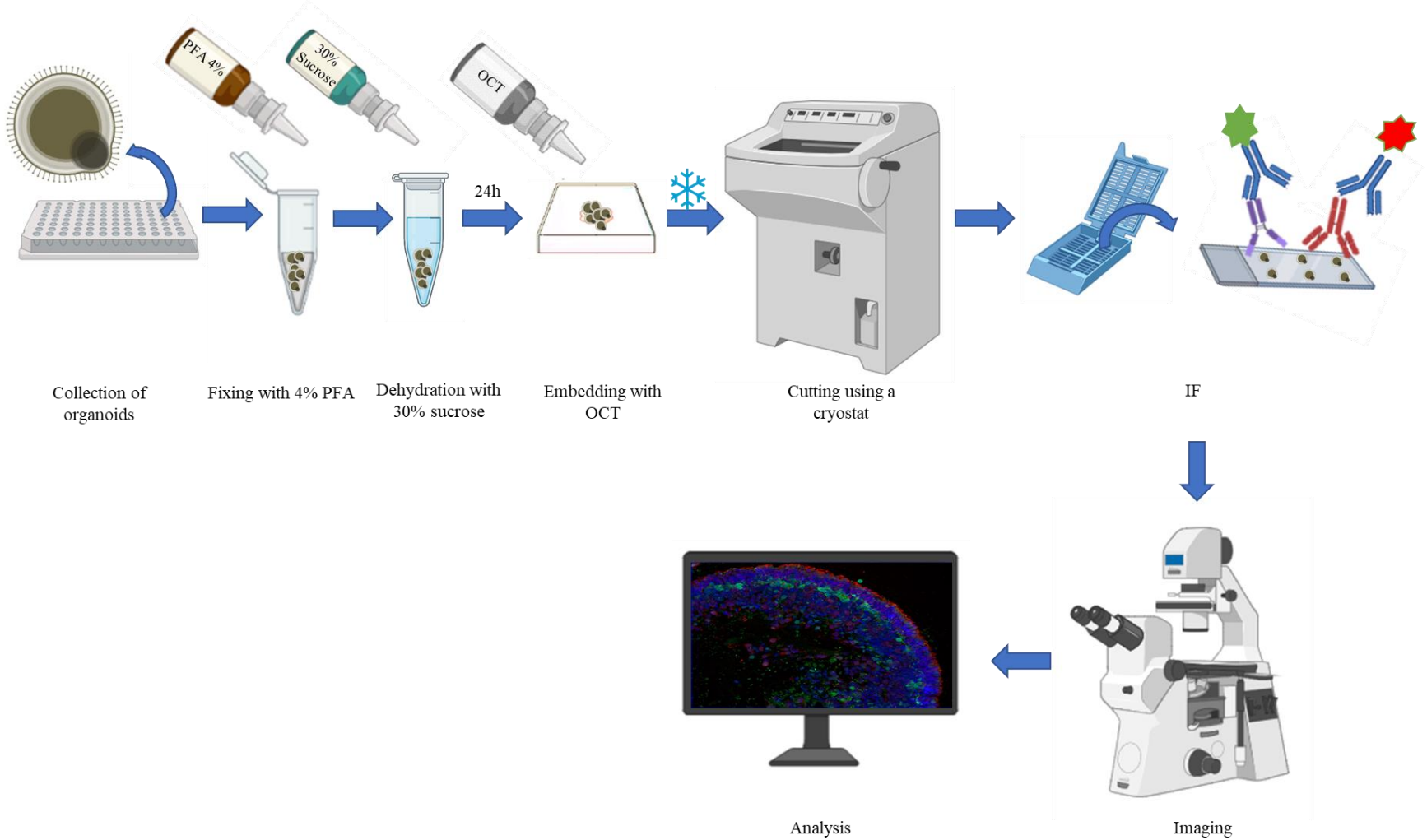

Figure 2-15: Schematic summary of the procedure from collection to analysis of retinal organoids. ROs were collected and then fixed with 4% PFA. Following overnight incubation with 30% sucrose, ROs were embedded in moulds with OCT and were cooled before sectioning. Sectioning of the ROs was performed using a cryostat. The sections were collected in glass slides. IF analysis was performed using retinal-related markers. Then, stained sections were analysed using Axio Imager upright microscope, and analysis of the images was performed using Ziss Zen blue software and Adobe Photoshop (Adobe Systems).

2.4. Results

Using an established protocol, human iPSCs were differentiated to retinal organoids (Kuwahara et al., 2015). Generated retinal organoids contain all key retinal cell types and synaptic connections and respond to electrophysiological stimuli. For the cryopreservation experiments, control hiPSC-derived retinal organoids at day 80 of differentiation or older were used.

Several different cryopreservation protocols were performed in this study, including vitrification, slow and fast freezing. The cryopreservation methodologies were obtained from previous cryopreservation studies that reported the successful cryopreservation of complex tissues (Pichugin et al., 2006, Richards et al., 2004, Fayomi et al., 2019, de Vries et al., 2019). These protocols were modified and assessed on retinal organoids. The cryopreservation methods used in this study are listed below:

1) Vitrification of retinal organoids using VEG or VM3 vitrification solutions, testing two different freezing rates, a slow (gradual vitrification) and fast (direct) freezing rate (Pichugin et al., 2006).
2) Cryopreservation using ES-HEPES vitrification solution (Richards et al., 2004).
3) Cryopreservation using 'Mouse retinal' protocol (Fayomi et al., 2019).
4) Excision of optic vesicles and cryopreservation (Eiraku et al., 2011, Fayomi et al., 2019).
5) Cooling experiment, cooling the organoids at -10°C and -20°C.
6) Liver supercooling (at -4°C) and Master Liver Supercooling (-60°C) protocol (de Vries et al., 2019).

2.4.1. VEG Vitrification

2.4.1.1. Effect of VEG Vitrification solution on gradually cryopreserved retinal organoids

To investigate the impact of VEG vitrification solution, day 80 WT3 organoids were cryopreserved as described previously (section 2.3.4.1). Bright-field images of organoids were taken before vitrification, immediately after thawing (day 1), on day 7 and day 14 post-thaw. The efficiency of the vitrification experiment was assessed by evaluating the overall structure of cryopreserved retinal organoids after 7 and 14 days of post-thaw culturing.

Bright-field images of WT3 retinal organoids were captured before vitrification, showing a bright, smooth, round bright phase neuroepithelium edge (red arrow) and OVs features. Following vitrification, retinal organoids shrunk and became darker (**Figure 2-16**). By day 14

post-thaw, the structure of some cryopreserved organoids disintegrated, and the bright phase neuroepithelium was lost (**Figure 2-16**).

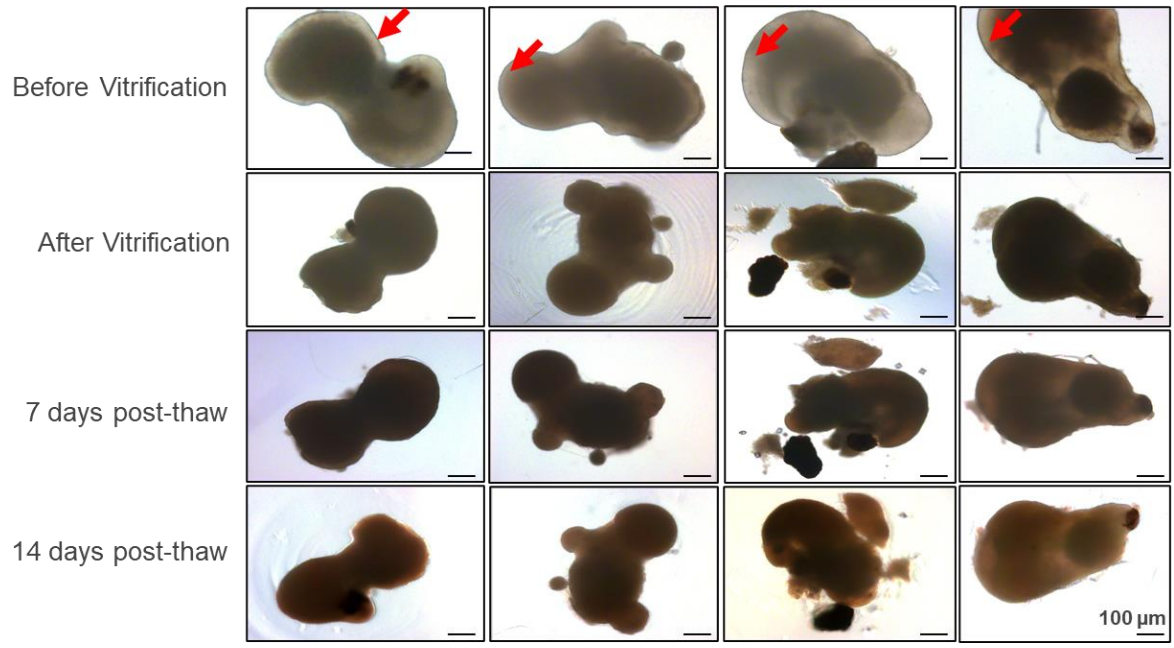

Figure 2-16: Representative images of WT3 retinal organoids before and after gradual vitrification using VEG vitrification solution. Bright-field images of day 80 retinal organoids before vitrification (representing the organoids before cryopreservation experiment), after vitrification (upon thawing of the organoids), at 7 and 14 days post-thaw (representing the recovery period of the organoids in a humidified environment at 37°C with 5% CO_2). Red arrows show the bright-phase neuroepithelium of retinal organoids. Scale bars=100 µm.

To assess the presence of retinal cell types in day 80 VEG gradually cryopreserved organoids, day 14 post-thaw organoids and control organoids were analyzed by IF analysis as mentioned in section 2.3.5.2. Control and gradually vitrified organoids were stained with retinal markers, including Recoverin (PR marker), HuC/D (ganglion and amacrine cell marker), AP2α (amacrine cell marker), RLBP1 (Müller glia cell marker), Crx (PR cell marker) and Prox1 (horizontal cell marker) (**Figure 2-17**). The IF results indicated that none of the retinal cell-specific markers were present in the gradually vitrified retinal organoids compared to the control organoids (**Figure 2-17**). Taken together, these results indicate that gradual vitrification of retinal organoids with VEG vitrification solution has a negative impact on the survival of retinal cells. Due to negative results, this experiment was not repeated.

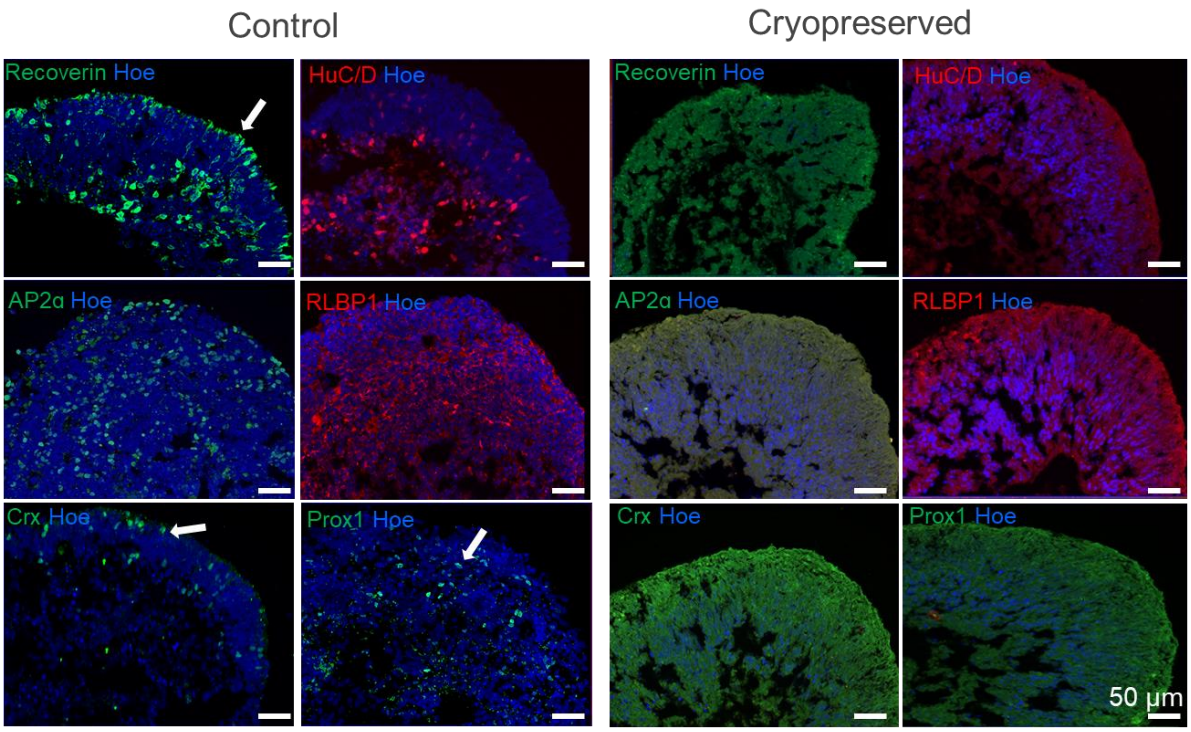

Figure 2-17: Immunostaining of control and gradually VEG vitrified day 80 retinal organoids 14 days post-thaw. Sections through control and cryopreserved day 80 retinal organoids. PR cells (Recoverin, green), amacrine and ganglion cells (HuC/D, red), amacrine cells (AP2α, green), Müller cells (RLBP1, red), PR cells (Crx, green), and horizontal cells (Prox1, green) were present in day 80 control retinal organoids. White arrows indicate positive cells. Gradually VEG vitrified organoids did not express any retinal markers. Nuclei were counterstained with Hoechst (Hoe, blue). Scale bars=50 µm.

2.4.1.2. Effect of VEG Vitrification solution on directly cryopreserved retinal organoids

Thereafter, to investigate whether a faster cooling rate could improve the survival of retinal organoids, day 98 retinal organoids were vitrified directly to -100˚C in a VEG vitrification solution as described in section 2.3.4.1. Similar morphological observations with gradually vitrified organoids were detected. Specifically, day 98 direct vitrified retinal organoids shrunk, turned black, and the bright phase neuroepithelium was lost after vitrification. By day 14-post thaw, retinal organoids partially disintegrated (**Figure 2-18**).

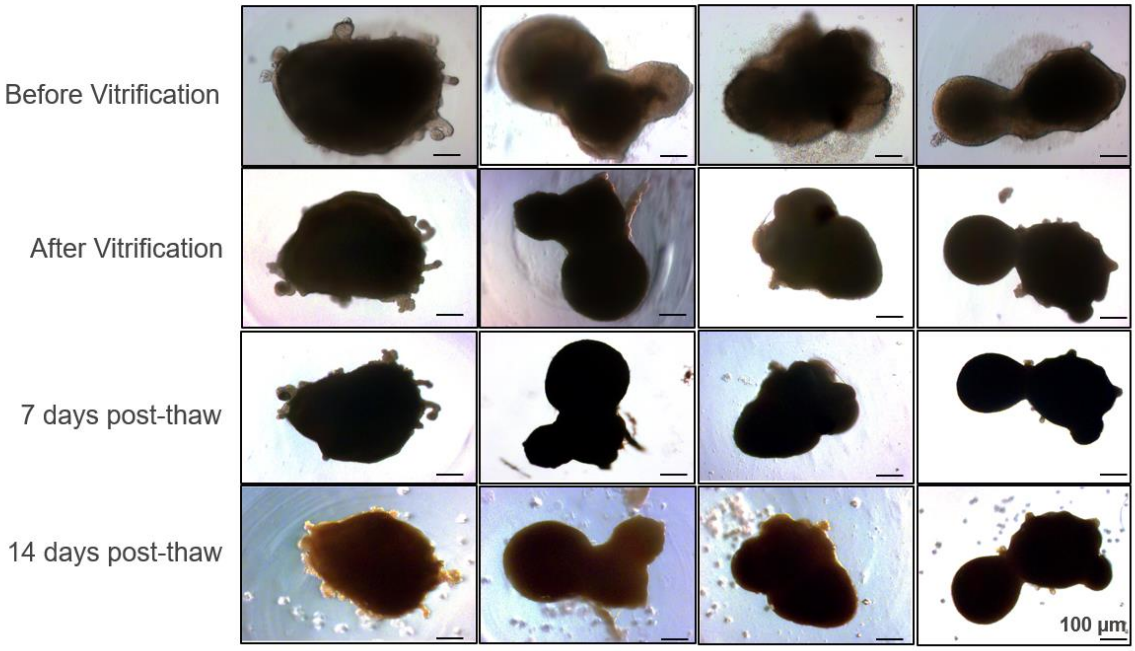

Figure 2-18: Representative images of WT3 retinal organoids before and after direct vitrification using VEG vitrification solution. Bright-field images of day 98 retinal organoids before vitrification (representing the organoids before cryopreservation experiment), after vitrification (upon thawing of the organoids), at 7 and 14 days post-thaw (representing the recovery period of the organoids in a humidified environment at 37°C with 5% CO_2). Scale bars=100 µm.

The survival of retinal populations in control and 14 days post-thaw organoids was evaluated by IF analysis. To identify maturing retinal cells, a panel of retinal-related markers including Recoverin (PR cells), HuC/D, (ganglion and amacrine cells), AP2α, (amacrine cells), RLBP1, (Müller glial cells), Crx (PR cells) and Prox1 (horizontal cells) was used (**Figure 2-19**). IF results confirmed that the overall structural integrity of VEG vitrified organoids was mainly preserved after 14 days post-thaw; however, no retinal-related cell markers were detected (**Figure 2-19**). Overall, these results indicate that freezing with VEG vitrification solution at a

fast cooling rate can maintain the overall structure of retinal organoids; however, the survival of retinal populations after 14 days post-thaw was affected (**Figure 2-19**). Therefore, no further repeats were performed due to negative results.

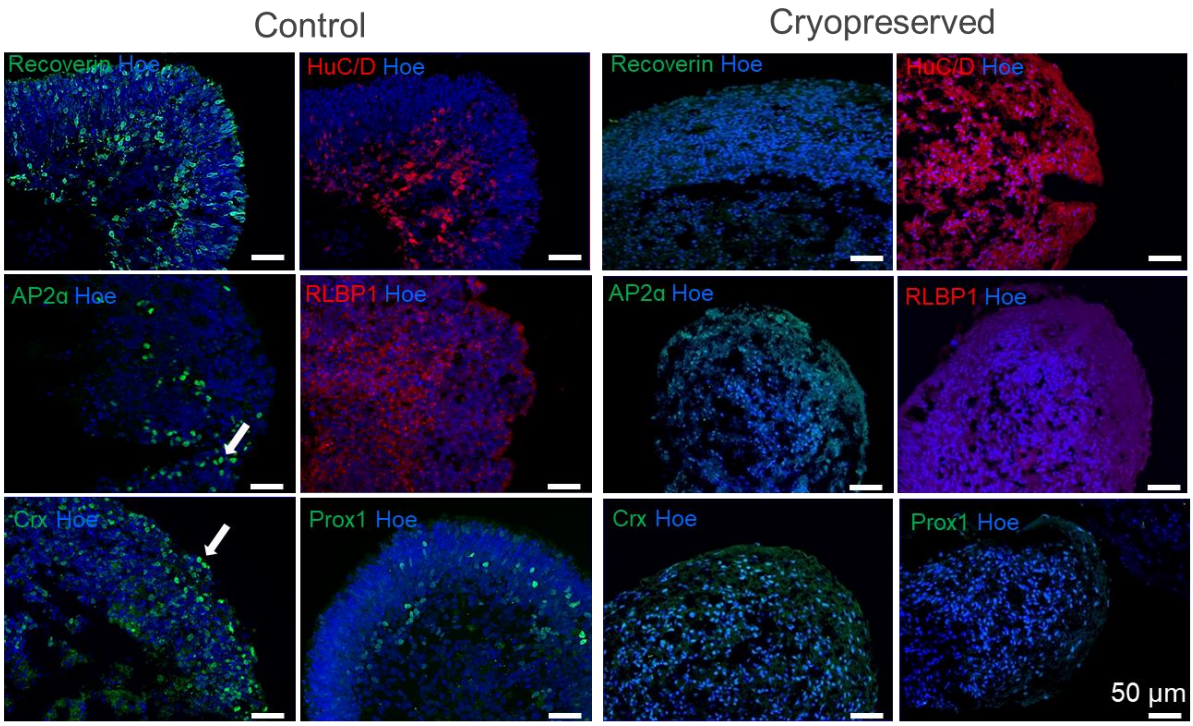

Figure 2-19: Immunostaining of control and directly VEG vitrified day 98 retinal organoids, 14 days post-thaw. Sections through control and cryopreserved day 98 retinal organoids. PRs (Recoverin, green), amacrine and ganglion cells (HuC/D, red), amacrine cells (AP2α, green), Müller cells (RLBP1, red), PRs (Crx, green), and horizontal cells (Prox1, green) were present in day 98 control retinal organoids. White arrows indicate positive cells. Gradually vitrified organoids did not express any retinal marker. Nuclei were counterstained with Hoechst (Hoe, blue). Scale bars=50 µm.

2.4.2. VM3 Vitrification

2.4.2.1. Effect of VM3 Vitrification solution on gradually cryopreserved retinal organoids.

To investigate the impact of VM3 vitrification solution, WT3 retinal organoids were cryopreserved as described in section 2.3.4.2. Bright-field images of day 84 retinal organoids were obtained before vitrification, after thawing (day 1), at day 7 and day 14 of post-thaw (**Figure 2-20**).

The morphology of WT3 retinal organoids before vitrification was characterized by a smooth, bright phase neuroepithelium edge across the apical layer. Also, some retinal organoids were characterised by pigmented patches resembling RPE cells. Immediately after thawing, vitrified organoids were characterised by a fluffy neuroepithelium, and the overall structure of the

organoids was rough. By day 14 post-thaw, the bright phase neuroepithelium was damaged, and the overall structural integrity of the vitrified organoids was lost (**Figure 2-20**).

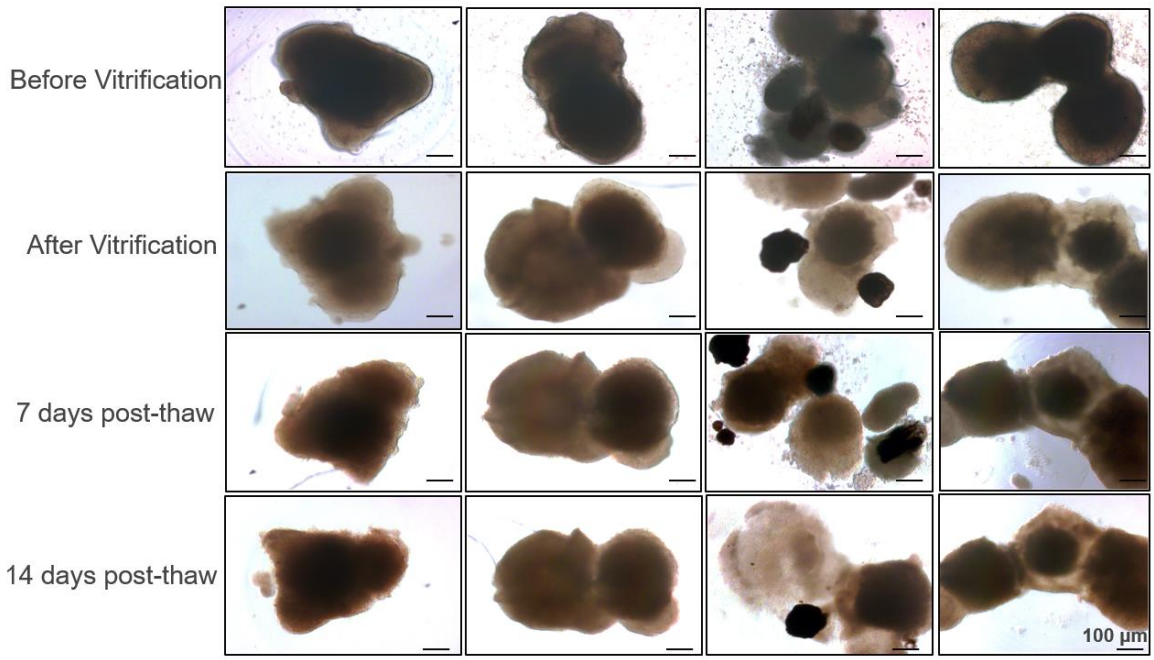

Figure 2-20: Representative images of WT3 retinal organoids before and after gradual vitrification using VM3 vitrification solution. Bright-field images of day 84 retinal organoids before vitrification (representing the organoids before cryopreservation experiment), after vitrification (upon thawing of the organoids) at 7 and 14 days post-thaw (representing the recovery period of the organoids in a humidified environment at 37°C with 5% CO_2). Scale bars=100 µm.

Cell survival was assessed by IF analysis. The structure of VM3 gradually vitrified retinal sections was damaged with gaps present throughout, and the nuclei were dotty. Also, no retinal-related markers such Recoverin, HuC/D, AP2α, RLBP1, Crx, and Prox1 were detected in day 84 VM3 vitrified retinal organoids (**Figure 2-21**). In contrast, control organoids were positive for Recoverin and Crx immunostaining, which were located at the apical side of the organoids representing PR cells (**Figure 2-21**). Additionally, retinal ganglion and amacrine cells stained with HuC/D were located at the basal layer of control organoids (**Figure 2-21**). AP2α and Prox1 immunopositive cells were located in the middle layer of control organoids representing amacrine and horizontal cells, respectively, and Müller glial cells extending throughout the retinal structure were detected by RLBP1 (**Figure 2-21**). Overall, these data indicated that VM3 vitrification solution affected retinal organoids' structure, morphology, and survival (**Figure 2-21**). As a result, no further repeats were performed for this experiment.

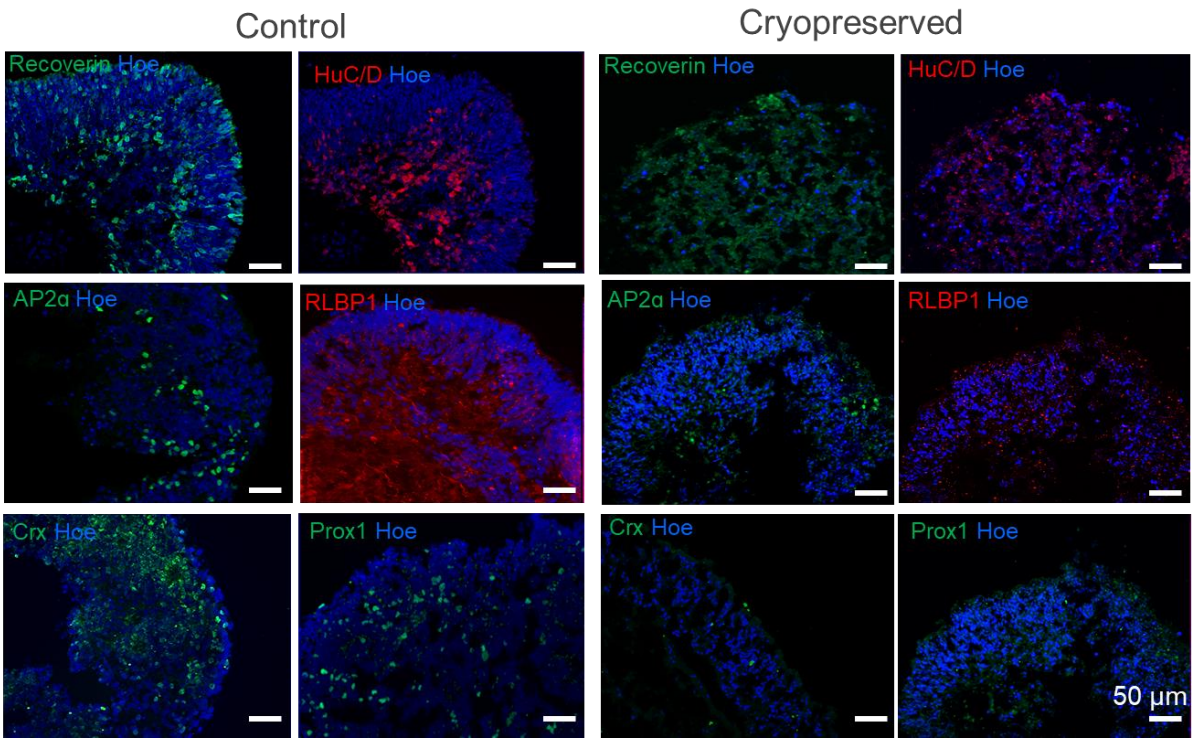

Figure 2-21: Immunostaining of control and gradually VM3 vitrified day 84 retinal organoids 14 days post-thaw. Sections through control and cryopreserved day 84 retinal organoids. PRs (Recoverin, green), amacrine and ganglion cells (HuC/D, red), amacrine cells (AP2α, green), Müller glial cells (RLBP1, red), PRs (Crx, green), and horizontal cells (Prox1, green) were present in day 84 control retinal organoids. Gradually vitrified organoids did not present any retinal marker, and the structure of some organoids was damaged. Nuclei were counterstained with Hoechst (Hoe, blue). Scale bars =50 µm.

2.4.2.2. Effect of VM3 Vitrification solution on directly cryopreserved retinal organoids

Thereafter, retinal organoids at day 92 of differentiation were used to assess whether direct vitrification of organoids using VM3 vitrification solution could effectively preserve the structure and survival of retinal organoids. The morphology of WT3 retinal organoids before vitrification was characterised by a bright phase neuroepithelium edge across the apical side, pigmented RPE patches, and budding OVs (**Figure 2-22**). Immediately after vitrification, the bright phase neuroepithelium layer of WT3 retinal organoids was lost, and by 14 days post-thaw, the overall structure of the organoids was degenerated completely (**Figure 2-22**). As a result, the organoids were not assessed further for IF analysis to determine cell survival and identity. Overall, the results indicate that vitrification of retinal organoids directly to -100˚C using VM3 vitrification solution at the specific concentrations used induced the degeneration of retinal organoids, and hence no further experimental replications were performed (**Figure 2-22**).

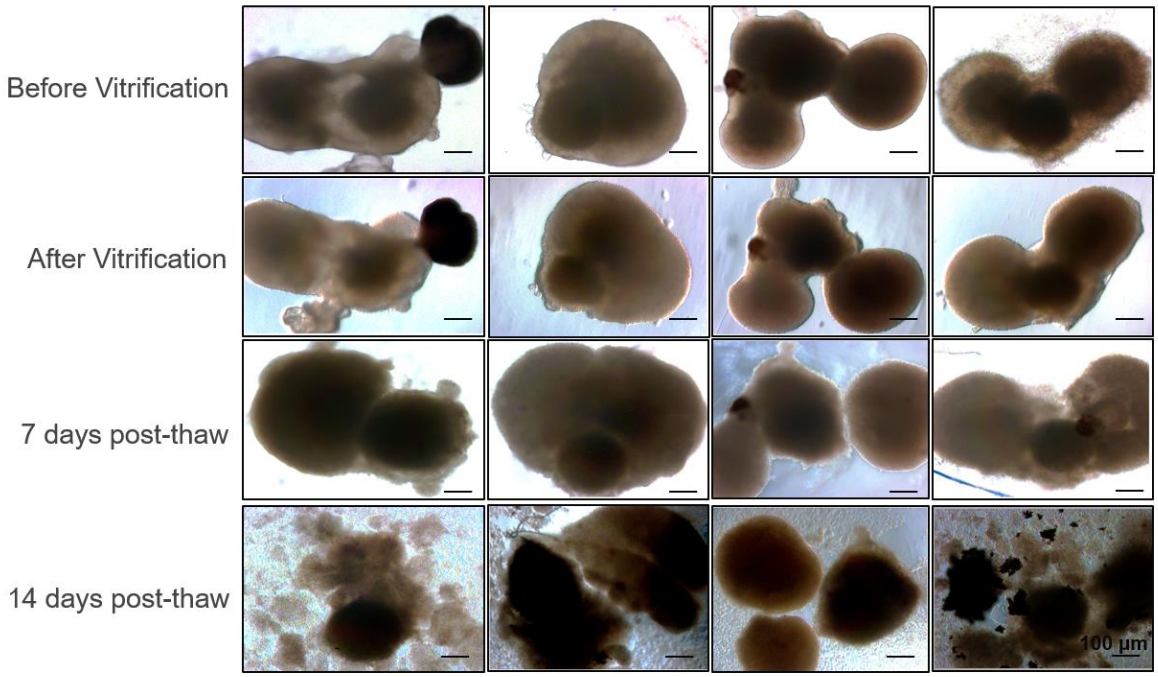

Figure 2-22: Representative images of WT3 retinal organoids before and after direct vitrification using VM3 vitrification solution. Bright-field images of day 92 retinal organoids before vitrification (representing the organoids before cryopreservation experiment), after vitrification (upon thawing of the organoids) at 7 and 14 days post-thaw (representing the recovery period of the organoids in a humidified environment at 37°C with 5% CO_2). Scale bars=100 µm.

2.4.3. Effect of ES-HEPES vitrification solution on retinal organoids

Bright-field images of day 91 retinal organoids were captured before and after cryopreservation to determine whether cryopreservation of retinal organoids using the ES-HEPEs solution (as mentioned in section 2.3.4.3), can preserve the overall structure and presence of retinal cells effectively. Before vitrification, retinal organoids' structure and morphology were characterised by a bright phase neuroepithelium and some pigmented RPE patches. After thawing, signs of continued deterioration were observed (**Figure 2-23**). By day 7 post-thaw, the bright phase neuroepithelium edge was lost. The organoids' overall structural integrity was disintegrated entirely, and over time, complete fragmentation of the organoids was observed (**Figure 2-23**). It is important to highlight the observation of tangled hair-like structures around the organoids immediately after thawing (**Figure 2-23**), which could probably be a sign of death. As a result of the complete disintegration of organoids, no IF analysis was performed. Overall, the results indicate that the ES-HEPEs solution is not suitable for the preservation of retinal organoids using this particular protocol. Hence, no further replications were performed.

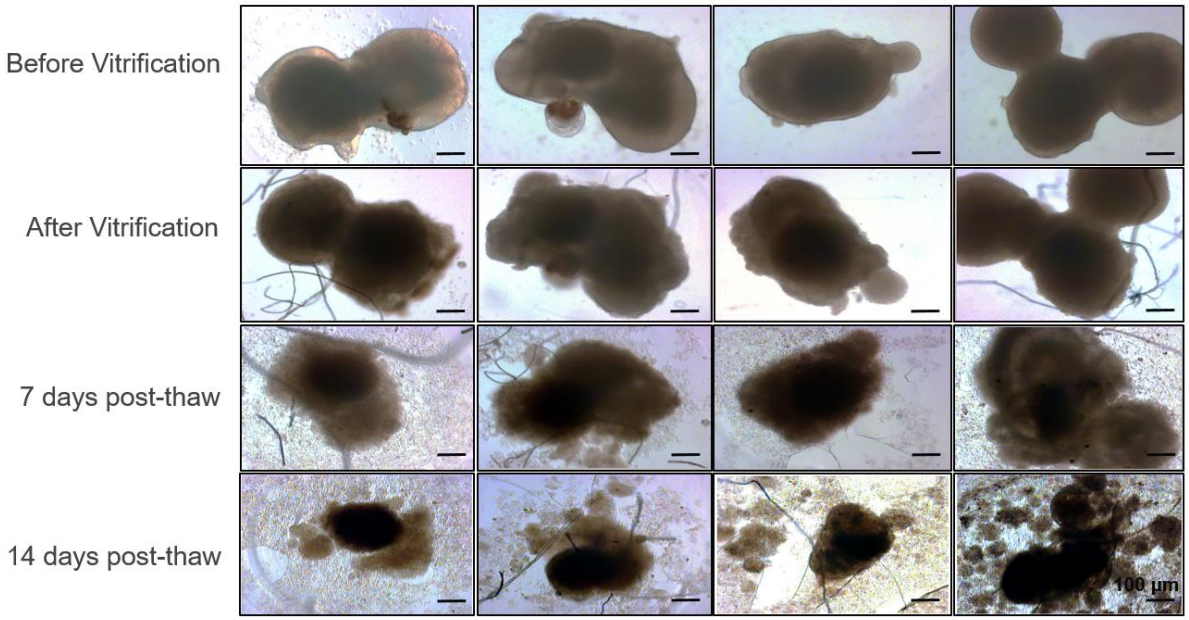

Figure 2-23: Representative images of WT3 retinal organoids before and after cryopreservation using ES-HEPES solution. Bright-field images of day 91 retinal organoids before vitrification (representing the organoids before cryopreservation experiment), after vitrification (upon thawing of the organoids), at 7 and 14 days post-thaw (representing the recovery period of the organoids in a humidified environment at 37°C with 5% CO_2). Scale bars=100 µm.

2.4.4. Effect of the 'Mouse retinal' protocol on retinal organoids

Recently, a cryopreservation protocol from Fayomi and colleagues reported that cryopreserved prepubertal testicular tissues were successfully grafted under the back skin of rhesus macaques and produced functional sperm (Fayomi et al., 2019). This study indicates that cryopreservation of testicular tissue before initiation of gonadotoxic treatments could preserve prepubertal patients' fertility. Considering the promising findings of this study, this protocol was assessed on WT3 retinal organoids day 105 of differentiation (Fayomi et al., 2019) as described in section 2.3.4.4.

Bright-field images of WT3 retinal organoids were captured before and immediately after thawing to examine whether the cellular identity, structure, and morphology of retinal organoids can be preserved after cryopreservation using MEMα solution.

Before cryopreservation, mature retinal organoids were characterised by a bright phase, smooth neuroepithelium edge, and OV morphology (**Figure 2-24**). Following cryopreservation, retinal organoids were thawed and washed with three different solutions: a) HBSS, b) HBSS with DMSO, and c) DMSO with culture media. Immediately after thawing, the bright phase neuroepithelium edge was darker with a 'fluffy' morphology. However, the overall structural integrity of the organoids was maintained (**Figure 2-24**) in all the three different thawing solutions that were used. As a result, no further examinations were performed to assess cell survival. Together these data suggest that cryopreservation of retinal organoids using this particular protocol could affect the overall survival of retinal organoids, and hence it is not considered as an optimal protocol for the preservation of retinal organoids. Due to the negative results observed, no more repeats were performed.

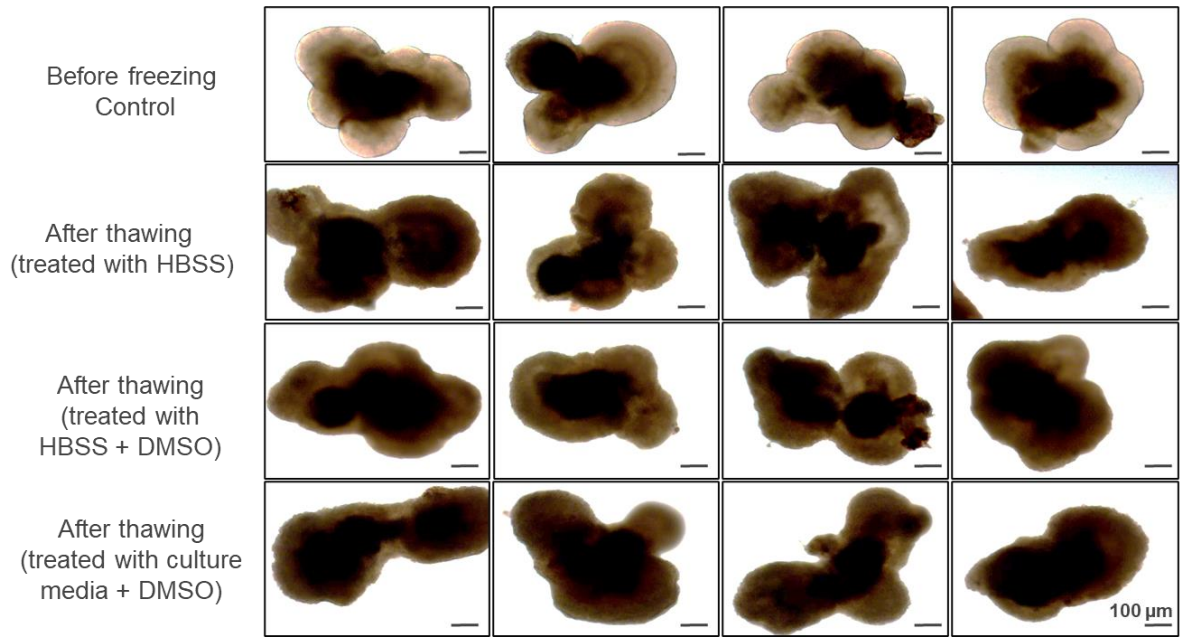

Figure 2-24: Representative images of WT3 retinal organoids before and after cryopreservation using the 'Mouse retinal' protocol. Bright-field images of day 105 retinal organoids before freezing (representing the organoids before cryopreservation experiment) and after thawing (upon thawing of the organoids) using HBSS only, HBSS supplemented with DMSO, and culture media supplemented with DMSO. Scale bars=100 µm.

2.4.5. Effect of freezing solution on excised retinal OVs

To assess the impact of freezing solution on retinal OVs, day 155 WT3 retinal organoids were excised as indicated by the red dotted lines (**Figure 2-25**) and pooled in culture for 4 days to recover before cryopreservation.

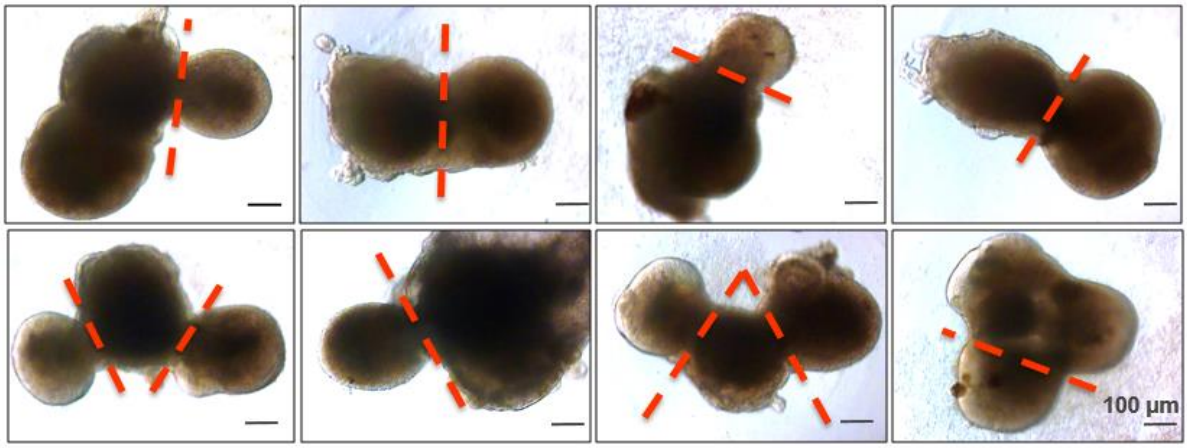

Figure 2-25: Representative images of WT3 retinal organoids, highlighting the regions of excising OVs from the main organoid with red dotted lines. Scale bars=100 µm

Following excision and recovery of the OVs, a cryopreservation solution was prepared, as mentioned in section 2.4.5, to test whether the structure of OVs and cellular identity were preserved after cryopreservation. Bright-field images of the OVs before and after freezing were captured to evaluate morphological differences (**Figure 2-26**).

Before freezing, the OVs were characterized by a smooth, round bright phase neuroepithelium. However, immediately after freezing, the OVs showed signs of continued deterioration, and by day 7 post-thaw, the OVs lost their spherical shape, and the bright phase of the neuroepithelium layer was lost (**Figure 2-26**). Due to the complete disintegration of the OVs observed after 7 days post-thaw, no more bright-field images were taken at 14 days post-thaw, and no further experimental repeats were performed (**Figure 2-26**). Overall, these results support that cryopreservation of OVs using this protocol could damage the structure and morphology of OVs (**Figure 2-26**).

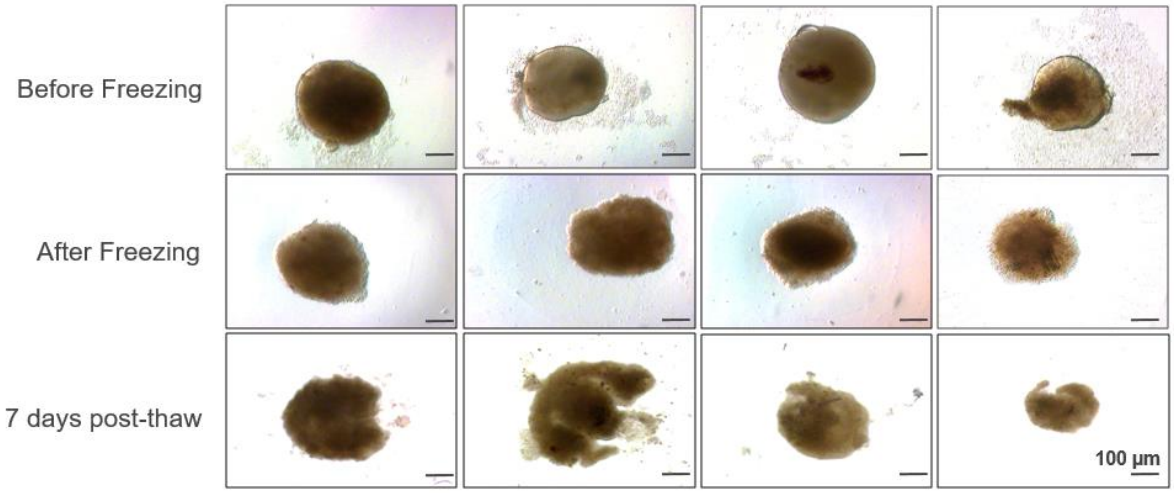

Figure 2-26: Representative images of WT3 retinal organoids before and after cryopreservation using the freezing solution. Bright-field images of day 155 retinal organoids before freezing (representing the organoids before cryopreservation experiment), after freezing (upon thawing of the organoids), at 7 days post-thaw (representing the recovery period of the organoids in a humidified environment at 37°C with 5% CO_2). Scale bars=100 µm.

2.4.6. Effect of cooling experiment on retinal organoids

To assess the effect of the cooling experiment, day 169 retinal organoids were cooled to -10˚C followed by either immediate thawing or overnight storage (24 hours), as described in section 2.3.4.6. To assess whether cooled organoids preserved their morphology and structure effectively after 14 days post-thaw, bright-field images before and after cooling were taken.

2.4.6.1. Effect of cooling experiment (-10°C) on retinal organoids followed by immediate thawing

Immediately after thawing, cooled organoids preserved their bright phase neuroepithelium across the apical edge, the spherical shape of the organoids was maintained, and the colour and size of the organoids were preserved. By day 14 post-thaw, the organoids maintained their morphology and structure and the bright phase neuroepithelium was present (**Figure 2-27**).

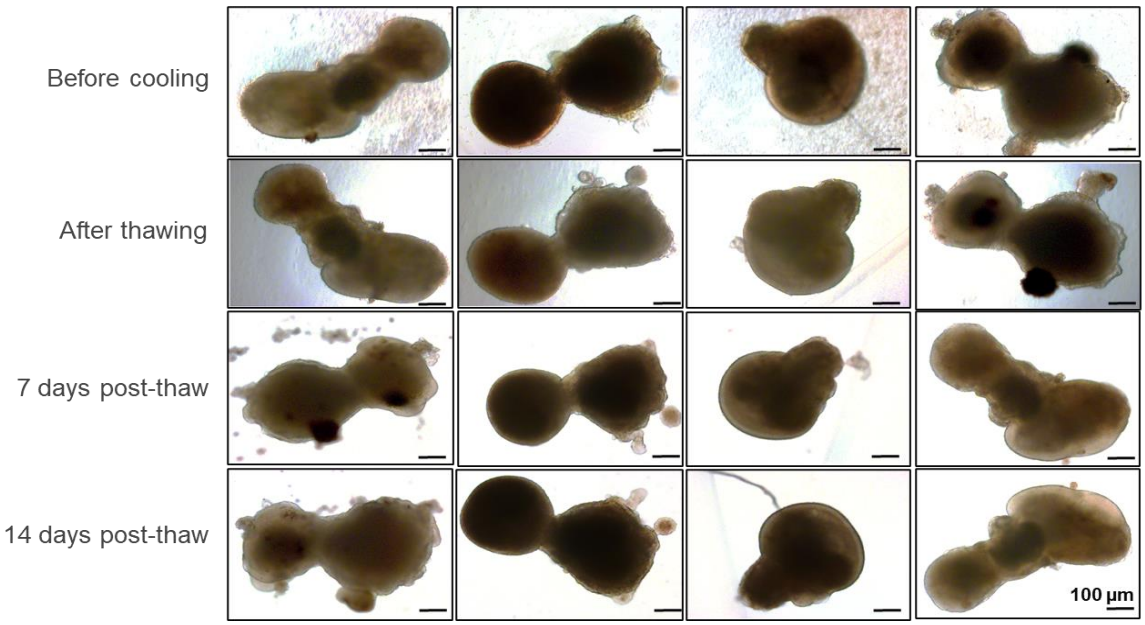

Figure 2-27: Representative images of WT3 retinal organoids before and after cooling to -10˚C followed by immediate thawing. Bright-field images of day 169 retinal organoids before cooling (representing the organoids before cryopreservation experiment), after thawing (upon thawing of the organoids), at 7 and 14 days post-thaw (representing the recovery period of the organoids in a humidified environment at 37°C with 5% CO_2). Scale bars=100 µm.

To further assess the presence of retinal-related cells, day 14 post-thaw retinal organoids were analyzed by IF as mentioned in section 2.3.5.2 and as shown in Figure 2-15. IF analysis indicated the presence of Recoverin positive cells, representing PR cells, which were mainly located in the apical layer in both control and cooled organoids. Additionally, cone PRs immunostained with Arrestin 3 were detected in both groups. S-Cone PRs (Opsin SW) and L/M cone PRs (Opsin MW/LW) were detected on the apical side of both control and cooled organoids (**Figure 2-28**). Cells positive for HuC/D, a ganglion and amacrine cell marker, were present mainly in the center of retinal organoids in both conditions (**Figure 2-28**). Additionally, IF analysis confirmed the presence of amacrine and horizontal cells in the basal layer of both control and cooled organoids using AP2α and Prox1 markers, respectively (**Figure 2-28**). However, the lamination and structure of cooled organoids were damaged, characterised by big gaps, suggesting the loss of nuclei (**Figure 2-28**). Also, Müller glial cells stained with RLBP1 marker were present in both groups (**Figure 2-28**). These results confirmed the presence of all main cellular populations in cooled organoids, although some structural disruptions were observed when compared to the control organoids (**Figure 2-28**). No quantification analysis of retinal markers was performed till these results were repeated in at least two more independent experiments.

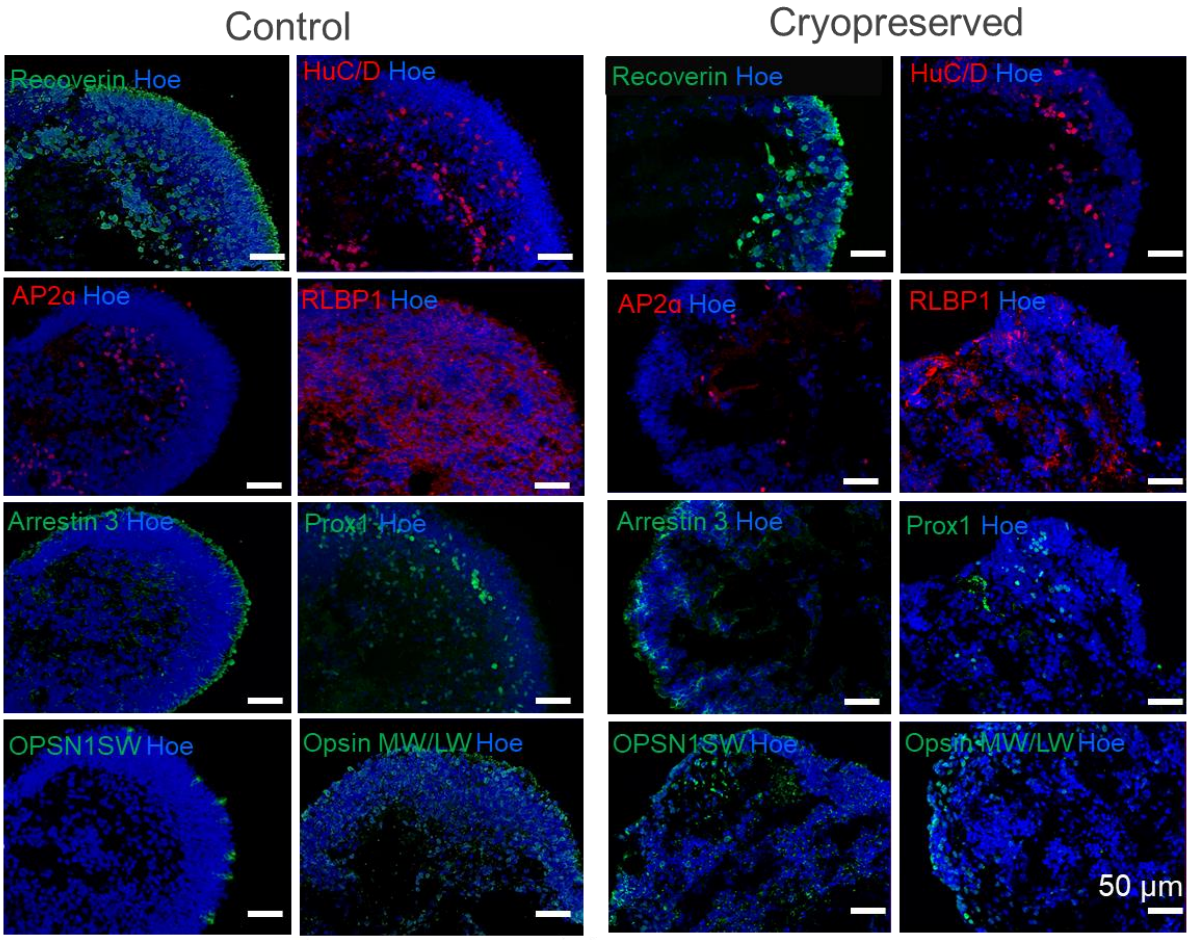

Figure 2-28: Immunostaining of control and cooled to -10˚C day 169 retinal organoids (thawed immediately) 14 days post-thaw. Sections through control and cryopreserved day 169 retinal organoids. PR cells (Recoverin, green), amacrine and ganglion cells (HuC/D, red), amacrine cells (AP2α, green), Müller cells (RLBP1, red), cone PRs (Arrestin 3, green), horizontal cells (Prox1, green) and cone PRs (OPSIN SW, green, OPSIN MW/LW, green) were present in day 169 control retinal organoids. Organoids cooled at -10˚C expressed all retinal markers identified in the control group, but the structure of some cryopreserved organoids was damaged. Nuclei were counterstained with Hoechst (Hoe, blue). Scale bars=50 µm.

2.4.6.2. Effect of cooling experiment (-10°C) on retinal organoids followed by overnight incubation (24 hours)

Next, WT3 retinal organoids (day 169 of differentiation) were used to assess whether the structure and morphology of retinal organoids can be preserved after cooling and storing them at -10˚C for 24 hours. Bright-field images before and after cooling were captured and compared. After thawing, the smooth, bright phase neuroepithelium edge was present, and no differences in the colour of the organoids were detected. However, by 14 days post-thaw, the organoids shrunk, and some organoids disintegrated (**Figure 2-29**).

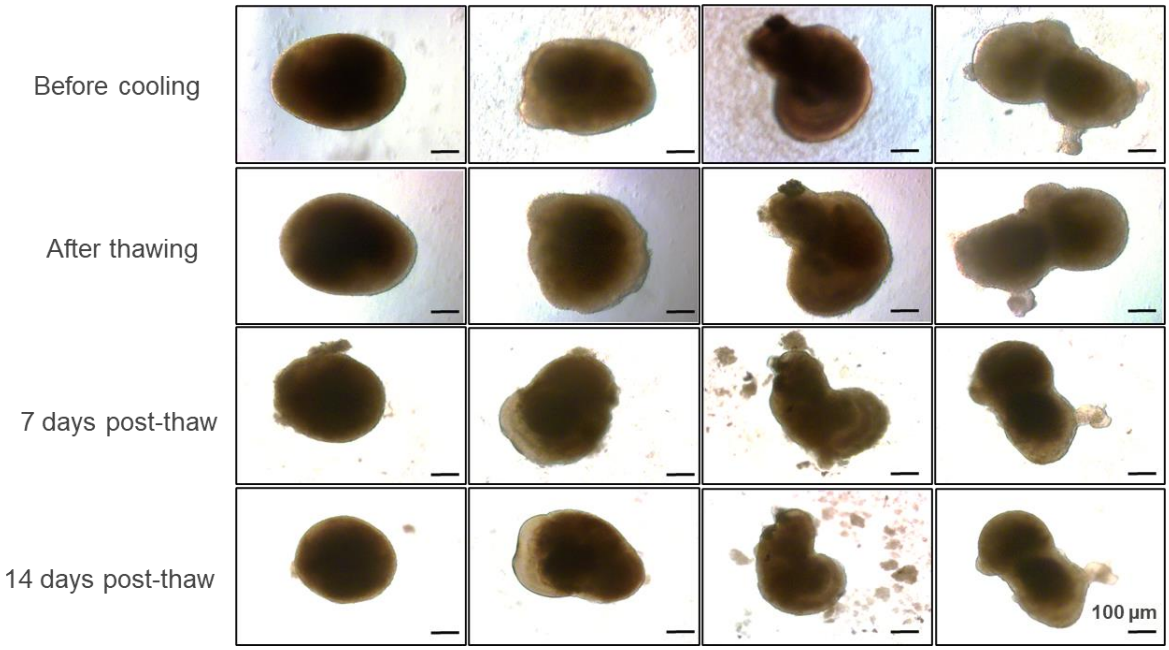

Figure 2-29: Representative images of WT3 retinal organoids before and after cooling to -10˚C followed by overnight incubation. Bright-field images of day 169 retinal organoids before cooling (representing the organoids before cryopreservation experiment) after thawing (upon thawing of the organoids) at 7 and 14 days post-thaw (representing the recovery period of the organoids in a humidified environment at 37°C with 5% CO_2). Scale bars=100 µm.

To evaluate the cell survival and retinal identity of cooled organoids, 14 days post-thaw organoids were analyzed by IF analysis. The analysis was performed using a panel of mature retinal-related markers (**Figure 2-30**). Based on the IF results, the cooled retinal organoids retained their cellular structure, although the lamination of some organoids was disrupted (**Figure 2-30**). However, cells positive for Recoverin, Opsin MW/LW and Arrestin 3, representing PR cells and cone PRs, were detected in the apical side of both control and cooled organoids (**Figure 2-30**). Additionally, PR connecting cilia were detected by ARL13B immunostaining in both conditions (**Figure 2-30**). HuC/D, AP2α and Prox1 detected the presence of ganglion, amacrine and horizontal cells, respectively, in the basal and middle layer

of the control and cooled organoids. However, the lamination of retina positive cells was affected in cooled organoids. Additionally, Müller glial cells extended through the retina were detected by the RLBP1 marker (**Figure 2-30**). These results support that thawing of WT3 organoids after 24 hours of incubation at -10˚C can preserve retinal cells. However, the structure and morphology of the retinal organoids were disrupted as the typical lamination was lost and big gaps lucking nuclei were detected (**Figure 2-30**). No quantification analysis of retinal markers was performed until the method was validated and replicated.

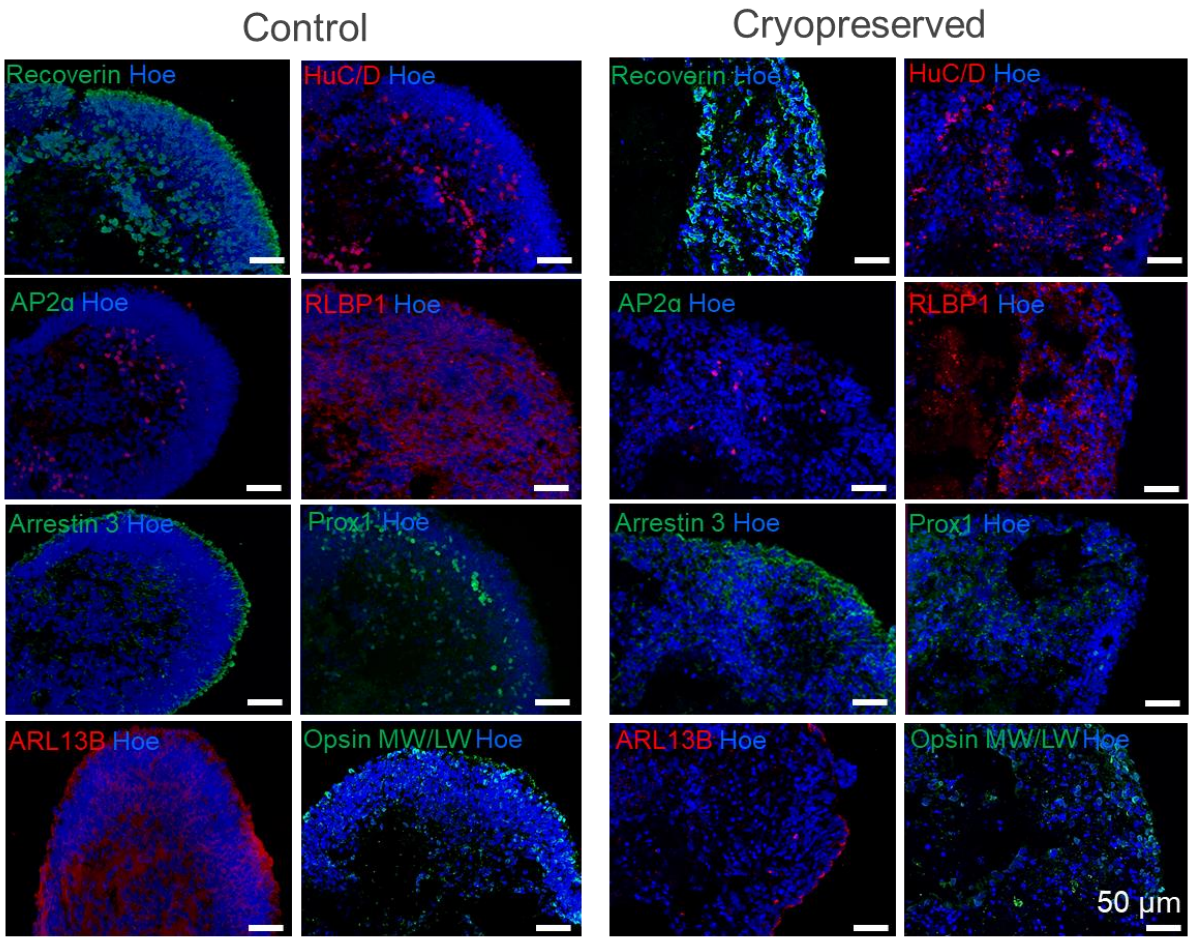

Figure 2-30: Immunostaining of control and cooled to -10˚C day 169 retinal organoids after 14 days post-thaw. Sections through control and cryopreserved day 169 retinal organoids. PR cells (Recoverin, green), amacrine and ganglion cells (HuC/D, red), amacrine cells (AP2α, green), Müller cells (RLBP1, red), cone PR cells (Arrestin 3 green), horizontal cells (Prox1, green), PR connecting cilium (ARL13B, red), and cone PRs (OPSIN MW/LW, green) were present in day 169 control retinal organoids. Organoids cooled to -10˚C expressed all retinal markers identified in the control group, but the structure of some cryopreserved organoids was damaged. Nuclei were counterstained with Hoechst (Hoe, blue). Scale bars=50 µm.

2.4.6.3. Effect of the cooling experiment (-10°C) on retinal organoids followed by overnight incubation with the addition of ROCK inhibitor in the thawing solution

The cooling experiment followed by overnight incubation was repeated alongside a modified cooling experiment to confirm the above results. The modification included the addition of an antiapoptotic factor (Y-27632, ROCK Inhibitor) in the thawing solution. Bright-field images of WT3 retinal organoids before and after the cooling experiment were taken to evaluate the impact of the cooling experiment on retinal organoids.

The results indicated that retinal organoids treated without ROCK Inhibitor lost their bright phase neuroepithelium edge, and signs of continued deterioration were observed immediately after thawing. By day 7 post-thaw, the organoids shrunk, and the overall structure of the organoids was destroyed (**Figure 2-31**). This is a second repeat of the experiment mentioned above, and differences in the structure of the cooled organoids were detected, showing variability between the two runs.

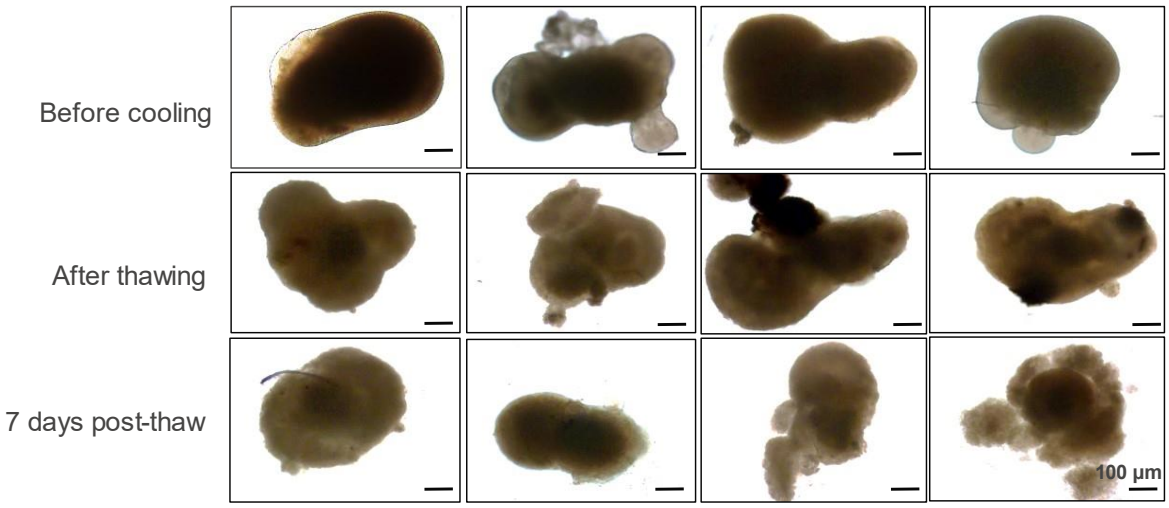

Figure 2-31: Representative images of WT3 retinal organoids before and after cooling to -10˚C followed by overnight incubation, without ROCK inhibitor in the thawing solution. Bright-field images of day 169 retinal organoids before cooling (representing the organoids before cryopreservation experiment), after thawing (upon thawing of the organoids), and at 7 days post-thaw, (representing the recovery period of the organoids in a humidified environment at 37°C with 5% CO_2). Scale bars=100 µm.

However, retinal organoids treated with ROCK inhibitor during thawing preserved their bright phase neuroepithelium edge immediately after thawing. However, by 7 days post-thaw, the bright phase neuroepithelial layer was lost, the organoids' overall size shrunk, and some organoids' structure was partially disintegrated (**Figure 2-32**). Due to the degeneration of organoids, no cellular analysis was performed. Overall, cooling of the organoids to -10˚C

indicated variability between the different runs suggesting that cooling of the organoids at -10˚C cannot be replicated, and hence, no further repeats were performed. This is possibly because the ice is randomly formed at this temperature, and uncontrol ice formation leads to variable results. Collectively, these results suggest that cooling of organoids at -10˚C using this particular protocol is not effective, and also, the addition of ROCK inhibitor in the thawing solution had no beneficial effects.

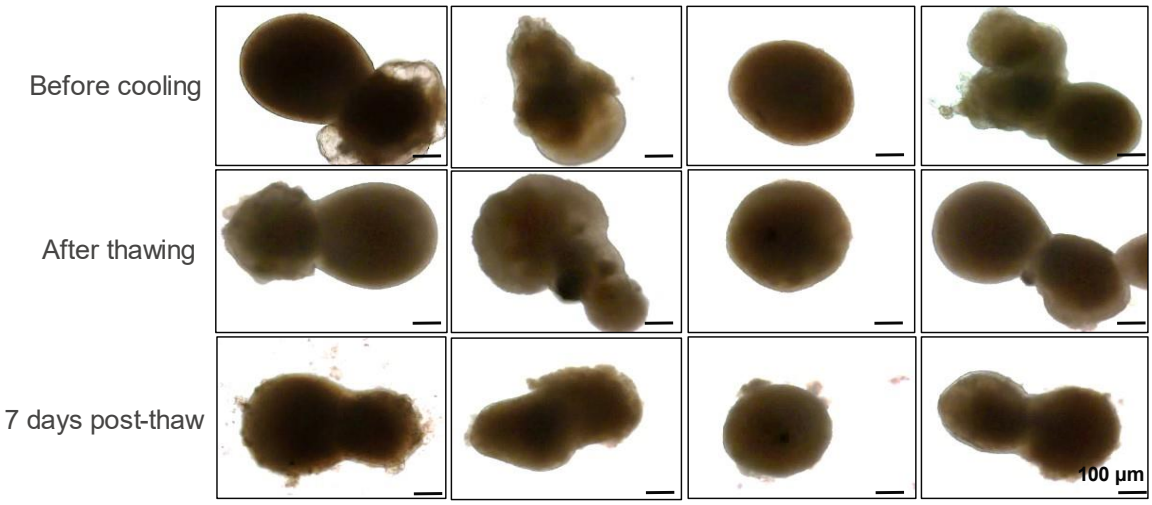

Figure 2-32: Representative images of WT3 retinal organoids before and after cooling to -10˚C followed by overnight incubation, with ROCK inhibitor in the thawing solution. Bright-field images of day 169 retinal organoids before cooling (representing the organoids before cryopreservation experiment), after thawing (upon thawing of the organoids), and at 7 days post-thaw (representing the recovery period of the organoids in a humidified environment at 37°C with 5% CO_2). Scale bars=100 µm.

2.4.6.4. Effect of the cooling experiment (-20°C) on retinal organoids followed by overnight incubation with the addition of ROCK inhibitor in the thawing solution

To achieve long-term storage of tissues, it is recommended to cryopreserve the tissues at low temperatures. Thus, WT3 retinal organoids were used to assess whether cooling at temperatures lower than -10˚C, such as -20˚C, followed by overnight storage, with or without the addition of ROCK inhibitor (Y-27632) in the thawing solution, can preserve the structure and morphology of the organoids. Therefore, bright-field images before and after cooling were taken. Based on the results, immediately after thawing, retinal organoids retained their morphology, the bright phase neuroepithelium was present, and RPE patches were detected in cooled organoids treated with and without ROCK inhibitor (**Figure 2-33 Figure 2-34**). However, by day 7 post-thaw, the bright phase neuroepithelium was lost, and complete disintegration was observed in both retinal organoids treated with or without ROCK inhibitor (**Figure 2-33 Figure 2-34**). Over time, the organoids shrunk and dispersed into pieces (**Figure 2-33**, **Figure 2-34**). Therefore, the survival of retinal cells was not assessed further, and no further repeats were performed. Together these results suggest that cryopreserving WT3 retinal organoids to -20˚C using this particular protocol is not effective, and also, the addition of the ROCK inhibitor has no additional beneficial effects on the preservation of organoids.

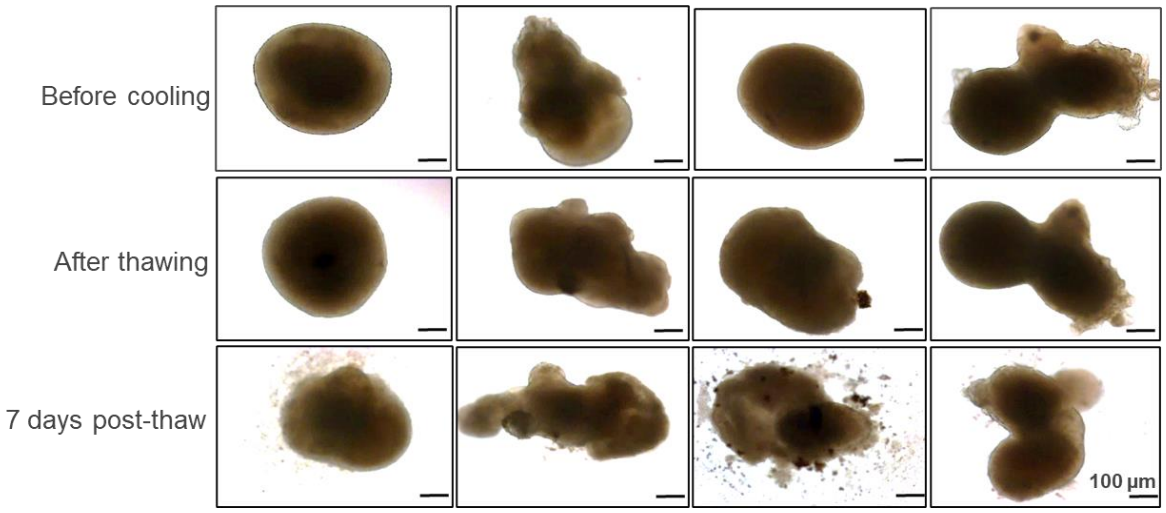

Figure 2-33: Representative images of WT3 retinal organoids before and after cooling to -20˚C followed by overnight incubation without ROCK inhibitor in the thawing solution. Bright-field images of day 169 retinal organoids before cooling (representing the organoids before cryopreservation experiment), after thawing (upon thawing of the organoids), and at 7 days post-thaw, (representing the recovery period of the organoids in a humidified environment at 37°C with 5% CO_2). Scale bars=100 µm.

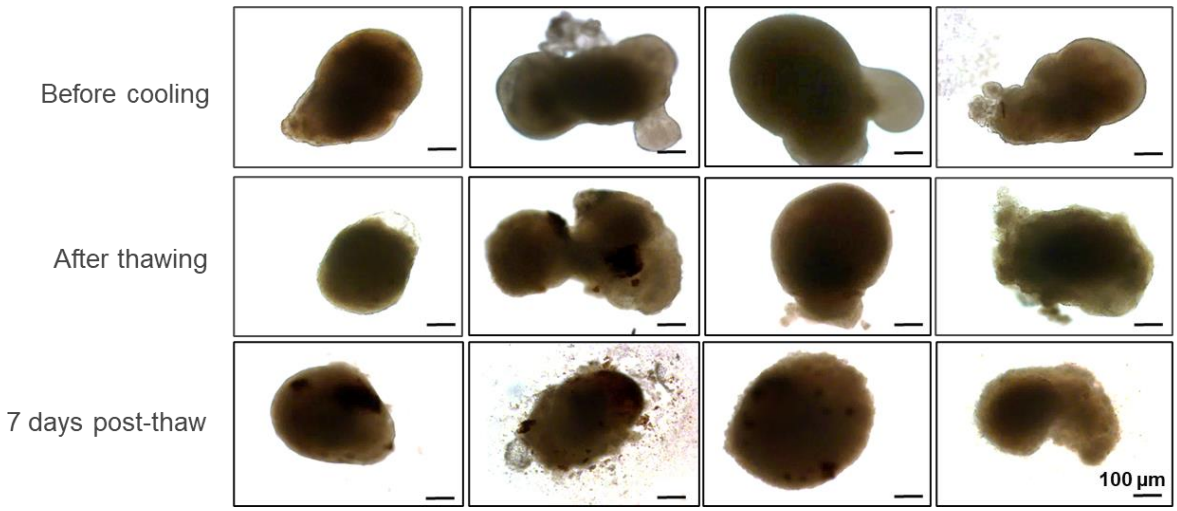

Figure 2-34: Representative images of WT3 retinal organoids before and after cooling to -20˚C followed by overnight incubation with ROCK inhibitor in the thawing solution. Bright-field images of day 169 retinal organoids before cooling (representing the organoids before cryopreservation experiment), after thawing (upon thawing of the organoids), and at 7 days post-thaw, (representing the recovery period of the organoids in a humidified environment at 37°C with 5% CO_2). Scale bars=100 µm.

2.4.7. Effect of 'Liver Supercooling' protocol on retinal organoids

Uygun and colleagues reported the successful preservation of liver organs followed by supercooling at -4˚C (de Vries et al., 2019). Therefore, supercooling of the liver organ, defined as the 'Liver Supercooling' protocol, was modified and adapted to the aims of the study following discussions with our collaborator Dr Peter Kilbride (Asymptote, Cytiva). Retinal organoids were assessed as described in section 2.3.4.7 to evaluate whether their structure and morphology could be preserved effectively. For long-term preservation, retinal organoids were supercooled at lower temperatures such as -60˚C, defined as the 'Master Liver Supercooling' protocol, as descibed in section 2.3.4.8. To determine the impact of the supercooling solution on retinal organoids, bright-field images were taken before and after supercooling, as well as at day 7 and day 14 post-thaw.

2.4.8. Effect of 'Liver Supercooling' (-4°C) and 'Master Liver Supercooling' (-60°C) protocols on retinal organoids

Before supercooling, bright-field images of WT3 retinal organoids day 160 were characterised by a smooth, bright phase neuroepithelium edge across the apical layer. However, retinal organoids supercooled to -4°C or to -60°C shrunk, became darker, and the bright phase neuroepithelium was lost immediately after thawing (**Figure 2-35**). Although over time the colour of the organoids recovered, the bright phase neuroepithelium was not clearly visible (**Figure 2-35**). Additionally, IF analysis was performed to assess cell survival in organoids supercooled to -4˚C and -60˚C. Retinal markers such as Recoverin, representing PR cells, and SNCG detecting ganglion cells were used. IF results revealed that the structure of retinal organoids supercooled to -4˚C was completely damaged, and no retinal cell markers were observed (**Figure 2-36 A**). Also, it was observed that the nucleus of supercooled organoids was dotty compared to the control organoids (**Figure 2-36 A**). However, Recoverin and SNCG positive cells representing PR cells and ganglion cells, respectively, were present in retinal organoids supercooled to -60˚C, but no RLBP1 positive cells were detected (**Figure 2-36 B**). Also, nuclei of supercooled organoids were dotty, and the lamination was disrupted compared to the control retinal organoids (**Figure 2-36 B**). These results suggest that supercooling of retinal organoids to -4˚C was detrimental; however, supercooling to -60˚C can preserve the overall structure of the organoids and the survival of some of the retinal cells assessed herein.

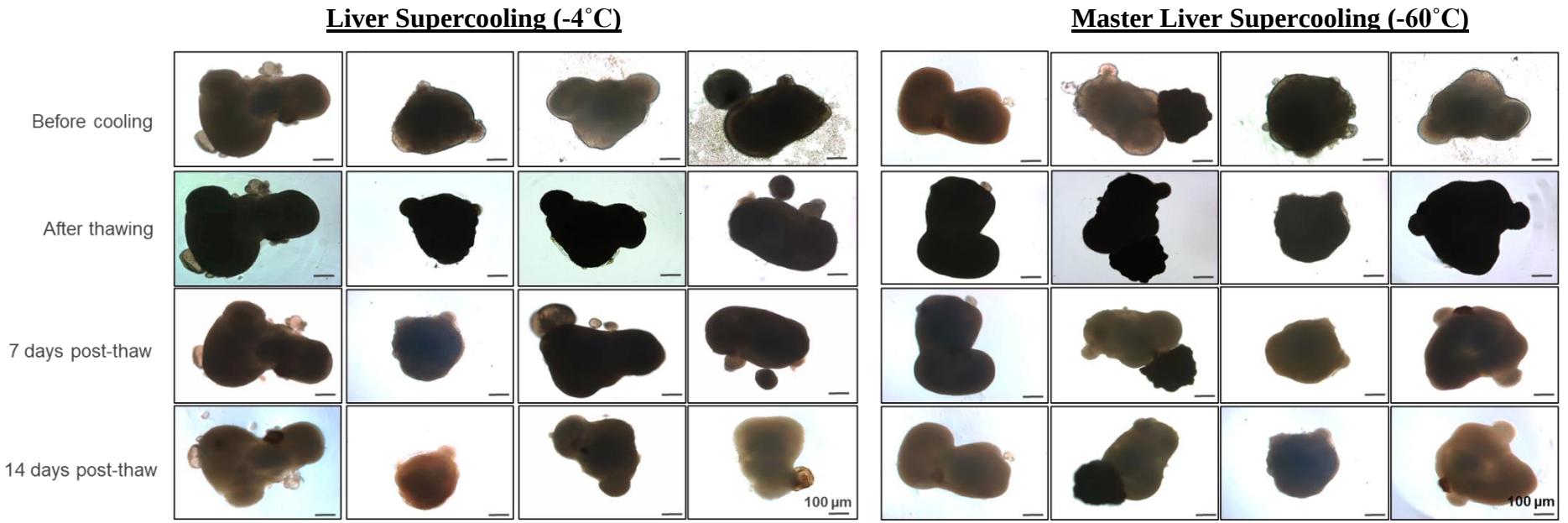

Figure 2-35: Representative images of WT3 retinal organoids before and after supercooling with the 'Liver Supercooling' (-4˚C) and 'Master Liver Supercooling' (-60˚C) protocol. Bright-field images of day 160 retinal organoids before cooling (representing the organoids before cryopreservation experiment), after thawing (upon thawing of the organoids) at 7 and 14 days post-thaw (representing the recovery period of the organoids in a humidified environment at 37°C with 5% CO_2). Scale bars=100 µm.

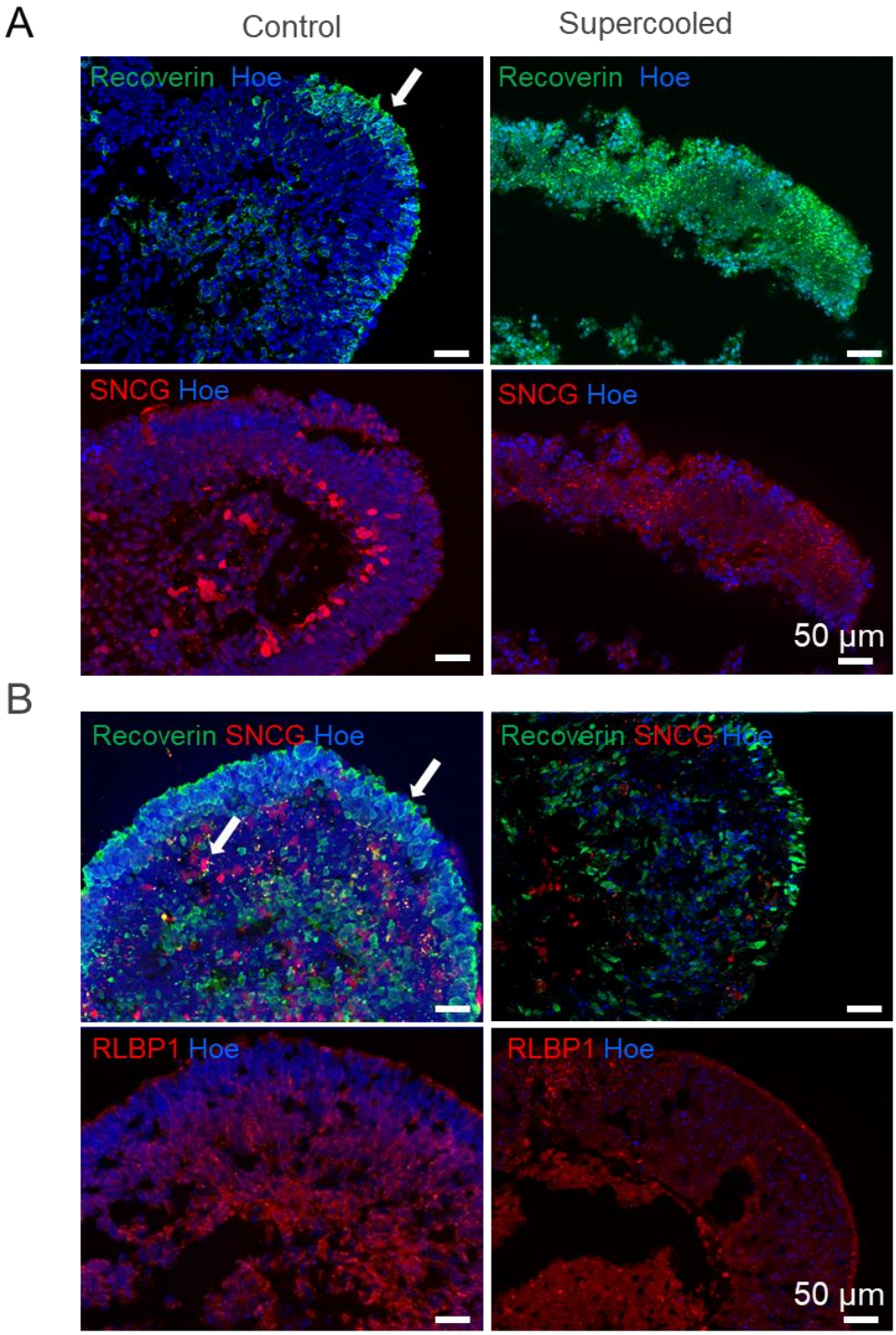

Figure 2-36: Immunostaining of control and supercooled day 160 retinal organoids after 14 days post-thaw. A) Sections through control and cryopreserved day 160 retinal organoids. PRs (Recoverin, green) and ganglion cells (SNCG, red) were present in day 160 control retinal organoids. However, organoids supercooled to -4˚C did not express any retinal markers, and the structure and morphology of organoids were damaged. B) Sections through control and cryopreserved day 160 retinal organoids. PRs (Recoverin, green), ganglion cells (SNCG, red), and Müller cells (RLBP1, red) were present in day 160 control retinal organoids. PRs (Recoverin, green), ganglion cells (SNCG, red) but not Müller glial cells (RLBP1, red) were present in supercooled to -60˚C retinal organoids. The structure of organoids supercooled to -60˚C was mainly maintained. Nuclei were counterstained with Hoechst (Hoe). Scale bars=50 µm.

2.4.8.1. Effect of 'Master Liver Supercooling' protocol in combination with enriched loading and thawing solutions for the cryopreservation of retinal organoids

To replicate and improve the results obtained from the 'Master Liver Supercooling' protocol, additional conditions were tested individually in combination with the original protocol as described in section 2.3.4.8.1. These conditions included: 1) addition of ROCK inhibitor and glutathione in the rinsing media to improve the recovery of ROs. This experiment was named condition 1. 2) Addition of 2.5% and 5% of DMSO in the loading solution 1 and 2, respectively, to improve cryoprotection during freezing. This experiment was named condition 2. 3) Addition of condition 1 (addition of ROCK inhibitor and glutathione in the rinsing media) together with condition 2 (addition of DMSO in the freezing media). This experiment was named condition 3.

Bright-field images of organoids treated with the 'Master Liver Supercooling' protocol without additional modifications showed that the overall structural integrity of organoids was preserved 14 days post-thaw. However, the organoids shrunk and became darker, and the bright phase neuroepithelium was lost after 14 days post-thaw (**Figure 2-37**).

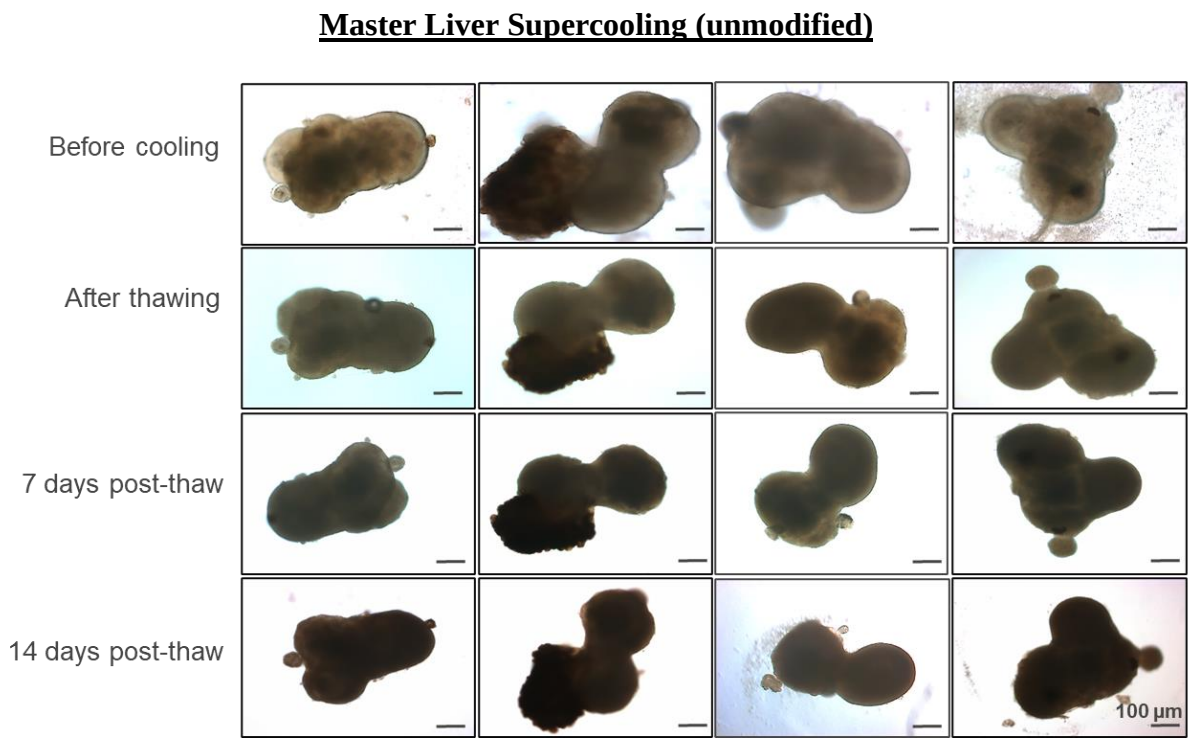

Figure 2-37: Representative images of WT3 retinal organoids before and after supercooling using the unmodified 'Master Liver Supercooling' protocol. Bright-field images of day 160 retinal organoids before cooling (representing the organoids before cryopreservation experiment), after thawing (upon thawing of the organoids), at 7 and 14 days post-thaw (representing the recovery period of the organoids in a humidified environment at 37°C with 5% CO_2). Scale bars=100 µm.

Retinal organoids treated with condition 1 (addition of ROCK inhibitor and glutathione in the rinsing media) were characterised with a darker appearance. Also, the organoids shrunk, and the bright phase of the neuroepithelium layer was lost after 14 days post-thaw (**Figure 2-38**). However, supercooled organoids treated with condition 2 (addition of DMSO in loading solutions 1 and 2) retained their morphology and structure by 14 days post-thaw. Still, organoids shrunk, and the apical bright phase neuroepithelial layer was dark and ragged (**Figure 2-39**). Similar observations with condition 1 were observed in organoids treated with condition 3 (condition 1 and condition 2 together). Specifically, bright-field images indicated that organoids were characterised with a darker colour, the organoids shrunk, and the bright phase neuroepithelium was lost by 14 days post-thaw. (**Figure 2-39**).

Condition 1

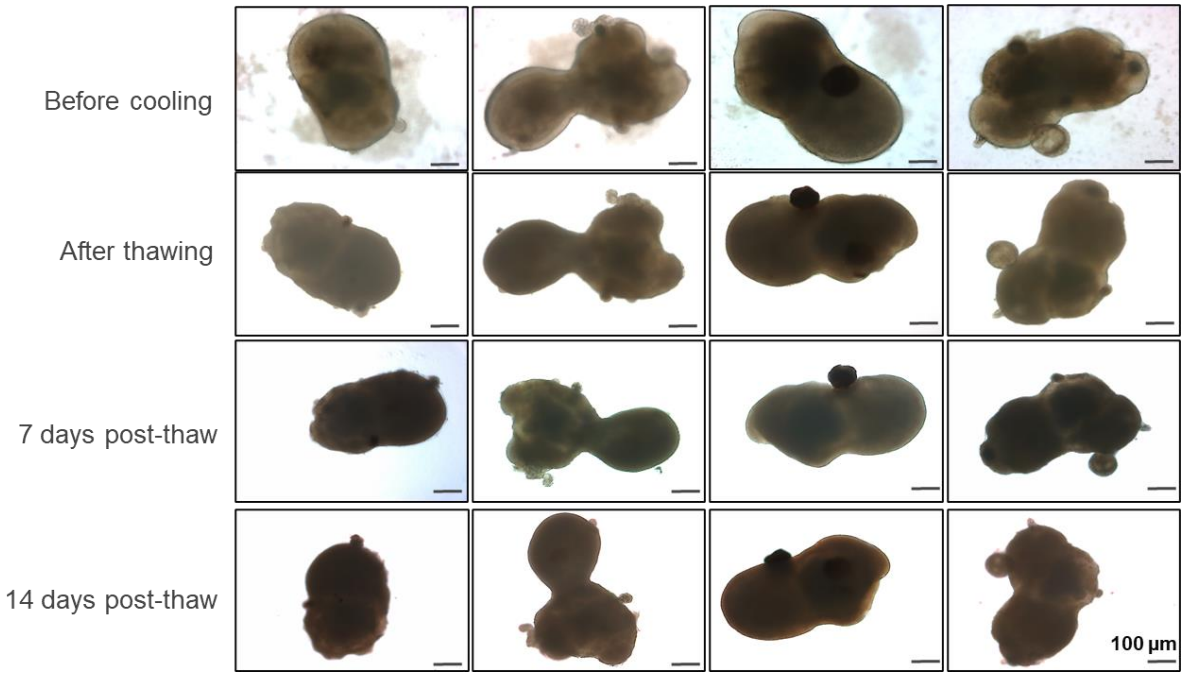

Figure 2-38: Representative images of WT3 retinal organoids before and after supercooling using the 'Master Liver Supercooling' protocol treated with condition 1. Bright-field images of day 160 retinal organoids before cooling (representing the organoids before cryopreservation experiment), after thawing (upon thawing of the organoids) at 7 and 14 days post-thaw (representing the recovery period of the organoids in a humidified environment at 37°C with 5% CO_2). Scale bars=100 µm.

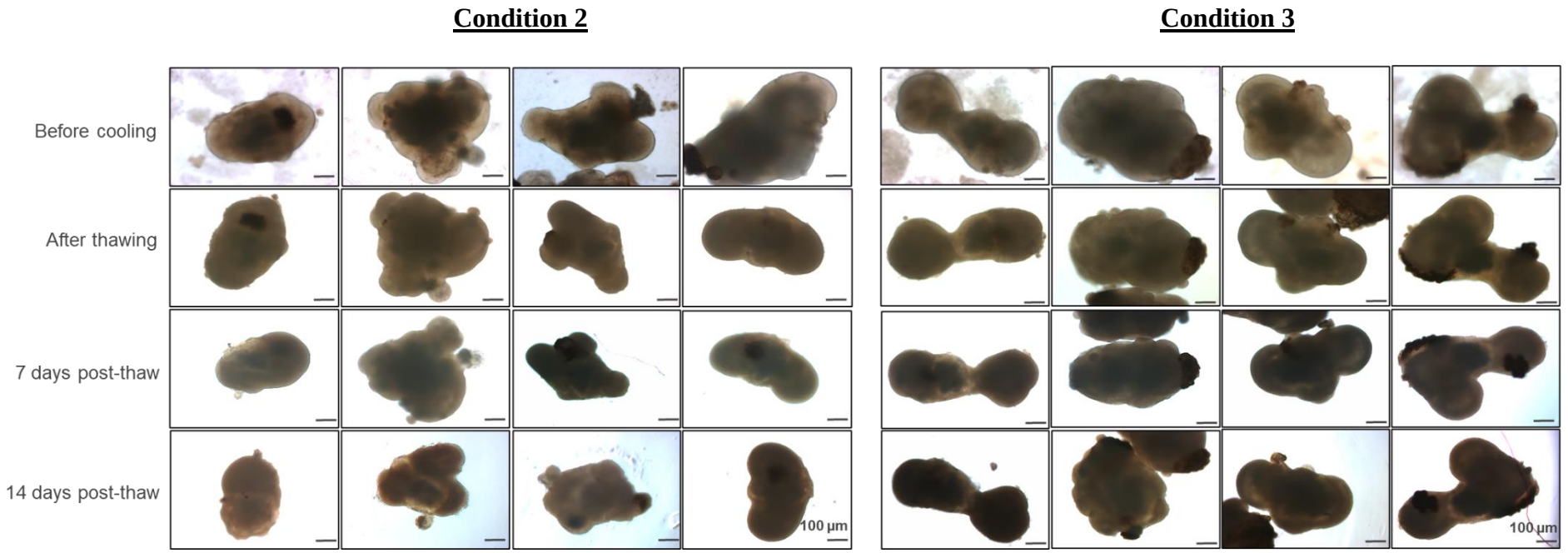

Figure 2-39: Representative images of WT3 retinal organoids before and after supercooling using the 'Master Liver Supercooling' protocol treated with conditions 2 and 3. Bright-field images of day 160 retinal organoids before cooling (representing the organoids before cryopreservation experiment), after thawing (upon thawing of the organoids), at 7 and 14 days post-thaw (representing the recovery period of the organoids in a humidified environment at 37°C with 5% CO_2). Scale bars=100 µm.

Cell survival of 14 days post-thaw retinal organoids from all the conditions was assessed by IF analysis using Recoverin, SNCG, Prox1 and RLBP1 markers. The overall structural integrity of the organoids treated with the unmodified 'Master Liver Supercooling' protocol was maintained, although the lamination of organoids was disrupted characterised with big gaps, suggesting the loss of nuclei and hence the death of retinal cells. The IF results revealed the presence of PR marker Recoverin, retinal Ganglion marker SNCG, Horizontal cell marker Prox1, and Müller glia marker RLBP1, which were expressed in both supercooled and control organoids (**Figure 2-40**). However, the structure of 14 days post-thaw organoids treated with condition 1 was completely disintegrated, the nuclei were dotty, and all the retinal-related cells were lost (**Figure 2-40**). Therefore, no retinal-related markers were expressed (**Figure 2-40**). Immunostaining of supercooled organoids treated with condition 2 indicated that the structure of supercooled organoids was partially disintegrated, and only Recoverin positive cells, representing PR cells, were detected after 14 days post-thaw (**Figure 2-40**). In contrast to organoids treated with condition 1, condition 3 supercooled organoids partially maintained their structure and lamination (**Figure 2-40**). Additionally, Recoverin positive cells representing PR cells, and SNCG positive cells indicating the presence of retinal Ganglion cells, were present in both supercooled and control organoids (**Figure 2-40**). Additionally, Müller glial cells stained with RLBP1 were detected in supercooled organoids after 14 days post-thaw, but horizontal cells positive for Prox1 were not detected (**Figure 2-40**). Taken together, these results indicate that condition 3 provided the most promising results among all the three modified protocols assessed in this experimental round. However, the 'Master Liver Supercooling' protocol, which was repeated without any modifications, provided the best results among all the modified 'Master Liver Supercooling' experiments.

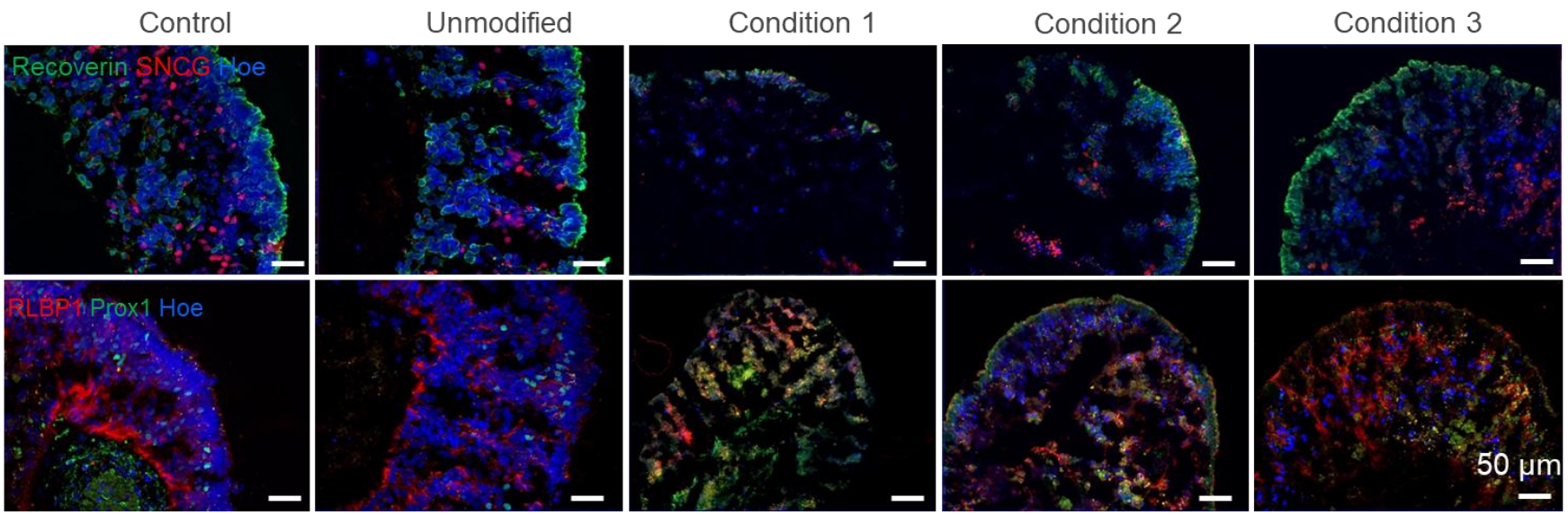

Figure 2-40: Immunostaining of control and supercooled day 160 retinal organoids treated with the 'Master Liver Supercooling' protocol, condition 1, condition 2, and condition 3, 14 days post-thaw. Sections through control and cryopreserved day 160 retinal organoids. PRs (Recoverin, green), ganglion cells (SNCG, red), Müller cells (RLBP1, red) and Horizontal cells (Prox1, green) were present in day 160 control organoids. The same retinal markers as in control organoids were expressed in day 160 supercooled retinal organoids treated with the unmodified 'Master Liver Supercooling' protocol, although gaps were present in the structure of organoids. Organoids treated with condition 1 were completely disintegrated, and no retinal cells were present. Organoids treated with condition 2 were partially damaged, the lamination was lost, and only PRs (Recoverin, green) were detected. PRs (Recoverin, green), ganglion cells (SNCG, red) and Müller cells (RLBP1, red) but not Horizontal cells (Prox1, green) were present in supercooled organoids treated with condition 3, but their structure and lamination were partially preserved. Nuclei were counterstained with Hoechst (Hoe). Scale bars=50 µm.

2.4.8.2. Effect of 'Master Liver Supercooling' protocol in combination with enriched RPE condition medium and ECM in loading and thawing solutions for the cryopreservation of retinal organoids

The most promising results from the previous experiment were obtained from the 'Master Liver Supercooling' experiment (with no additional modifications). Therefore, to improve the efficacy of the 'Master Liver Supercooling' protocol, four different conditions were tested individually alongside the original protocol as described in section 2.3.4.8.2.

Briefly, five cryovials containing 10 retinal organoids in each were supercooled to –60˚C followed by overnight storage. For the unmodified 'Master Liver Supercooling' experiment, the organoids were treated as mentioned previously in section 2.3.4.8. Modifications to improve the survival of organoids were assessed alongside. The first modification included the addition of RPE condition medium (CM) during the recovery period. This experiment was named condition A. The second modification included the addition of ECM in the recovery medium. This experiment was named condition B. The third modification included the addition of RPE CM and ECM during the recovery time. This experiment was named condition C. The fourth modification included the addition of both RPE CM and ECM prior to supercooling for 7 days and during the recovery period. This experiment was named condition D. For all the different conditions, bright-field images were acquired before cooling, after thawing, 7 and 14-days post-thaw.

Bright-field images before supercooling indicated that organoids were characterised by a smooth, bright phase neuroepithelium. After thawing, retinal organoids treated with the unmodified 'Master Liver Supercooling' protocol retained their overall structural integrity; however, by day 14 post-thaw, the bright phase neuroepithelial layer was lost, the colour of the organoids was darker, and their overall size was smaller (**Figure 2-41**). Retinal organoids treated with condition A (addition of RPE CM during the recovery period) retained their overall structural integrity after 14 days post-thaw. However, retinal organoids were darker immediately after thawing, and by 14 days post-thaw, the organoids shrunk, and the bright phase neuroepithelial layer was lost (**Figure 2-42**). Bright-field images of retinal organoids treated with condition B (addition of ECM during the recovery period) indicated that the overall structural integrity of the organoids was preserved after 14 days post-thaw; however, the bright phase neuroepithelial layer was lost, the organoids shrunk, and the colour of the organoids was darker suggesting cell death (**Figure 2-42**). Bright-field images of organoids treated with condition C (addition of RPE CM and ECM during the recovery period) indicated that although retinal organoids retained their overall structural integrity after 14 days post-thaw, the organoids

shrunk in size immediately after thawing, the colour of the organoids was darker, and by 14 days post-thaw the apical layer of the neuroepithelium was lost (**Figure 2-43**). Bright-field images from organoids treated with condition D (addition of RPE CM and ECM before supercooling and during the recovery period) revealed that organoids retained their structure, size and bright apical neuroepithelium 7 days after preconditioning. Following supercooling and upon thawing, bright-field images showed that organoids shrunk, the bright phase neuroepithelium edge was lost, and the organoids' appearance was darker (**Figure 2-44**).

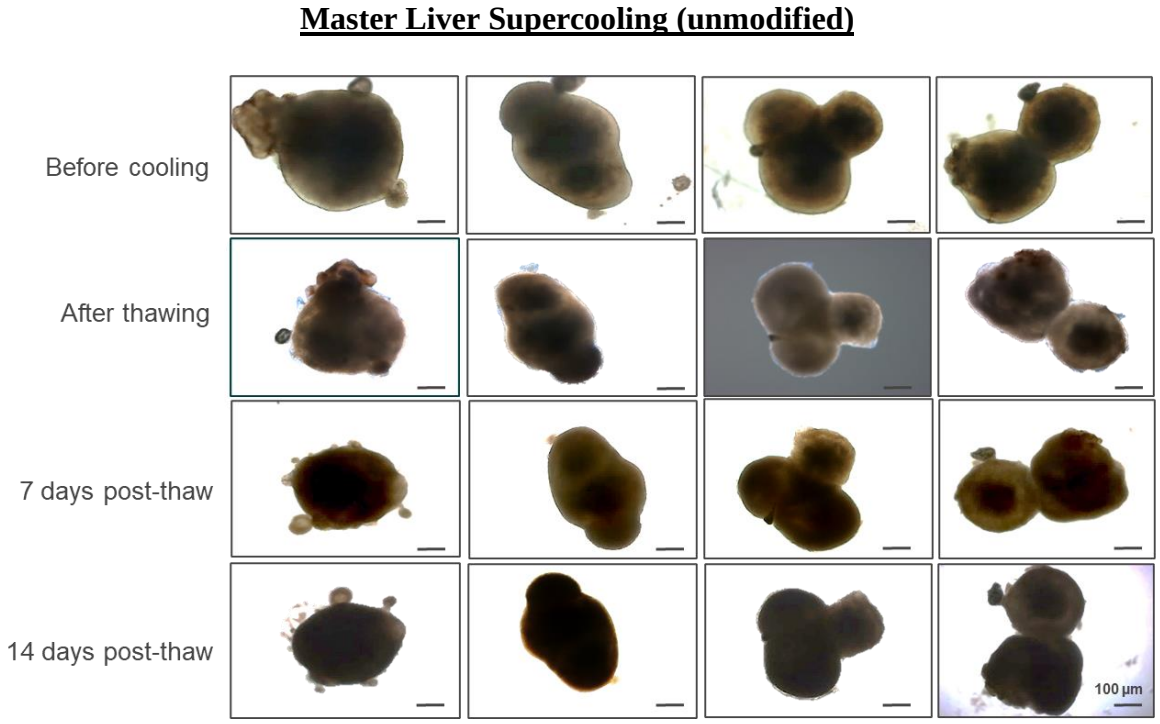

Figure 2-41: Representative images of WT3 retinal organoids before and after supercooling using the unmodified 'Master Liver Supercooling' protocol. Bright-field images of day 150 retinal organoids before cooling (representing the organoids before cryopreservation experiment), after thawing (upon thawing of the organoids) at 7 and 14 days post-thaw (representing the recovery period of the organoids in a humidified environment at 37°C with 5% CO_2). Scale bars=100 µm.

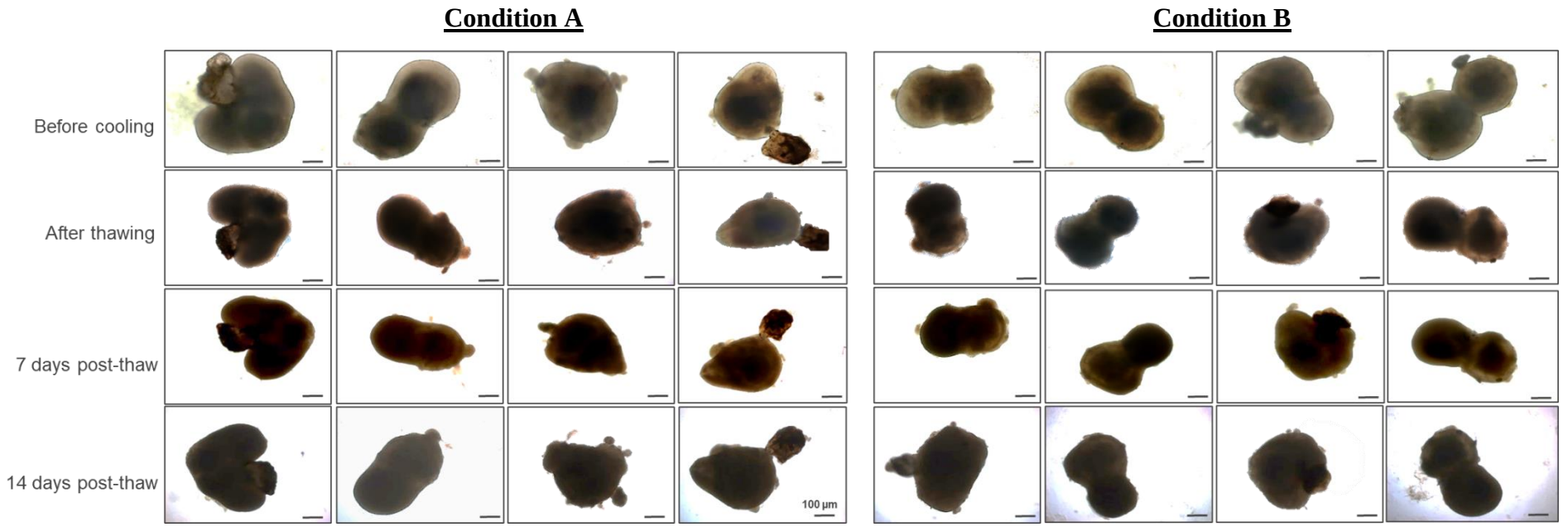

Figure 2-42: Representative images of WT3 retinal organoids before and after supercooling using the 'Master Liver Supercooling' protocol treated with condition A and B. Bright-field images of day 150 retinal organoids before cooling (representing the organoids before cryopreservation experiment), after thawing (upon thawing of the organoids), 7 and 14 days post-thaw, (representing the recovery period of the organoids in a humidified environment at 37°C with 5% CO_2). Scale bars=100 µm.

Condition C

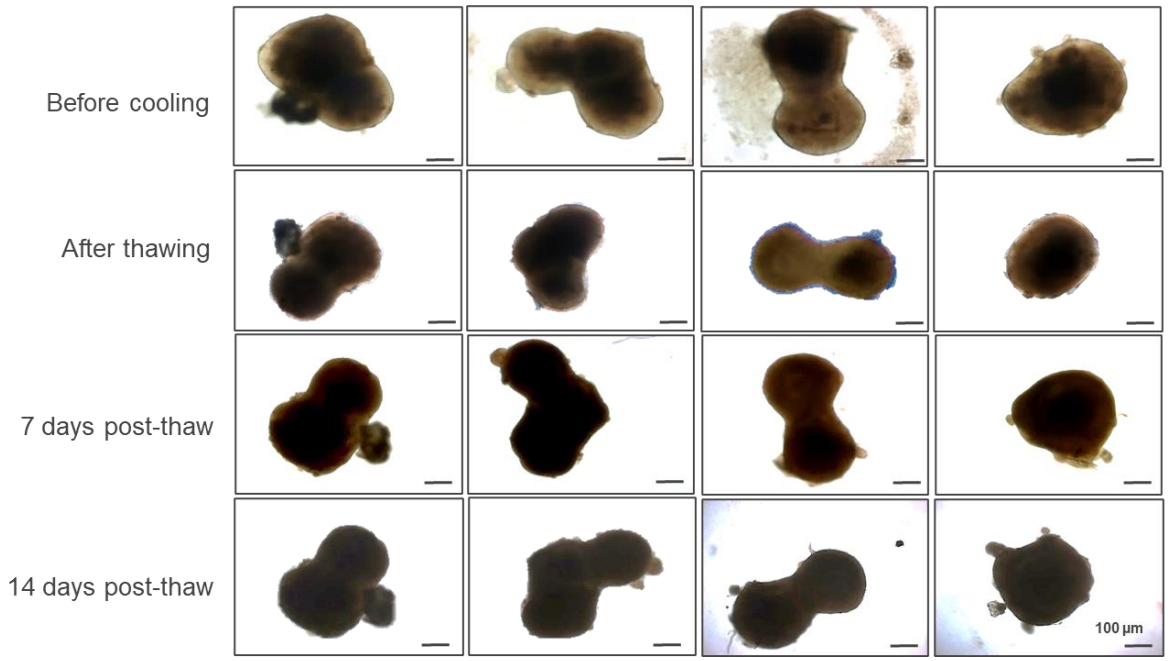

Figure 2-43: Representative images of WT3 retinal organoids before and after supercooling using the 'Master Liver Supercooling' protocol treated with condition C. Bright-field images of day 150 retinal organoids before cooling (representing the organoids before cryopreservation experiment), after thawing (upon thawing of the organoids), 7 and 14 days post-thaw, (representing the recovery period of the organoids in a humidified environment at 37°C with 5% CO_2). Scale bars=100 µm.

Condition D

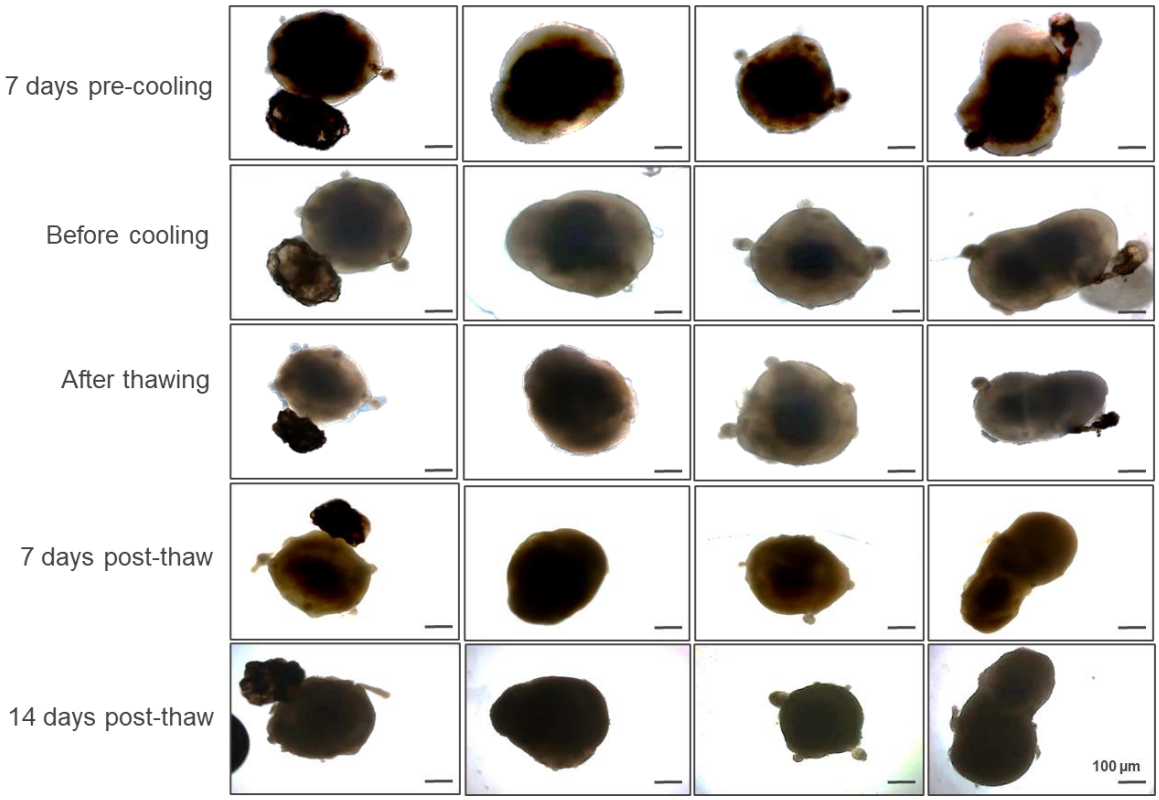

Figure 2-44: Representative images of WT3 retinal organoids before and after supercooling using the 'Master Liver Supercooling' protocol treated with condition D. Bright-field images of day 150 retinal organoids 7 days pre-cooling (representing organoids before incubation with RPE CM and ECM), before cooling (representing the organoids before cryopreservation experiment, after being treated with RPE CM and ECM for 7 days), after thawing (upon thawing of the organoids), 7 and 14 days post-thaw (representing the recovery period of the organoids in a humidified environment at 37°C with 5% CO_2). Scale bars=100 µm.

To further assess the presence of retinal-related markers on 14 days post-thaw retinal organoids treated with the unmodified 'Master Liver Supercooling' protocol as well as with conditions A-D, IF analysis using Recoverin, SNCG, Prox1 and RLBP1 markers was performed. IF analysis of the organoids treated with the unmodified 'Master Liver Supercooling' protocol showed that the structure of 14 days post-thaw organoids was patchy, characterised with big gaps, indicating the loss of nuclei. Additionally, the lamination of organoids was disrupted with fewer and dotty nuclei, and not all retinal cells were expressed. Specifically, Recoverin (PR cells), SNCG (retinal Ganglion cells) and RLBP1 (Müller glial cells) positive cells were present in both supercooled and control organoids, but Prox1 positive cells representing Horizontal cells were not found in supercooled organoids (**Figure 2-45**). IF analysis of 14 days post-thaw retinal organoids treated with condition A indicated that the structure of the organoids was damaged compared to the control organoids. Also, IF analysis revealed the presence of PR cells marked by Recoverin immunostaining, but Ganglion cells, Müller glial and Horizontal cells were not detected in supercooled organoids. Additionally, the nuclei were dotty and reduced in number compared to the control retinal organoids (**Figure 2-45**). Similarly to organoids treated with condition A, only PR cells were detected in retinal organoids treated with condition B. However, organoids treated with condition B preserved their lamination, and the nuclei were detected despite that the overall structure was damaged. Similar results observed in organoids treated with condition A were observed in organoids treated with Condition C. The lamination of the organoids was disrupted compared to the control organoids, and only PR cells (Recoverin positive cells) were detected. Also, the number of nuclei observed in organoids treated with condition C was less than control organoids (**Figure 2-45**). Similar results with organoids treated with condition C were observed in organoids treated with condition D, suggesting that possibly pre-conditioning of organoids for 7 days with RPE CM and ECM did not improve the survival of retinal cells (**Figure 2-45**). Taken together, these results indicated that the 'Master Liver Supercooling' protocol (without any additional modifications) provided the most promising results among all the other experiments that were performed alongside, despite that the structure and survival of supercooled organoids were not fully preserved. A lot more work is required to preserve the organoids' structure fully and maintain the survival of all the retina-related markers (**Figure 2-45**).

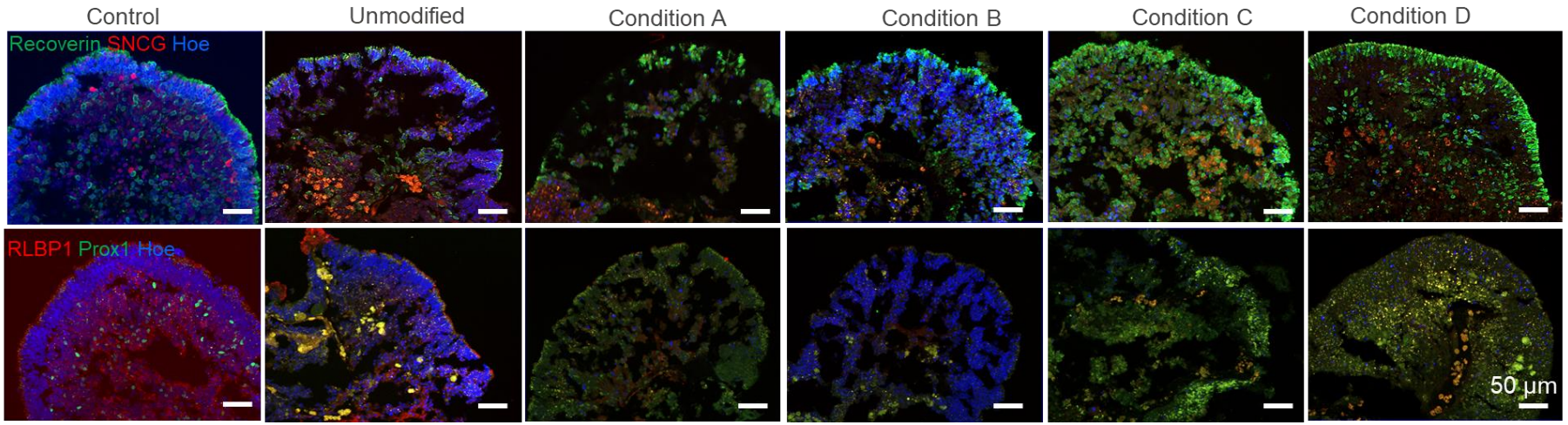

Figure 2-45: Immunostaining of control and supercooled day 150 retinal organoids treated with the 'Master Liver Supercooling' protocol, condition A, condition B, condition C, and condition D, 14 days post-thaw. Sections through control and cryopreserved day 150 retinal organoids. PRs (Recoverin, green), ganglion cells (SNCG, red), Müller cells (RLBP1, red) and Horizontal cells (Prox1, green) were present in day 150 control retinal organoids. Organoids treated with the unmodified 'Master Liver Supercooling' expressed all the markers identified in control organoids apart from Prox1 positive cells, representing Horizontal cells. The structure of the organoids was disrupted. Organoids treated with condition A disintegrated, the lamination was lost, and only PR cells were detected. Organoids treated with condition B were damaged, and only PRs (Recoverin, green) were detected. PRs (Recoverin, green) cells only detected in retinal organoids treated with condition 3, but the structure of the organoids was damaged, and the nuclei were dotty. Recoverin positive cells representing PR cells were present in supercooled organoids treated with condition D, but the nuclei were dotty and less in number. Nuclei were counterstained with Hoechst (Hoe). Scale bars=50 µm.

2.4.8.3. Effect of 'Master Liver Supercooling' protocol with extended pre-cooling incubation times on retinal organoids

The 'Master Liver Supercooling' protocol (including no additional modifications) provided the most promising results for preserving retinal organoids after cryopreservation. However, to improve further the efficacy of the protocol, two additional modifications were assessed individually in combination with the original protocol as described in section 2.3.4.8.3. These modifications included the extension of pre-conditioning incubation from 20 minutes to 2 hours and 3 hours to assess whether longer incubation of organoids with CPAs could prevent intracellular ice formation and improve organoids' survival.

Bright-field images from retinal organoids that were pre-incubated with loading solution 1 for 20 minutes ('Master Liver Supercooling' without modifications) showed that organoids maintained their overall structural integrity after 14 days post-thaw; however, the bright apical layer of the neuroepithelium was lost, the organoids shrunk and turned black over time (**Figure 2-46**). Similar observations were detected in organoids pre-incubated with loading solution for 2 hours. Bright-field images revealed that the overall structural integrity of the organoids was preserved after 14 days post-thaw. However, the bright phase neuroepithelium was lost, the organoids shrunk, and the appearance of the organoids was darker (**Figure 2-47**). Also, bright-field images from organoids pre-incubated with loading solution for 3 hours have shown that the overall structure of retinal organoids was preserved by day 14 post-thaw. However, the organoids shrunk and were characterised by a darker colour. Also, the bright phase neuroepithelial layer was lost upon thawing and was not recovered by day 14 post-thaw (**Figure 2-48**).

.

Master Liver Supercooling – pre-incubation with loading solution for 20 minutes

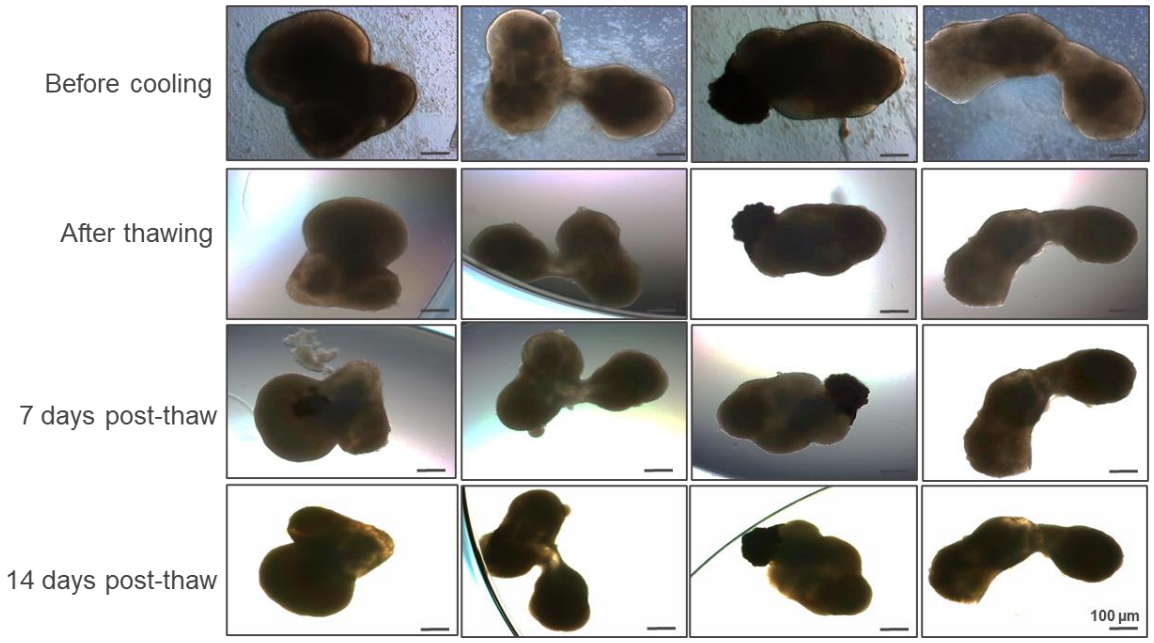

Figure 2-46: Representative images of WT3 retinal organoids before and after supercooling using the 'Master Liver Supercooling' protocol pre-incubated with loading solution for 20 minutes. Bright-field images of day 160 retinal organoids before cooling (representing the organoids before cryopreservation experiment), after thawing (upon thawing of the organoids) at 7 and 14 days post-thaw (representing the recovery period of the organoids in a humidified environment at 37°C with 5% CO_2). Scale bars=100 µm.

Master Liver Supercooling – pre-incubation with loading solution for 2 hours

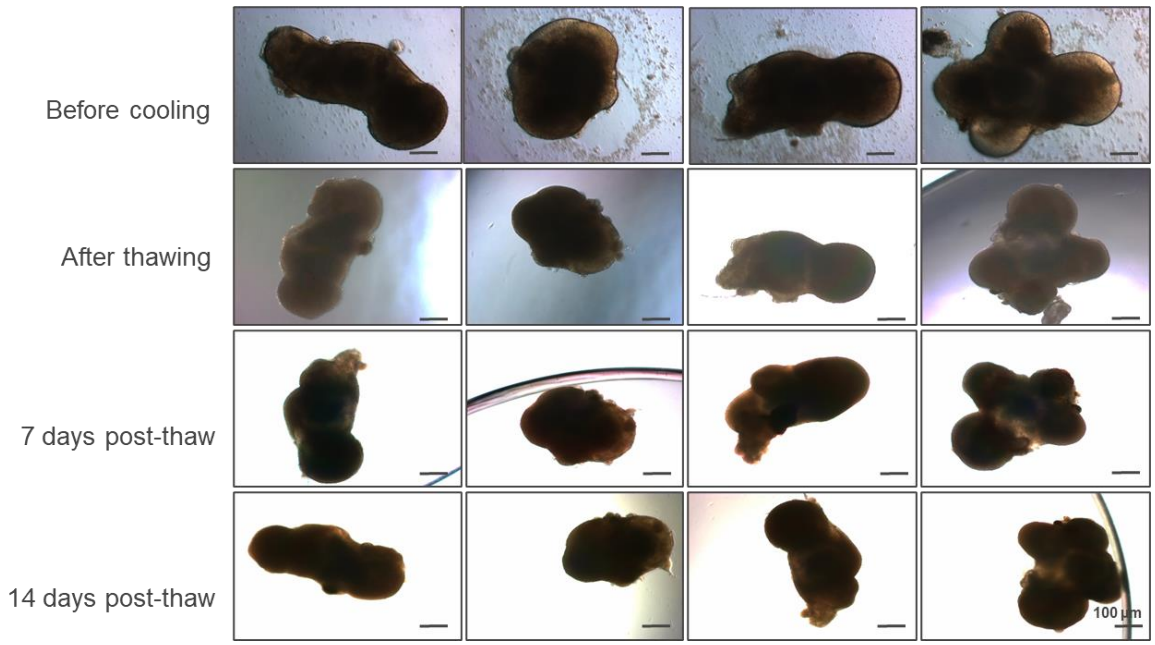

Figure 2-47: Representative images of WT3 retinal organoids before and after supercooling using the 'Master Liver Supercooling' protocol pre-incubated with loading solution for 2 hours. Bright-field images of day 160 retinal organoids before cooling (representing the organoids before cryopreservation experiment), after thawing (upon thawing of the organoids) at 7 and 14 days post-thaw (representing the recovery period of the organoids in a humidified environment at 37°C with 5% CO_2). Scale bars=100 µm.

Master Liver Supercooling – pre-incubation with loading solution for 3 hours

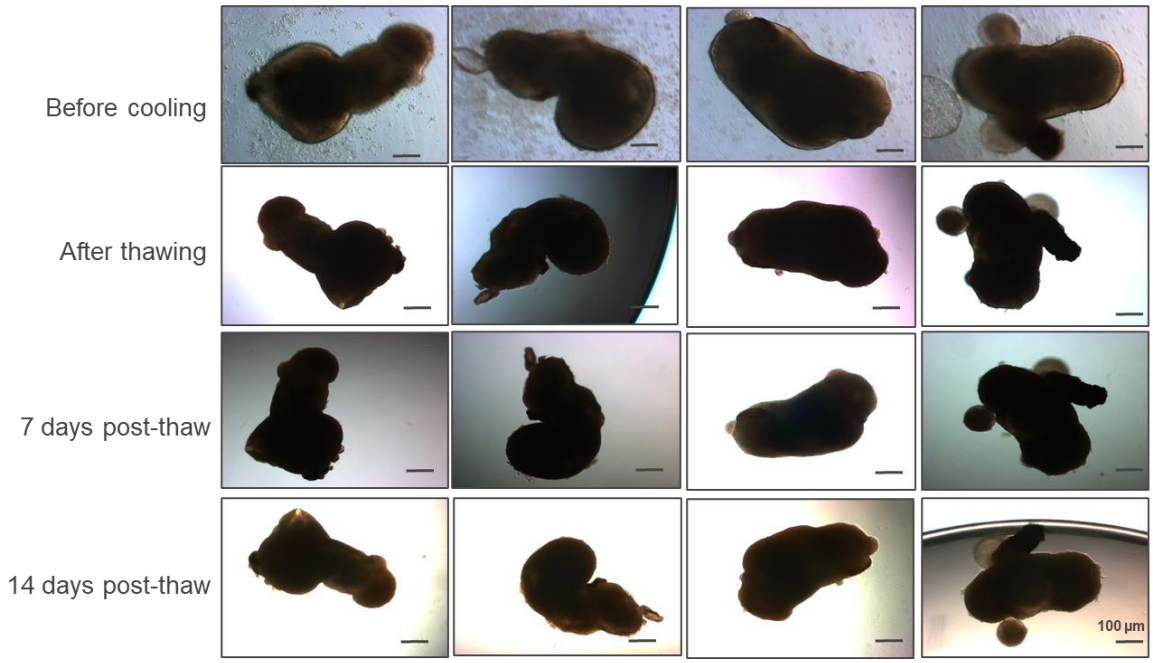

Figure 2-48: Representative images of WT3 retinal organoids before and after supercooling using the 'Master Liver Supercooling' protocol pre-incubated with loading solution for 3 hours. Bright-field images of day 160 retinal organoids before cooling (representing the organoids before cryopreservation experiment), after thawing (upon thawing of the organoids) at 7 and 14 days post-thaw (representing the recovery period of the organoids in a humidified environment at 37°C with 5% CO_2). Scale bars=100 µm.

The cell survival of 14 days post-thaw retinal organoids was assessed by IF analysis using Recoverin, SNCG, Prox1 and RLBP1 markers. The lamination of 14 days post-thaw organoids pre-incubated with loading solution for 20 minutes (unmodified 'Master Liver Supercooling' protocol) was disrupted. IF analysis revealed that PR cells stained with Recoverin were present; however, SNCG (retinal Ganglion cells), RLBP1 (Müller glial cells) and Prox1 (Horizontal cells) positive cells were not detected (**Figure 2-49**). Similar results were observed in organoids pre-incubated for 2 and 3 hours, showing that only PR cells survived after 14 days post-thaw (**Figure 2-49**). Collectively these results suggest that longer incubation of organoids with CPA solutions did not improve the survival of retinal cells, and thus the 'Master Liver Supercooling' protocol is currently the most effective protocol used for the cryopreservation of organoids.

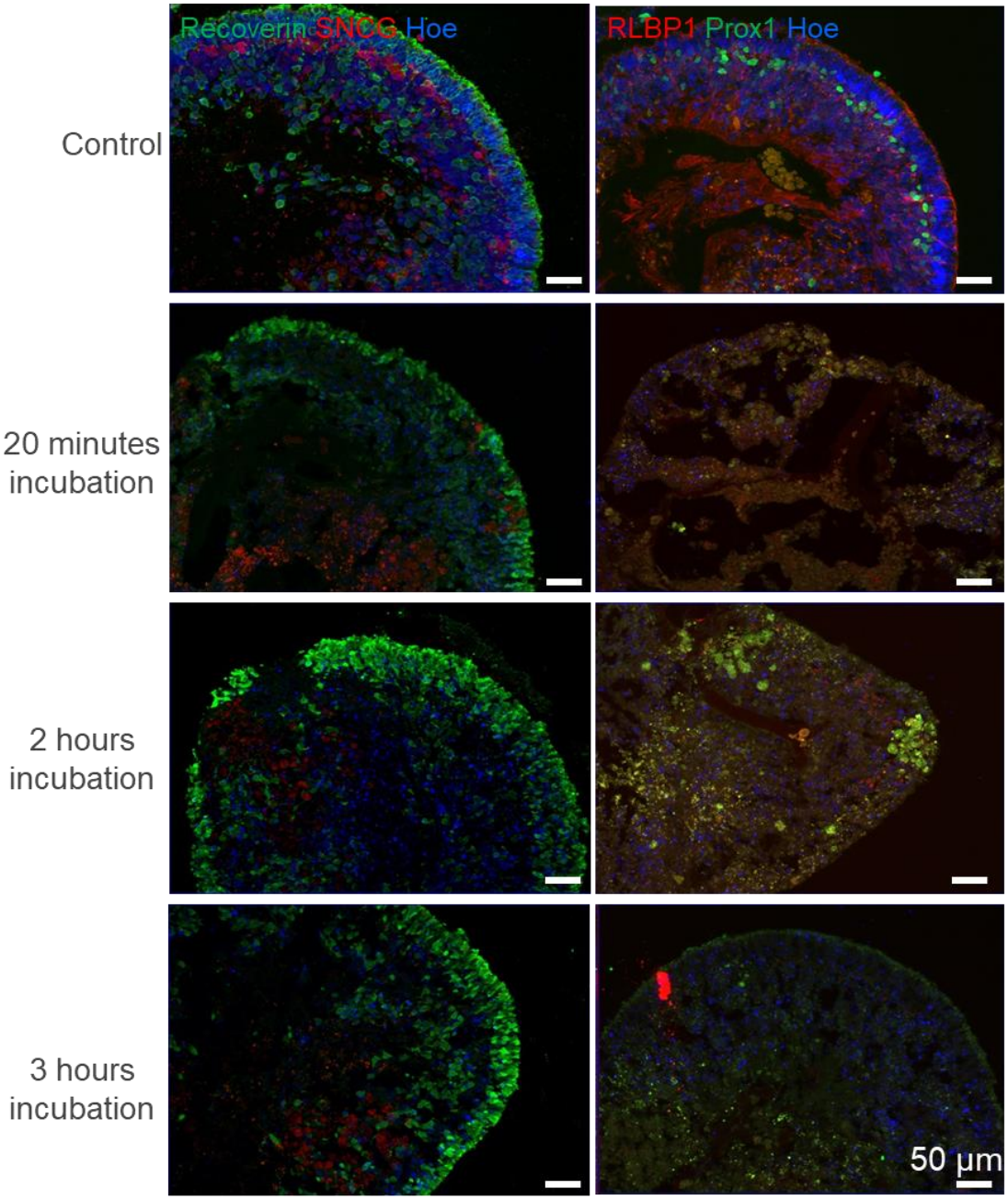

Figure 2-49: Immunostaining of control and supercooled day 160 retinal organoids treated with the 'Master Liver Supercooling' protocol, and extended pre-cooling incubation times for 2 hours and 3 hours, 14 days post-thaw. Sections through control and cryopreserved day 160 retinal organoids. PRs (Recoverin, green), ganglion cells (SNCG, red), Müller cells (RLBP1, red) and horizontal cells (Prox1, green) were present in day 160 control retinal organoids. For the unmodified 'Master Liver Supercooling' protocol (20 minutes), the structure of supercooled organoids was disrupted, and only Recoverin positive cells representing PRs have survived. Organoids pre-incubated for 2 hours with loading solution preserved only PR cells. PRs (Recoverin, green) only were present in supercooled organoids treated with loading solution for 3 hours. The structure of the organoids from all the conditions was damaged, and the nuclei were dotty. Nuclei were counterstained with Hoechst (Hoe). Scale bars= 50 µm.

2.4.8.4. Effect of 'Master Liver Supercooling' protocol in combination with matrigel-enriched rinsing media for cryopreservation of retinal organoids

The 'Master Liver Supercooling' protocol has provided the most promising results based on the previous results. Nevertheless, to enhance cell survival and prevent progressive apoptosis of cells, an additional modification, including the addition of matrigel in the rinsing media, was assessed in parallel with the unmodified 'Master Liver Supercooling' protocol as described in section 2.3.4.8.4. In addition to WT3 retinal organoids used before, another control cell line, WT2, was used to determine whether the results could be applied to more cell lines. Bright-field images were acquired before cooling, after thawing, on day 7 and day 14 post-thaw.

Bright-field images of WT3 retinal organoids treated with the unmodified 'Master Liver Supercooling' protocol (without matrigel) showed that the overall structural integrity of the organoids was maintained after 14 days post-thaw. However, the bright apical layer of the neuroepithelium was lost. Also, the overall size of the organoids was reduced, and the appearance of supercooled organoids was darker immediately after thawing (**Figure 2-50**). Similar observations were detected in WT3 retinal organoids treated with the modified 'Master Liver Supercooling' protocol (with matrigel in the rinsing media). Specifically, bright-field images revealed that the overall structural integrity of the organoids was preserved after 14 days post-thaw; however, the bright phase of neuroepithelium was lost, the organoids shrunk, and the appearance of the organoids was darker (**Figure 2-50**). Bright-field images of WT2 retinal organoids treated with the 'Master Liver Supercooling' without matrigel showed similar characteristics to WT3 organoids treated with the same condition (**Figure 2-51**). The same observations were also detected in WT2 organoids treated with the modified 'Master Liver Supercooling' protocol **(Figure 2-51).**

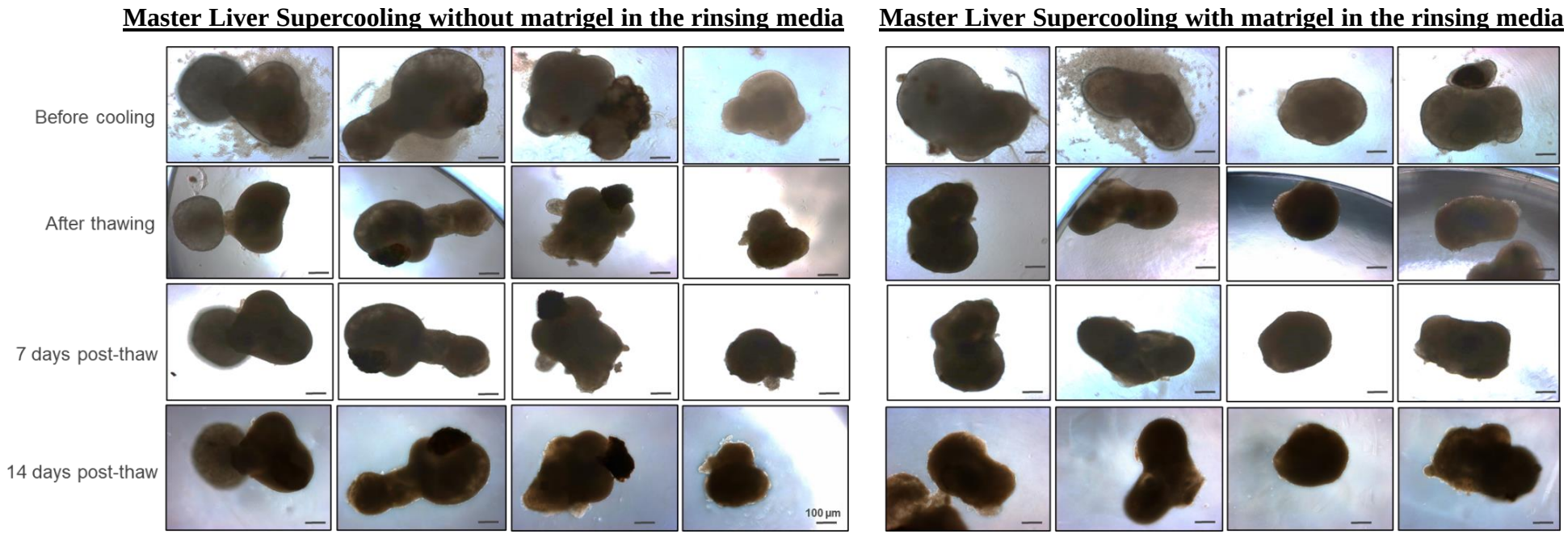

Figure 2-50: Representative images of WT3 retinal organoids before and after supercooling using the 'Master Liver Supercooling' with and without the addition of matrigel in the rinsing media. Bright-field images of day 160 retinal organoids before cooling (representing the organoids before cryopreservation experiment), after thawing (upon thawing of the organoids) at 7 and 14 days post-thaw (representing the recovery period of the organoids in a humidified environment at 37°C with 5% CO_2). Scale bars=100 µm.

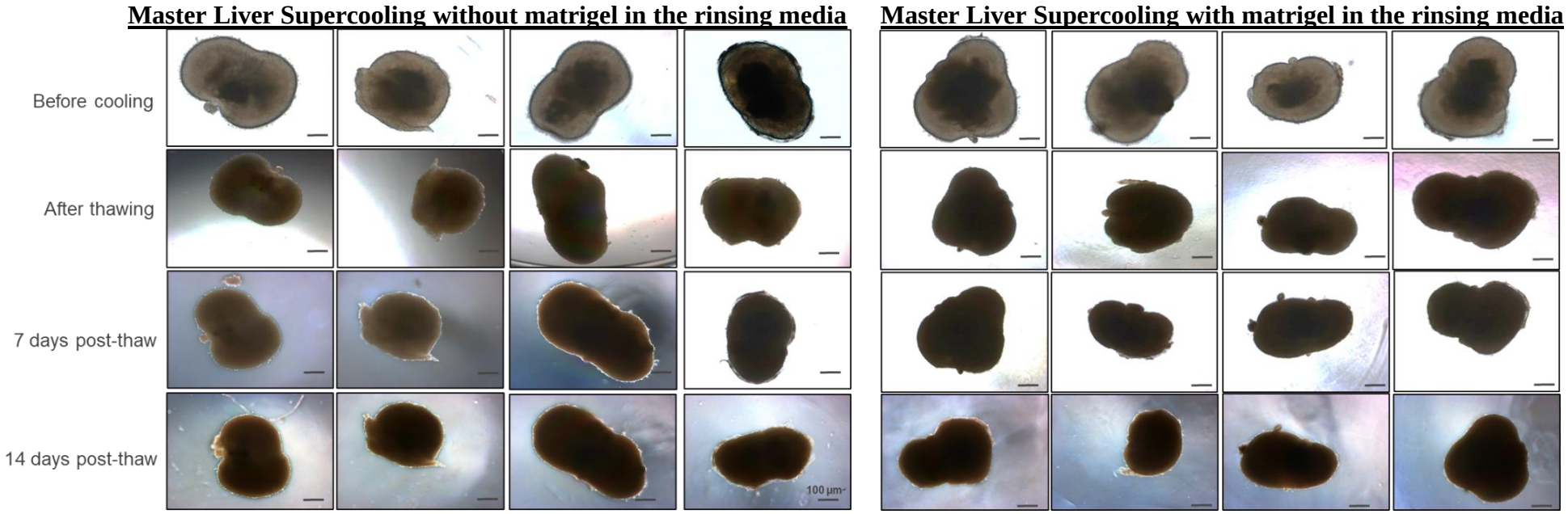

Figure 2-51: Representative images of WT2 retinal organoids before and after supercooling using the 'Master Liver Supercooling' with and without the addition of matrigel in the rinsing media. Bright-field images of day 160 retinal organoids before cooling (representing the organoids before cryopreservation experiment), after thawing (upon thawing of the organoids) at 7 and 14 days post-thaw (representing the recovery period of the organoids in a humidified environment at 37°C with 5% CO_2). Scale bars=100 µm.

Subsequently, IF analysis was performed to assess the cell survival of 14 days post-thaw retinal organoids treated with or without matrigel during the recovery period. For the IF analysis, Recoverin, SNCG, Prox1 and RLBP1 markers were used. WT3 retinal organoids treated with or without matrigel retained their overall structural integrity after 14 days post-thaw. Additionally, PR and ganglion cells stained with Recoverin and SNCG markers were detected. Also, RLBP1 and Prox1 positive cells representing Müller glial and Horizontal cells, respectively, were expressed (**Figure 2-52**). Although the overall structure of cryopreserved organoids was maintained and all retinal-related cells were detected, the structure of cryopreserved organoids was disrupted. The nuclei were less in number and dotty than the control organoids. Similar observations were detected in WT2 cryopreserved organoids treated with or without matrigel, showing that retinal organoids preserved PRs, ganglion cells, Müller glial and horizontal cells immunostained with Recoverin, SNCG, RLBP1 and Prox1, respectively. However, big gaps were detected in the structure of WT2 cryopreserved organoids indicating degeneration of the organoids. Also, the nuclei in both cryopreserved groups (organoids treated with or without matrigel in the rinsing media) were dotty (**Figure 2-53**). These results suggest that the addition of matrigel in the rinsing media did not improve the survival of retinal cells, indicating that the unmodified 'Master Liver Supercooling' protocol remains the most effective protocol from all the protocols tested in this thesis for the cryopreservation of organoids.

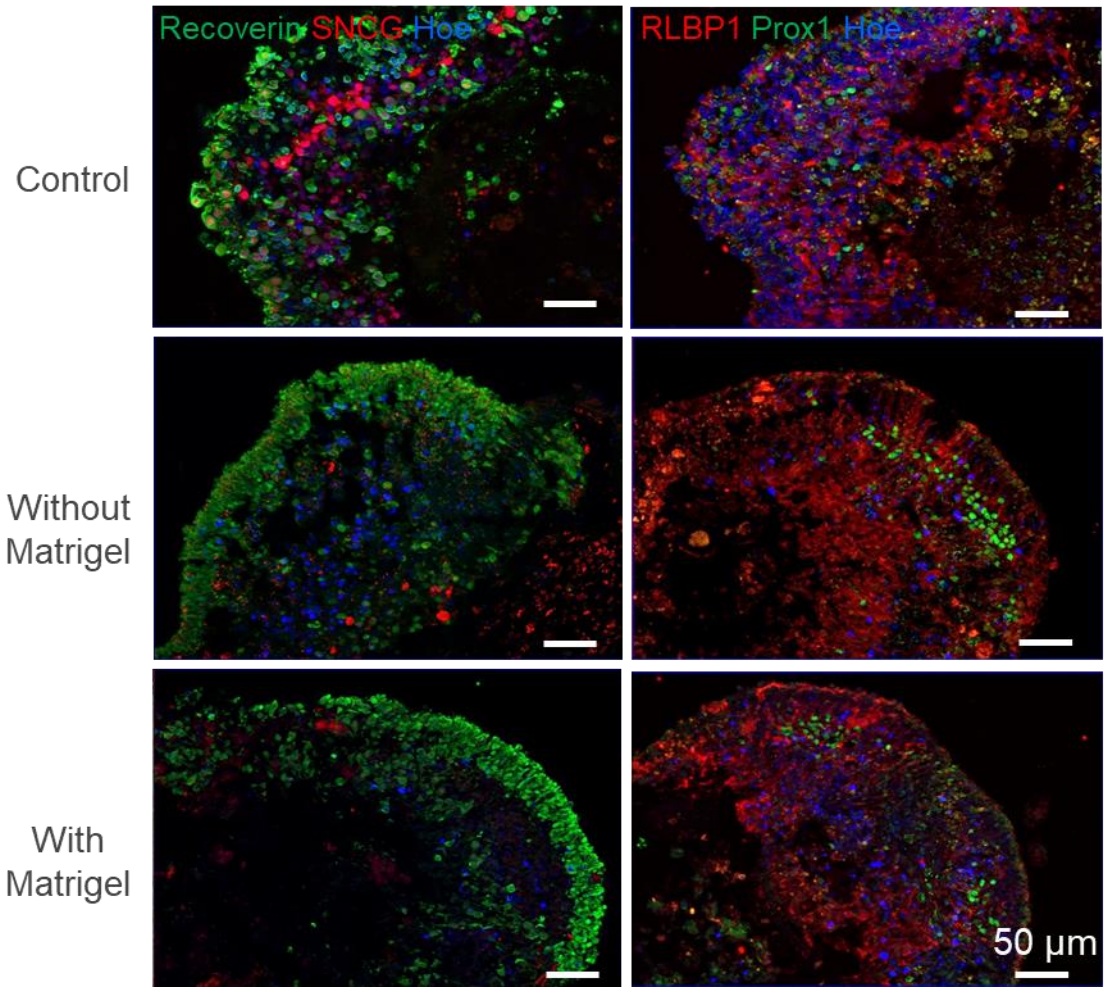

Figure 2-52: Immunostaining of control and supercooled day 160 WT3 retinal organoids treated with the 'Master Liver Supercooling' protocol, with and without matrigel in the rinsing media, 14 days post-thaw. Sections through control and cryopreserved day 160 retinal organoids. PRs (Recoverin, green), ganglion cells (SNCG, red), Müller cells (RLBP1, red) and horizontal cells (Prox1, green) were present in day 160 control retinal organoids. For the unmodified 'Master Liver Supercooling' experiment without matrigel, the structure of supercooled organoids was preserved, and all retinal-related cells were detected. PRs (Recoverin, green), ganglion cells (SNCG, red), Müller cells (RLBP1, red) and horizontal cells (Prox1, green) were present in day 160 supercooled retinal organoids treated with matrigel. However, the structure of the organoids was slightly damaged when compared to the control organoids. Also, the nuclei in both groups were dotty compared to the control. Nuclei were counterstained with Hoechst (Hoe). Scale bars=50 µm.

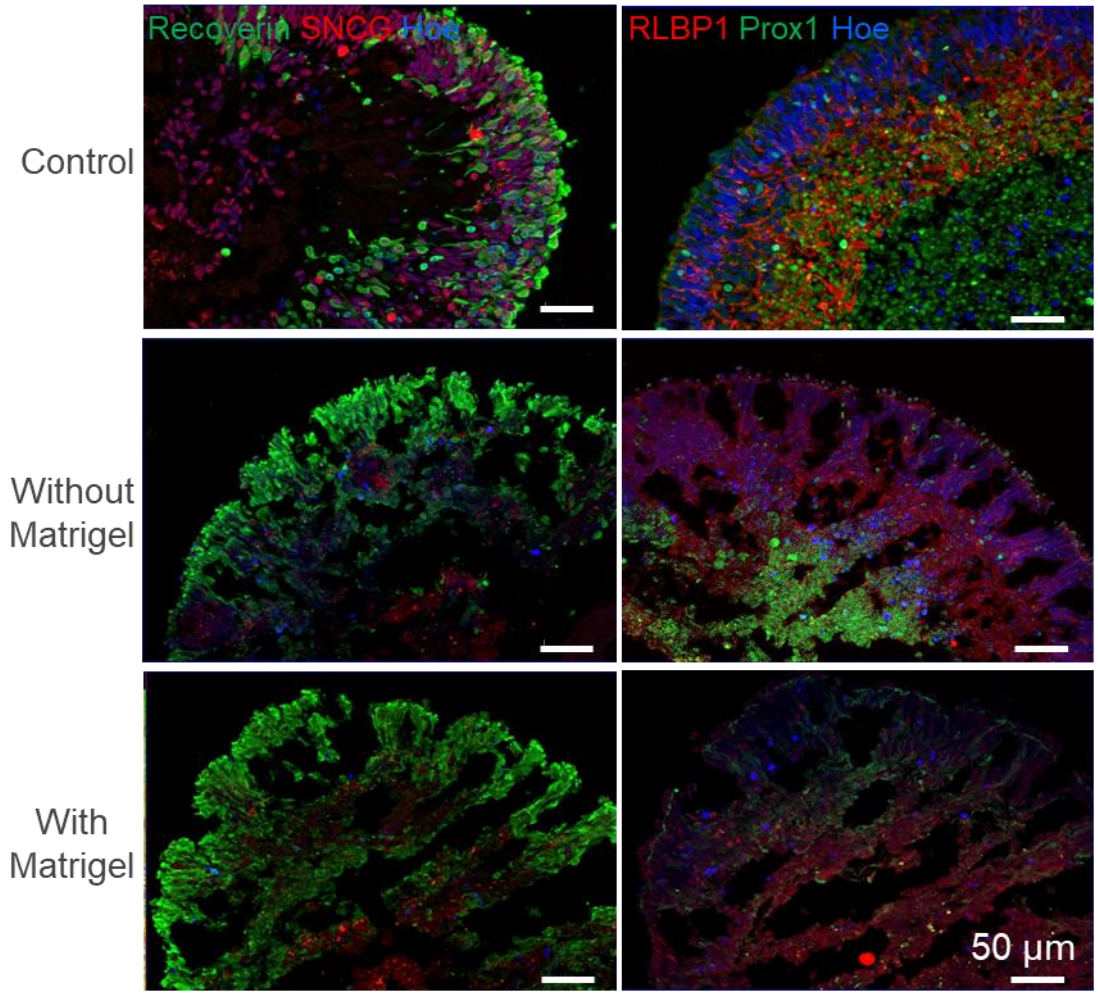

Figure 2-53: Immunostaining of control and supercooled day 160 WT2 retinal organoids treated with the 'Master Liver Supercooling' protocol with and without matrigel in the rinsing media, 14 days post-thaw. Sections through control and cryopreserved day 160 retinal organoids. PRs (Recoverin, green), ganglion cells (SNCG, red), Müller cells (RLBP1, red) and horizontal cells (Prox1, green) are present in day 160 retinal organoids. For the 'Master Liver Supercooling' protocol without matrigel, the structure of supercooled organoids was mainly preserved, but gaps were observed, and all retinal-related cells were detected. PRs (Recoverin, green), ganglion cells (SNCG, red), Müller cells (RLBP1, red) and horizontal cells (Prox1, green) were present in day 160 supercooled retinal organoids treated with matrigel. However, the structure of the organoids was slightly damaged when compared to the control organoids. Also, the nuclei in both groups were dotty compared to the control. Nuclei were counterstained with Hoechst (Hoe). Scale bars=50 µm.

2.4.8.5. Effect of 'Master Liver Supercooling' protocol with the addition of glycerol in the pre-conditioning stage for cryopreservation of retinal organoids

Several studies have shown that the survival of cryopreserved tissues can be enhanced by pre-incubating the samples with CPAs (Terry et al., 2006). This allows the CPAs to enter the intracellular space and fully equilibrate, improving their beneficial effects during cryopreservation. A widely used CPA that can act as a permeable and as a non-permeable CPA is glycerol. Therefore, it was hypothesised that pre-conditioning organoids with glycerol could improve their post-thaw viability and function. To investigate the effect of pre-conditioning with glycerol, day 160 retinal organoids were cryopreserved as described in section 2.3.4.8.5 . Bright-field images of organoids that have or have not pre-incubated with glycerol were acquired before cooling, after thawing, at day 7 and day 14 post-thaw. Bright-field images have shown that WT2 organoids treated with the unmodified 'Master Liver Supercooling' protocol maintained their overall structural integrity after 14 days post-thaw. However, the bright phase neuroepithelium of organoids was lost, the colour of the organoids was darker, and immediately after thawing the organoids shrunk (**Figure 2-54**). The same observations were detected in organoids pre-conditioned with glycerol followed by supercooling with the 'Master Liver Supercooling' protocol (**Figure 2-54**).

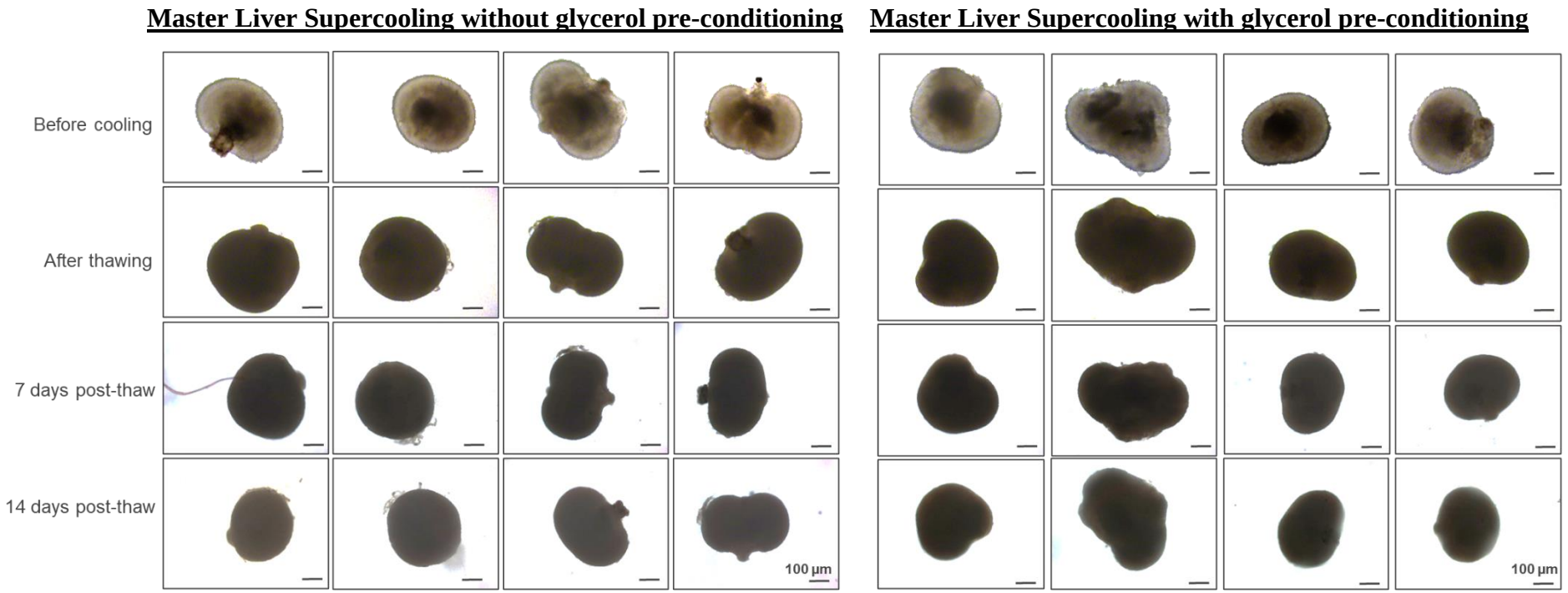

Figure 2-54: Representative images of WT2 retinal organoids before and after supercooling using the 'Master Liver Supercooling' protocol with and without <u>glycerol</u> pre-conditioning. Bright-field images of day 160 retinal organoids before cooling (representing the organoids before cryopreservation experiment), after thawing (upon thawing of the organoids) at 7 and 14 days post-thaw (representing the recovery period of the organoids in a humidified environment at 37°C with 5% CO_2). Scale bars=100 µm.

The presence and survival of retinal cells in 14 days post-thaw retinal organoids that have or have not pre-incubated with glycerol was assessed by IF analysis. The results showed the presence of Recoverin and SNCG positive cells in both groups of organoids. However, RLBP1 and Prox1 positive cells representing Müller glial and Horizontal cells, respectively, were not present in any condition (**Figure 2-55**). The overall structure of cryopreserved organoids pre-incubated either with or without glycerol was maintained; however, structural disruptions such as gaps in the lamination of cryopreserved organoids were detected (**Figure 2-55**). Collectively, these results suggest that pre-conditioning of retinal organoids with glycerol did not improve further the survival of retinal cells, suggesting that the most promising from all cryopreservation experiments tested herein were acquired from the unmodified 'Master Liver Supercooling' protocol.

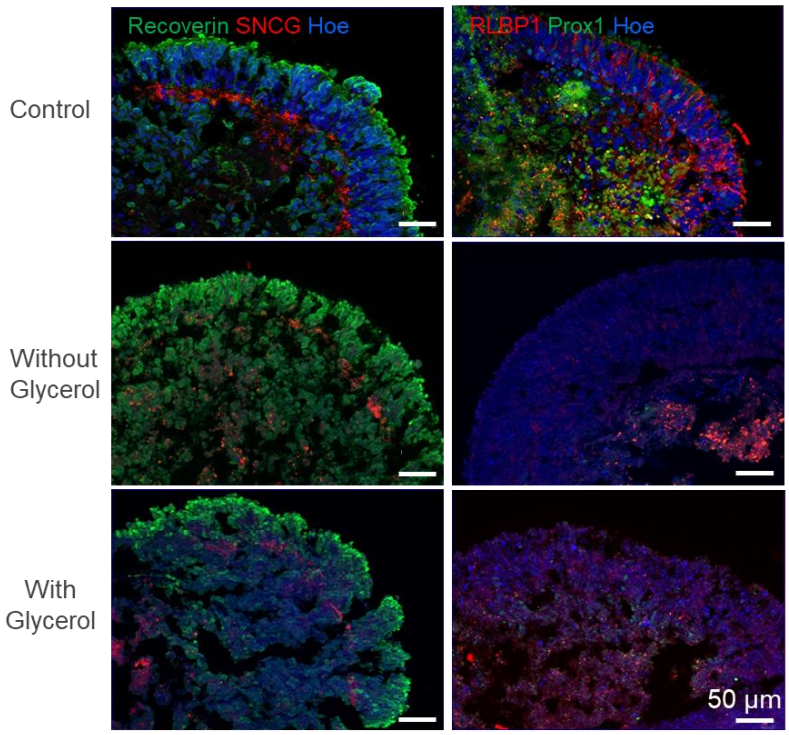

Figure 2-55: Immunostaining of control and supercooled day 160 WT2 retinal organoids treated with the 'Master Liver Supercooling' protocol with and without pre-conditioning with glycerol, 14 days post-thaw. Sections through control and cryopreserved day 160 retinal organoids. PRs (Recoverin, green), ganglion cells (SNCG, red), Müller cells (RLBP1, red) and horizontal cells (Prox1, green) were present in day 160 control retinal organoids. The structure of supercooled organoids treated with the 'Master Liver Supercooling' experiment without glycerol was preserved, and PRs (Recoverin, green), ganglion cells (SNCG, red), Müller cells (RLBP1, red) and horizontal cells (Prox1, green) were detected. PRs (Recoverin, green), ganglion cells (SNCG, red), Müller cells (RLBP1, red) and horizontal cells (Prox1, green) were present in supercooled organoids pre-conditioned with glycerol. However, the structure of the organoids was slightly damaged compared to the control organoids. Also, the nuclei in both groups were dotty compared to the control. Nuclei were counterstained with Hoechst (Hoe). Scale bars=50 µm.

2.5. Discussion

Cryopreservation offers a substantial number of advantages in biomedicine, drug discovery, and regenerative medicine. Long-term storage of biological materials at low temperatures not only provides the possibility of using multiple cells from the same batch for therapeutical purposes but from a commercial perspective, cryopreservation provides the product with a shelf life and also obviates the necessity of long-term culture with possible consequent problems of epigenetic changes and genetic drift (Hunt, 2019). The aim of this study was to develop an optimal protocol that could cryopreserve effectively retinal organoids. To achieve that, different cryopreservation methods, including slow and fast freezing, cooling, and vitrification, were tested on retinal organoids. The effects and the efficacy of cryopreservation experiments on hiPSC-derived retinal organoids were assessed by a bright-field microscope examining the presence of the bright phase neuroepithelium, the morphology, and the structure of retinal organoids. Also, the presence of retinal cells was examined by IF analysis only in cases where the structural integrity of organoids was maintained. These results are summarized in Table 2-15.

To generate and establish a novel reproducible cryopreservation method, we have tested several cryopreservation methodologies which were adapted from previous cryopreservation studies that reported the successful cryopreservation of complex tissues (Pichugin et al., 2006, Richards et al., 2004, Fayomi et al., 2019, de Vries et al., 2019). The cryopreservation methods tested are listed below:

1) Vitrification of retinal organoids using VEG or VM3 vitrification solutions, testing two different freezing rates, a slow (gradual vitrification) fast (direct) freezing rate (Pichugin et al., 2006).
2) Cryopreservation using ES-HEPES vitrification solution (Richards et al., 2004).
3) Cryopreservation using Mouse retinal protocol (Fayomi et al., 2019).
4) Excision of optic vesicles and cryopreservation (Eiraku et al., 2011, Fayomi et al., 2019).
5) Cooling experiment, cooling the organoids at -10°C and -20°C.
6) Liver supercooling, freezing the organoids at -4°C and -60°C (de Vries et al., 2019).

Building upon previously published cryopreservation methodologies, some factors such as the concentration of the CPAs, the freezing temperature, the exposure time of organoids to CPAs, and the cooling and thawing rate were modified according to the aims of the study following discussions with our collaborator Dr Peter Kilbride (Asymptote, Cytiva), to investigate the optimal cryopreservation conditions for retinal organoids. Among all the cryopreservation experiments, the most promising was the “Master Liver Supercooling” protocol which

preserved the overall structural integrity and morphology of retinal organoids and retained the presence of PR markers; however, not all retina cells survived.

Table 2-15: Summary of cryopreservation experiments.

Freezing Method		Temperature	Number and age of retinal organoids	CPA	Effects of CPAs on organoids					
					Shrinkage	Dark colour	NE	Structural Integrity	Loss of nuclei	Retinal cells
VEG	**Gradual**	-100˚C	16 retinal organoids Day 80	24.2% DMSO, 13.96% Formamide, 16.84% EG, 0.8 mM Vitamin C, 300 mM Mannitol, Carrier solution (Glucose 90 mM Mannitol 45 mM)	√	√	Lost	Partially preserved		No cells expressed
	Direct		16 retinal organoids Day 98		√	√	Lost	Partially preserved		No cells expressed
VM3	**Gradual**	-100˚C	16 retinal organoids Day 84	22.3% DMSO, 12.86% Formamide, 16.84% EG, 7% PVP K12, 1% Supercool X-1000, 1% Supercool Z-1000, 300 mM Mannitol, Carrier solution (90 mM Glucose, 45 mM Mannitol)			Lost	Rough	√	No cells expressed
	Direct		16 retinal organoids Day 92				Lost	Completely damaged		
ES-HEPES		-100˚C	20 retinal organoids Day 91	**ES-HEPES Solution:** 78% DMEM Knockout, 20% FBS, 2% 1M HEPES, 10% vitrification solution, 80% HEPES, 10% DMSO, 10%, EG **20% Vitrification solution 2:** 30% ES-HEPES, 30% 1M Sucrose Stock, 20% EG, 20%DMSO, **1M sucrose stock:** 624.5 mM Sucrose, 87.5% ES-HEPES Solution, 12.5% **0.2M sucrose Stock:** 20%, 1M Sucrose Stock, 80% ES-HEPES Solution, 0.1M sucrose stock, 10% 1M Sucrose Stock, 90% ES-HEPES Solution			Lost	Completely damaged		
Mouse retinal protocol		-160˚C	20 retinal organoids Day 105	**Freezing media:** 90% MEMa**,** 5% FBS**,** 5% DMSO **Thawing media A:** 100% HBSS, 100% maintenance media **Thawing media B:** 95%, 97%, 99% HBSS, 5%, 2%, 1% DMSO, 100% maintenance media **Thawing media C:** 95%, 97% 99% maintenance media, DMSO 5%, 2%, 1%, 100% HBSS		√	Lost	Mainly preserved		

Freezing Method		Temperature	Number and age of retinal organoids	CPA	Effects of CPAs on organoids					
					Shrinkage	Dark colour	NE	Structural Integrity	Loss of nuclei	Retinal cells
Eexcision of optic vesicles		-100˚C	20 retinal organoids Day 155	**Freezing Solution:** 5% FBS, 90% DMEM F12, 5% DMSO **Thawing Solution** 100%, HBSS, 100% maintenance Media			Lost	Completely damaged		
Cooling protocol	**Immediate thawing**	-10˚C	20 retinal organoids WT3 Day 169	**Basic Thawing Solution:** 1% P/S, 1% Glutamine, 31.9 mM Glucose, 98% DMEM F12 **Freezing Medium:** 90%FBS, 10%DMSO **Complete Thawing Medium:** 25% FBS, 25% HBSS, 50% Basic Medium			Preserved	Overall maintained, but lamination was damaged		Expressed Recoverin, HUCD, AP2a, RLBP1, Arrestin, Prox1, Opsin SW, Opsin MW/LW
	24 hours incubation	-10˚C			√		Preserved	Partially preserved		Expressed Recoverin, HUC/D, AP2a, Prox1, RLBP1, Arrestin 3, ARL13B, Opsin MW/LW
		-10˚C		**Without Rock inhibitor in the thawing solution**	√		Lost	Signs of damage		
		-10˚C		**With Rock inhibitor in the thawing solution**	√		Lost	Partially damaged		
		-20˚C		**Without Rock inhibitor in the thawing solution**	√		Lost	Partially damaged		
		-20˚C		**With Rock inhibitor in the thawing solution**	√		Lost	Partially damaged		

Freezing Method		Temperature	Number and age of retinal organoids	CPA	Effects of CPAs on organoids					
					Shrinkage	Dark colour	NE	Structural Integrity	Loss of nuclei	Retinal cells
Liver supercooling		-4˚C	20 retinal organoids WT3 Day 160	**Pre - supercooling recovery solution:** 0.8% P/S, 100 mM PEG, 100 mM 3-O-Methyl-D-glucose, 92.2% Maintenance media **Loading Solution 1:** 100 mM PEG, 5% Glycerol, 100 mM D-(+)-Trehalose dihydrate, 3mM Glutathione, 100 mM Lactobionic Acid, 30 mM Raffinose, 2.5% DMSO **Loading Solution 2:** 100 mM PEG, 10% Glycerol, 100 mM D-(+)-Trehalose dihydrate, 3 mM Glutathione, 100 mM Lactobionic Acid, 30 mM Raffinose, 5% DMSO **Unloading Solution:** 0.8% P/S, 100 mM PEG, 2 mM Trolox, 5% Glycerol, 100 mM D-(+)-Trehalose dihydrate **Post-supercooling recovery solution:** 0.8% P/S, 2 mM Trolox, 100 mM PEG **Rinsing media:** 10 µM Ri, 3 mM Glutathione	√	√	Lost	Partially damaged		No cell expressed
Master Liver Supercooling		-60˚C	20 retinal organoids WT3 Day 160		√	√	Lost	Mainly preserved but lamination was disrupted		Expressed Recoverin SNCG
Master Liver Supercooling	**Unmodified**	-60˚C	20 retinal organoids WT3 Day 160	No modifications made	√	√	Lost	Mainly preserved but lamination was disrupted		Expressed Recoverin SNCG Prox1 RLBP1
	Condition 1			Addition of 10 µM Rock inhibitor and 3 mM Glutathione in the rinsing media	√	√	Lost	Completely damaged		No cell expressed

Freezing Method		Temperature	Number and age of retinal organoids	CPA	Effects of CPAs on organoids					
					Shrinkage	Dark colour	NE	Structural Integrity	Loss of nuclei	Retinal cells
Master Liver Supercooling	**Condition 2**	-60˚C	20 retinal organoids WT3 Day 160	2.5% and 5% of DMSO in loading solution 1 and loading solution 2, respectively	√	√	Lost	Lamination was degenerated	√	Expressed Recoverin
	Condition 3			2.5% and 5% of DMSO in loading solution 1 and loading solution 2, respectively and the addition of 10 µM Rock inhibitor and 3 mM Glutathione in the rinsing media.	√		Lost	Lamination was degenerated		Expressed Recoverin SNCG RLBP1
Master Liver Supercooling	**Unmodified**	-60˚C	20 retinal organoids WT3 Day 150	No modifications made	√	√	Lost	Mainly preserved but lamination was disrupted		Expressed Recoverin SNCG RLBP1
	Condition A			RPE condition medium	√	√	Lost	Mainly preserved but lamination was disrupted	√	Expressed Recoverin SNCG RLBP1
	Condition B			8 mg/ml ECM	√	√	Lost	Mainly preserved but lamination was disrupted		Expressed Recoverin
	Condition C			RPE CM and 8 mg/ml ECM during the recovery period	√	√	Lost	Mainly preserved but lamination was disrupted	√	Expressed Recoverin
	Condition D			RPE CM and 8 mg/ml ECM 7 days prior to supercooling, and also during the recovery period						

Freezing Method		Temperature	Number and age of retinal organoids Age	CPA	Effects of CPAs on organoids					
					Shrinkage	Dark colour	NE	Structural Integrity	Loss of nuclei	Retinal cells
Master Liver Supercooling	**20 minutes incubation**	60˚C	20 retinal organoids WT3 Day 160		√	√	Lost	Mainly preserved but lamination was disrupted		Expressed Recoverin
	2 hours incubation									
	3 hours incubation									
Master Liver Supercooling	**Without Matrigel**	60˚C	20 retinal organoids WT3 Day 160	No modifications made	√	√	Lost	Mainly preserved but lamination was disrupted	√	Expressed Recoverin SNCG Prox1 RLBP1
	With Matrigel			2mg Matrigel						
	Without Master		20 retinal organoids WT2 Day 160	No modifications made						
	With Matrigel			2mg Matrigel						
Master Liver Supercooling	**Without Glycerol**	60˚C	20 retinal organoids WT2 Day 160	No modifications made	√	√	Lost	Mainly preserved but lamination was partially affected	√	Expressed Recoverin SNCG
	With Glycerol			2.5% Glycerol						

Vitrification is a relatively new cryopreservation technique that enables the cooling of cells at very low temperatures preventing dehydration of the samples and intracellular ice formation. Vitrification has been used for the preservation of spermatozoa (Isachenko et al., 2004), oocytes (Chen et al., 2000), embryos (Rezazadeh Valojerdi et al., 2009) as well as ESCs (Zhou et al., 2004). Additionally, this method has been used for the cryopreservation of more complex tissues such as hippocampal rat slices using VEG and VM3 vitrification solutions, showing that the structure of complex neural networks can be successfully maintained after vitrification (Pichugin et al., 2006). Vitrification of retinal organoids with VEG vitrification solutions indicated that the structural integrity of organoids was maintained; however, the survival of retinal populations was affected. No major differences were observed between gradually or fast rate vitrified organoids, suggesting that degeneration observed in VEG vitrified organoids is not attributed to the cooling rate. The observed degeneration can result from other factors such as the thawing rate, the tissue complexity (e.g multicellular tissue), the storage temperature, and the concentration and type of CPAs (Pegg, 2007). Similar results were observed in VM3 gradually vitrified retinal organoids suggesting that ice blockers used such as supercool X-1000 and supercool Z-1000 had no beneficial effects on the survival of organoids. However, our results do not agree with other studies which have shown that adding both Supercool X-1000 and Supercool Z-1000 in the vitrification solution can increase the survival rate of mouse embryos post-thaw (Badrzadeh et al., 2010). Interestingly, retinal organoids vitrified with the VM3 vitrification solution at a fast cooling rate disintegrated completely by day 14 post-thaw, suggesting that the cooling rate plays a vital role in the cryopreservation of retinal organoids, and further optimisation is required.

Additionally, complete disintegration was observed when retinal organoids were vitrified with ES-HEPES solution. Our results contradict the findings of a previous study that has shown to preserve a high percentage of viable hESC colonies after vitrification (Richards et al., 2004). Degeneration observed in our results could be attributed to the extremely high cooling rates that are required during vitrification, which are often not easily achievable. Also, vitrification is suitable for small scale of samples and can be achieved by increasing the concentrations of CPAs; however, for a larger scale of samples, which is the aim of the project, this is not a possibility leaving slow cooling the only available and practicable approach at the moment (Paynter, 2008).

Alternative cryopreservation methods such as slow freezing were adopted from other studies (Fayomi et al., 2019) and tested on retinal organoids. Slow rate freezing (freezing at a slow cooling rate) is widely used for the cryopreservation and storage of variable samples and cells.

A recent study has reported the successful cryopreservation of prepubertal testicular tissues following slow rate freezing, which grafted under rhesus macaques' back skin and produced functional sperm (Fayomi et al., 2019). However, when this protocol was assessed on retinal organoids, our results showed that the appearance of organoids upon thawing was darker for the freezing conditions and concentrations of the DMSO used, suggesting cell death. Similar observations were detected upon cryopreservation of OVs using a similar protocol. Our results suggest that this is probably attributed to the addition of DMSO, which is toxic at high temperatures (above 4°C) or at increased concentrations. Also, prolonged exposure to DMSO can be detrimental for the cells (Santos et al., 2003, Syme et al., 2004).

Additionally, to investigate an optimal freezing temperature, cooling the organoids at higher sub-zero temperatures (-10˚C and -20˚C) was attempted. Our results were variable between different experimental runs, and also disorganization of the lamination was detected by IF analysis. No significant improvements were observed when the ROCK inhibitor was supplemented in the thawing solution, which has been shown to reduce post-thaw apoptosis in hESC colonies (Martin-Ibanez et al., 2008). These results suggest that post-thaw apoptosis is probably triggered by other apoptotic mechanisms rather than caspase-based mechanisms. Also, the degeneration of organoids and the variability observed between runs could be a result of the enzymatic activities of the cells, which are reduced but remain active between 0˚C and -25˚C. Also, the uncontrol formation of ice crystals, which are randomly formed causing cellular damage at such temperatures, could explain the variability observed between experimental runs (Bakhach, 2009).

In addition, cryopreservation of retinal organoids was performed using a supercooling protocol adopted from a recent study (de Vries et al., 2019). When retinal organoids were supercooled to -4˚C, it was observed that retinal sections disintegrated completely. However, supercooling at a lower temperature (-60˚C), retinal-related cells were preserved, despite the differences observed in the structure and lamination between the control and supercooled organoids. A possible speculation is that at high subzero temperatures, the enzymatic activity of the cells is reduced but not completely inactive, causing cell death. This could be investigated in future studies by assessing the enzymatic activity of cryopreserved organoids. Aiming at reducing cell death, we supplemented loading solutions with DMSO. Also, we tested the addition of glutathione, which has been shown to protect sperm motility and fertility from cryodamage (Shi et al., 2018), with a ROCK inhibitor, which has been shown to reduce apoptosis (Martin-Ibanez et al., 2008), in the rinsing media. However, our results did not show any significant improvements in the overall survival of cryopreserved organoids compared to control

organoids, suggesting that the use of different antioxidants at different concentrations might be more successful.

An effort to improve the survival of organoids after supercooling of organoids using the 'Master Liver Supercooling' protocol was attempted by supplementing CPA solutions with RPE CM and/or ECM. ECM is pivotal in maintaining cell-matrix interaction and retaining an organized 3D structure, preserving thus the structural and functional signals (Urbani et al., 2017, Kim et al., 2004). However, supplementation of CPA solution with RPE CM, either alone or in combination with ECM, did not improve the overall survival of organoids; instead, cryopreserved organoids shrunk. Upon adding CPAs, water effluxes from the cells by osmosis, and CPAs enter the cell to substitute the water. However, the failure of CPAs to enter the cells, either because CPAs could not cross the plasma membrane or due to slow entrance of CPAs in the cells, induces osmotic injuries such as dehydration and shrinkage (Meryman, 2007). In this case, this is a possibility, explaining why PR cells located at the ONL (outer side of the organoids) survived and retinal-related cells located on the INL (inner side of the organoids) were lost.

Thereafter, an effort to improve the survival of organoids using the 'Master Liver Supercooling' protocol was attempted by extending the incubation time of loading solutions from 20 minutes to 2 and 3 hours before supercooling of organoids. This extends the incubation of cells with CPAs and allows sufficient penetration of CPAs in the cells (Raju et al., 2021). However, our results did not show any beneficial effects on the overall survival of organoids following longer incubation of organoids with CPAs. These results suggest that extending the incubation time of cells with CPAs before freezing using this particular protocol has no beneficial effects on the overall survival of organoids, and maybe other factors such as the pre-treatment of organoids with different CPAs could improve the survival of organoids.

Therefore, a strategy to improve the survival of organoids was attempted by supplementing matrigel in the rinsing media. Although the addition of matrigel has been shown from other studies to improve the recovery of stem cells after cryopreservation (Ji et al., 2004), our results showed that the addition of matrigel in the rinsing media did not improve further the survival of retinal cells, suggesting that the survival of cells observed is not attributed to the addition of matrigel.

Several studies have reported that the beneficial effects of CPAs can be enhanced by incubating the samples with CPA before freezing (Terry et al., 2006). This gives more time to the CPAs to enter the cells and protect them during cryopreservation. Considering the complex

mechanism of action of glycerol, which acts as a permeable agent at physiological temperatures and as a non-permeable agent at low temperatures (0˚C) (Bakhach, 2009), retinal organoids were pre-treated with glycerol for 30 minutes at 37˚C followed by cooling, to investigate whether glycerol could protect the cells intracellularly and extracellularly. Our results did not show any beneficial effects in the overall survival of cryopreserved organoids compared to control organoids, and also no major differences were observed between cryopreserved organoids treated with or without glycerol. Our results suggest that pre-incubation of retinal organoids with glycerol at the specific concentration used did not improve the survival of organoids.

To improve the survival of retinal organoids, modifications on the 'Master Liver Supercooling' protocol were performed. In parallel, the unmodified 'Master Liver Supercooling' protocol was repeated in each experimental run for comparison. Interestingly, differences were observed in the structure (lamination), the presence of retinal-related cells, and the number of nuclei between all the unmodified 'Master Liver Supercooling' experiments (**Figure 2-56**), suggesting variability between the different runs. Although several studies have attempted to cryopreserve tissues or 3D complex structures, difficulties in the repetition of the experiments and differences in the results were reported. The differences between experimental runs following cryopreservation of 3D organoids may arise from the differences in cryotolerance and permeability of the variable interconnected single cells that constitute these multicellular systems. In combination with the differences in the diffusion of water and CPAs that each cell or organoid is experienced, these factors could lead to differences in the freezing environment (Ehrhart et al., 2009). These differences induce tissue degeneration, changes in the metabolic activities, distortion of the tissue's shape, reduced cell number, and loss of cell-specific function. The variable changes experienced by individual cells or organoids during cryopreservation explain the differences observed between technical and biological experimental repeats.

2.6. Conclusion

In respect to all cryopreservation methods tested, the 'Master Liver Supercooling' protocol provided the most promising results, indicating that it is possible to cryopreserve whole retinal organoids to some extent at sub-zero temperatures. However, more work is required to improve further the structure, morphology and cell survival of retinal organoids. To achieve this, future studies to understand the pathways activated upon freezing and thawing are required. Also, more work is required to understand the chemical and biological properties of the freezing and

thawing cycle that will provide a successful method for the cryopreservation of mature retinal organoids.

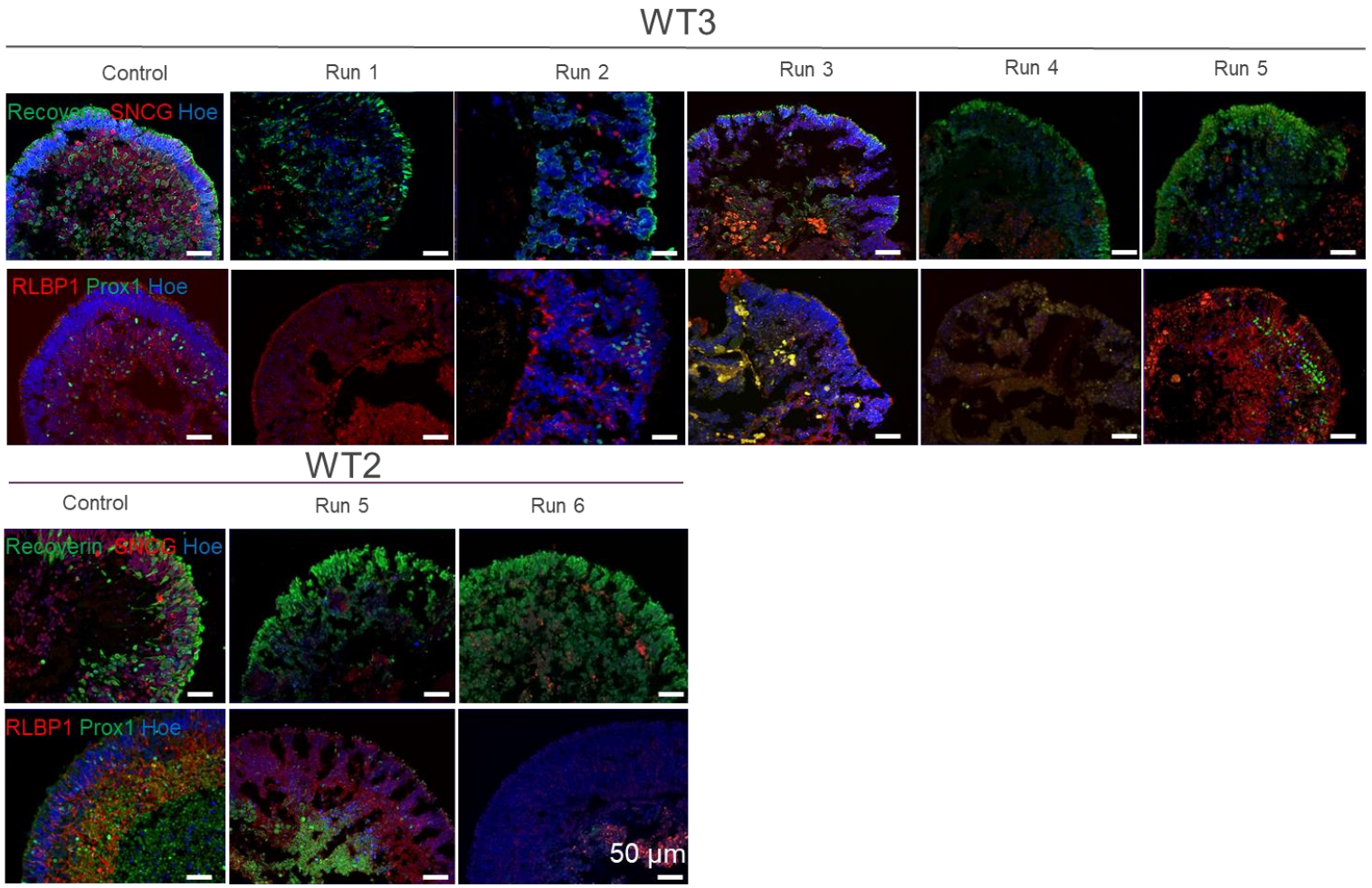

Figure 2-56: Summary of all 'Master Liver Supercooling' experimental runs. WT3 and WT2 retinal organoids cryopreserved using the 'Master Liver Supercooling' protocol stained with Recoverin (PRs, green), SNCG, (ganglion cells, red), RLBP1 (Müller cells, red) and Prox1 (horizontal cells, green). Variability in the structure of the organoids and in the presence of retinal organoids was detected between different runs. Nuclei were counterstained with Hoechst (Hoe). Scale bars=50 µm.

Chapter 3

Chapter 3. Shipping of hiPSC derived retinal organoids at room temperature

3.1. Introduction

A new technology, the large-scale generation of three-dimensional (3D) retinal organoids, has emerged by differentiating human embryonic stem cells (hESCs) and human-induced pluripotent stem cells (hiPSCs) into “synthetic retinae”. These 3D retinal structures contain all major retinal cell subtypes with distinct layers that largely mimic the human retina's structural, morphological, and functional properties. The development of 3D retinal structures has a multidimensional role as retinal organoids can be used as disease models to understand better human retinal diseases; they can provide novel insights into human retinal development, reveal unknown mechanisms of pathogenesis, and provide new avenues for drug screening and cell-based replacement therapies.

The generation of retinal organoids is a labour-intensive and time-consuming procedure that requires specially trained researchers and considerable expertise and infrastructure. Therefore, this technology is only available to some specialized labs worldwide. Hence, transportation or shipping will facilitate the widespread application of well-characterised retinal organoids and make this technology more accessible globally. The availability of 3D retinal structures in multiple centres could facilitate and enhance the collaboration between research centres, pharmaceutical companies and medical centres.

Transportation of samples depends on the nature of the cells or tissues (preserved or live) and the shipment method (air or road). Transportation of live tissues should ensure that the samples are shipped immediately using the shortest possible route to retain the survival, cellular structure, and functionality of the tissue. Additionally, transportation of tissues could take place using special containers that maintain the temperature within a specific range. This is critical as fluctuations to very high or low temperatures can affect the biological and mechanical activity of the tissue, causing cell injury and intracellular degeneration. Currently, many options are available for temperature-controlled shipments, but not always economically practical. Due to the frequent transportation of cells or samples between research centres, low-cost and efficient methods have been developed for long-distance shipments.

A very common method that is widely used for the shipping of cryopreserved samples is dry ice transport. Several published studies reported the successful transportation of tissues at cooled or frozen conditions using commercially available containers. Rooney and colleagues have tested the shipping of allografts (Achilles tendon and femoral head) at -40°C using a

commercially available package. The study revealed that although the package including the samples was exposed to 37°C, the temperature was preserved at -40°C for at least 48 hours, indicating that human tissue safety and quality could be maintained during transportation. Despite the advantages that this method provides, dry ice is a hazardous material that can explode or cause suffocation. Due to its high risks, more than 50% of countries worldwide do not allow shipments that include dry ice, reducing the availability of cells globally (Stefan et al., 2001). Also, shipping cryopreserved samples using dry ice can be risky, especially if there are delays in the shipment, as dry ice evaporates after a few days and thus samples can be lost (Lou et al., 2014).

Alternative methods have been introduced for shipping live cells internationally without using dry ice. A research study has developed an agarose gel coating method to transport live cells, such as human lung adenocarcinoma epithelial (A549) cells and Human Embryonic Kidney 293 (HEK-293) cell culture plates at ambient temperatures. This was performed using a 1% agarose-medium mixture, which was heated at 45°C, then added to the plates to cover live cells, followed by their transportation. This study has successfully reported the survival of cells up to 6 days under these conditions (Yang et al., 2009). However, this method cannot be used widely as not many cells can survive when exposed to high temperatures. In another study, NIH3T3 cells were covered with gelatin solution prepared from animal skin. This study reported the survival of cells at 10°C and 23°C; however, at higher temperatures (37°C), the gelatin mixture melts, risking the survival of cells. This method also limits the shipment of cells at ambient temperature.

Other studies have used insulated containers to transport samples to test whether temperature fluctuations can affect the tissue. Specifically, Miller and colleagues have reported the successful transportation of corneal tissues using insulated shipping containers at cooling temperatures (8˚C or lower) for the required duration (Miller et al., 2013). Another study has tested the effects of temperature fluctuations during the shipping of bone matrix putty. This study has shown that after continuous exposure of the sample to +50°C and multiple freeze-thaw cycles, the osteoinductive potential or handling characteristics of the grafts were not affected (Schallenberger et al., 2016). Additionally, Hori and colleagues have demonstrated a new technology for shipping RPE tissues at room temperature (RT) by using a heat-insulating container to minimise the physical and chemical stress on the cells (Hori et al., 2019). Also, a new protocol for shipping retinal organoids at 37°C to facilitate the preclinical studies in animal models and potentially for transplantation purposes was reported. This protocol provides temperature control and live monitoring of the shipment conditions to maintain the viability of

the tissues over long distances preventing tissue damage (Singh et al., 2020). Shipping samples at ambient temperature could eliminate the necessity to freeze samples, thus facilitating substantial savings in time and money. Also, shipping at ambient temperature prevents freezing of the samples and hence preserves the tissue from possible degeneration from cryoinjuries that can be caused during cryopreservation.

3.2. Aims

The aim of this chapter is to determine whether storage of retinal organoids followed by shipment at RT at normal (0.04%) CO_2 levels can affect the morphology, cellular dynamics and functionality of organoids compared to control organoids that were maintained in a humidified environment at 37°C with 5% CO_2.

3.3. Materials and Methods

3.3.1. Cell lines

Adult human dermal fibroblast cells (HDFs) were collected from healthy volunteers to generate control hiPSCs. Two hiPSCs lines, WT3 (Ad4, CC-2511 Female, 84-year-old female) and WT4 (MJN1, Male, 57 years old), were derived and characterised in Lako's group (Buskin et al., 2018, Melguizo-Sanchis et al., 2018).

3.3.2. Room Temperature experiment and Shipping of retinal organoids

For the RT experiment, day 360 WT4 (MJN1) retinal organoids were maintained at RT conditions for five days. This was defined as 'day -5' (Figure 3-1 **A**). After 5 days of incubation at RT, the organoids were transferred to the incubator at 37°C with 5% CO_2; this was defined as 'day 0' (**Figure 3-1 A**). The organoids were kept in the incubator for 15 days before their collection for IF analysis. This was defined as 'day 15' of the RT experiment (**Figure 3-1 A**).

The shipment experiment was performed at two different time points during retinal differentiation: day 135 and 160. Before shipment, 96-well culture plates of retinal organoid were fed with 100 µl of fresh retinal organoid media as mentioned in section 2.3.3. The 96-well plates were covered with parafilm to prevent any leakage and were further sealed with a plastic sealed bag containing absorbent material and placed horizontally in a specific shipping container at RT in a controlled ambient environment system (QuickSTAT). The plates were

surrounded with tissue to prevent the movements of the plates and their leakage in the shipping container. According to the manufacturer's instructions, temperature control was activated and placed inside the box to record the temperature throughout the shipping.

The parcel was delivered by car to London and then shipped by plane to Frankfurt, Germany, at RT at normal CO_2 levels (0.04%). The day of delivering and shipping WT3 retinal organoids was defined as 'day -3' (**Figure 3-1 B**). Three days later, the parcel returned back to the Biosciences Institute at Newcastle, via the same route. The arrival of WT3 day 135 and 160 retinal organoids back at the Institute was recorded as 'day 0' (**Figure 3-1 B**). Retinal organoids were placed into the incubator at 37°C upon delivery, and media changes were performed every 2 days. The organoids were maintained in the incubator for 7 days to recover before collecting for IF analysis (**Figure 3-1 B**). For comparison, control plates with WT3 day 135, 160 and WT4 day 360 retinal organoids were maintained in a humidified environment at 37°C with 5% CO_2. These control organoids were collected at the same time points as the RT and shipped organoids.

3.3.3. TUNEL staining

Slides containing thin sections (10 μm) of retinal organoids were incubated with PBS and subsequently with Proteinase K. Thereafter, the slides were incubated with 3% hydrogen peroxide (H_2O_2) for 10 minutes at RT, followed by 30 minutes incubation with reaction buffer. Thereafter, tunnel assay (Biovision, Mountain View, CA, USA) was used according to the manufacturer's instructions to detect apoptotic and necrotic cells. Dead cells were detected with dark colour using the Axio Imager microscope with Apotome structured illumination fluorescence (Zeiss AxioVert 2 Germany). All images were acquired using the same magnification. Batch process analysis of the brown stained cells was performed by processing all images (from both control and RT conditions) together without distinguishing the category of each image at the time of the analysis. This was performed to achieve unbiased analysis and quantification. Analysis was performed using ImageJ by adjusting the brightness and contrast of all the images using the same threshold to mask the non-brown stained cells. Therefore, using the automated analysis button, the number of brown-stained cells per image was calculated. Following analysis, the identity of each image was revealed, and graphs were performed by using Prism (GraphPad, USA).

3.3.4. Transmission electron microscopy (TEM)

Retinal organoids were collected and fixed using 2% gluteraldehyde in 0.1 M sodium cacodylate buffer and kept at 4°C. The samples were processed at the Newcastle University electron microscopy facility, where 1% of osmium tetroxide was used to fix further the samples. Thereafter, retinal organoids were dehydrated and embedded using gradient acetone, and epoxy resin, respectively. Heavy metals (uranyl acetate and lead citrate) were used to stain ultrathin sections (70 nm) on copper grids. Images were taken on a Philips CM100 TEM with high-resolution digital image capture.

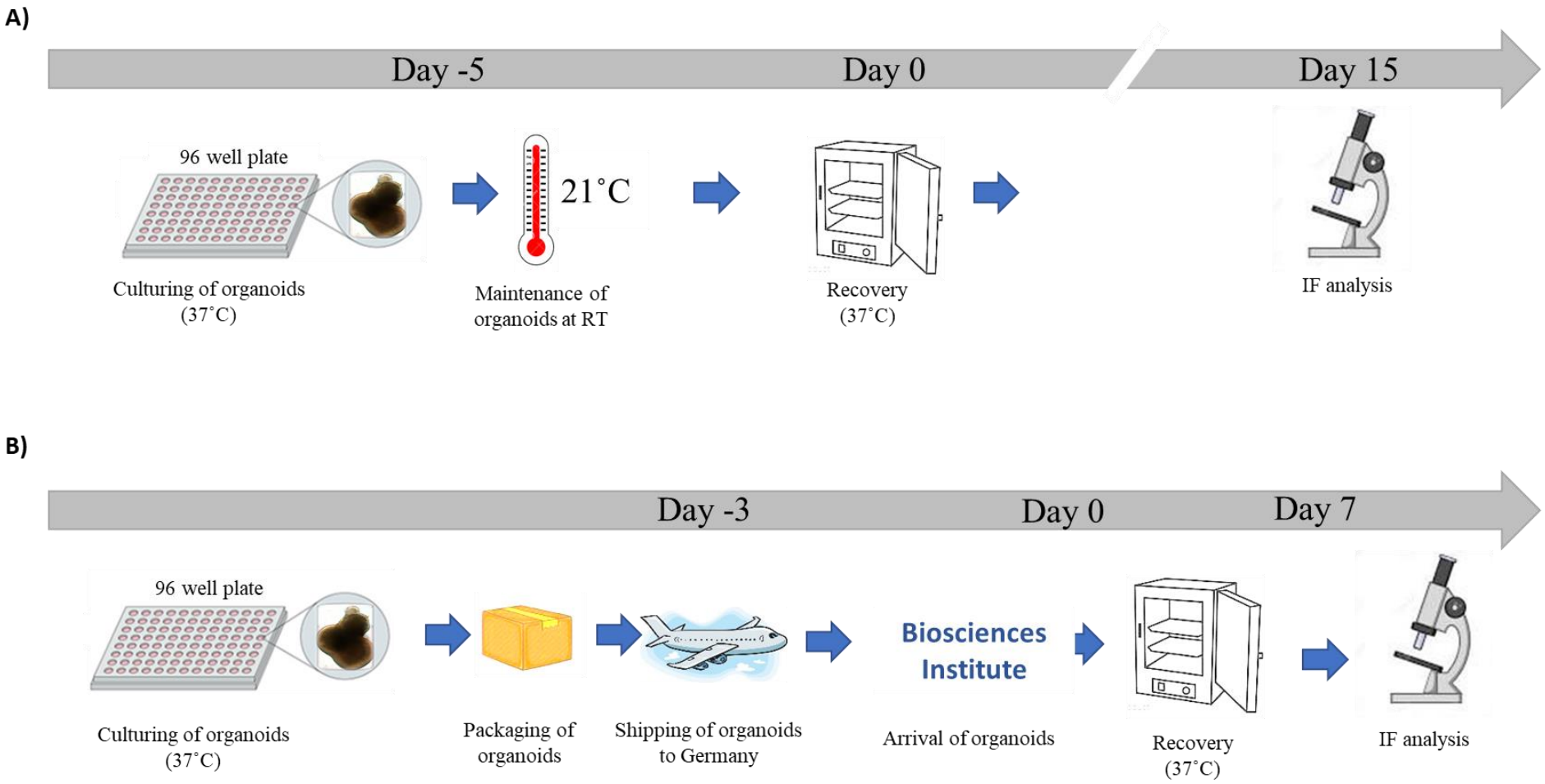

Figure 3-1: Schematic diagram of RT and shipping experiments. A) RT experiment. WT4 retinal organoids were maintained at RT conditions for five days (day -5). Then retinal organoids were transferred to the incubator at 37°C with 5% CO_2 (day 0), where they were maintained for 15 days to recover before their collection (day 15) for IF analysis. B) Shipment experiment. WT3 and WT4 retinal organoids were packed and shipped to Germany at RT at normal CO_2 level (day -3). After three days, retinal organoids returned to the Biosciences Institute at Newcastle via the same route (day 0). Retinal organoids were kept in the incubator at 37°C with 5% CO_2 for 7 days to recover (day 7) before their collection for IF analysis.

3.3.5. Immunofluorescence (IF) analysis

Immunofluorescence analysis of control, RT incubated and shipped organoids was performed as mentioned in section 2.3.5.2. Primary (**Table 3-1**) and secondary antibodies (**Table 3-2**) used are mentioned below.

Table 3-1: List of primary antibodies used for IF analysis on retinal organoids.

Antibody	Conjugate/Tissue	Host	Source	Cat. No.	Dilution
Recoverin	photoreceptors and midget OFF bipolar cells	Rabbit	Millipore	AB5585	1:1000
HuC/D	Amacrine and retinal Ganglion Cells	Mouse	Invitrogen	A21271	1:200
Prox 1	Horizontal and Amacrine cells	Rabbit	Millipore	AB5475	1:1000
Opsin red/green	L/M cone photoreceptors	Rabbit	Millipore	AB5405	1:200
ARL13B	Connecting cilium	Rabbit	Abcam	ab83879	1:250
Opsin Blue	S cone photoreceptors	Rabbit	Abcam	AB5407	1:200
RetP1 (Rhodopsin)	Rod photoreceptors	Mouse	Sigma	O4886	1:200
Ap2a	Amacrine cells	Mouse	Santa Cruz	sc-12726	1:200
SNCG	Retinal ganglion cells	Mouse	Abnova	H00006623-M01A	1:500
PKCa	Bipolar Cells	Mouse	BD Transduction Laboratories,	610107	1:200
Vimentin	Müller glial cells	Rabbit	Abcam	ab92547	1:200
Sox9	Müller glial cells	Mouse	Abcam	ab76997	1:100

Table 3-2: List of secondary antibodies used for IF analysis on retinal organoids. r=rabbit, m=mouse, GT=goat.

Antibody	Host	Source	Cat. No.	Dilution
Gt a-r Alexa (488)	Jackson ImmunoResearch	Goat	111545144	1:800
Gt a-m Cy3	Jackson ImmunoResearch	Goat	115165003	1:800

3.3.6. Microscopy and image analysis

Analysis of the images was performed using the Axio Imager upright microscope with Apotome structured illumination fluorescence (Zeiss, Germany). Fluorescent filters were used to cover multiple dyes such as Hoechst, Cy3, and Alexa 488. Using 20 x objective, hiPSCS- derived retinal organoids were analysed. 8-10 organoids were analysed per condition. Images are presented as a maximum intensity projection (MIP), and brightness and contrast were adjusted using Adobe Photoshop (Adobe Systems).

3.3.7. Image Quantification

Image quantification was performed using the MATLAB software (Mathworks, MA), and software codes were provided by Dr Yuchun Ding (Newcastle University, UK). The data were presented as images where background noise was filtered out before analysis. Using MATLAB's region props property, information about the size, the length and the average intensity of each retinal cell was calculated. The total size and percentage of positive cells in relation to nuclear stained cells was exported in an Excel file for additional analysis. However, the percentage of ciliated cells was calculated as cilia numbers/total cell numbers (DAPI) in putative outer nuclear layer x 100. For the quantification and analysis of each retinal-related marker, five to six representative images per condition were quantified. Further analysis of the results was performed using Microsoft Excel and Prism (GraphPad, USA).

3.3.8. Measurement of the neuroepithelium thickness

The thickness of the bright phase neuroepithelium (NE) was measured using bright-field images of retinal organoids which were captured using Axiovision 4.3 (Zeiss) microscope. The bright-field images were taken using 5x magnification. Bright-field images from control and RT organoids were batched processed together by applying the same phase-contrast threshold to all images to distinguish the bright NE. Thereafter, vertical lines were drawn from the center of the organoids (dark colour) towards the edge of the organoids to measure the thickness of the NE in µm. 6 measurements were taken across the bright phase NE in 10 organoids from each condition, using ImageJ software. Unbiased analysis was performed by processing all images together without distinguishing the identity of each image the time of the analysis. (**Figure 3-2**). The average NE thickness from each condition was statistically analysed using Prism (GraphPad, USA).

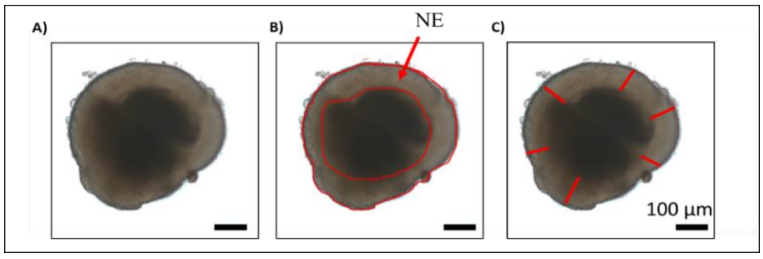

Figure 3-2: Measurements of neuroepithelium thickness in retinal organoids. (A) Bright-field images of retinal organoids were taken, and the scale bar was set to 100 µm. (B) The bright phase neuroepithelium on the apical side of the organoids was identified (red circled area is an example of the bright phase neuroepithelium of the organoids). (C) 6 measurements across the bright phase neuroepithelium in each organoid were taken by drawing vertical lines (red) from the apical side of the neuroepithelium to the basal side using the ImageJ, (USA). 10 organoids were used per condition. NE= neuroepithelium. Scale bars=100 µm

3.3.9. Electrophysiological recordings

Electrophysiological recordings of retinal organoids and analysis of the results were performed by Dr Gerrit Hilgen and Dr Birthe Dorgau, as described in Dorgau and Felemban et al., 2019 (Dorgau et al., 2019). Briefly, 24 hours prior to electrophysiological recordings, retinal organoids were incubated with 9-*cis*-retinal (10 nM; Sigma-Aldrich, UK). The organoids were incubated in artificial cerebrospinal fluid (aCSF) containing 118 NaCl, 25 NaHCO3, 1 NaH2 PO4, 3 KCl, 1 MgCl2, 2 CaCl2, 10 glucose, 0.5 l-Glutamine, and 0.01 9-cis-retinal. The organoids were placed onto a 4096 channel multielectrode array (MEA), with the presumed RGC layer facing down. The organoids were flattened on the electrodes using a translucent polyester membrane filter (Sterlitech Corp., Kent, WA, USA), and were left for minimum 2 hours to settle. BioCam4096 MEA platform with BioChips 4096S+ (3Brain GmbH, Lanquart, Switzerland) was used to record the data.

Full field white light pulses (WLP, 200 ms, 217 µW/cm2 irradiance, 1Hz) were flashed for 5 minutes onto the organoids following recording spontaneous activity in the dark for 5 minutes. Also, stimulations from blue light were used (SBL, 2 minutes darkness, 2 minutes SBL, 2 minutes darkness), same irradiance as WLP) to record responses from intrinsically photosensitive RGCs (ipRGCs). The cGMP drug (8-Bromoguanosine 3',5'-cyclic monophosphate, Sigma-Aldrich, MO) was puffed in the recording chamber (final concentration: 100µM) and readings from continuous 4 minutes, starting at 2 minutes before the puff were recorded. Firing-rate analyses were performed by using MATLAB (Mathworks, MA), and statistical significance tests (Mann-Whitney test) were evaluated using Prism (GraphPad, CA). Retinal ganglion cells were considered responsive if they changed their spiking activity at least 25% (increase or decrease) during 30 seconds after WLP onset compared to the similar time window before the light stimulus (dark condition).

3.3.10. Statistical Analysis

Statistical analysis was performed using Prism (GraphPad, USA). Two-tailed Student's *t*-test was used to test statistical significance between the groups. Error bars represent standard error of the mean (SEM) unless indicated otherwise. Statistical significance of pairwise comparisons is indicated by asterisks: * p-value <0.05, ** p-value <0.01, ***= p-value <0.001. ***= p-value ****<0.0001.

3.4. Results

3.4.1. Short-term storage of WT4 day 360 retinal organoids at RT does not induce phenotypic or structural differences

Retinal organoids were generated by differentiating hiPSCs using an established protocol (section 2.3.3) (Kuwahara et al., 2015). To evaluate the effect of RT storage, day 360 organoids were kept outside of the incubator (at RT) for 5 days (**Figure 3-1 A**). Following 5 days of incubation at RT, retinal organoids were transferred to the incubator for 15 days to recover, as mentioned in section 3.3.2. Bright-field images from both day 360 control and RT incubated organoids were taken at day -5, 0, and day 15 of the RT experiment (**Figure 3-1 A**), showing no morphological changes between the control and RT group. The colour, size, and bright phase neuroepithelial layer were preserved after storage of organoids at RT for 5 days. Additionally, the bright phase neuroepithelial thickness was measured, showing no significant differences between the two groups (**Figure 3-3 B**).

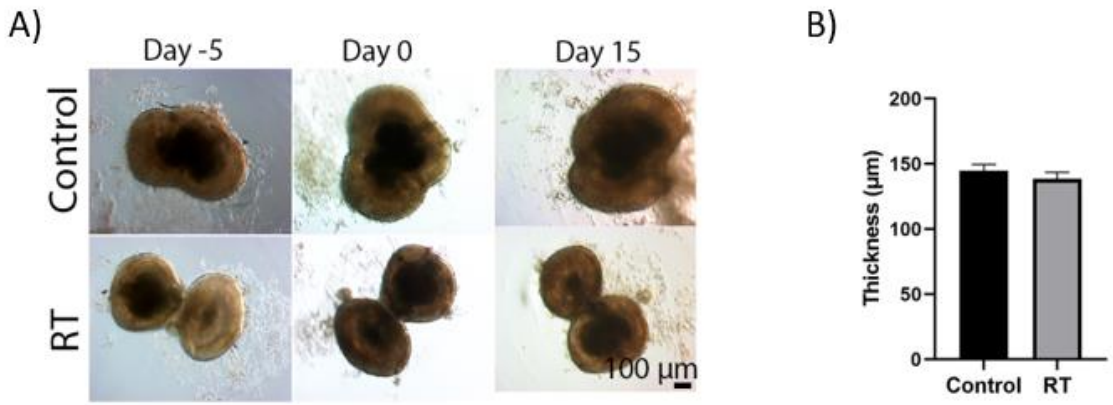

Figure 3-3: Morphological characteristics of control and RT retinal organoids before and after exposure to RT conditions. A) Representative examples of hiPSCs-derived retinal organoids at day 360 of differentiation. Top images represent control retinal organoids that remained in a humidified environment at 37 °C with 5% CO_2. Bottom images represent retinal organoids that were kept at RT for 5 days. Day -5 represents the first day of storing organoids at RT, day 0 represents the day that the organoids were transferred to the incubator at 37 °C with 5% CO_2, and day 15 represents the recovery period of the organoids, before their collection, in a humidified environment at 37 °C with 5% CO_2. Scale bars=100 µm. B) The thickness of the neuroepithelial layer across the whole organoid was measured in µm using the ImageJ software. Data are shown as mean ± SEM. 10 organoids were used and analysed per condition. Student's unpaired *t*-test was performed to estimate differences in the neuroepithelial thickness between the control and RT organoids showing no significant differences between the groups (p=0.3713).

The morphology and structure of day 360 retinal organoids were evaluated in detail by immunofluorescence staining, which revealed the presence of all key retinal cell types in control and RT conditions (**Figure 3-4**). The expression of pan PR marker Recoverin was observed at the apical side of the organoids (**Figure 3-4**), while HuC/D positive cells, representing ganglion and amacrine cells, were mainly located in the basal layer of the organoids (**Figure 3-4**). Also, immunostaining for gamma synuclein (SNCG) was also used to identify the putative retinal ganglion cells (**Figure 3-4**). All cone types, long-wavelength, /middle wavelength, and short-wavelength (LW/MW and SW), were also found in both conditions (**Figure 3-4**). Rod PR cells were identified by Rhodopsin at the apical layer of control and RT organoids (**Figure 3-4**). The presence of Müller glial cells was confirmed by Vimentin staining neurofilaments, which extended throughout the retina, and Sox9 staining the nucleus of Müller glial cells (**Figure 3-4**). Bipolar and amacrine cells identified by PKCα and AP2α respectively were also identified in both conditions (**Figure 3-4**). Putative horizontal cells detected with Prox1 antibody were mainly found in the middle layer of the organoids (**Figure 3-4**).

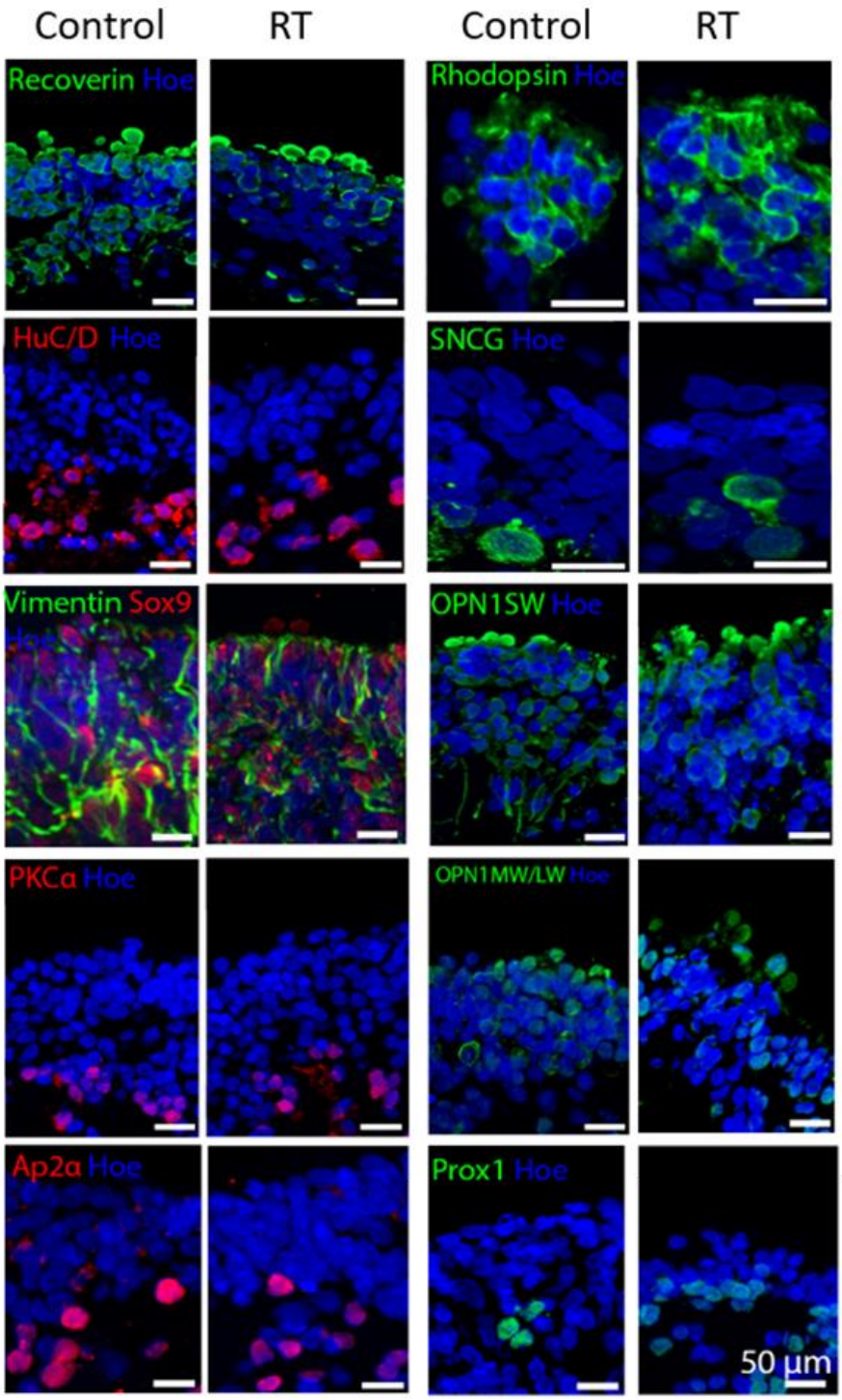

Figure 3-4: Immunofluorescence analysis of retinal markers of control and RT retinal organoids after 15 days of recovery from storage at RT for 5 days. Presence of PRs (Recoverin, green), amacrine and ganglion cells (HuC/D, red), Müller cells (Vimentin – green, Sox9 - red), bipolar cells (PKCα, red), Rod PRs (Rhodopsin, green), ganglion cells (SNCG, green), amacrine cells (AP2α, red), S cone PRs (Opsin SW, green), L/M cone PRs (Opsin MW/LW, green) and horizontal cells (Prox1, green). Nuclei were counterstained with Hoechst (Hoe, blue). Scale bars=50 µm.

To investigate whether storage of retinal organoids for 5 days had an impact on the survival of retinal cells, quantification analysis of retinal cells positive for Recoverin, HuC/D, PKCα, Rhodopsin, SNCG, Opsin MW/LW, AP2α, Prox1, ARL13B, and Opsin SW was performed. The results indicated that there were no significant differences between RT and control organoids (**Figure 3-5**), suggesting that storage of organoids for 5 days at RT did not affect the survival of retinal cells.

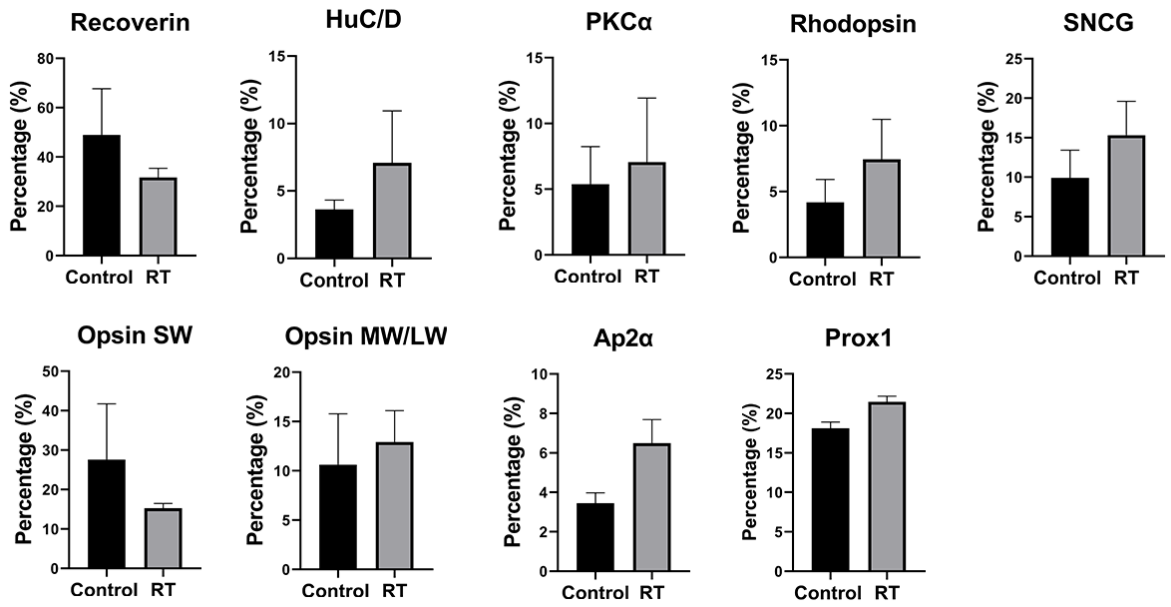

Figure 3-5: Quantification analysis of immunopositive cells in control and RT organoids. Recoverin (p=0.4766), HuC/D (p= 0.3463), PKCα (p= 0.6996), Rhodopsin (p= 0.1608), SNCG (p= 0.1254), AP2α (p= 0.1506), Opsin SW (p= 0.2012), Opsin MW/LW (P = 0.5941) and Prox1 (P = 0.0624), analysis revealed no significant difference in the percentage of immunoreactive-positive cells between control and RT conditions. Data are shown as mean ± SEM, n= 5 representative images per cell marker were quantified per condition.

To further evaluate the survival of hiPSCs derived retinal organoids following storage at RT for 5 days, the number of dead cells in control and RT condition was assessed by Tunel assay as mentioned in section 3.3.3. This method stains with brown colour the necrotic and apoptotic cells. The results revealed no significant differences between the control and RT incubated organoids (**Figure 3-6 A**). Therefore, to confirm the results, quantification analysis of the brown-stained cells was performed, confirming that there were no significant differences between the two groups (**Figure 3-6 B**). These results suggest that storage of retinal organoids for 5 days at RT has no effects on the structure or the morphology of retinal organoids; instead, the morphology of organoids and the number of retinal cells were maintained.

Additionally, ultrastructural analysis of day 360 control and RT organoids was performed by TEM to identify differences between control and RT organoids. The TEM results revealed the presence of developing OS, inner segments (IS), outer limiting-like membrane (OLM), connecting cilia (CC), basal body (bb) and mitochondria (mt) in both conditions (**Figure 3-6 C**), showing no differences between the two groups. In conclusion, these data suggest that retinal organoids can survive at RT for 5 days without affecting the structure or the morphology of organoids or the survival of retinal cells.

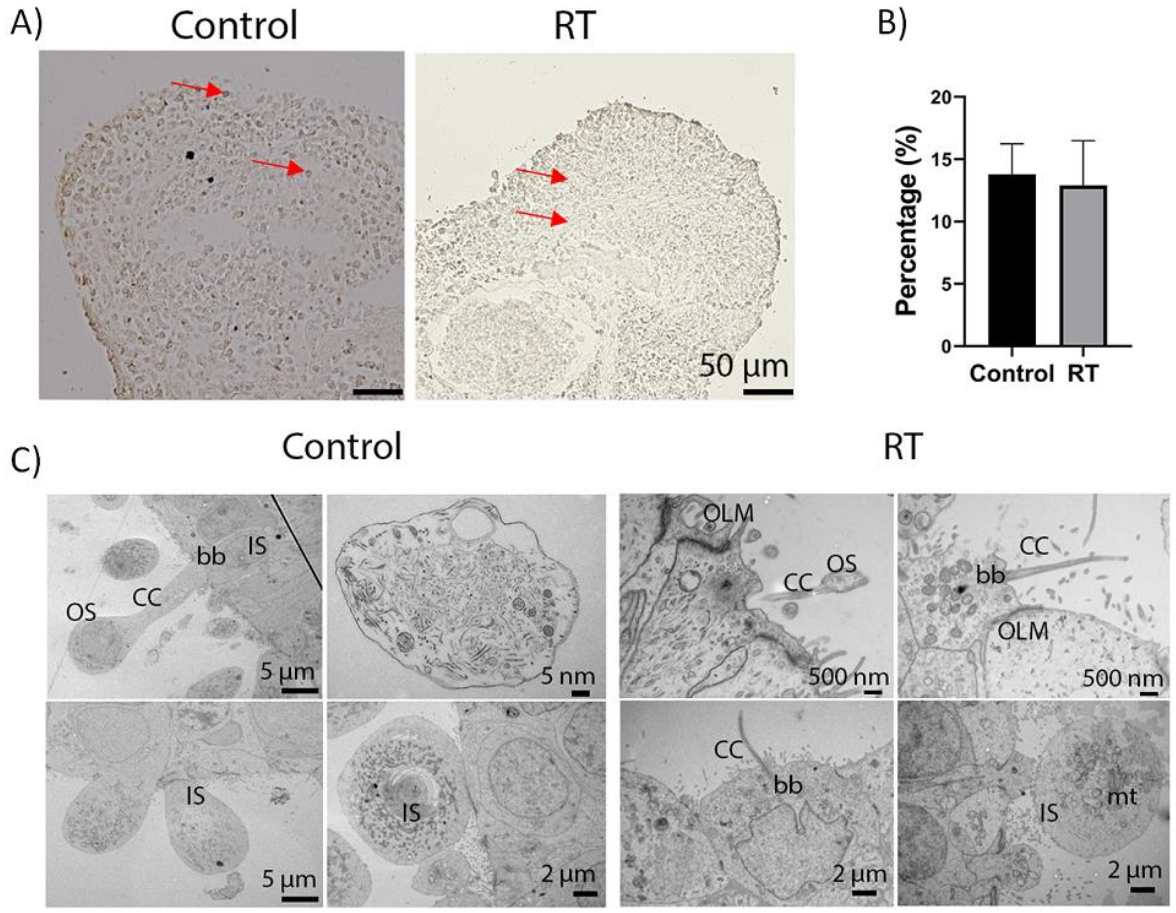

Figure 3-6: Ultrastructural characteristics of WT4 day 360 retinal organoids after storage at RT. A) Bright-field images of apoptotic cells stained with dark brown colour, indicated by red arrows, in control (left image) and RT (right image) condition. Scale bars=50 µm. 10 organoids were used and analysed per condition. B) Quantification analysis of apoptotic cells was performed, showing no significant differences between the two conditions (p= 0.8442). Data are shown as mean ± SEM. 10 images were quantified per condition. C) Ultrastructural analysis of recovered RT and control retinal organoids revealed the presence of outer segments (OS), inner segments (IS) connecting cilium (CC), basal body (bb), outer limiting membrane (OLM), and mitochondria (mt).

3.4.3. Transportation of organoids at RT conditions

Following the successful storage of retinal organoids for 5 days at RT, we investigated whether retinal organoids could be shipped abroad in a controlled environment (**Figure 3-7 A**). Therefore, WT3 retinal organoids aged day 135 and 160 were delivered from our lab in Newcastle to London by car and then shipped to Frankfurt by air at ambient temperature, using temperature control to monitor the temperature of the environment. Following three days, the parcel returned back to the lab via the same route (**Figure 3-7 B & C**). Based on the temperature control that was used, records indicated temperature fluctuations between 23.8 and 18.8˚C (**Figure 3-7 C**). Upon arrival in our laboratory, the organoids were placed in the incubator for 7 days to recover and then collected and compared to the control group, which was maintained in standard culture conditions (at 37°C with 5% CO_2).

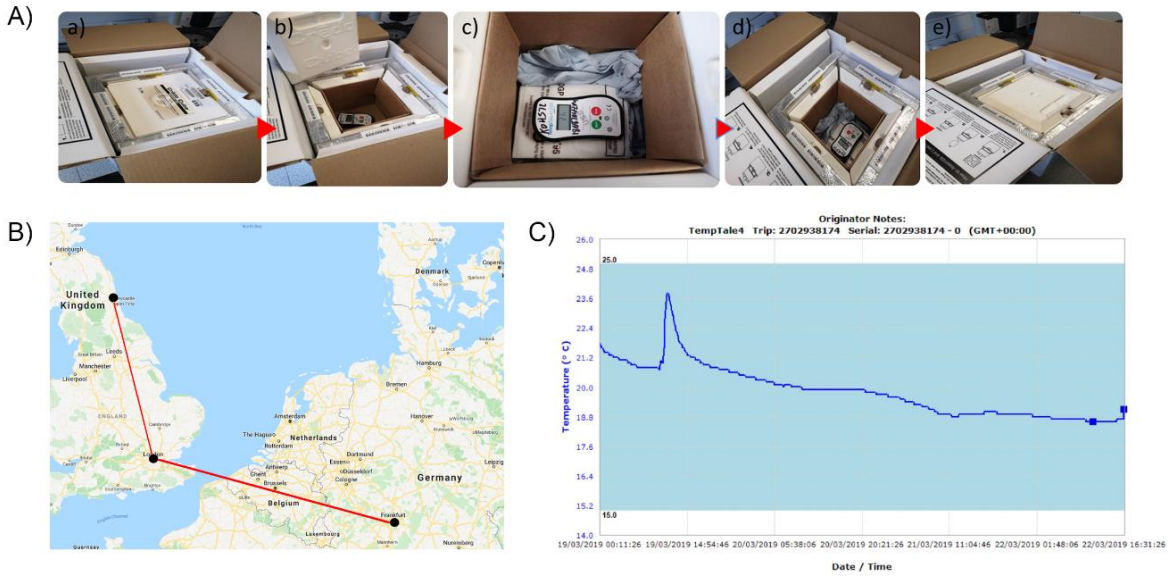

Figure 3-7: Shipment of WT3 retinal organoids. A) Retinal organoids were covered with parafilm to prevent leakage and were further sealed with a plastic bag containing absorbent material and placed horizontally in a special container at RT. Temperature control was activated and placed inside the box according to the manufacturer's instructions to record the temperature throughout the shipping. B) The parcel was delivered by car to London and then by plane to Frankfurt, Germany, at RT at normal CO_2 levels (0.04%). After three days, the parcel returned back to the Biosciences Institute at Newcastle via the same route. C) The graph is a record of temperature changes during the shipping of the organoids.

3.4.3.1. Comparison of control and shipped WT3 organoids at day 135

To assess whether retinal organoids survived after shipping at ambient temperature, bright-field images of day 135 organoids were taken before and after shipment and after 7 days of recovery in the incubator. The overall structure and bright phase neuroepithelium of organoids were

maintained after shipping. Also, the bright phase edges, the structure, the colour, and the size of shipped organoids were retained 7 days post-recovery (**Figure 3-8 A**). To confirm that there were no differences in the thickness of the bright phase neuroepithelium between shipped and control organoids, quantification was performed as descripted in section 3.3.8. The results confirmed our previous observations, indicating no significant differences between day 135 shipped and control organoids (**Figure 3-8 B**).

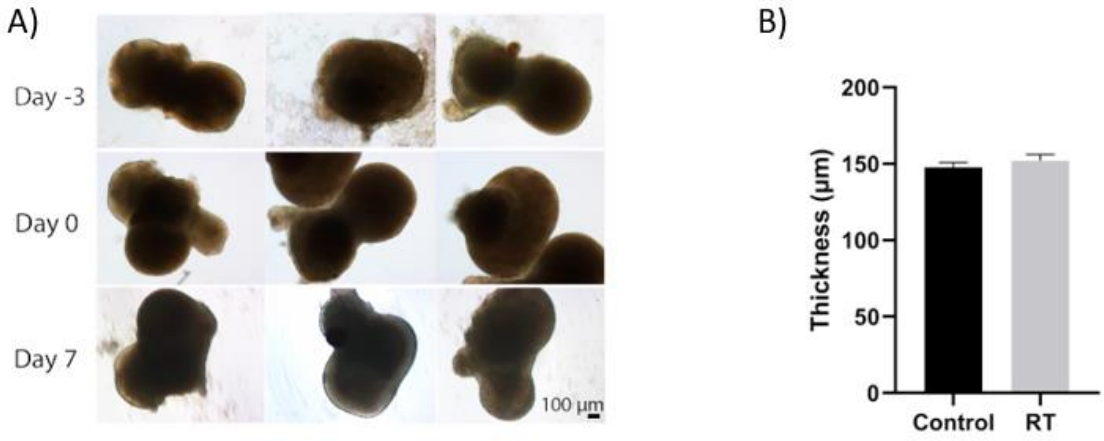

Figure 3-8: Morphological characteristics of WT3 day 135 control and RT shipped retinal organoids before and after shipping. A) Bright-field images of day 135 hiPSCs-derived retinal organoids were captured on day -3 (representing the organoids before shipping), day 0 (arrival of shipped organoids) and day 7 (representing the recovery period of the organoids in a humidified environment at 37 °C with 5% CO_2). Scale bars=100 µm. B) The thickness of the bright phase neuroepithelium of day 135 RT shipped retinal organoids compared to control organoids. Data are shown as mean ± SEM. 10 organoids were used and analysed per condition. Statistical analysis was performed using Student's unpaired *t*-test. No statistically significant differences were observed between the two groups, p=0.4104.

The localisation and presence of retinal cells in day 135 shipped retinal organoids were assessed by IF analysis. To identify maturing retinal cells, a panel of retinal-related markers including Recoverin, HuC/D, SNCG, Rhodopsin, AP2α, ARL13B, Prox1, Vimentin and Sox9 were used. IF results revealed no significant differences in percentage and position of Recoverin positive PR cells between control and shipped organoids (**Figure 3-9 A and B**). Additionally, cells positive for HuC/D, a marker of amacrine and ganglion cells, were present in the centre of the retinal organoids in both conditions (**Figure 3-9 A**). Also, the presence of ganglion cells was detected by the SNCG marker in both conditions (**Figure 3-9 A**). Rod PR cells were identified by Rhodopsin at the apical layer of control and shipped retinal organoids. Horizontal and amacrine cells stained by Prox1 and AP2α respectively were observed in the middle layer or the organoids in both conditions (**Figure 3-9 A)**. ARL13B was detected at the apical side above

PR cell nuclei in both control and shipped organoids, indicating the formation of connecting cilia (**Figure 3-9 A**). The presence of Müller glial cells was confirmed by Vimentin that stains the neurofilaments extended throughout the retina. Sox9 was used to detect the nucleus of Müller glial cells (**Figure 3-9 A**). Subsequently, quantification analysis of retinal markers was performed to assess whether the percentage of retinal cells in control and shipped organoids was similar. Quantification analysis confirmed that there were no significant differences between shipped and control organoids (**Figure 3-9 B**).

Thereafter, the viability of hiPSCs derived shipped retinal organoids was evaluated by Tunel assay as mentioned in section 3.3.3, where the apoptotic and necrotic cells were detected by dark brown colour. Stained sections of control and shipped retinal organoids revealed no differences in the number of dead cells between the two groups (**Figure 3-9 C**). These observations were further confirmed by quantification analysis of brown-stained cells that indicated no significant differences between the two groups (**Figure 3-9 D**). These results suggest that day 135 retinal organoids can retain their structure and morphology following shipment at RT conditions.

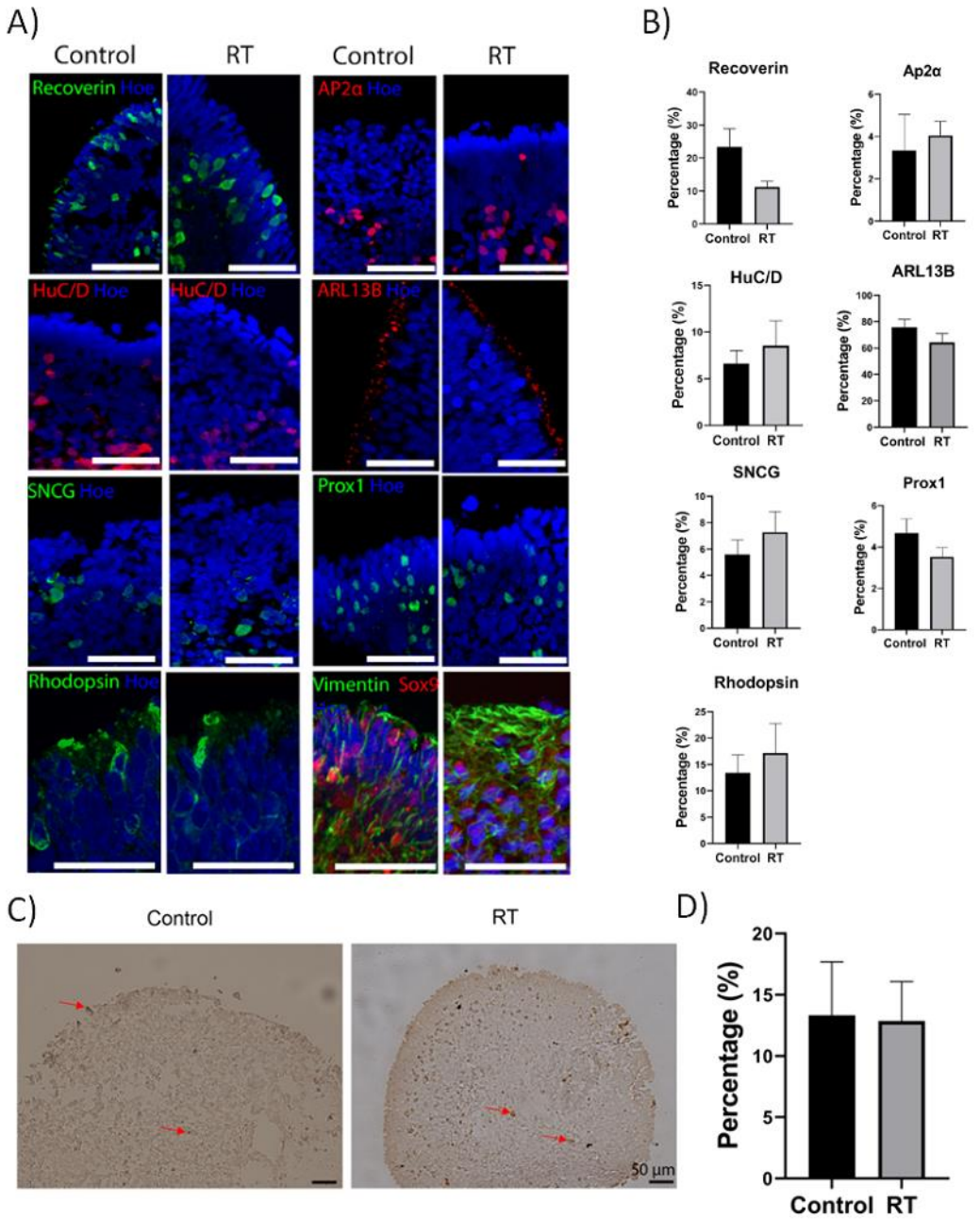

Figure 3-9: Analysis of WT3 day 135 retinal organoids after shipment. A) Expression of retinal markers in both control and shipped retinal organoids revealed the presence of PRs (Recoverin, green), rod PRs (Rhodopsin, green), amacrine cells (AP2α, red), amacrine and ganglion cells (HuC/D, red), ganglion cells (SNCG), connecting cilium (ARL13B red), Müller cells (Vimentin – green, Sox9 – red) and horizontal cells (Prox1, green). Nuclei were counterstained with Hoechst (Hoe, blue). Scale bars=50 µm. B) Quantification graphs of Recoverin ($p= 0.1120$), AP2α ($p= 0.7156$), HuC/D ($p= 0.5570$), ARL13B ($p= 0.2566$), SNCG ($p= 0.4259$), Prox1 ($p= 0.2329$) and Rhodopsin ($p= 0.5804$) revealed no significant differences in the percentage of immunoreactive-positive cells between control and RT shipped organoids. Data are shown as mean ± SEM. 5 representative images per cell marker were quantified per condition. C) Bright-field images of apoptotic and necrotic cells were detected in control (left image) and shipped organoids (right image), stained with dark brown colour, indicated by red arrows. Scale bars=50 µm. 10 organoids were used and analysed per condition. D) No significant differences were observed between control and shipped organoids ($p= 0.9355$). Data are shown as mean ± SEM. 10 images were quantified per condition.

Thereafter, the physiological functionality of day 135 retinal organoids that were shipped and further placed in the incubator for another 45 days (day 180 of organoids' differentiation) was assessed using multielectrode recordings. This experiment was carried out by Dr Birthe Dorgau, as mentioned in section 3.3.9. In both conditions, putative OFF retinal ganglion cells (RGCs) revealed a decrease in their spiking activity after white light pulses (WLP) (**Figure 3-10 A**), indicating no significant differences between the two groups (Figure 68 B; p= 0.77). In the same way, presumed ON RGCs, which increase their spiking activity when exposed to WLP showed no differences between both conditions (**Figure 3-10 B**; p= 0.18). Taken together, these results support that day 135 retinal organoids can retain their structure, morphology and function following shipment at RT conditions.

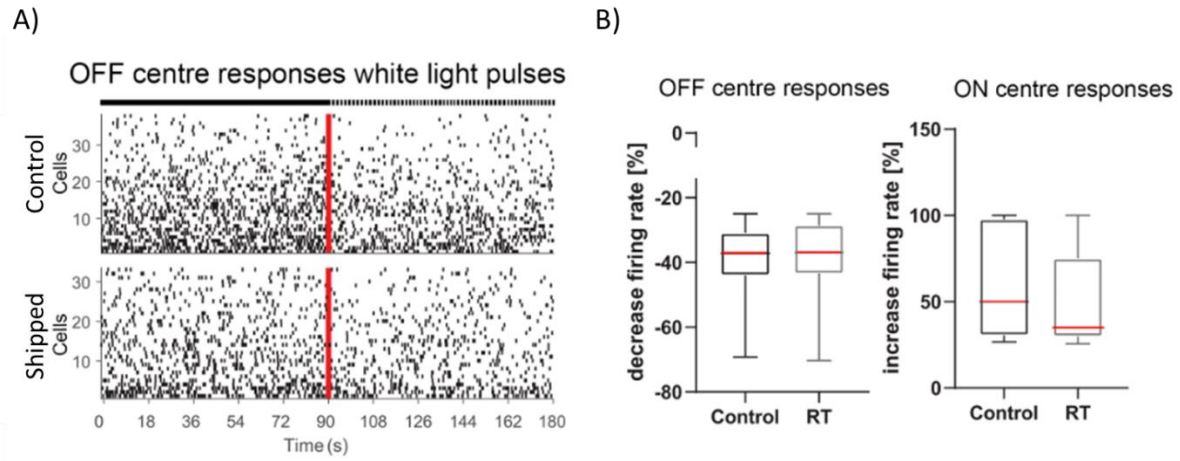

Figure 3-10: Functionality of WT3 day 135 retinal organoids after shipping. A) Spike raster plots (top) and firing rate histogram (bottom) from putative OFF retinal ganglion cells (RGCs) of control and shipped day 135 organoids revealed that their spiking activity decreased after white light pulses (WLP). Each row in the raster plot (y-axis) represents a different RGC, and each vertical bar represents a spike from the corresponding RGC. The red line illustrates the stimulus onset, whereas the left half before indicates the spontaneous activity before WLP exposure and the right half when exposed to WLP. B) Box plot indicates the decreased firing rate (in%) of putative OFF RGCs (top) and ON RGC (bottom) in control and shipped at RT retinal organoids. In both cases, no significant differences were observed (Mann Whitney test; p= 0.77 for OFF RGCs and p= 0.18 for ON RGCs). The box plot shows the median (red line).

3.4.3.2. Comparison of control and shipped WT3 organoids at day 160

To identify whether retinal organoids at advanced differentiation stage would be affected by the shipment at RT conditions, day 160 retinal organoids were shipped to Germany, returned back in our lab 3 days after, and maintained in the incubator to recover for 7 days, as mentioned in section 3.3.2. To assess the morphology and neuroepithelium thickness of day 160 organoids, bright-field images were taken. The results indicated that the morphology and structure of

organoids were preserved after shipment. Also, the size and the colour of shipped organoids were retained after 7-days post-shipment, and the bright phase neuroepithelium was present (**Figure 3-11 A**). Therefore, quantifications analysis of the neuroepithelium thickness between control and shipped organoids was performed, indicating no significant differences between the two groups (**Figure 3-11 B**).

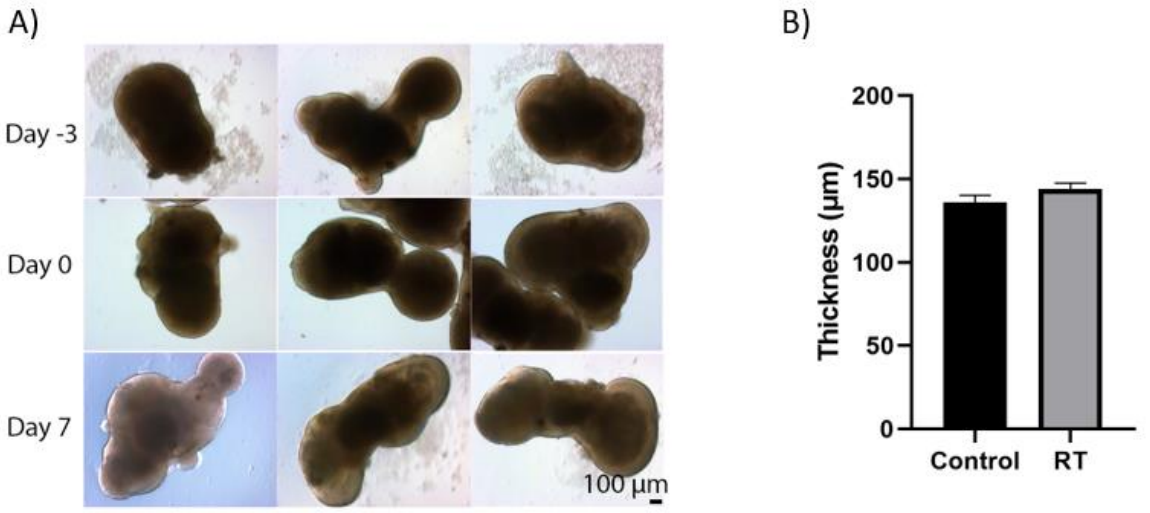

Figure 3-11: Morphological characteristics of WT3 day 160 control and RT shipped retinal organoids after shipping. A) Bright-field images of day 160 hiPSCs-derived retinal organoids were captured on day -3 (representing the organoids before shipping), day 0 (arrival of shipped organoids), and day 7 (representing the recovery period of the organoids in a humidified environment at 37 °C with 5% CO_2). Scale bars=100 µm. B) Measurement of neuroepithelial thickness of day 160 shipped and control organoids. Data are shown as mean ± SEM. 10 organoids were used and analysed per condition. The thickness of the neuroepithelium was measured in µm. Student's unpaired *t*-test was performed to estimate differences in the thickness of the bright phase neuroepithelium between the control and RT organoids, indicating no significant differences between the two groups, p=0.1328.

Therefore, IF analysis was performed to reveal the presence of retinal cells in day 160 shipped organoids. The results revealed the presence of Recoverin positive PR cells in the apical layer in both control and shipped organoids (**Figure 3-12 A**). Additionally, AP2α positive cells were found in the middle layer, indicating the presence of amacrine cells in both conditions (**Figure 3-12 A**). HuC/D and SNCG positive cells were detected in the basal layer of both control and shipped retinal organoids, revealing the presence of ganglion cells (**Figure 3-12 A**). A small percentage of Prox1 positive cells, indicating the presence of horizontal cells, was observed in both shipped and control organoids (**Figure 3-12 A**). Müller glial cells identified by Vimentin and Sox9 were also found to span the length of the control and shipped organoids (**Figure 3-12 A**). ARL13B positive cilia were observed in the apical layer above PR nuclei in both groups,

suggesting the presence of connecting cilia and the beginning of OS formation (**Figure 3-12 A**). The presence of rod PRs was assessed by Rhodopsin in the apical layer in both conditions (**Figure 3-12 A**). To confirm our observations, quantification analysis of retinal-related markers including Recoverin, HuC/D, Rhodopsin, SNCG, AP2α, Prox1, ARL13B, Vimentin and Sox9, was performed, indicating no significant differences in the percentage of positive cells between control and shipped retinal organoids (**Figure 3-12 B**).

To detect the number of apoptotic and necrotic cells in control and shipped organoids, Tunel assay was used, as mentioned in section 3.3.3. The apoptotic and necrotic cells indicated by red arrows showed no significant differences between the two conditions (**Figure 3-12 C**). This was confirmed by quantification analysis of Tunel positive cells (**Figure 3-12 D)**, suggesting that shipment of retinal organoids does not affect their structure or morphology.

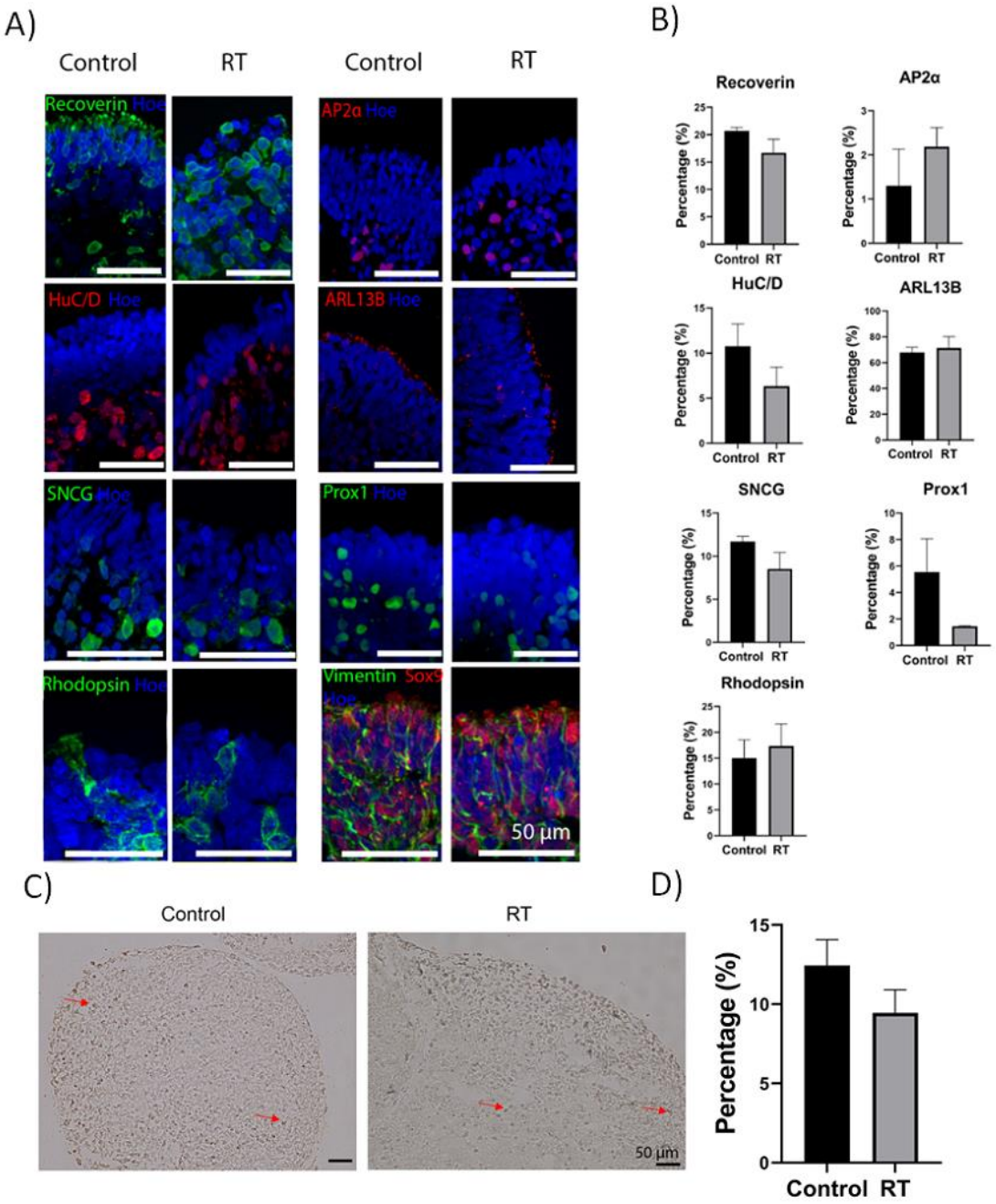

Figure 3-12: Analysis of WT3 day 160 retinal organoids after shipment. A) Expression of retinal marker for PRs (Recoverin, green), amacrine cells (AP2α, red), amacrine and ganglion cells (HuC/D, red), ganglion cells (SNCG, green), connecting cilium (ARL13B red), Müller cells (Vimentin – green, Sox9 - red), Rod PRs (Rhodopsin, green) and horizontal cells (Prox1, green) in control and shipped organoids. Nuclei were counterstained with Hoechst (Hoe, blue). Scale bars=50 µm. B) Quantification of retinal marker protein expression for Recoverin (p= 0.2648) AP2α (p= 0.4005), HuC/D (p= 0.1785), SNCG (p= 0.1594), ARL13B (p= 0.6913), Rhodopsin (p= 0.7023) and Prox1 (p= 0.1785) revealed no significant difference in the percentage of immunoreactive-positive cells between control and shipped organoids. Data are shown as mean ± SEM. 5 representative images per cell marker were quantified per condition. C) Bright-field images illustrate with red arrows the apoptotic and necrotic cells in control (left image) and shipped organoids (right image), stained with dark brown colour. Scale bars=50 µm. 10 organoids were used and analysed per condition. D) No significant differences were observed between control and shipped day 160 organoids (p= 0.1888). Data are shown as mean ± SEM. 10 images were quantified per condition.

Functional assays using multielectrode recordings was performed by Dr Birthe Dorgau at the collaborator's lab (Prof. Evelyne Sernagor) as discussed in section 3.3.9, to assess the physiological function of shipped organoids in response to light stimulation. Following 20 days of incubation after shipping (day 180 of organoids' differentiation), the shipped and control retinal organoids exhibited similar retinal ganglion cells responses. For example, presumed OFF centre RGC responses showed a reduction in their spiking activity in both conditions and putative ON centre RGC responses, which increased their spiking activity after light exposure (**Figure 3-13 A**). There were no significant differences between the control and the shipped group (OFF centre responses: p= 0.56, ON centre responses p= 0.86; **Figure 3-13 B**), which indicates that shipment of day 160 retinal organoids has no effect on their function. Overall, these data suggest that the structure, morphology or function of retinal organoids is not affected by short term storage or shipment.

Thereafter, ultrastructural analysis of control and shipped organoids at day 160 was performed by TEM as mentioned in section 3.3.4. The results revealed the presence of organised PR-like ultrastructural features, including the PR OS, IS, connecting cilium (CC) and outer limiting membrane (OLM) residing in the apical layer of retinal organoids (**Figure 3-13 C**). In addition, basal body (bb) located at the base of connecting cilium and PR IS-rich in mitochondria were observed (**Figure 3-13 C**). These results confirmed the previous findings and indicated no ultrastructural differences between RT and control organoids.

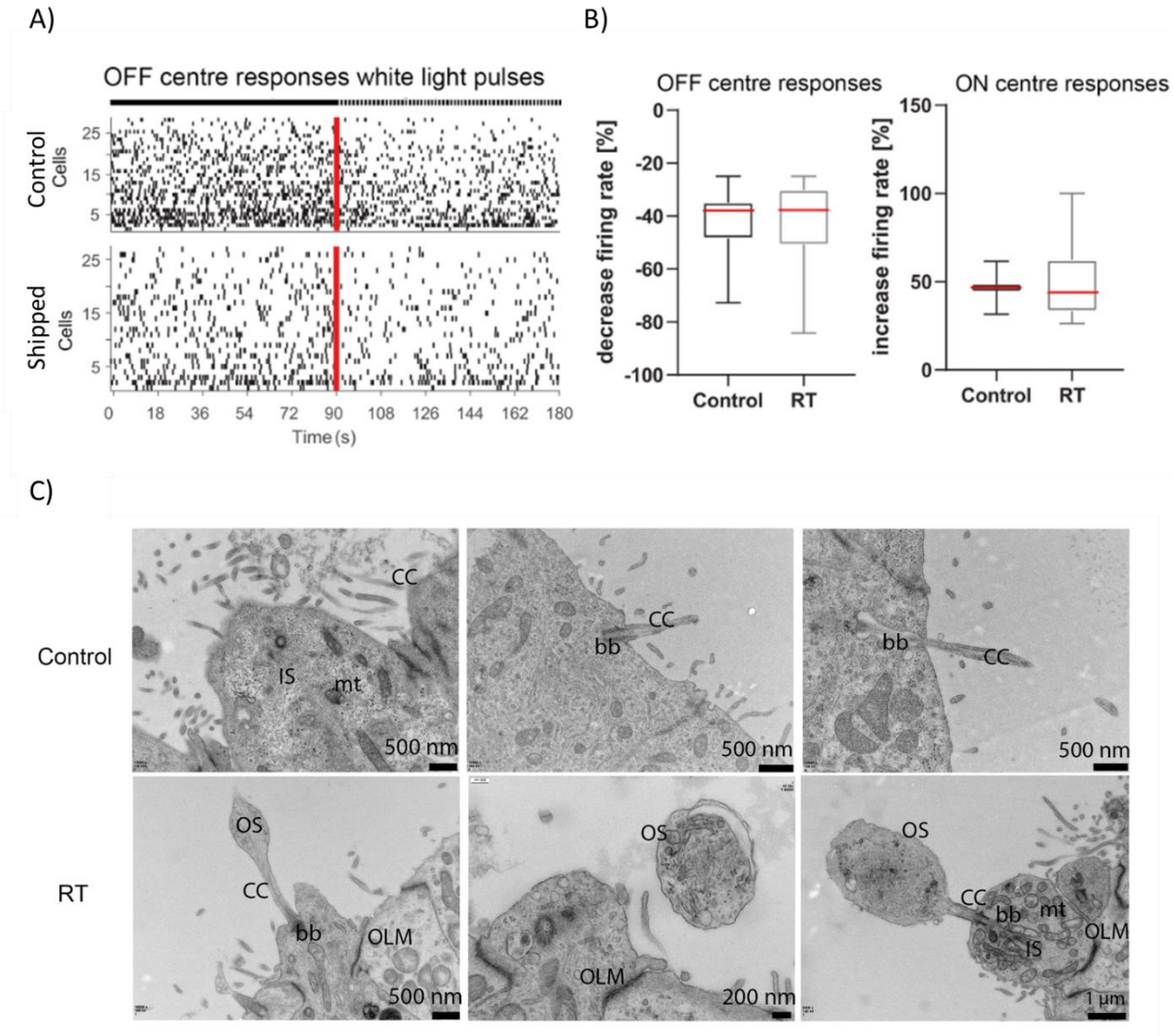

Figure 3-13: Functionality and ultrastructural characteristics of WT3 day 160 retinal organoids after shipping. A) Spike raster plots (top) and firing rate histogram (bottom) from putative OFF RGCs of control and shipment group (day 160) showed a decreased spiking activity after white light pulses (WLP). B) Box plot revealed the decreased firing rate (in%) of putative OFF RGCs (top) and ON RGC (bottom) in control and RT condition. There were no significant differences between both conditions (Mann Whitney test; p= 0.56 for OFF RGCs and p= 0.86 for ON RGCs). The box plot shows the median (red line). (C) Ultrastructural analysis of day 160 retinal organoids revealed the presence of connecting cilium (CC), basal body (bb), outer segments (OS), PRs possessing inner segments (IS), outer limiting membrane (OLM) and mitochondria (mt) in both shipped and control organoids.

3.5. Discussion

In the last decade, improvements in the generation of retinal organoids from hiPSCs have been reported in several key studies (Hallam et al., 2018a, Mellough et al., 2019b, Mellough et al., 2019a, Zhong et al., 2014, Nakano et al., 2012), leading to the generation of 3D aggregates, which resemble the adult retina in terms of cell-type composition and layering and to some extent the electrophysiological function. However, the generation of organoids requires skills and expertise, which may not be available in every lab; thus, validation of most optimal transport conditions which maintain their structure and function is very important for ensuring worldwide applications in drug discovery and cell therapy-based studies.

Shipment of retinal tissue should be performed as quickly as possible at optimal conditions to prevent sample damage. Temperature is a critical factor for the transportation of samples. Several studies have attempted to transport samples (either cryopreserved or live) at variable temperatures and reported the temperature's effects on samples' viability. Any changes in the temperature that can damage the tissue are costly and can delay the project for 3 to 6 months, which is the time needed to differentiate hiPSCs to mature retinal organoids. Additionally, delays in transportation can induce degeneration of the tissue affecting tissue viability. In addition, another critical factor that can influence tissue viability during transportation is the type of containers in which samples are transported. Although many studies have reported the shipping of frozen samples using dry ice, this method has many drawbacks, including the hazardous effects of dry ice and defrosting of samples in case of delays. Additionally, transportation of frozen samples requires thawing, which necessitates expertise to avoid degeneration of tissues due to apoptosis caused by mishandling of the samples. Therefore, other more convenient, low-cost, and fast methods have been used for transporting samples at long distances. Some studies have used special containers that control and maintain the environment at ambient temperature, preventing temperature fluctuations and thus minimising the risk of cell death or functional impairment of tissues. Importantly, maintaining the organoids at RT conditions facilitates a quick recovery period, enabling experiments and tests to be performed quicker, avoiding lost time, structural damage and toxicity effects associated with cryopreservation (Jang et al., 2017).

Recently, Singh and colleagues have reported the development of a new protocol for shipping retinal organoids at 37°C using a battery-driven portable shipping container. This study provides a new method to ship viable retinal tissue over long distances facilitating collaboration between research centres (Singh et al., 2020). However, shipment of retinal tissue at 37°C using a battery-driven portable shipping container to maintain the temperature could induce many

implications. Such containers may be heavy and therefore less cost-effective for shipping purposes. Also, battery failure during transportation may delay results for the next 5-7 months (Singh et al., 2020).

In this study, to facilitate the widespread application of retinal organoids in multiple research centres for drug discovery and cell therapy-based studies, it is important to validate the most optimal transport conditions that will retain retinal organoids' structural and functional characteristics. This study investigated the impact of five-day storage and three-day shipment at RT on retinal organoids. A special container with a temperature tracker was used to observe whether the environment was maintained at ambient temperature, detecting temperature fluctuations throughout shipping. The results of this study indicated that retinal organoids generated from two different hiPSC lines retained their morphology at RT conditions following subsequent recovery period. Moreover, the study confirmed that shipment of retinal organoids at different developmental stages did not affect the structure, morphology, biological activity or physiological function, thus providing an optimal solution for increasing their applications to a large number of labs. These results were peer-reviewed and published (Georgiou et al., 2020). Our findings provide an optimal and cost-effective solution for shipping viable hiPSCS-derive retinal organoids worldwide, facilitating cross-collaboration between research centres and increasing their availability to many research and pharma labs globally.

3.6. Conclusion

In summary, our data indicated that shipment of retinal organoids at RT using a controlled environment container maintained their structural features and biological activity. Therefore, live shipment at RT can provide the method of choice to enable collaboration between laboratories. The organoid recovery time is short and the costs of transportation low, making this an optimal and cost-effective solution for broad application in research and cell-based therapies. This work was published in (Georgiou et al., 2020).

Chapter 4

Chapter 4. Investigating the role of alternative splicing in autosomal dominant retinitis pigmentosa using a PRPF31 patient-specific hiPSC disease model

4.1. Introduction

Retinitis Pigmentosa (RP) is the most common among all inherited retinal disorders causing blindness, with an incidence of 1 in 4000 people and more than 1 million affected individuals worldwide (Hartong et al., 2006). The major pathological events in autosomal dominant RP (adRP) cases are the progressive degeneration of PRs and the loss of retinal pigmented epithelium (RPE) cells (McKie et al., 2001). Remodelling of the retina cells leads to gradual loss of peripheral cells and subsequently constriction of the visual field, causing partial or complete blindness, depending on the severity of the disease (Ferrari et al., 2011).

The high heterogeneity seen in RP patients is associated with the diverse genetic defects related to the disease. In the early 90s, the identification of the first gene involved in adRP, known as *Rhodopsin* (*RHO*), was reported (Dryja et al., 1990). Since then, and every year, new genes associated with non-syndromic RP have been added to the list, with more than 80 genes identified up to date (Verbakel et al., 2018). Most causative genes are retina-specific, meaning that they have a distinct role and/or expression in the retinal and RPE cells (Ferrari et al., 2011). However, other genes, which are expressed in all cell types, have been associated with RP. These include pre-mRNA processing factors (PRPFs) such as PRPF3, PRPF8, PRPF31, PAP1 and SNRN200 (Farkas et al., 2014).

PRPFs are all components of the U4/U6.U5 tri-snRNP complex that constitute the spliceosome, a large macromolecular complex essential for the catalysis of pre-mRNA splicing (Utz et al., 2013). Mutations in *PRPFs* constitute 15% of adRP cases and affect the spliceosome assembly, leading to mis-splicing of genes important for retinal function (Buskin et al., 2018). About 10% of adRP cases are caused by defects in *PRPF31*, an essential component for the assembly and stability of the tri-snRNP (Waseem et al., 2007). This type of RP is known as RP11. Mutations in *PRPF31* have been shown to cause PR degeneration in animal models such as zebrafish and have been linked with RPE disorders causing retinal disease phenotype with no evidence of other symptoms (Yin et al., 2011). However, the mechanisms associating defects in splicing genes and retinal-specific phenotype are still unclear. A possible hypothesis is that defects in splicing factors affect all tissues; however, only retinal cells are affected due to their high demands for mRNA production. An alternative theory supports that splicing defects are associated only with retina-specific transcripts either due to the susceptibility of PR cells to

splicing stress during the renewal of OSs, or due to reduced splicing activity. This theory is associated with our previous findings which showed that mutations in *PRPF31* are associated with retinal-specific spliceosome downregulation which contribute to retinal specific phenotypes (Buskin et al., 2018).

Up to now, several animal and cellular models have been used to understand the effects of *PRPF* mutations in RPE and PR cells. A research study with *PRPF31* mutations in zebrafish models reported the morphological changes in PR cells and diminished transcription of PR-specific genes (Yin et al., 2011), suggesting that the defects in rod PRs are probably a result of the incorrect splicing and reduced transcription of retina-specific transcripts (Yin et al., 2011). Subsequent studies that used transgenic mice with mutations in *PRPF3, PRPF8,* and *PRPF31* indicated reduced phagocytic function of RPE cells (Farkas et al., 2014). These results are consistent with the findings from the Graziotto study (Graziotto et al., 2011), supporting that mutations in RNA splicing factors affect the RPE cells primarily (Farkas et al., 2014).

Using hiPSC-derived retinal cells, Lako's group previously reported the presence of large deposits in the basal side of RP11-RPE cells. Notably, patient-specific RPE cells (but not PR cells or non-retinal cells) were characterised by the presence of mutant PRPF31 protein, suggesting that RPE cells are the most affected cell types (Buskin et al., 2018). Recently, findings by Diaz-Corrales and colleagues have demonstrated the aggregation of mutant PRPF31 protein in the cytoplasm of RPE cells in the *Prpf31*$^{A216P/+}$ mouse model (Valdés-Sánchez et al., 2019) accompanied by the overexpression of HSPA4L chaperone (Valdés-Sánchez et al., 2019). This study supports the hypothesis that chaperones are probably activated and recruited in the cytoplasmic aggregates to rescue the misfolded proteins by correcting and reassembling them (Valdés-Sánchez et al., 2019).

Published evidence indicates that mammalian cells with *PRPF3* mutations are characterised by less soluble proteins that are more prone to aggregation (Comitato et al., 2007). For example, mutations in *PRPF3* affect the localisation of PRPF3 protein itself, leading to the aggregation of misfolded proteins, which trigger the apoptosis of PR cells (Comitato et al., 2007). Additionally, defects in the *Rhodopsin* gene, the most commonly affected gene causing RP, induce its accumulation and aggregation within the cell, prohibiting its translocation to the plasma membrane to form the visual pigment (Surgucheva et al., 2005). These aggregates are ubiquitinated and targeted for degradation by the proteasome (Illing et al., 2002). However, saturation of the proteolytic machinery enhances the accumulation of rhodopsin aggregates (Saliba et al., 2002). Nevertheless, the role of misfolded aggregates in disease pathogenesis and their association with PR cell death has not been fully understood.

Aggregation and accumulation of misfolded proteins is also a common feature of many multiple neurodegenerative diseases (NDs) such as Alzheimer disease (AD), Parkinson disease (PD), Amyotrophic Lateral Sclerosis (ALS), Macular Degeneration, and others (Hyttinen et al., 2014). Aberrant accumulation of self-aggregating proteins intracellularly and extracellularly causes cellular toxicity due to the formation of insoluble non-native aggregates, which disrupt protein homeostasis and eventually lead to cellular dysfunction or cell death (Sweeney et al., 2017). Although protein aggregates differ in protein composition, size and structure in distinct NDs, they share common cytotoxic effects and accumulate progressively over time (Soto and Pritzkow, 2018).

An initial cellular response to misfolded proteins is the activation of molecular chaperone machinery which plays an important role in NDs. Under normal conditions, chaperones protect the cells by stabilising folding intermediates to prevent protein misfolding and aggregation. However, misfolded proteins that cannot reassemble correctly are ubiquitinated and targeted for degradation by the proteolytic degradation machinery. In the case where UPR malfunctions, an intrinsic apoptotic pathway is activated as a secondary response to degrade the accumulated proteins. However, dysregulation of autophagy often leads to protein aggregation diseases (Hyttinen et al., 2014).

In this chapter, PRPF31 patient-specific RPE cells were utilised to better understand disease pathomechanisms. RP caused by PRPF31 mutations is classified as RP11, thus all patient cell lines for this chapter are named as RP11 followed by ‘S’ for Severe and ‘VS’ for Very Severe clinical phenotype.

4.2. Aims

The aim of this chapter was to identify the disease mechanisms causing PRPF31-RP. The specific aims were:

- Differentiate hiPSC from patients with *PRPF31* mutations and unaffected controls to RPE cells.
- Investigate the impact of *PRPF31* mutations on the proteome of RPE cells using mass spectrometry.
- Select key candidates and validate their expression and location using Western Blot and IF analysis.
- Integrate the information to discover the mechanism of PRPF31-RP.

4.3. Materials and Methods

4.3.1. Human cell lines

All samples used in this study were obtained with informed consent according to the protocols approved by Yorkshire and the Humber Research Ethics Committee (REC ref. no. 03/362). PRPF31-hiPSC lines used in this study were derived from three patients with severe (RP11S1, RP11S3) and very severe (RP11VS) phenotypes as described in our earlier work (Buskin et al., 2018). RP11VS and RP11S1 cell lines harbour the same *PRPF31* mutation (c.1115_1125 del11) but vary in the severity of the disease, and RP11S3 harbours a different mutation (c.522_527+10del). CRISPR/Cas9 corrected (Cas9-RP11VS) and unaffected cell line (WT1) were used as controls (Buskin et al., 2018).

4.3.2. Culture of hiPSCs

hiPSCs from patient cell lines harbouring *PRPF31* mutation, control, and isogenic control cell lines were cultured on 6-well plates pre-coated with matrigel (Corning, 354230), using mTeSR™1 (StemCell Technologies, 05850) media supplemented with 1% penicillin/streptomycin (P/S) (Gibco, 15140). Media changes were performed on a daily basis. Every 4-5 days, when hiPSCs reached approximately 80% confluency, they were passaged using Versene (EDTA 0.02%) (Lonza, BE17-771E) solution for 3-5 minutes at 37°C. The hiPSCs were split at a ratio of 1:6 and transferred to a new matrigel coated plate. All cultures were maintained at 37°C, in a humidified environment, with 5% CO_2. Freezing of the hiPSCs was performed using freezing media containing 90% Fetal Bovine Serum (Gibco, 10270), 10% Dimethyl Sulfoxide (DMSO) (Sigma D2650), and 10 µM ROCK inhibitor (Y-27632, Chemdea, CD0141).

4.3.3. Directed RPE Differentiation

Differentiation of hiPSCs to RPE cells was performed as described by Regent and colleagues (Regent et al., 2019). Briefly, control and patient-derived hiPSCs were cultured on Matrigel-coated 6-well plates using mTeSR™1 media. When 80-95% confluency was reached, mTeSR™1 media was replaced with 2 ml of differentiation medium containing Dulbecco's modified Eagle's medium (high glucose, Thermo Fisher Scientific) supplemented with 55 µM β-mercaptoethanol, 1% minimum essential medium–nonessential amino acids (MEM-NEA, Thermo Fisher Scientific), and 20% of knockout serum replacement (KOSR). The day of

adding the differentiation media in the cells was defined as 'day 0' of differentiation (**Figure 4-1)**. The basal differentiation medium was supplemented with additional small molecules at specific time points. Between day 0-7, cells were supplemented with 10 mM of Nicotinamide (Sigma) (**Figure 4-1**). Subsequently, from day 7 to day 14, Nicotinamide was replaced with 100 ng/ml Activin A. Thereafter, Nicotinamide was substituted with 3 µM CHIR99021 (Sigma, SML1046) from day 14 to 42 (**Figure 4-1**). From day 42 onwards until harvesting of the RPE patches, the cells were fed three times a week with a differentiation medium containing DMEM (High Glucose), 50 µM β-mercaptoethanol, 1 x MEM NEAA and 4% KOS. RPE patches were mechanically collected between day 90 and 120 using a scalpel. The collected RPE patches were dissociated in TrypLE (10×) (Invitrogen, USA) for 20 minutes at 37°C. The RPE cells were sieved using a 40 µm cell strainer and re-plated at 1.5×10^5 and 150.000 cells on 12-well plates or on 24-well transwell inserts (GreinerBioOne, 662641), respectively. Half-medium changes were performed 3 times a week until RPE cells became confluent and formed a pigmented monolayer.

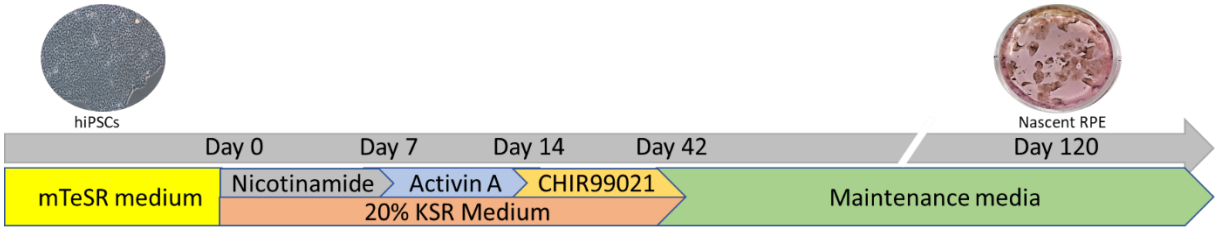

Figure 4-1: Differentiation of hiPSCs to RPE cells.

4.3.4. Assessment of RPE maturity

4.3.4.1. Pigmentation and Cellular morphology

Maturation of RPE cells has been evaluated based on qualitative criteria, such as cellular morphology and pigmentation (Al-Ani et al., 2020), and quantitative methods, such as transepithelial resistance (TER).

4.3.4.2. Measurement of transepithelial resistance (TER)

TER is a measurement of RPE maturity, measuring the transepithelial resistance or barrier function of RPE cells. The TER values were measured from 24 transwell inserts using a Millicell ERS-2 Voltohmmeter (Millipore, MERS00002), which contains two electrodes, a short electrode and a long electrode. Before measuring the resistance in transwells containing

RPE cells, the resistance of a blank TW containing PBS (Gibco, 14190) was measured by inserting the tip of the short electrode in the inner side of the transwell insert, and the tip of the longer electrode in the outer side of the transwell insert. Three measurements were obtained from each transwell insert. After that, the readings from the blank transwells were subtracted from the readings obtained from transwells containing RPE cells. Based on the formula Unit area resistance = Resistance (Ω) x Effective Membrane Area (cm2), the results were multiplied by 0.3, which is the membrane area of a transwell, and final values were given in ohms (Ω). TER measurements were performed one day after feeding the RPE cells to avoid variability in the TER readings.

4.3.5. Protein extraction

RPE cells from wild type hiPSCs, patient-specific RP11-hiPSCs (RP11S1, RP11VS, RP11S3) and CRISPR/Cas9 isogeneic control (Cas9-RP11VS) were plated on 12-well plates until they were fully confluent and pigmented before their collection. RPE cells from all the cells lines were collected at passage 3 for consistency. For the collection, RPE cells were washed with PBS and then were collected using a cell scraper. The cells were centrifuged at 1000 x g for 3 minutes and processed immediately. RPE cells were incubated with a lysis buffer (40 mM HEPES-NaOH, 150 mM NaCl, 0.5 mM DTT, 1% Triton X-100, 1 PhosStop tablet (phosphatase inhibitor) per 10 ml, 1 complete ULTRA tablet (EDTA-free protease inhibitor)), for 20 minutes on ice. Following centrifugation at 1000 x g for 20 minutes at 4ºC, the supernatant was collected and transferred to a fresh Eppendorf tube which was processed immediately or stored at -80 ºC.

4.3.6. Isolation of insoluble fractions in RPE cells

RPE cells from control and RP11 patients were washed with PBS and collected using a cell scraper. Cell pellets were lysed using lysis buffer containing 10 mM Tris-HCL (Sigma, 1185-53-1), pH 7.5, 5 mM EDTA, 1% NP-40 (Sigma, 127087-87-0), 0.5% deoxycholate, 150 mM NaCl (Sigma, 7647-14-5) and 1 complete ULTRA tablet (EDTA – free protease inhibitor) (Sigma, 06 538 282 001). The lysates were incubated on ice for 15 minutes, followed by vortexing at 4˚C for 15 minutes. Thereafter, the lysates were sonicated for three 5-seconds intervals to prevent heating of the samples. Following centrifugation for 15 minutes at 13,000 x g, the supernatant was transferred in a fresh tube and labelled as the soluble fraction. The remaining pellets were mixed with 20 µl of a lysis buffer (60 mM Tris-HCL (Sigma,

10812846001) pH 7,2% SDS and 2.5% 2-Mercaptoethanol (Sigma, 60-24-2), and sonicated on ice for 15 minutes with 2-second intervals. The samples were centrifuged at 16,000 x g for 20 minutes at 4˚C, and the collected supernatant was labelled as the insoluble fraction.

4.3.7. Quantification of protein concentration

Protein quantification of RPE lysates was performed using a Pierce BCA assay kit (Pierce, ThermoFisher Scientific) following the manufacturer's instructions. Following 30 minutes of incubation at 37ºC, colourimetric readings were recorded by measuring absorbance at 562 nm using a Varioskan LUX multimode Microplate reader (ThermoFisher Scientific). A linear standard curve to estimate protein concentration was performed based on the colourimetric readings of the standards used.

4.3.8. Protein separation by gel electrophoresis

Following protein quantification, protein samples were reduced and denatured using a loading buffer containing 4x lithium dodecyl sulphate (LDS) sample buffer, reducing agents (NuPAGE, ThermoFisher Scientific) and distilled H_2O, followed by heating of the samples for 5 minutes at 95°C. Subsequently, the samples were cooled on ice for 10 minutes. Protein separation was performed by loading 20 µl of the protein mixture onto each well of the polyacrylamide gel electrophoresis (NuPAGE, 4 to 12% Bis-Tris 1.0-mm mini gel, NP0322BOX, ThermoFisher Scientific), which was inserted in an electrophoresis chamber. Alongside with protein samples, 5 µl of a molecular weight protein marker (26619, PageRuler Plus prestained protein ladder 250µl, ThermoFisher Scientific) was loaded. Running buffer, either MOPS (3-(N-morpholino)propanesulfonic acid) for high molecular weight proteins, or MES (2-(N-morpholino)ethanesulfonic acid), for low molecular weight proteins, were used to run the gels. Gels were run at 200 V until proteins were fully separated.

4.3.9. Western Blotting

Following separation of the proteins by SDS-PAGE, proteins were transferred into a polyvinylidene difluoride (PVDF) membrane using an iBlot2 system (IB24002, ThermoFisher Scientific). The transfer was performed by inserting the gel containing the resolved proteins between two stacks of a copper-coated electrode and on top of the pre-activated PVDF transfer

membrane. The transfer was performed at 200 V for 7 minutes. The PVDF membranes were stained by Ponceau S (Sigma-Aldrich) for approximately 3 minutes followed by three 5 minutes washes with distilled H_2O and were then exposed to a photographic film to detect whether the transfer of the proteins was successful. Ponceau staining was washed using tris-buffered saline (TBS) solution substituted with 0.05% Tween (TBS-T). The PVDF membranes were blocked with 5% non-fat milk in TBS-T for one hour at RT. Thereafter, the membranes were incubated overnight at 4°C with primary antibodies (**Table 4-1**) in 5% milk with TBS-T. Following washes of the membranes with TBS-T three times for 5 minutes each, the membranes were incubated with the appropriate HRP-conjugated secondary antibodies (**Table 4-2**) for 1 hour at RT. Thereafter, the membranes were washed three times with TBS-T for 5 minutes each. Protein bands were detected using SuperSignal West Pico PLUS Chemiluminescent Substrate (ThermoFisher, 34578), and the signal was developed using Amersham Imager 600, where bands were visualised and analysed (**Figure 4-2**).

4.3.10. Immunofluorescence (IF) analysis of RPE cells

hiPSC-derived RPE cells grown on 24-well PET hanging cell culture inserts (Merck) (pore size 0.4 μm) were fixed with 4% paraformaldehyde (PFA) (Sigma, 47608) for 20 minutes at RT. Before blocking, the pigmentation of RPE cells was removed using Melanin Bleach Kit (Polysciences), followed by 3 washes with PBS. RPE cells were blocked for 1 hour at RT in PBS supplemented with 10% donkey serum and 0.3% Triton-X100 (Sigma, T8787) to permeabilise the cells. For p62 and LC3, methanol fixation was used instead, and no bleaching prior to immunostaining was carried out. The RPE cells were incubated with primary antibodies (**Table 4-1**) overnight at 4°C. Following three washes with PBS, RPE cells were incubated with secondary antibodies (**Table 4-2**) diluted in antibody dilution buffer (PBS, 1% donkey serum, and 0.1% Triton X-100) and stored overnight at 4°C. Nuclei were stained with Hoechst (Life Technologies, UK). Then, RPE cells were mounted with Vectashield and sealed with a coverslip. The RPE cells were stored at 4°C until microscopic analysis using the Axio Imager upright microscope.

4.3.11. Image acquisition and analysis

Fluorescent images of RPE cells were captured using the Axio Imager upright microscope with Apotome structured illumination fluorescence (Zeiss, Germany). Fluorescent filters were used to cover multiple dyes such as Hoechst, FITC, Alexa 488, Alexa 546 and Alexa 647. Using 20x

objective, 40x and 63x oil objectives, hiPSC-derived RPE cells were analyzed. Approximately five to six representative images were taken per condition for each sample. Images were presented as a MIP, and brightness and contrast were adjusted using Adobe Photoshop (Adobe Systems).

Table 4-1: List of primary antibodies

Antibody	Host	Source	Cat. No.	Dilution
ACTB	Mouse	Santa Cruz Biotechnology	sc-47778	WB: 1:500
ATG5	Rabbit	Sigma-Aldrich	A0856	WB: 1:500
Beclin 1	Rabbit	Abcame	ab210498	WB: 1:500
Caspase-3	Rabbit	Cell Signaling Technology	9661S	IF: 1:400
FK1	Mouse	Enzo Life Sciences	PW8805	IF: 1:500 WB: 1:500
Fus	Rabbit	Proteintech	11570-1-AP	IF: 1:50 WB: 1:500
GAPDH	Mouse	Santa Cruz Biotechnology	sc-47724	WB: 1:500
HSPA2	Mouse	Antibodies-online GmbH	ABIN561382	IF: 1:100 WB: 1:500
HSPA4L	Rabbit	Novus Biologicals	NBP2-48700	IF: 1:250 WB: 1:500
HSPB1	Mouse	Insight Biotechnology	OASG03654	IF: 1:250 WB: 1:500
LC3B	Rabbit	Cell Signaling Technology	3868S	IF: 1:500 WB: 1:500
MAP1LC3B	Rabbit	Cell Signaling Technology	3868S	IF: 1:200 WB: 1:500
p62	Mouse	BD Biosciences	610832	IF: 1:200 WB: 1:500
PRPF31	Goat	Sigma	SAB2500828	IF: 1:250 WB: 1:500
p-S6 (Ser235/236)	Rabbit	Cell Signaling Technology	4858S	WB: 1:500
20S proteasome α/β subunits	Rabbit	Enzo Life Sciences	BML-PW8155-0025	WB: 1:1000
RLBP1	Mouse	Abcam	ab15051	IF: 1:100 WB: 1:500
S6	Rabbit	Cell Signaling Technology	2217S	WB: 1:1000
ZO1	Goat	St John's Laboratory	STJ140055	IF: 1:50
ZO1	Rabbit	Invitrogen	61-7300	IF: 1:50
ZO1	Mouse	Thermo Scientific	33-9100	IF: 1:50

Table 4-2: List of secondary antibodies

Antibody	Source	Cat. No.	Dilution
Donkey anti-Goat Alexa 488	Life Technologies	A11055	1:800
Donkey anti-Goat Alexa 647	ThermoFisher	A21447	1:800
Donkey anti -Mouse FITC	Jackson ImmunoResearch	715-095-151-JIR	1:800
Donkey anti-Mouse Alexa 488	Life Technologies	A21202	1:800
Donkey anti-Rabbit Alexa 546	Life Technologies	A10040	1:800
Donkey anti-Mouse Alexa 488	Life Technologies	A21202	1:800
Donkey anti-Rabbit Alexa 546	Life Technologies	A10040	1:800
Polyclonal Swine Anti-Rabbit Immunoglobulins/HRP,	Agilent Dako	P0399	1:2000
Rabbit Anti-Mouse Immunoglobulins/HRP	Agilent Dako	P0260	1:2000
Polyclonal Rabbit Anti-Goat Immunoglobulins/HRP	Agilent Dako	P0449	1:2000

4.3.12. Proteasome Activity Assay

RPE cells from control and patient cell lines were washed with PBS and collected using a cell scraper. Pellets were resuspended in lysis buffer containing 0.5% NP-40 supplemented in distilled H_2O and incubated on ice for 30 minutes, followed by centrifugation at 13,000 x g for 20 minutes at 4°C. To measure the protein concentration, the supernatant was collected and analysed by Pierce BCA Protein Assay kit (Pierce, ThermoFisher Scientific). Proteasome substrate Bz‐VGR‐AMC (BW9375, Biomol International) was used to measure the trypsin-like activity of the proteasome. As a control, a proteasome inhibitor, MG132, was used. The trypsin-like activity was measured at excitation/emission wavelength of 360 nm/460 nm, respectively, using a Varioskan LUX multimode Microplate reader (**Figure 4-2**) (ThermoFisher Scientific).

4.3.13. Transmission electron microscopy (TEM)

Transwell inserts of RPE cells were washed with PBS and then fixed with 2% glutaraldehyde in 0.1 M sodium cacodylate buffer. The samples were processed at the Newcastle University electron microscopy facility, where they were further fixed in 1% osmium tetroxide, dehydrated in gradient acetone, and embedded in epoxy resin. Sections of 70 nm thickness were picked up on coper grids, stained with uranyl acetate and lead citrate and imaged using a Philips CM100 transmission electron microscope with high-resolution digital image capture (**Figure 4-2**).

4.3.14. Phagocytosis assay to assess functionality of RPE cells

Bovine rod POSs (InVisionBioResources, 98740) were centrifuged at 2600 × g for 4 minutes, and the pellet was resuspended with 0.4 mg/ml FITC (Sigma, F7250) for 1 hour at RT followed by agitation in the dark. Following centrifugation at 2600 × g for 4 minutes and washing of the POSs three times with PBS (Gibco, 14190), POSs were resuspended in AdRPMI 1640 (12633, Gibco) media supplemented with B-27 Supplement (Gibco, 17504) and FBS (Gibco, 10270). The staining of POSs was confirmed under a Bioscience Axiovert microscope. RPE cells were treated with unlabeled and FITC-labelled POSs (20 POSs per cell) and incubated for 4 hours at 37°C. However, as a control, RPE cells were treated with FITC-labeled POSs but were incubated at 4°C for 4 hours. Both control and RP11-RPE cells were washed with PBS and were detached from the wells using 200 µl of TrypLE Express (Gibco, 12604013) for 15 minutes. Then, control and RP11-RPE cells were resuspended in flow buffer (PBS with 2% FBS) and were transferred into Eppendorf tubes followed by centrifugation at 300 × g. To distinguish cells from debris and unbound POSs, RPE cells were incubated with 5 mM DRAQ5 (Biostatus, DR50200; 1:200) for 5 minutes. Also, to quench fluorescence from unbound POSs, cells were incubated with 0.2% trypan blue solution (Sigma, T8154) for 10 minutes. RPE cells were washed 3 times with PBS, and cell pellets were resuspended in flow buffer. Samples were run on a LSRII flow cytometer, and 10,000 events were collected per sample. Results were analyzed using FacsDiva software (**Figure 4-2**).

4.3.15. Evaluation of cytoplasmic aggregates in RP11 and control RPE cells after feeding with POSs.

Monolayers of control and RP11-RPE cells were cooled for 30 minutes at 17°C and were incubated with unlabeled POSs or FITC-labelled POSs (20 POSs /cells) for another 30 minutes at 17°C. Cooling at 17°C was performed to maximize the binding of POSs in RPE cells. Then, media and unbound POSs were aspirated and replaced with fresh warmed media. RPE cells were kept in a humidified incubator at 37°C with 5% CO_2. RPE cells were collected at 0, 48, 96 and 144 hours post-POSs feeding. The RPE cells were washed with PBS twice and then fixed with 4% PFA before immunofluorescence analysis.

4.3.16. Drug treatments

RPE cells were treated with Rapamycin, Trehalose, Arimoclomol, Salubrinal and STF-083010, of which final concentrations were prepared using the appropriate diluent (**Table 4-3**). RPE cells were treated for 7-days with daily media changes containing freshly added drugs. The drug concentrations were adopted from previous published studies (**Table 4-3**).

Table 4-3: Drug treatments of RPE cells.

Drug	**Final Concentration**	**Drug concentrations adopted from the following studies**	**Diluent**	**Company**	**Cat. number**
Rapamycin	500 nM	(Cerniauskas et al., 2020)	DMSO	InvivoGen	53123-88-9
Trehalose	50 mM	(Abokyi et al., 2020)	diH_2O	Sigma Aldrich	90210
Arimoclomol	1 µM	(Parfitt et al., 2014)	DMSO	Carbosynth	FA159627
Salubrinal	25 µM	(Matsuoka and Komoike, 2015)	DMSO	Sigma Aldrich	SML0951-5MG
STF-083010	50 µM	(Barez et al., 2020)	DMSO	Sigma Aldrich	SML0409-5MG

4.3.17. Statistical analysis

Statistical analysis was performed using Prism (GraphPad, USA). Comparisons between variables and statistical significance between groups were performed using ANOVA or Two-tailed Student's *t*-test. Error bars represent the standard error of the mean (± SEM) unless indicated otherwise. Statistical significance was established as indicated by asterisks *P< 0.05, **P<0.01, *** P<0.001, and **** P<0.0001.

4.3.18. Proteomic analysis

To prepare cell lysates, 1 million RPE cells per cell line were used according to the protocol described from Pierce Mass Spec Sample Prep Kit (Thermo Scientific). Protein samples from each cell line were digested using trypsin overnight at 37 °C, following sonication of the lysates using Covaris S220 ultrasonicator (Covaris). Using the Pierce BCA protein assay kit, protein concentration was measured, and 100 µg of the total proteins from patient and control cell lines were labelled with tandem mass tag (TMT)-isotopes using TMTduplex Isobaric Mass Tagging

Kit (Thermo Scientific). Analysis of the labelled peptides was performed in triplicates using an Orbitrap Fusion or a Q Exactive HF-X mass spectrometer. On the orbitrap fusion, from a survey MS1 scan the most intense precursors in the m-z range of 400-1200 Th, with 2-7 charge state were selected for MS2 fragmentation. Then from MS2 scan, up to 10 top resulting fragments were collected for MS3 subsequent analysis, which was performed using HCD fragmentation and detected in orbitrap with 30.000 resolution. However, for samples measured on the Q Exactive HF-X, the 20 most intense precursors in the m/z range of 350–1600 Th were selected for MS2 fragmentation. MS2 spectra were acquired in Orbitrap with a resolution of 15,000. This work was performed by our collaborator Dr Sina Mozzafari-Jovin (Max-Planck Institute of Biophysical Chemistry, Göttingen, Germany).

4.3.19. TMT labelling for mass spectrometry

Total cell lysates were prepared from RP11 and control RPE cells using Pierce Mass Spec Sample Prep Kit (Thermo Scientific) (**Figure 4-2**). Lysates were diluted and sonicated. Protein concentrations were determined using the Pierce BCA protein assay kit (Thermo Scientific), and 100 µg of the total proteins from each cell line were labelled with 6-plex isobaric tandem mass tag (TMT6) reagents (Thermo Scientific) following the manufacturer's instruction. To this end, samples were reduced by the addition of tris(2-carboxyethyl)phosphine, alkylated with iodoacetamide and acetone precipitated. Protein pellets were resuspended in 50 mM triethyl ammonium bicarbonate (TEAB) buffer and were digested with trypsin overnight at 37°C. Patient RPE cell lines, RP11S1, RP11VS, RP11S3, were labelled with TMT6-127, TMT6-128 and TMT6-129 reagents, respectively, and control WT1 samples were labelled with TMT6-126 reagent. Proteomics data from RP11VS and Cas9-RP11VS RPE cells obtained in our early study were also included for analysis (Buskin et al., 2018). Reactions were quenched by 5% hydroxylamine for 15 minutes. Fifty micrograms of TMT-labelled peptides from RP11 and control cells were combined and cleaned up using C18 spin columns (Harvard Apparatus), dried by SpeedVac (Eppendorf) and subjected to peptide pre-fractionation using high-pH reversed-phase chromatography. After constituting the dried, TMT-labelled peptides in 100 µl buffer A (10 mM NH4OH), fifty microliters of peptide mixtures were injected into an XBridge BEH C18 HPLC column (150mm × 1 mm ID, 3.5 µm; Waters) and separated in 80 fractions using a gradient of buffer B (10 mM NH4OH, 80% acetonitrile) over 90 min. Collected fractions were combined into 20 fractions, dried and resuspended in 20 µl of 0.1% trifluoroacetic acid (TFA) for mass spectrometry analysis. This work was performed by our collaborator Dr Sina Mozzafari-Jovin.

4.3.20. LC/MS/MS analysis

Peptides in each fraction were analysed in three replicates using either an Orbitrap Fusion or a Q Exactive HF-X mass spectrometer (Thermo Fisher Scientific), both coupled with an UltiMate 3000 RSLCnano HPLC system (Thermo Fisher Scientific), as previously described (Buskin et al., 2018). This work was performed by our collaborator Dr Sina Mozzafari-Jovin.

4.3.21. Data processing

MS/MS spectra were searched against a Swiss-Prot human database containing 20,341 reviewed protein entries using Mascot algorithm (Matrix Science) via Proteome Discoverer 2.2 (PD, Thermo Fisher Scientific) and were processed as previously described (Buskin et al., 2018). At least two quantifiable unique peptides in each replicate were required for protein quantification. Protein ratios were log-transformed and then median normalised in Perseus. These data were combined with our previous proteomic data from RP11VS and its Cas9-corrected isogenic control (Buskin et al., 2018). The reported RP11/control ratios are the average of at least two replicates. To identify the differentially expressed (DE) proteins, those proteins with mean a log2 fold change (LFC) less than −0.5 or greater than +0.5 were defined as regulated. Gene Ontology (GO) enrichment analyses were carried out by Metascape (p-value cut-off 0.02) (Zhou et al., 2019) or by the Perseus software version 1.6.2.2 with a Benjamin–Hochberg FDR 2% (Tyanova et al., 2016).

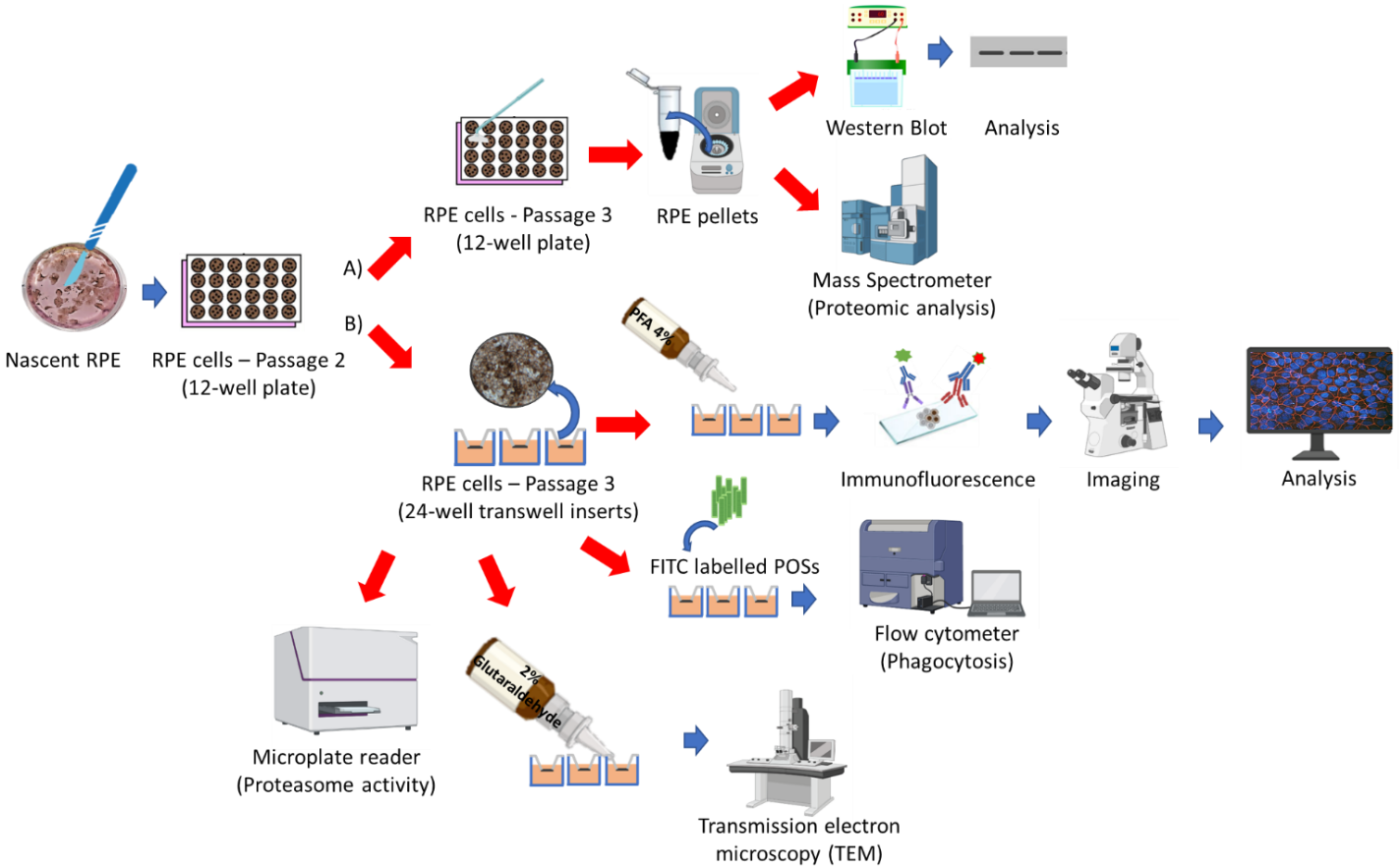

Figure 4-2: Schematic summary of the procedure from collection to analysis of RPE cells. Following differentiation, RPE patches were manually collected and plated in a 12-well plate. After passage 2, RPE cells were passaged either in 12-well plates or 24-well transwell inserts. A) RPE cells were collected using a cell scraper, transferred in Eppendorf tubes and centrifuged. RPE pellets were used for Western blot analysis or were used for proteomic analysis. B) RPE cells on 24 trans-wells were used for IF analysis after being fixed with 4% PFA. Staining was performed using the appropriate antibodies. The RPE sections were imaged using Axio Imager upright microscope, and analysis was performed using Zeiss Zen blue software and Adobe Photoshop (Adobe Systems). RPE cells were fed with FITC-labelled POSs to assess the phagocytosis activity of RPE cells. RPE transwell inserts were used for the proteasome assay as well as for the TEM analysis, which was performed after fixation of RPE cells with 2% glutaraldehyde.

4.4. Results

4.4.1. Derivation and characterization of hiPSCs from PRPF31 patients

The generation and characterisation of patient and controls hiPSCs was reported in our previous publication (Buskin et al., 2018). Clinical data on all RP11 patients for this study are summarised in Table 4-4.

Table 4-4: Information of clinical data from Control and PRPF31 patients (Buskin et al., 2018).

Case No.	Sample No.	Lab ID.	Age (biopsy)	Age (onset of symptoms)	Sex	Type	Genotype	Phenotype
Control	WT1	AD2	51	-	M	-	-	Unaffected [Lonza, CC-2511]
1	RP11S1	F116	69	10	F	*PRPF31*	c.1115_1125 del11	Severe - Presented with night blindness aged 10yrs old with decreased central vision by 30yrs. Cataract requiring surgery in 50s. Current visual acuity 6/60 and 6/24. Bilateral extensive bone spicular fundal pigmentation, attenuated arterioles and pale optic discs with small, preserved islands of RPE in macula.
2	RP11VS	F119	45	10	M	*PRPF31*	c.1115_1125 del11	Very Severe - Presented with night blindness aged 10yrs old with decreased central vision by 30yrs. Also has right optic nerve hypoplasia. Current visual acuity - No perception of light right eye and 6/18 left. Bilateral extensive bone spicular fundal pigmentation, attenuated arterioles and pale optic discs and visual field restricted to around 5 degrees from fixation.
3	RP11S3	F150	50	15	F	*PRPF31*	c.522_527+10del	Severe – Presented with night blindness aged 15yrs old with decreased central vision by 30yrs. Current visual acuities 6/18 and 6/36 with a refraction of -2 and bilateral posterior subcapsular cataracts. Bilateral extensive bone spicular fundal pigmentation, attenuated arterioles and pale optic discs.

4.4.2. Differentiation of hiPSCs into Retinal Pigmented Epithelium Cells

Differentiation of control and RP11-RPE cells was performed as described in section 4.3.3. The differentiation of RPE cells was variable among all the cell lines concerning the size, the number and the morphology of the patches. RPE patches derived from RP11VS-Cas9 and RP11VS hiPSCs were small in size and rare, whereas patches derived from WT1, RP11S1 and, RP11S3 hiPSCs were larger in size (**Figure 4-3 A**). Although hiPSC-derived RP11S1 and RP11S3 RPE cells generated multiple patches, differences in the morphology of the patches were observed. RP11S1 hiPSC-derived RPE patches were expanded into irregular shapes with darker edges and brighter interiors. However, hiPSC-derived RP11S3 RPE patches were spherical. A similar shape was observed in the patches derived from WT1, although WT1 patches were darker (**Figure 4-3 A**). Despite the differences in size, number and morphology of the RPE patches observed during the differentiation, RPE cells from all cell lines were characterised with brown pigmentation and hexagonal shape after been seeded for 12 weeks into 12-well transwell inserts (**Figure 4-3 B**).

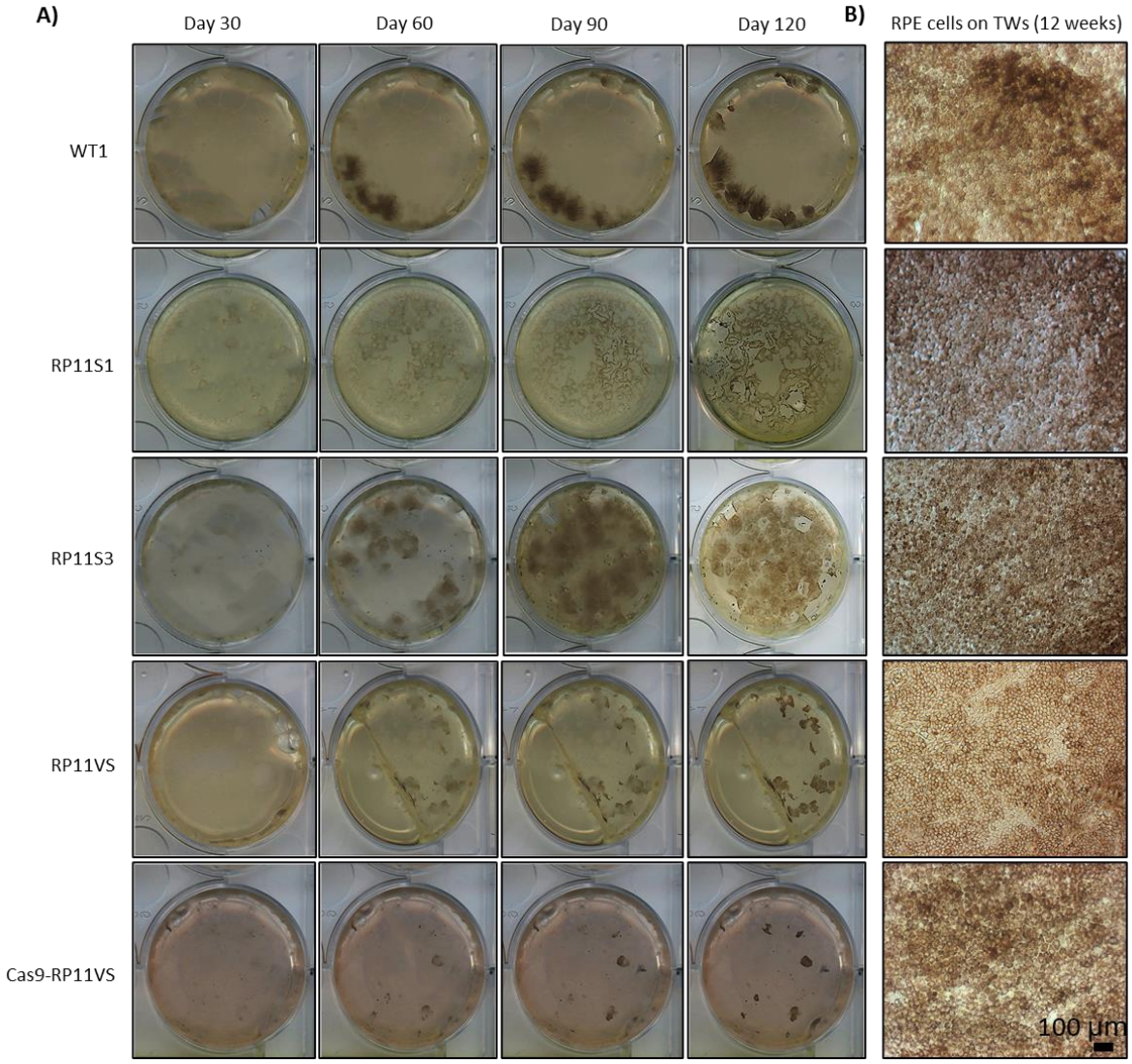

Figure 4-3: Representative images of RPE differentiation from control and PRPF31-hiPSCs. A) The images were scanned from 6-well plates at day 30, 60, 90 and day 120 of differentiation of control (WT1), isogenic control (Cas9-RP11VS), and patient (RP11VS, RP11S1, and RP11S3) cell lines. B) Control and patient RPE cells at 12 weeks of post-plating in 24-well transwell inserts. Representative images from 5 independent experiments.

4.4.3. Expression of PRPF31 in control and RP11-RPE cells

In the earlier study from our group, a decreased PRPF31 expression and the presence of long mutant form of PRPF31 was detected only in RP11-RPE cells (Buskin et al., 2018). To assess the localisation of PRPF31 in detail, immunofluorescence analysis in three RP11-RPE cells (RP11VS, RP11S1, and RP11S3) harbouring either the *PRPF31* c.1115_1125del11 or the *PRPF31* c.522_527+10del heterozygous mutation was performed using an antibody against the N-terminus of PRPF31 that detects both the WT and PRPF31 isoforms. Clear differences were observed with PRPF31 being localised in the nucleus of control RPE cells and predominantly in the cytoplasm of RP11-RPE cells (**Figure 4-4 A)**. Additionally, the tight junctions stained with ZO1 antibody were disrupted in RP11-RPE cells compared to the control cells (**Figure 4-4 A)**. These results corroborate previous observations from a study showing that tight junction and adherens junctions were associated with protein modifications in the retina of an animal model of autosomal dominant RP (adRP) (Campbell et al., 2006).

To distinguish localisation of PRPF31 variants in soluble and insoluble fractions, a Western blot of the two fractions was performed as described in sections 4.3.6 and 4.3.9, revealing a dramatic decrease in the amount of PRPF31 in the soluble fraction of RP11-RPE compared to control cells (**Figure 4-4 B**). Notably, whilst the wild type PRPF31 protein could be detected in the insoluble fraction of both control and RP11 RPE cells, the long mutant isoform was only detected in the insoluble fraction of RP11-RPE (**Figure 4-4 B**). Together our data suggest that a significant fraction of cytoplasmic aggregates in RP11-RPE is composed of the mutant PRPF31.

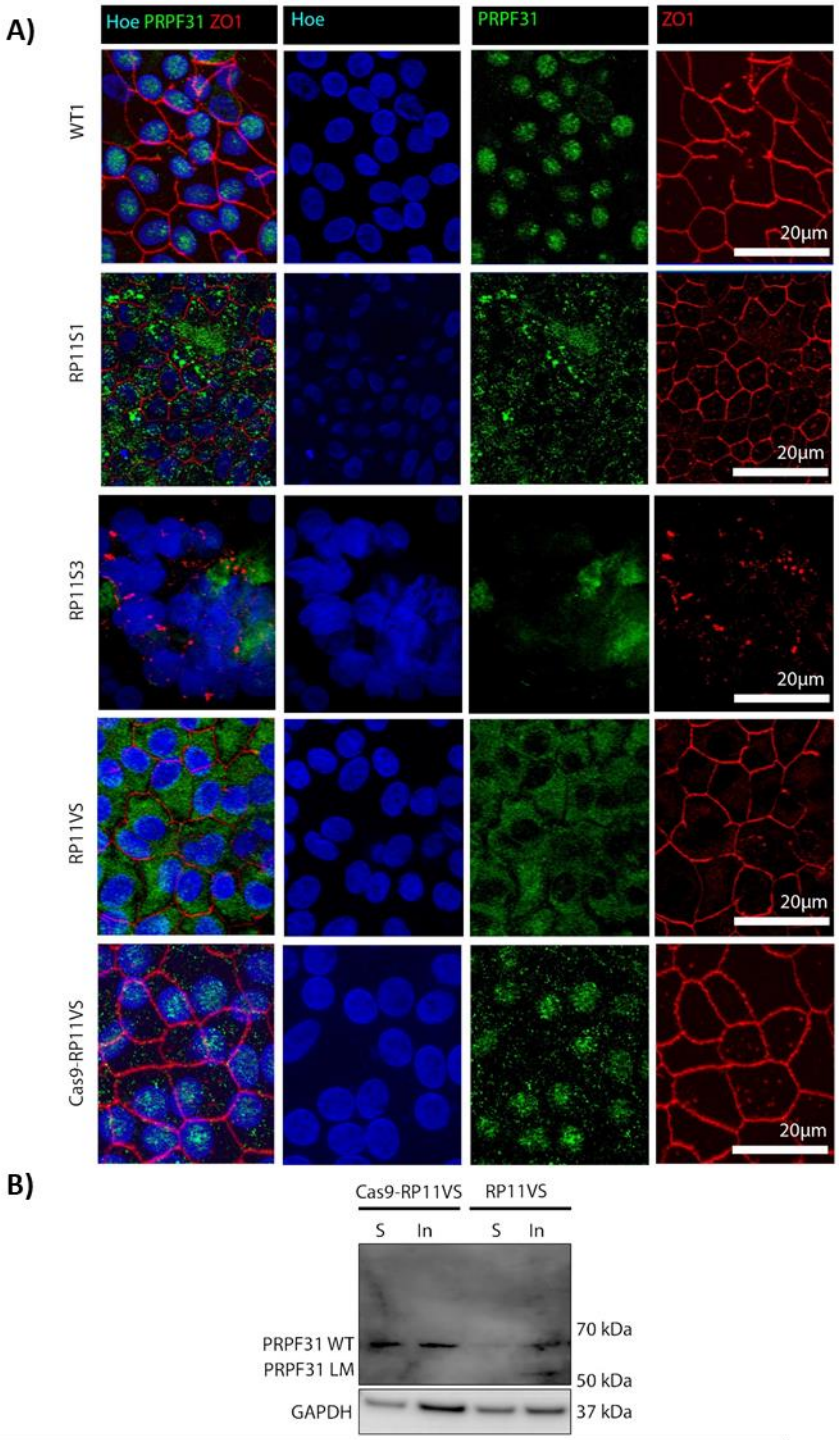

Figure 4-4: Assessment of PRPF31 localisation in RPE cells from control, patient-specific RP11-RPE and CRISPR/Cas9 isogeneic control. A) Control and RP11-RPE cells were immunostained with an anti-PRPF31 N terminus (green) and ZO1 (red) antibodies. Cell nuclei (blue) were stained with Hoechst. Immunofluorescence analysis showing localisation of PRPF31 protein mainly in the nucleus of WT1 and RP11VS-Cas9 RPE cells in speckle-like structures and predominantly in the cytoplasm in an aggregate-like pattern in RP11-RPE cells. Scale bars=20 µm. B) Western blot showing the expression of WT and mutant PRPF31 protein in the soluble and insoluble fractions of RP11VS-Cas9 and RP11VS RPE cells with anti-PRPF31 N terminal antibody. GAPDH was used as a loading control. Representative images from three independent experiments. LM= Long Mutant, WT= Wild Type.

4.4.4. Proteomic analysis

4.4.4.1. Differential Protein expression in RP11-RPE cells compared to unaffected control and isogenic control RPE cells

To assess changes in protein abundance between control and RP11-RPE cells, quantitative proteomic analysis using Tandem Mass Tag (TMT)-labelling and Mass spectroscopy was performed (as mentioned in sections 4.3.18 and 4.3.19) by our collaborators, Professor Reinhard Luhrman and Dr Sina Mozzafari-Jovin (Goettingen, Germany). Quantitative proteomics analysis of RPE cells derived from control (WT1, Cas9-RP11VS) and RP11 patients (RP11S1, RP11S2, RP11VS) identified a total of 5310 proteins, of which 1304 proteins were differentially expressed (Georgiou et al., 2021). These data were published in BioArchive in this link, https://www.biorxiv.org/content/10.1101/2021.10.11.463925v1 (Supplementary Table 2).

Thereafter, differentially abundant proteins in RP11-hiPSCs derived RPE cells revealed from mass spectrometry analysis were subjected to the Gene Ontology Biological Process (GOBP) database to identify biological processes and pathways that were significantly affected. GOBP analysis revealed, amongst others, enrichment of the differentially expressed (DE) proteins in RNA splicing, the spliceosome complex, retinoid metabolic process and visual perception, and protein folding pathways.

4.4.4.2. RNA Splicing pathway

Based on the GOBP enrichment analysis, 90 DE proteins were involved in RNA splicing pathway. Of the 90 DE proteins in the RNA splicing pathway, Fused in Sarcoma (FUS) was the most downregulated protein (**Figure 4-5 A, B**). Western blot and immunofluorescence analysis corroborated these results and moreover showed that FUS was predominantly localised in the cytoplasm of RP11-RPE in an aggregate-like pattern, unlike control cells where expression was nuclear (**Figure 4-5 C**).

Fus is a DNA and RNA binding protein that is involved in many cellular RNA metabolic processes, including mRNA transport (Kanai et al., 2004), spicing (Zhou et al., 2013), transcription (Yang et al., 2014), stabilization (Udagawa et al., 2015) and DNA repair (Wang et al., 2018). The mis-localisation of FUS from the nucleus to the cytoplasm has been reported previously by other studies, and it has been associated with neurotoxicity (Monahan et al., 2017) and amyotrophic lateral sclerosis (ALS) (Tyzack et al., 2019).

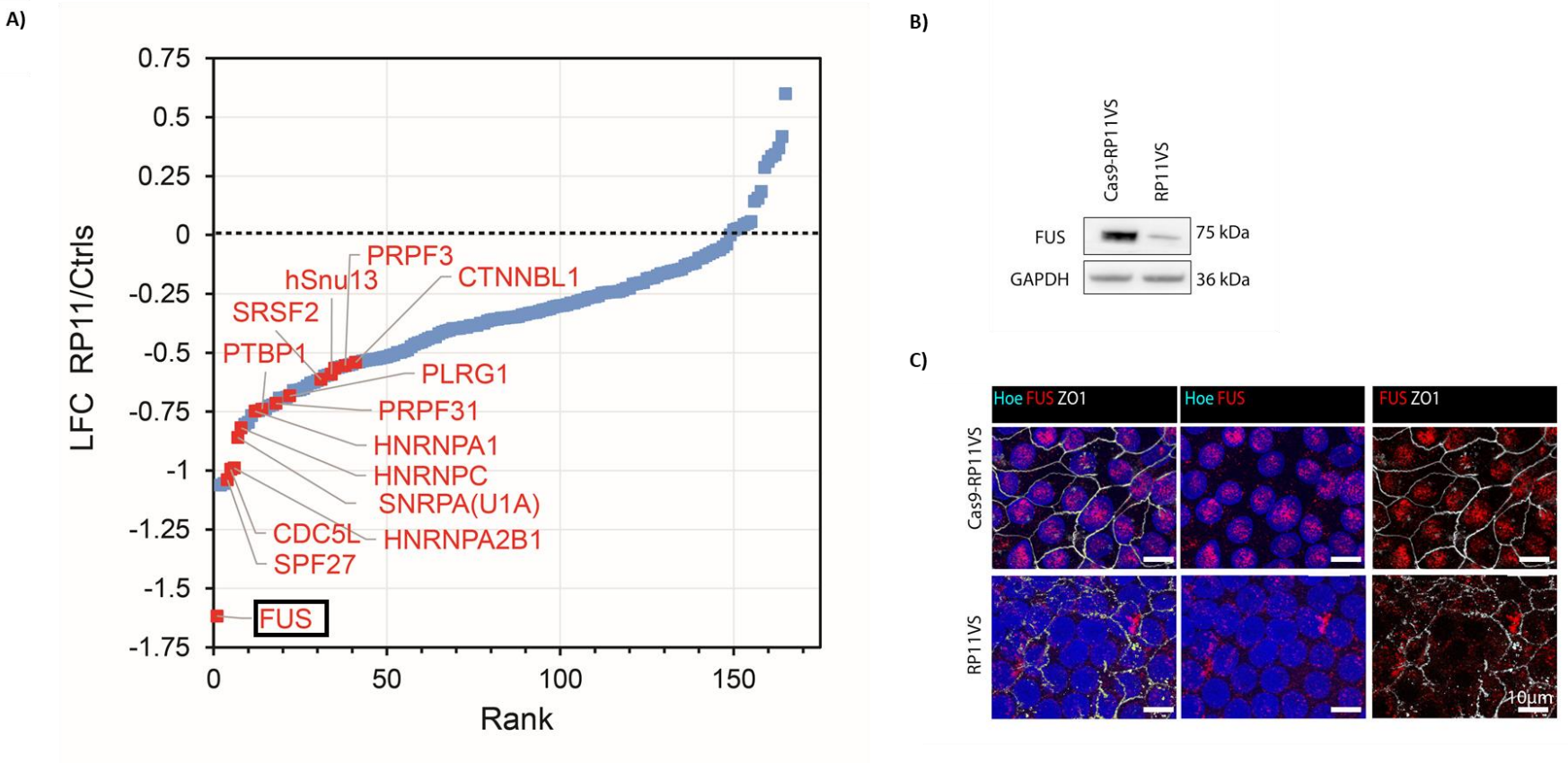

Figure 4-5: GO analysis reveals enrichment of proteins involved in 'RNA splicing' pathway in RP11-RPE cells. A) GO analysis showing DE proteins involved in RNA splicing highlighting with black square FUS, which was the most downregulated protein in RP11-RPE cells. B) Western blot showing downregulation of FUS in RP11-RPE cells. GAPDH was used as a loading control. Immunostaining of RP11-RPE and control RPE cells with FUS (red) and ZO1 (white). Cell nuclei were stained with Hoechst. Scale bars=10 µm. Analysis performed 12 weeks post-plating of RPE cells in transwell inserts. Representative images from three independent experiments.

4.4.4.3. Retinoid Metabolic Process and Visual Perception

The GOBP analysis identified 19 DE proteins involved in visual perception, and 18 DE proteins in the retinoid metabolic pathway. The classical visual cycle pathway involves the cycling of retinoids between the POSs and the RPE cells (Tsin et al., 2018). This is known as the phototransduction pathway and is important for the regeneration of 11-*cis*-retinal, a photosensitive derivative of vitamin A that is transported from the RPE cells to the PRs. Conversion of all-*trans* retinal back to 11-*cis*-retinal is important for visual continuity, and this is achieved by a series of reactions including several proteins and enzymes (Travis et al., 2007).

Among the DE proteins detected in the visual perception pathway, the most consistently upregulated protein between all RP11-RPE cells was RLBP1 (**Figure 4-6 A**). RLBP1 is a soluble retinoid carrier, which plays an important role in the regeneration of 11-*cis*-retinol during the visual cycle (Kiser et al., 2014). The upregulation of RLBP1 protein in RP11-RPE cells was further confirmed by Western blotting (**Figure 4-6 B**) and by IF analysis. Interestingly it was observed that RLBP1 is accumulated in an aggregate-like pattern only in RP11-RPE cells (as indicated by the yellow arrow), but not in control RPE cells (**Figure 4-6 C**). Additionally, the tight junctions stained with the ZO1 marker were disrupted, and the nuclei were absent in areas containing these large aggregates (**Figure 4-6 C**).

Interestingly, RLBP1 immunostained aggregates were associated with PRPF31 in aggregate like structures only in RP11-RPE cells (**Figure 4-7**). Upregulation of visual cycle genes in RPE cells has been associated with the accumulation of retinoid by-products in the aged RPE cells (Butler et al., 2021). These results suggest that RP11-RPE cells might develop similar features to aged RPE.

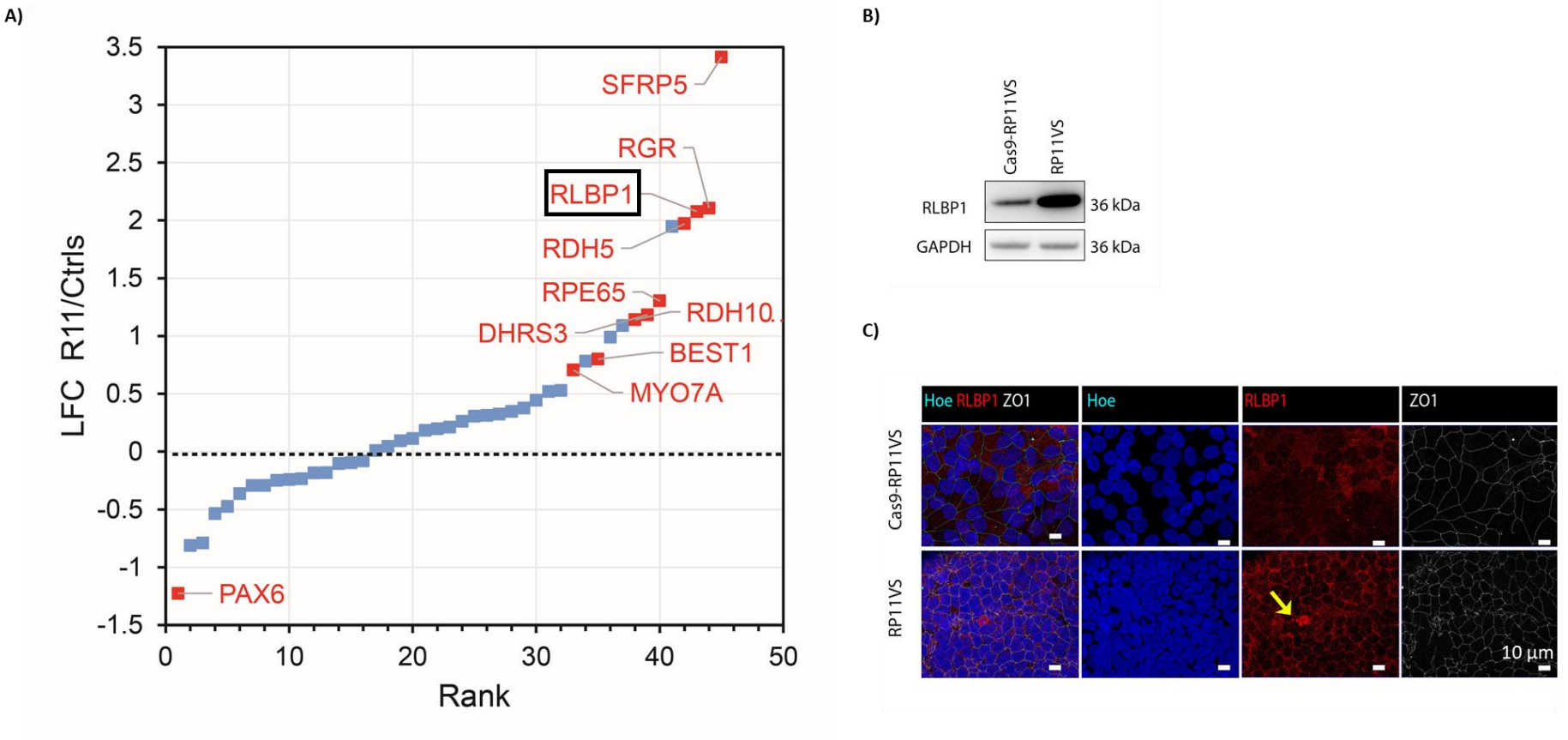

Figure 4-6: GO analysis reveals enrichment of proteins involved in the 'Retinoid metabolism and visual perception' pathway in RP11-RPE cells. A) GO analysis showing DE proteins involved in the 'Retinoid metabolism and visual perception' pathway, highlighting RLBP1 with a black square. B) Western blot showing the upregulation of RLBP1 in RP11-RPE cells. GAPDH was used as a loading control. C) Immunostaining of RP11-RPE and control RPE cells with RLBP1 (red). ZO1 (white) was used to define the tight junctions of RPE cells. Accumulated of RLBP1 in the cytoplasm of RP11-RPE cells in the form of aggregates (shown by yellow arrow) but not in control RPE cells. Scale bars=10 µm. Analysis performed 12 weeks post-plating of RPE cells in transwell inserts. Representative images from three independent experiments.

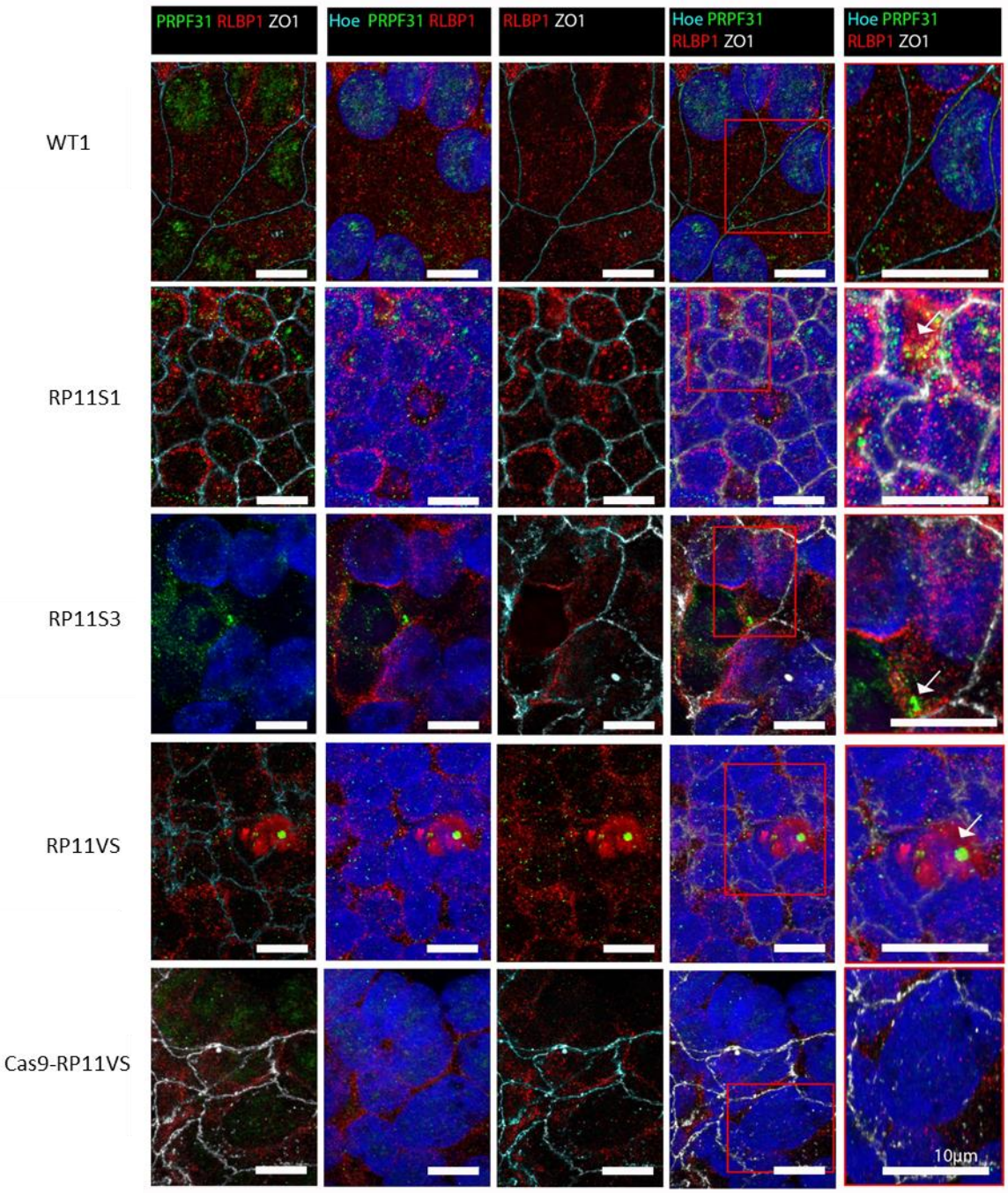

Figure 4-7: Increased expression of RLBP1 protein in patient-specific RP11-RPE cells. Magnified images showing increased expression of RLBP1 and association with PRPF31 in aggregate-like pattern in RP11-RPE cells (RP11VS, RP11S1, and RP11S3), but not in control (WT1) or isogenic control (Cas9-RP11VS) RPE cells. White arrows showing the association of PRPF31 with RLBP1. RLBP1 (red), PRPF31 (Green), and ZO1 (white). Nuclei were counterstained with Hoechst (Blue). Scale bars=10 µm. Analysis performed 12 weeks post-plating of RPE cells in transwell inserts. Representative images from five independent experiments.

4.4.4.4. Protein Folding pathway - Unfolded Protein Response

The third pathway revealed from GOBP enrichment analysis was the protein folding pathway. The protein folding pathway is an intracellular signalling pathway that is activated in response to misfolded proteins to restore protein conformation and to prevent protein aggregation (Adams et al., 2019). Upon activation, translation of most mRNAs is downregulated to prevent further accumulation of misfolded proteins (Rao and Bredesen, 2004), which interrupt the normal function of the ER, causing ER stress (Sano and Reed, 2013). Also, molecular chaperones such as heat shock proteins (HSPs) are upregulated to facilitate protein folding (Hartl, 1996).

The GOBP analysis revealed 23 DE proteins that were enriched in the protein folding pathway. Three molecular chaperones involved in the protein folding/UPR pathway, namely HSPB1, HSPA2 and HSPA4L, which are activated in response to misfolded proteins to restore protein conformation and to prevent protein aggregation, were upregulated in RP11-RPE cells (**Figure 4-8 A**). The upregulation of HSPB1, HSPA2 and HSPA4L in RP11VS RPE cells compared to RP11VS-Cas9 RPE cells was confirmed by Western blotting (**Figure 4-8 B**), and thereafter by IF analysis demonstrating HSPB1 and HSPA2 expression in an aggregate-like pattern (as indicated by yellow arrows) predominantly located in areas lacking nuclei and characterised by disrupted ZO1 staining (**Figure 4-8 C**). Also, HSPA4L was significantly overexpressed in RP11-RPE compared to control cells (**Figure 4-8 C**). Notably, strong punctate PRPF31 was associated with the HSPB1 and HSPA2 immunostained aggregates in RP11VS RPE cells compared to control RPE cells. Furthermore, association of HSPA4L with PRPF31 was observed in the cytoplasm of RP11-RPE but not control RPE cells (**Figure 4-8 C**). Our results corroborate recent results by Valdés-Sánchez and colleagues showing association of HSPA4L with PRPF31 in the cytoplasm of RP11-RPE cells (Valdés-Sánchez et al., 2019). Additionally, the expression of HSPB1 in combination with PRPF31 was assessed in all RP11-RPE cells that harbour different mutations and vary in the severity of the disease, confirming the association of HSPB1 with punctate PRPF31 in the cytoplasm of all RP11-RPE cells (**Figure 4-9**). Taken together, our results suggest the activation of protein folding pathway in response to the accumulation of misfolded proteins in RP11-RPE cells.

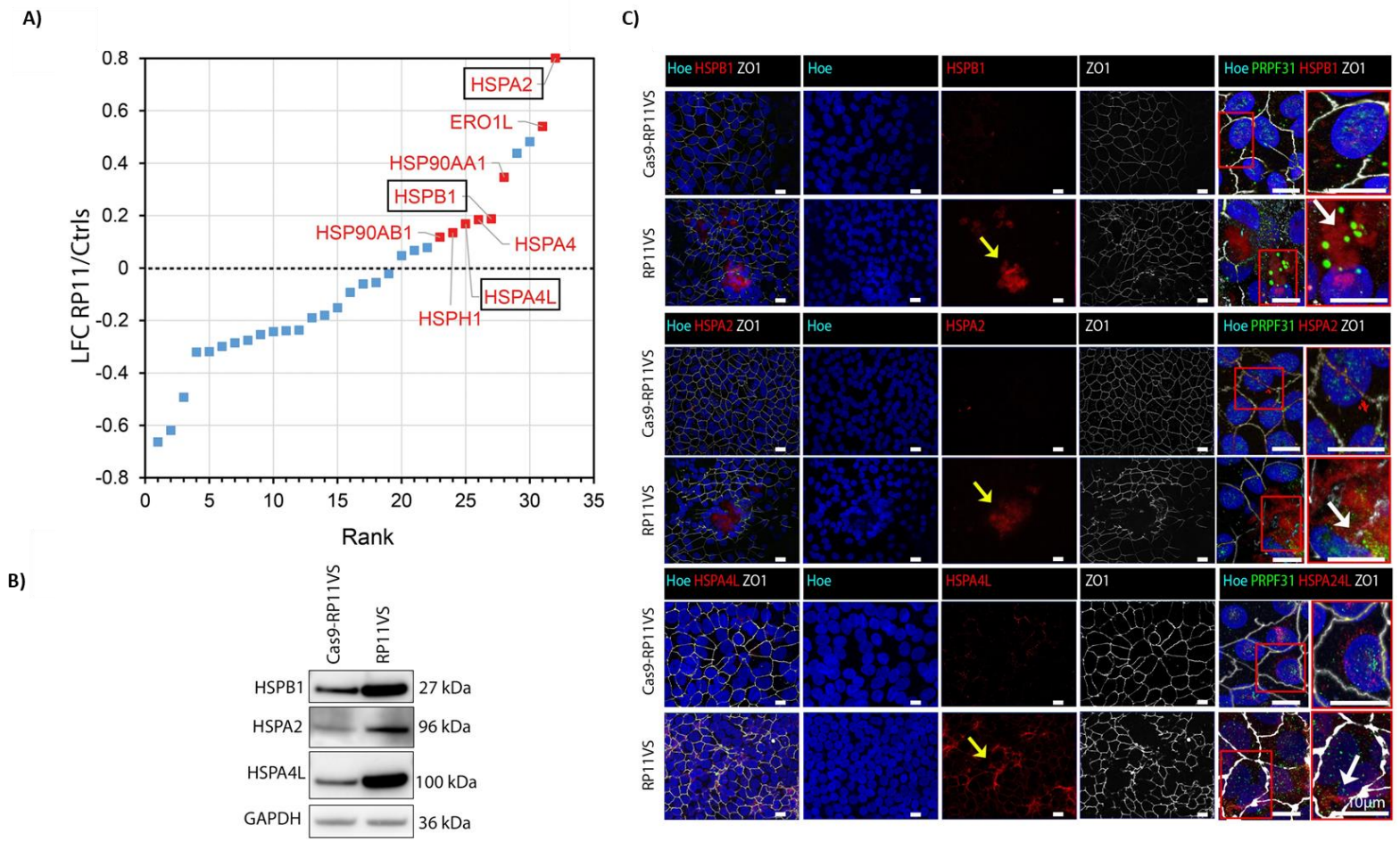

Figure 4-8: GO analysis reveals enrichment of proteins involved in the 'Protein folding' pathway in RP11-RPE cells. A) GO analysis showing the upregulation of proteins involved in the protein folding pathway, highlighting with black square three HSPs; HSPB1, HSPA2 and HSPA4L. B) Western blot showing the upregulation of HSPB1, HSPA2 and HSPA4L in RP11-RPE cells. GAPDH was used as a loading control. C) Immunostaining of RP11-RPE and control RPE cells with HSPs (red). ZO1 (white) was used to define the tight junctions of RPE cells. Accumulation of HSPs in the cytoplasm of RP11-RPE cells in the form of aggregates (shown by yellow arrow) but not in control cells. Cell nuclei were counterstained with Hoechst (blue). Scale bars=10 µm. Analysis performed 12 weeks post-plating of RPE cells in transwell inserts. Representative images from three independent experiments.

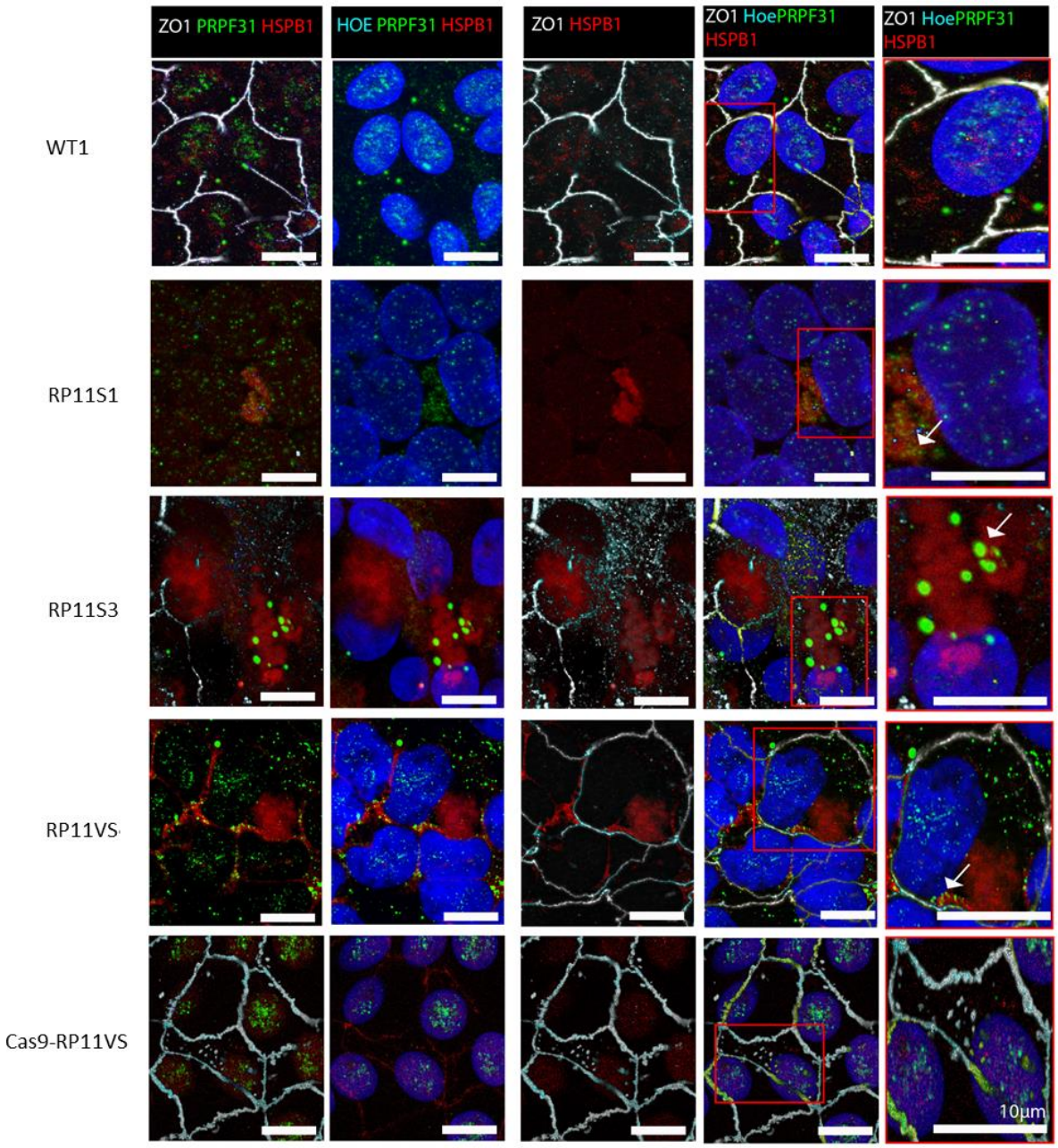

Figure 4-9: Increased expression of HSPB1 protein in patient-specific RP11-RPE cells. Magnified images showing increased expression of HSPB1 in association with PRPF31 in aggregate-like pattern in the cytoplasm of RP11-RPE cells (RP11VS, RP11S1, and RP11S3), but not in control (WT1), or isogenic control (Cas9_RP11VS) RPE cells. White arrows showing the association of PRPF31 with HSPB1. HSPB1 (red), PRPF31 (Green), and ZO1 (white). Cell nuclei were counterstained with Hoechst (blue). Scale bars=10 µm. Analysis performed 12 weeks post-plating of RPE cells in transwell inserts. Representative images from three independent experiments.

4.4.5. Proteomic analysis to investigate the composition of aggregates

Our results have shown the presence of wild type and mutant PRPF31 protein in the insoluble aggregates of RP11-RPE cells (**Figure 4-4 B**). To assess in detail the composition of the insoluble fraction, comparative proteomic analysis of the insoluble fractions prepared from control and RP11-RPE cells separated by SDS-PAGE and analyzed by mass spectrometry was performed as described in sections 4.3.6 and 4.3.19. Mass spectrometry was performed by Dr Sina Mozaffari-Jovin.

Proteomic analysis detected a total of 4061 proteins, of which 934 were DE in patient RP11-RPE cells (LFC cut off value of 1). Data were published in BioArchive and can be found in the following link: https://www.biorxiv.org/content/10.1101/2021.10.11.463925v1 (Supplementary Table 3) (Georgiou et al., 2021). To graphically display the quantitative data, a volcano plot of $\log_{10}$(*P*-value) *vs.* $\log_2$(fold change of patients/control) – was constructed (**Figure 4-10 A**). Based on a comparative analysis performed using Venn diagram, the results indicated that 19.4% of the total (soluble and insoluble) DE proteins identified in the cellular extract fraction fall into the insoluble category, including proteins belonging to the visual cycle (RLBP1, DHRS3), protein folding (HSPB1) and splicing (PRPF31) (**Figure 4-10 B**). Furthermore, GOBP enrichment analysis performed by Metascape showed that 934 DE proteins were involved in several key pathways, including mRNA splicing, protein folding, response to ER stress and UPR (**Figure 4-10 C**), some of which were mentioned earlier (section 4.4.4) to be affected in RP11-RPE cells. Notably, several key spliceosomal tri-snRNP proteins, including PRPF8, SNRNP200 (Brr2) and PRPF6, implicated in RP, as well as EFTUD2 (Sunu114), USP39, SART1 and SART3 were amongst the splicing factors whose amounts were significantly increased in the insoluble fraction (**Figure 4-10 C**). Moreover, the abundance of several HSPs is notably increased, including components of the HSP90/R2TP chaperone system (HSP90, RUVBL1 and 2), previously implicated in the assembly of U4 and U5 snRNPs (Malinova et al., 2017). Together these data suggest that key components of mRNA splicing, waste disposal, ER stress/UPR are deposited within the insoluble aggregates, preventing proper functions of these vital processes in RP11-RPE cells.

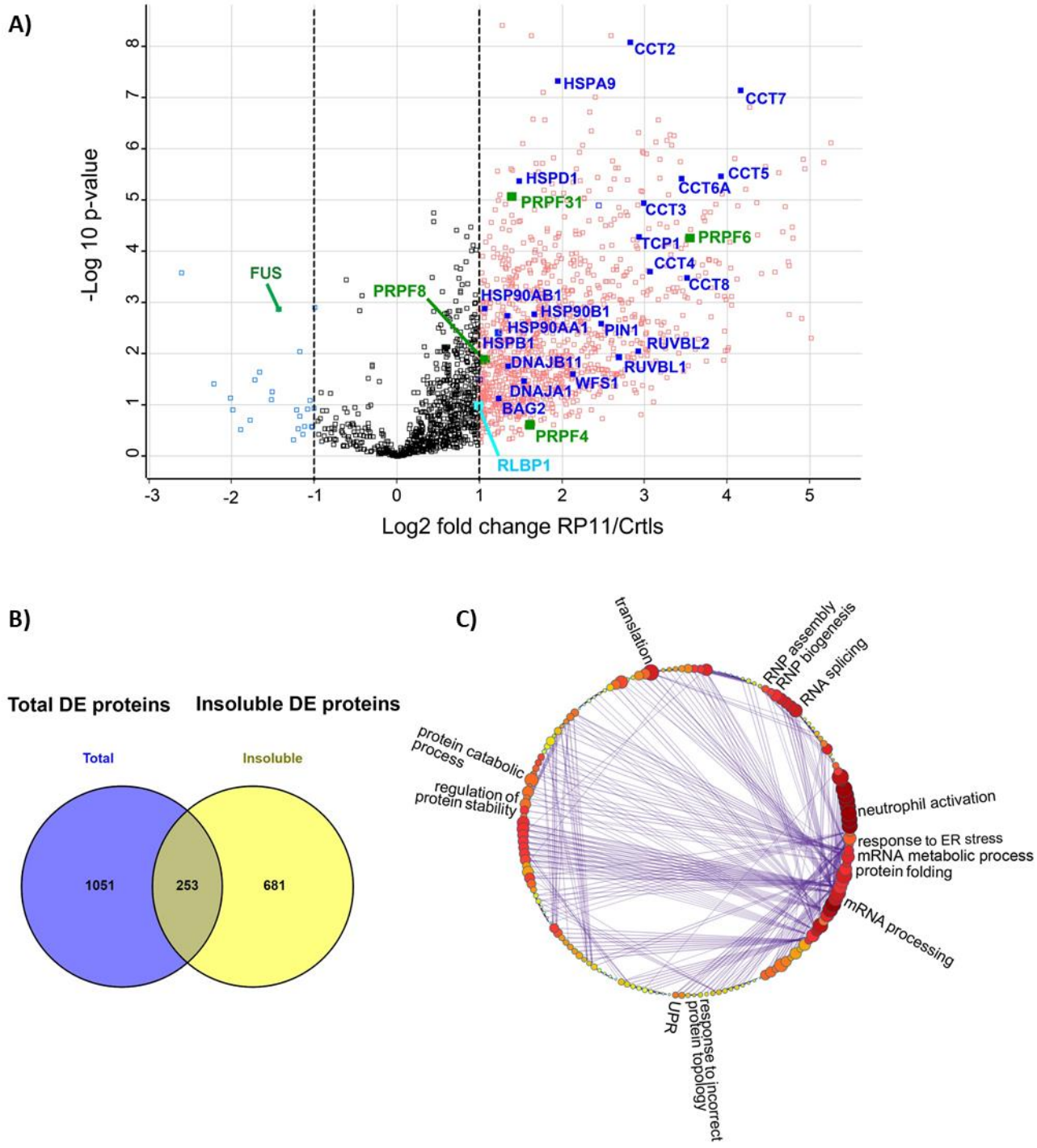

Figure 4-10: Differential protein abundance in the insoluble fractions of RP11-RPE cells. A) Volcano plot indicating the DE proteins in the insoluble fractions of RP11-RPE cells highlighting protein folding or unfolded protein response (blue), retinoid metabolism and visual perception (cyan) and spliceosome related (green) proteins. A Log2 fold change cut off 1 was applied for the identification of significantly regulated proteins between insoluble fractions of control and RP11-RPE cells. B) Venn diagram showing overlapping proteins between DE proteins detected from total cell extract (blue) and insoluble fractions (yellow) of RP11-RPE cells. C) Cluster illustrating the affected pathways of enriched GOBP insoluble proteins, including RNA splicing, mRNA processing, mRNA metabolic process, protein folding, UPR, regulation of protein stability, protein catabolic process, translation and RNP assembly and biogenesis.

4.4.6. Accumulation of misfolded ubiquitin - conjugated proteins in RP11-RPE cells

Intracellular misfolded or damaged proteins are selectively degraded to amino acids and are replaced by newly synthesized proteins to maintain fundamental cellular homeostasis (Glickman and Ciechanover, 2002). Initially, most proteins targeted for degradation are labelled by ubiquitin molecules and then are degraded into small peptides by a large proteolytic complex, the 26S proteasome, that prevents the accumulation of non-functional and potentially toxic proteins (Goldberg, 2003).

Given that the GO analysis showed the enrichment of proteins involved in protein folding and proteolysis in RP11-RPE cells, an FK1 antibody that detects polyubiquitin–conjugated protein chains was used to identify ubiquitin-conjugated misfolded proteins. Western blot analysis performed as described in section 4.3.9 showed an increased abundance of ubiquitin-conjugated proteins in RP11-RPE compared to the control cells (**Figure 4-11 A**). The Western blot results were further validated by IF analysis, which revealed an increased expression of ubiquitin-conjugated proteins in an aggregate-like pattern in patient-specific RP11-RPE cells but not in control cells, suggesting an increase in the number of misfolded proteins targeted for degradation in RP11-RPE cells (**Figure 4-11 B**). Importantly, these FK1 positive large aggregates were found in areas with disrupted tight junctions (ZO-1 staining) and devoid of nuclei (**Figure 4-11**).

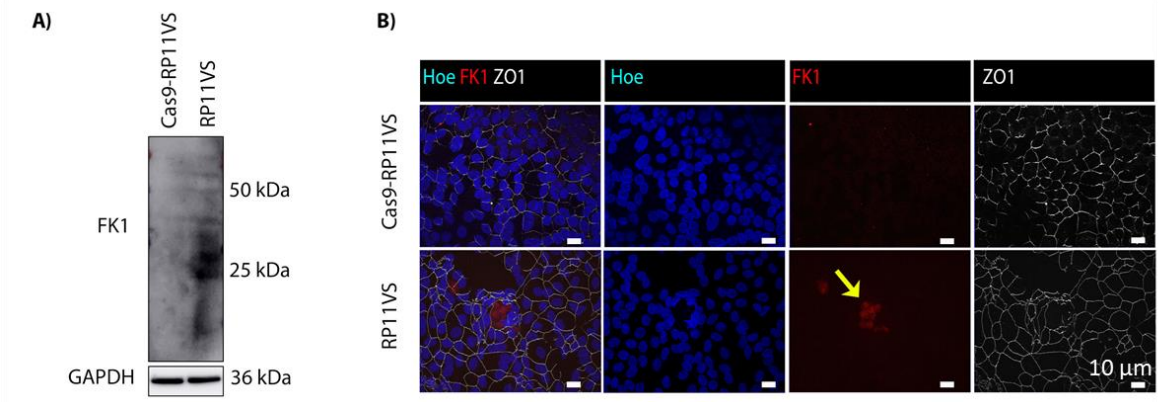

Figure 4-11: Accumulation of ubiquitin-conjugated proteins in RP11-RPE cells. A) Western blot showing upregulation of FK1 (ubiquitin-conjugated proteins) in RP11VS-RPE cells compared to control Cas9-RP11VS-RPE cells. GAPDH was used as a loading control. B) Immunostaining of RP11VS-RPE and control Cas9-RP11VS-RPE with FK1 (red) and ZO1 (white) showing accumulation of FK1 in RP11VS-RPE cells in the form of aggregates (shown by yellow arrow) but not in control cells. Cell nuclei were counterstained with Hoechst (blue). Scale bars=10 µm. Analysis performed 12 weeks post-plating of RPE cells in transwell inserts. Representative images from three independent experiments.

Importantly, PRPF31 itself was associated with these FK1 positive aggregates. This was observed only in RP11-RPE cells and not in control RPE cells (**Figure 4-12**). Taken together, these results suggest that misfolded proteins destined for degradation are accumulated in the form of large aggregates in RP11-RPE but not in control RPE cells, which indicates some dysfunction in the proteasome-mediated degradation system in patient-specific RP11-RPE cells.

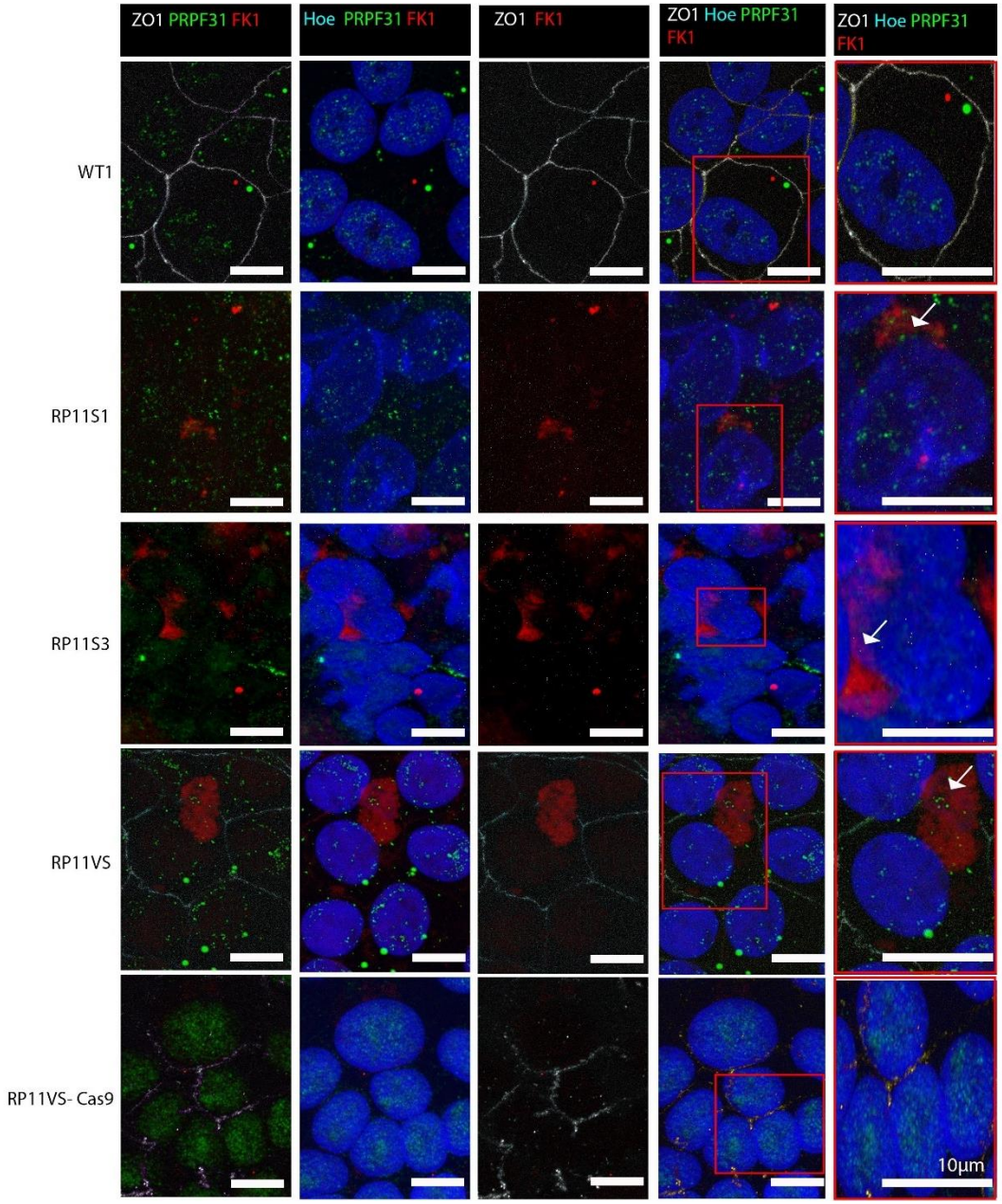

Figure 4-12: Increased expression of FK1 protein in patient-specific RP11-RPE cells. Magnified images showing increased expression of FK1 in association with PRPF31 in an aggregate-like pattern only in RP11-RPE cells (RP11VS, RP11S1, and RP11S3), but not in control (WT1) or isogenic control (Cas9-RP11VS) RPE cells. White arrows showing the association of PRPF31 with FK1. FK1 (red), PRPF31 (green), and ZO1 (white). Cell nuclei were counterstained with Hoechst (blue). Scale bars=10 µm. Analysis performed 12 weeks post-plating of RPE cells in transwell inserts. Representative images from three independent experiments.

4.4.7. Accumulation of aggregates in RP11-RPE cells

The results of this study revealed the accumulation of visual cycle proteins, chaperones, and misfolded proteins in the cytoplasm of RP11-RPE cells in an aggregate-like pattern. To validate the presence of cytoplasmic aggregates in RP11-RPE cells, TEM analysis was performed as described in section 4.3.13, revealing striking differences between control and RP11-RPE cells. Control RPE cells were characterised by normal cuboidal morphology, presenting long cilia on the apical side, with no visible signs of degeneration (**Figure 4-13**). However, RP11-RPE cells were characterised by the presence of multivesicular bodies (MVBs) (indicated by red arrowheads) as well as big vacuoles filled with electrodense material suggesting the accumulation of cytoplasmic aggregates (**Figure 4-13**). Additionally, big gaps between RP11-RPE cells filled with debris (black arrowheads) were detected (denoted by red dotted lines), suggesting the accumulation of aggregates between RP11-RPE cells and disruption of tight junctions. Additionally, TEM images revealed the presence of expanded ER (red arrows) and the presence of stress vacuoles (indicated by" V") in patient-derived RP11-RPE cells (**Figure 4-13**).

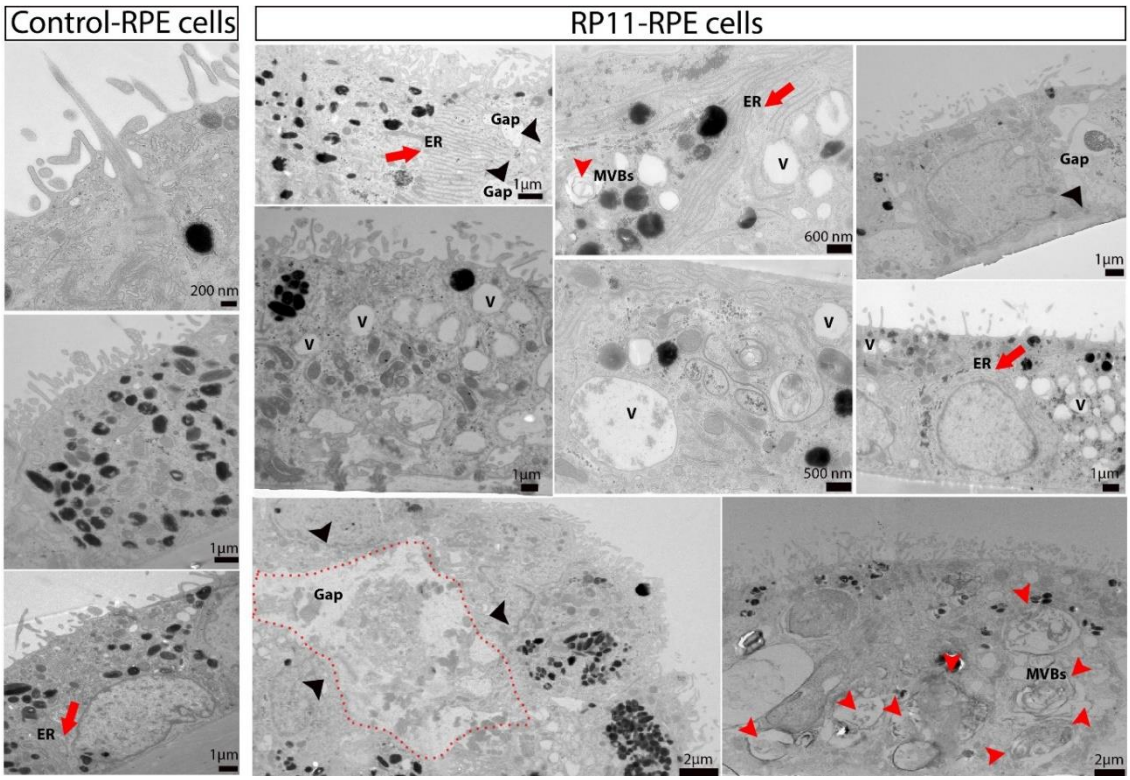

Figure 4-13: Accumulation of misfolded protein in RP11-RPE cells. Representative TEM images of control and RP11-RPE cells showing the accumulation of amorphous electrodense material (black arrowheads) located between patient-derived RPE cells (red dotted line), the presence of stress vacuoles (V), expanded endoplasmic reticulum (ER) (red arrow), and multivesicular bodies (MVBs) (red arrowhead). Control RPE cells were characterised by normal cuboidal morphology, with no signs of degeneration.

4.4.8. Evaluation of tight junction integrity in RP11-RPE cells

The findings of this study revealed the presence of cytoplasmic aggregates containing the mutant PRPF31 and misfolded, ubiquitin conjugated proteins and visual cycle proteins in RP11-RPE cells. Our results have shown that cytoplasmic aggregates affect the tight junctions in RP11-RPE cells. The tight-junction integrity is a general phenotype of healthy RPE cells, and it can be measured using trans-epithelial resistance (TER) as described in section 4.3.4.2. Therefore, to evaluate the tight-junction integrity, the TER measurements from control and RP11-RPE cells that have been seeded on TWs for 12 weeks were taken. The results indicated that control and isogenic control cell lines have significantly higher TER values compared to RP11-RPE cells (**Figure 4-14**). These results corroborate our previous observations that tight-junction integrity is affected in RP11-RPE cells.

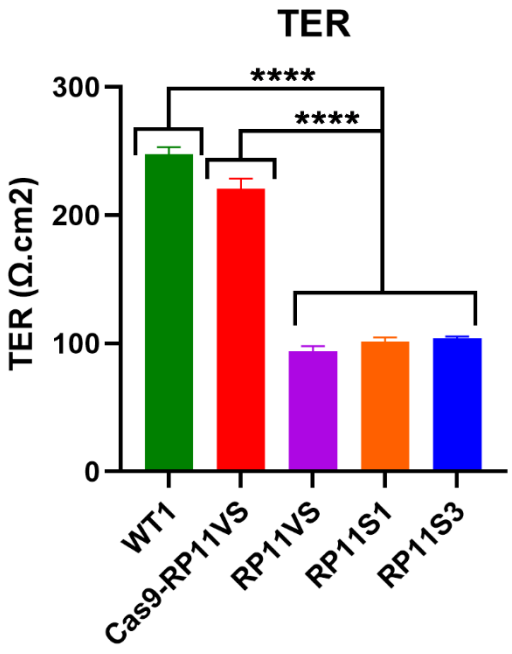

Figure 4-14: Trans-epithelial resistance of controls and RP11-RPE cells. TER values indicate a significant difference between control and RP11-RPE cells. Data are shown as mean ± SEM, n=5.

4.4.9. Disfunction of the waste disposal mechanisms in RP11-RPE cells

In all tissues, the initial cellular defence mechanism is the ubiquitin proteasomal degradation pathway which, together with the chaperone system, degrades the majority of misfolded proteins (Hyttinen et al., 2014). Most of the misfolded proteins are targeted for degradation by ubiquitin proteins and thus degraded by the 26S proteasome. The 26S proteasome is composed of two 19S regulator complexes

that cap the catalytic core cylinder known as the 20S. Degradation of the proteins occurs in the central 20S catalytic chamber, which is composed of numerous subunits, although proteolytic activities are specifically performed by β1, β2, β5 subunits, which have caspase-like, trypsin-like, and chymotrypsin-like specificities, respectively (Tanaka, 2009).

Based on our previous observations, it was detected that misfolded proteins are accumulated in the cytoplasm of RP11-RPE cells in the form of aggregates. Also, quantitative proteomic analysis revealed the downregulation of proteins responsible for the enzymatic activities of chymotrypsin-like (PSMB8), caspase-like (PSMB9) and trypsin-like (PSMB10) in RP11-RPE cells compared to the control cells. Therefore, to validate these results, Western blot was performed using an antibody to the PSMB10 protein (involved in the trypsin-like activity), which was the most downregulated proteasomal related protein (mean LFC = -0.656). The results confirmed the downregulation of PSMB10 protein in RP11-RPE compared to control cells **(Figure 4-15 A)**. Thereafter, the trypsin-like activity was further evaluated, as outlined in section 4.3.12, showing a significant decrease in the activity in RP11-RPE compared to control cells **(Figure 4-15 B)**. Together these results suggest a significant downregulation of the proteasome proteolytic activity in RP11-RPE cells, which may impair the clearance of misfolded proteins, leading to their accumulation in the cytoplasm of patient-specific RPE cells.

Overwhelming of the chaperone and ubiquitin-proteasome systems that mediate refolding and degradation of ubiquitinated proteins, respectively, leads to the activation of an intrinsic apoptotic pathway, the autophagy pathway (Kroemer et al., 2010), which aids the degradation of accumulated ubiquitin-labelled proteins (Hyttinen et al., 2014).

Therefore, to identify whether the autophagy pathway is activated in response to accumulated cytoplasmic aggregates, the expression of key components involved at different steps (autophagosome initiation, formation, and degradation) in the autophagy pathway was assessed. Western blot results indicated a significant increase in pS6, S6, p62, and LC3-I expression in RP11-RPE compared to control cells, but no differences in expression of Beclin 1 or ATG5-ATG12 were observed (**Figure 4-15 C**), suggesting a block in the late stages of the autophagy-lysosome pathway. Immunofluorescence assays fully corroborated these data revealing increased p62 and LC3 expression in RP11-RPE cells (**Figure 4-15 D**). Quantification analysis confirmed that p62 and LC3 were significantly upregulated in RP11VS RPE cells compared to control RPE cells (**Figure 4-15 E**). Malfunctioning of the autophagy pathway due to accumulation of protein aggregates has been reported in other neurodegenerative diseases such as Huntington's disease (Metcalf et al., 2012)

(Ravikumar et al., 2004). Our findings suggest the activation of the mTOR pathway and inhibition of autophagy, which together with dysfunction of the proteasome-mediated degradation may lead to accumulation of misfolded proteins in cytoplasmic-like aggregates.

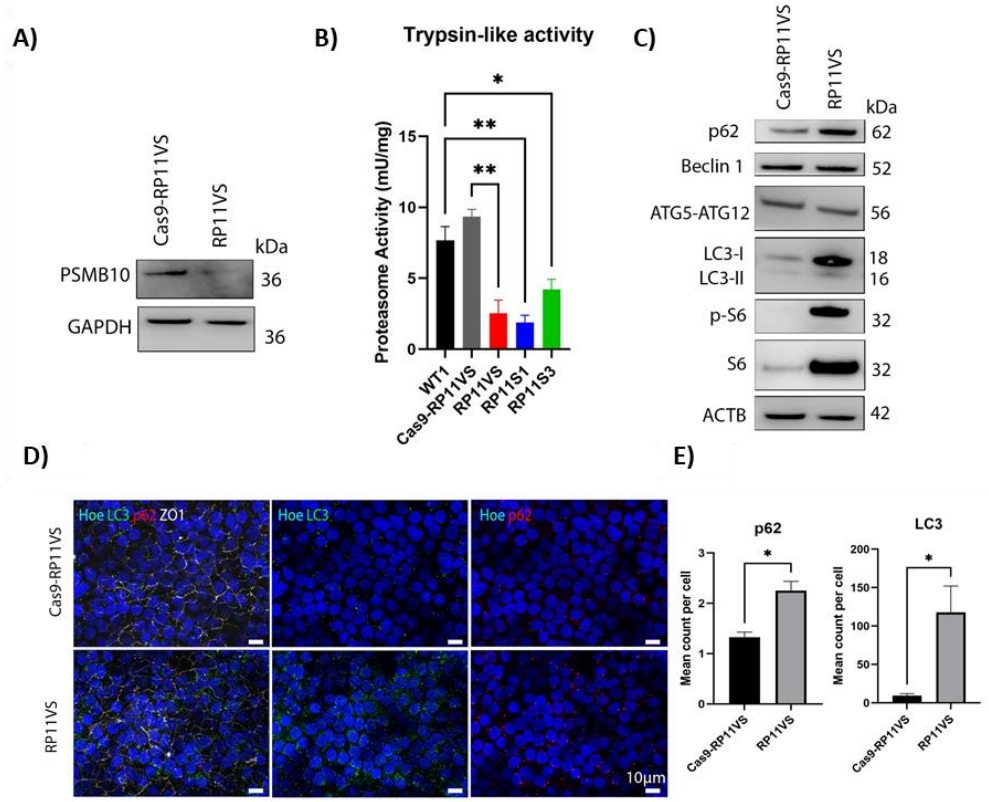

Figure 4-15: Dysfunction of waste disposal mechanisms RP11-RPE cells. A) Western blot of RPE samples showing downregulation of PSMB10 protein in RP11VS RPE cells compared to Cas9-RP11VS RPE cells. GAPDH was used as a loading control. B) Reduced proteasome Trypsin-like activity in RP11-RPE cells compared to control RPE cells. Statistically significant differences were determined by t-test (*P<0.001, **P<0.001). The data are shown as mean ± SEM, n=3. C) Western blot of key autophagic components showing upregulation of p62, LC3-I, p-S6 and S6 expression in RP11-RPE cells compared to Cas9-RP11VS RPE cells. Actin B was used as a loading control. D) Immunofluorescence analysis showing upregulation of p62 (red) and LC3 (green) in RP11-RPE compared to Cas9-RP11VS RPE cells. ZO1 (white) was used to define the tight junctions of RPE cells. Cell nuclei were counterstained with Hoechst. Scale bars=10 µm. E) Quantification analysis of LC3 and p62. Statistically significant differences were indicated by *t*-test (* p-value <0.05). The data are shown as mean ± SEM, n=5. Analysis performed 12 weeks post-plating of RPE cells in transwell inserts. Representative images from three independent experiments.

4.4.10. Progressive accumulation of cytoplasmic aggregates in RP11-RPE cells

Misfolding, aggregation, and deposition of abnormal proteins is a common hallmark event of multiple neurodegenerative diseases such as Alzheimer's, Huntington's, Parkinson's, and Amyotrophic Lateral Sclerosis (ALS) (Ciechanover and Kwon, 2015) (Takalo et al., 2013). All these diseases are characterised by progressive pathology. Accumulation of self-aggregating proteins intracellularly and extracellularly occurs progressively due to the formation of insoluble non-native aggregates, which accumulate over time, disrupting protein homeostasis and eventually lead to cellular dysfunction or cell death.

To investigate whether this also occurs in RP11 and assess the kinetics of aggregate accumulation in RP11-RPE cells, IF analysis at weeks 4, 8 and 12 post-plating of RP11-RPE cells in transwell inserts was performed, using RLBP1, HSPB1 and FK1 antibodies, which we showed earlier to accumulate in an aggregate-like pattern. At week 4, RP11-RPE cells displayed increased expression of RLBP1 and HSPB1 but not FKI compared to control cells (**Figure 4-16**). Further increases in the expression of RLBP1, HSPB1 were noticeable in RP11-RPE cells assessed at week 8. At this time point, RLBP1 was the only protein that showed accumulation in an aggregate-like pattern (**Figure 4-16**). At 12 weeks, all three markers displayed this aggregate-like accumulation but only in patient RP11-RPE cells, corroborating our earlier data. These results suggest a progressive accumulation of visual cycle proteins, chaperones, and misfolded-ubiquitinated proteins in the cytoplasm of RP11-RPE cells.

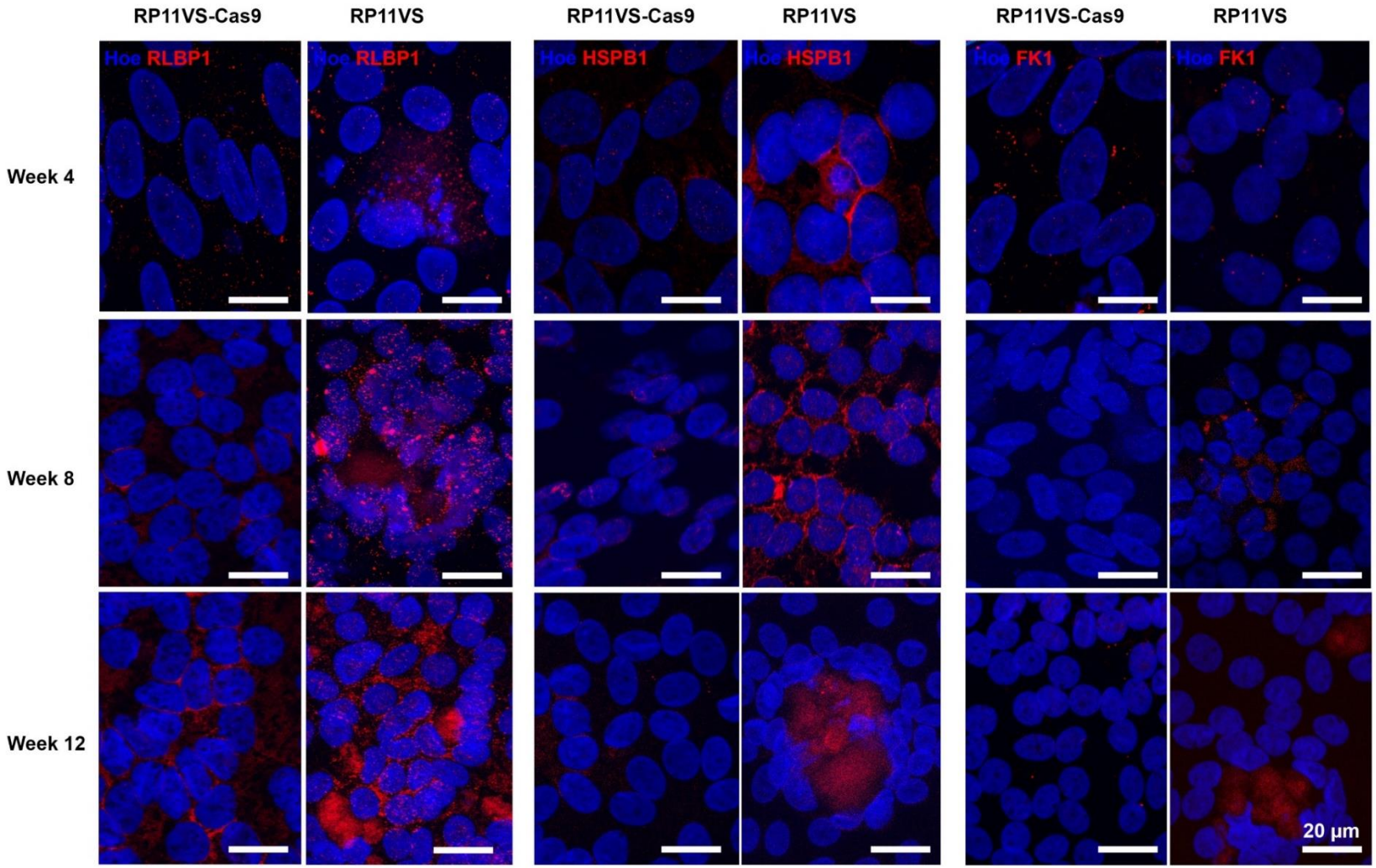

Figure 4-16: Progressive accumulation of cytoplasmic aggregates in RP11-RPE cells. Immunofluorescent images of control (Cas9-RP11VS) and RP11 (RP11VS) RPE cells at week 4, 8 and 12 post-plating of RP11-RPE cells in transwell inserts showing a gradual increase and accumulation of RLBP1, HSPB1, and FK1 (red), forming large aggregates. Cell nuclei were counterstained with Hoechst (blue). Scale bars=20 µm. Representative images from three independent experiments.

4.4.11. Daily feeding of RP-11 RPE cells with photoreceptor outer segments accelerates cytoplasmic aggregate accumulation

One of the main functions of RPE cells is the engulfment and phagocytosis of POSs, which are shed from PRs daily at a very high rate. To assess the aggregate accumulation under physiologically relevant conditions, the control and RP11-RPE cells that were differentiated in transwell inserts for 4 weeks were fed with unlabeled POSs (as outlined in section 4.3.15) and collected at 0, 48, 96 and 144 hours post-feeding. Also, FITC-labelled POSs were used as a control to confirm phagocytosis of POSs by RPE cells. Thereafter, the presence of intracellular aggregates containing RLBP1, HSPB1 and/or FK1 was analysed by immunofluorescence microscopy.

RP11-RPE cells fed with POSs at 0 hours did not show any differences in the expression of RLBP1, HSPB1 and FK1 compared to control RPE cells (**Figure 4-17**). However, at 48 hours post-feeding with POSs, RP11-RPE cells showed a significant increase in the accumulation of cytoplasmic aggregates containing RLBP1, HSPB1 or FK1 (**Figure 4-17**). A further accumulation of proteins was observed at 96 and 144 hours post-feeding, with RLBP1, HSPB1 and FK1 expressed as large aggregates in the cytoplasm of RPE cells disrupting the tight junctions between the cells (**Figure 4-17**). However, in control RPE cells, no differences were observed in the expression of RLBP1, HSPB1 or FK1 at 0, 48, 96 and 144 hours post-feeding with POSs (**Figure 4-17**), suggesting that accumulation of cytoplasmic aggregates containing RLBP1, HSPB1 or FK1 is prevented in control cells. Under normal steady-state conditions, these cytoplasmic aggregates should be digested by autophagy or proteasome-mediated degradation.

Additionally, the expression of LC3 and p62 was assessed, showing a gradual increase in the expression of autophagic proteins with time post POSs feeding (**Figure 4-17**), resulting in the formation of large aggregates akin to those observed in RP11-RPE cells at the later time points of differentiation (12 weeks). Accumulation of p62 and LC3 was observed only in RP11-RPE cells (**Figure 4-17**), suggesting that the waste disposal mechanism is impaired or overwhelmed, resulting in aggregate accumulation. Additionally, phagocytosis of POSs was observed after feeding of RP11 and control RPE cells with FITC-labelled POSs. Interestingly, FITC-labelled POSs accumulated and aggregated in RP11VS RPE cells compared to Cas9-RP11VS RPE cells. Altogether these results suggest that daily feeding of RP11-RPE cells with POSs accelerates the accumulation of cytoplasmic aggregates containing amongst others RLBP1, FK1 and HSPB1 proteins in RP11-RPE cells.

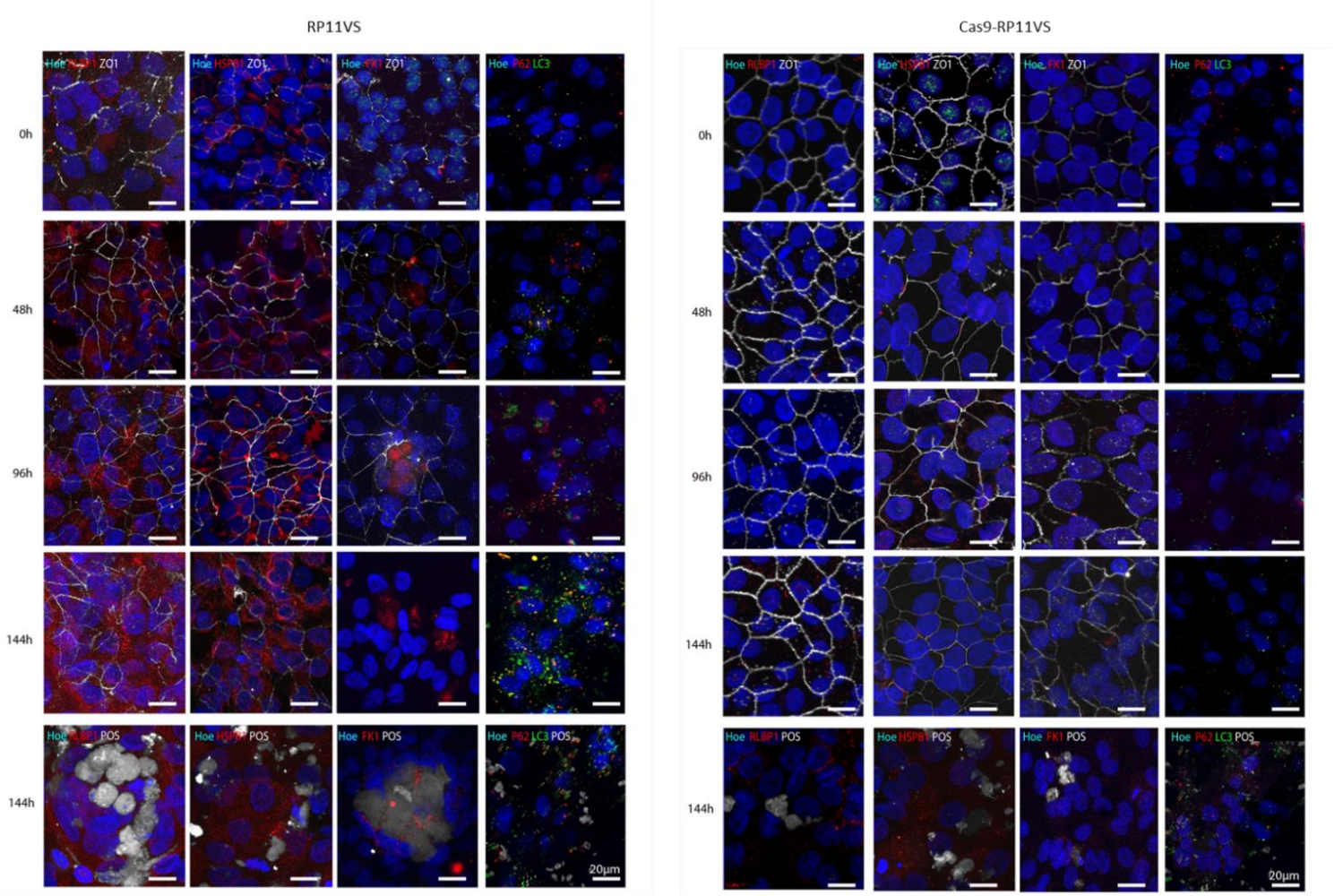

Figure 4-17: Evaluation of cytoplasmic aggregates in RP11 and control RPE cells after feeding with POSs. Representative immunofluorescent images of RP11-RPE and Cas9-RP11-RPE cells after daily feeding with unlabelled POSs (20 POSs/cell) and collection at different time points (0, 48, 96 and 144 hours post-feeding). Accumulation of cytoplasmic aggregates (containing RLBP1, HSPB1 and FK1 (red) and autophagic markers, LC3 (green) and p62 (red) in RP11-RPE cells only. To ensure internalisation of POSs, control and RP11-RPE cells were fed with FITC-labelled POSs (white) and were collected at 144 hours post-feeding. Cell nuclei were counterstained with Hoechst. Scale bars=20 µm. Representative images from 3 independent experiments.

4.4.12. Cytotoxic effects of cytoplasmic aggregates in RP11-RPE cells

To assess the impact of cytoplasmic aggregate accumulation on cell survival, control and RP11-RPE cells were immunostained with a Caspase-3 antibody as described in section 4.3.10. Caspase-3 is synthesised as an inactive proenzyme and is localised in the cytoplasm. However, during apoptosis, Caspase-3 is proteolytically cleaved (Luo et al., 2010), activated, and translocated into the nucleus causing fragmentation of DNA damaging essential cellular proteins, including enzymes involved in DNA repair (Kamada et al., 2005).

To identify the localization of Caspase-3 in control and RP11-RPE cells, IF analysis was performed. Using an anti-cleaved Caspase-3 antibody, the results revealed that Caspase-3 was predominantly expressed in the cytoplasm in control RPE cells in contrast to RP11-RPE cells (RP11VS) where Caspase-3 was mainly expressed in the nucleus (**Figure 4-18**), suggesting the activation of Caspase-3 in the latter.

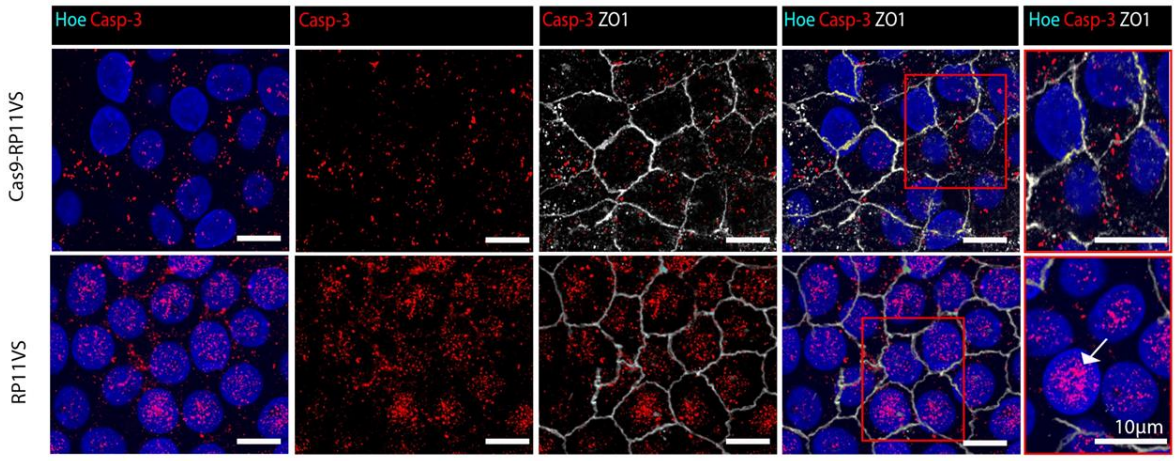

Figure 4-18: Activation of Caspase-3 in RP11-RPE cells. Immunofluorescence images of RP11VS and RP11VS-Cas9 RPE cells stained with Caspase-3 (red) and ZO1 (white) showing nuclear localisation of Caspase-3 in RP11-RPE cells (shown by white arrow) and cytoplasmic localisation in control RPE cells. Cell nuclei were counterstained with Hoechst. Scale bars =10µm. Analysis performed 12 weeks post plating of RPE cells in transwell inserts. Representative images from three independent experiments.

Taken together, our findings revealed the accumulation of cytoplasmic cellular aggregates containing amongst others both the wild type and mutated PRPF31 isoforms, misfolded ubiquitin-conjugated, chaperones, and visual cycle proteins in RP11-RPE cells. The proteasome-mediated and autophagy degradation pathways are both impaired, resulting in the progressive accumulation of these cytoplasmic aggregates with time. This process is exacerbated under physiological conditions, leading to disruption of tight junctions and cell death through apoptosis.

4.4.13. Elimination of aggregates in RP11-RPE cells by pharmacological interventions

In this current study, progressive accumulation of visual cycle proteins, chaperones, and misfolded-ubiquitinated proteins in the cytoplasm of RP11-RPE cells was detected. Therefore, to assess whether the cytoplasmic accumulation of aggregates could be eliminated, different pharmacological approaches were used as described in section 4.3.16; These are activators HSPs (Arimoclomol), inhibitors of UPR (Salubrinal and STF-083010) and activators of autophagy (Rapamycin and trehalose) (**Figure 4-19**).

4.4.13.1. Inducer of HSPs

Arimoclomol is a heat-shock protein co-inducer that has been shown to enhance the expression of HSPs *in vitro* (Vígh et al., 1997) and (Kieran et al., 2004) and to alleviate protein aggregation (**Figure 4-19**). Arimoclomol is an investigational drug currently in phase III of a clinical trial for ALS (Benatar et al., 2018) that has been shown to improve the survival of motor neurons in ALS mouse model (SODG93A). Additionally, Arimoclomol has been shown to reduce aggregation of P23H rod opsin in mutant rhodopsin-expressing cells (P23H rod opsin RP) to preserve retinal function and prolong the survival of PRs in P23H rhodopsin transgenic rat models (Parfitt et al., 2014).

4.4.13.2. Inhibitors of UPR

Another strategy to eliminate misfolded proteins is to target the UPR, which is mainly regulated by three distinct pathways known as IRE1α, ATF6 and PERK. Salubrinal is a selective inhibitor of the PERK pathway that blocks eIF2α leading to further inhibition of the protein synthesis (**Figure 4-19**) (Wang et al., 2019). Salubrinal protects the cell against apoptosis and has been shown to induce neuroprotective effects in ALS animal models (Huang et al., 2012, Saxena et al., 2009). A novel pharmacological compound known as STF-083010 is an effective inhibitor of IRE1 that blocks the splicing of *XBP1* (**Figure 4-19**) which mediates the UPR. Treatment with STF-083010 has been shown to decrease cell death and attenuate oxidative stress (Liu et al., 2018b).

4.4.13.3. Inducers of autophagy

Another strategy to eliminate accumulated misfolded proteins is to activate autophagy by inhibiting the mammalian target of rapamycin (mTOR) (Kim and Guan, 2015). mTOR exists in two complexes, mTORC1 and mTORC2. A common selective inhibitor of mTORC1 that activates autophagy is Rapamycin (**Figure 4-19**). Positive results have been obtained from a randomized please II clinical trial in which the efficacy of Rapamycin in the clearance of harmful cytoplastic aggregate-prone-proteins in patients with ALS was reported (Mandrioli et al., 2018). An alternative strategy to activate autophagy is through an AMPK-dependent activator. An example is Trehalose, which has been shown to activate autophagy in neural cells and confer beneficial effects in eliminating cytoplasmic aggregate-prone proteins (**Figure 4-19**) (Chen et al., 2016).

The effects of pharmacological agents on cytoplasmic aggregates were assessed following 7-day treatment of RP11S1-RPE cells (as mentioned in section 4.3.16) differentiated on trans-wells for 12 weeks. Immunostaining with RLBP1, HSPB1 and FK1 was performed to detect cytoplasmic aggregates. The data showed no obvious differences in the accumulation of cytoplasmic aggregates containing RLBP1, HSPB1 or FK1 in RP11VS-RPE cells treated with Salubrinal, Arimoclomol, STF-083010 or Trehalose (**Figure 4-20 A**). Interestingly, a significant reduction in cytoplasmic aggregate accumulation was observed in RP11VS-RPE cells treated with Rapamycin only (**Figure 4-20 A**). The same results were obtained in RP11S3-RPE cells harbouring a different *PRPF31* mutation (c.522_527+10del) (**Figure 4-21**). Also, Western blot analysis was performed to assess whether autophagy was indeed activated in RP11-RPE cells after treatment with Rapamycin, demonstrating a decrease in the expression of pS6 and S6 in the Rapamycin-treated RP11-RPE cells and an increase in the expression of LC3-I to LC3-II (**Figure 4-20 B**) However, no differences were detected in the expression of LAMP1 and p62. Furthermore, a decrease in the expression of RLBP1 and HSPB1 was detected after treatment of RP11S3 RPE cells with Rapamycin, suggesting that Rapamycin induced the activation of autophagy in RP11-RPE cells leading to a significant elimination of aggregates containing RLBP1, HSPs or FK1 in RP11-RPE cells (**Figure 4-20 B**). Together, our results suggest that Rapamycin has induced the activation of autophagy in RP11-RPE cells, providing beneficial effects in eliminating aggregates containing RLBP1, HSPs or FK1 in RP11-RPE cells. Our results agree with other studies using *Drosophila* (Berger et al., 2006) and mouse models (Ravikumar et al., 2004), which are characterised with aggregate-prone proteins, showing the clearance of cytoplasmic aggregates after treatments with Rapamycin. These

results demonstrate the potential of Rapamycin for therapeutic use in diseases associated with aggregate accumulation (Berger et al., 2006, Ravikumar et al., 2004).

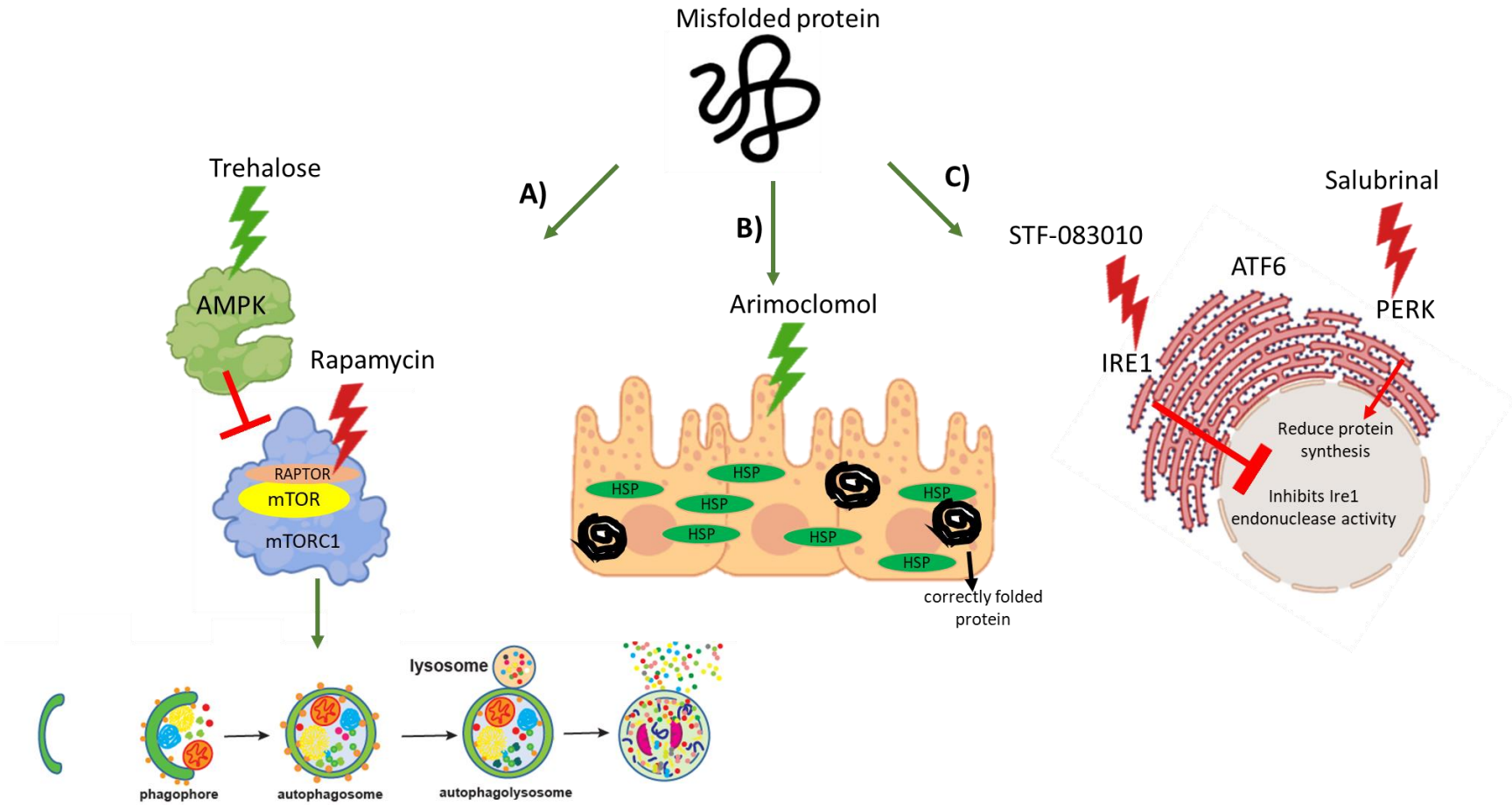

Figure 4-19: Overview of pharmacological strategies to target misfolded proteins. Activation of autophagy by targeting the mTOR-dependent pathway and the mTOR-independent pathway using Rapamycin (that blocks mTORC1) and Trehalose, respectively. Misfolded proteins can be rescued, and protein aggregates could be clear by B) HSPs, which their production is amplified by Arimoclomol. C) Another strategy to reduce misfolded and aggregated proteins is by targeting the UPR pathway by selectively blocking any of the three distinct pathways. Salubrinal inhibits PERK by selectively blocking eIF2α. Inactivation of eIF2α prevents further the influx of proteins in the ER lumen and hence reduce protein synthesis. Also, STF-083010 selectively inhibits IRE1 endonuclease activity inhibiting cell death.

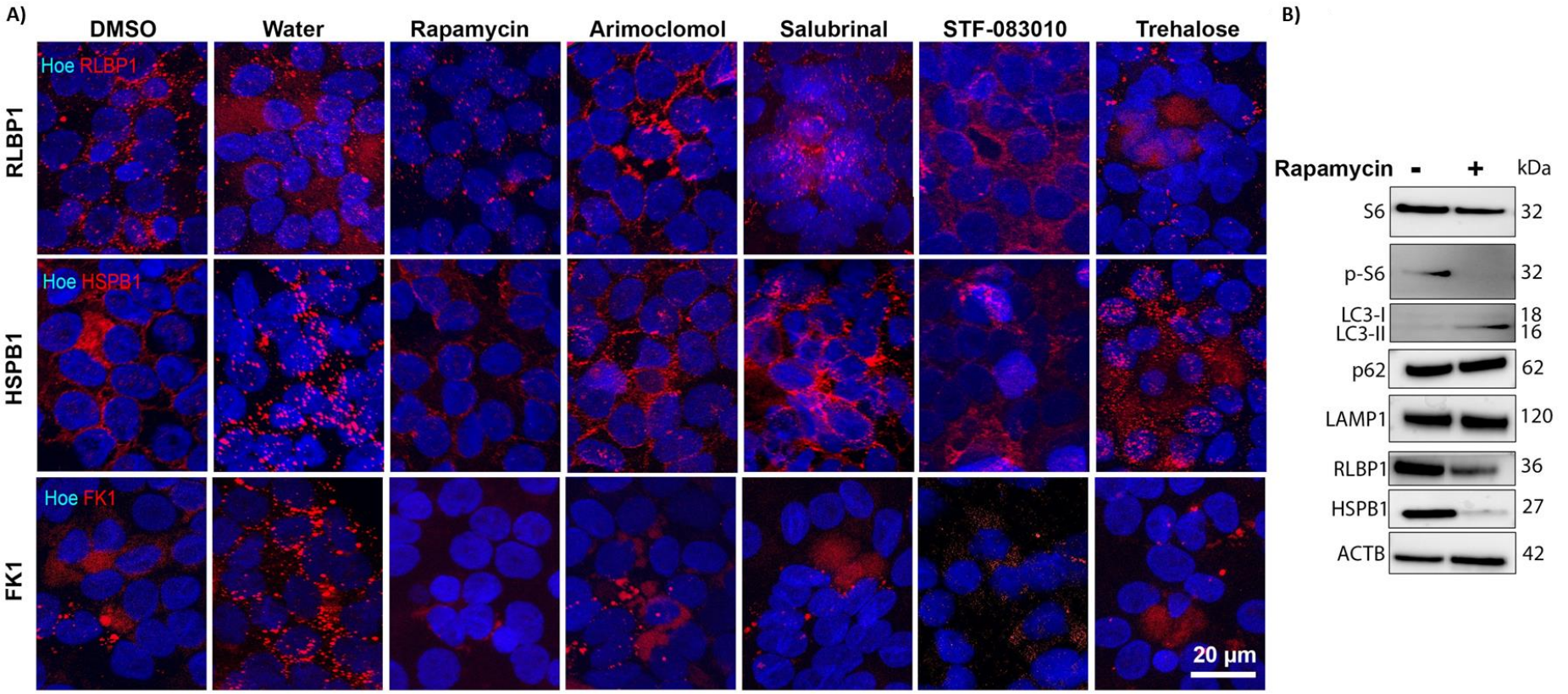

Figure 4-20: Elimination of aggregates in RP11-RPE cells by application of pharmacological interventions. A) Immunostaining of RP11S1-RPE cells showing a significant decrease of cytoplasmic aggregates containing RLBP1, HSPB1 and FK1 (red) upon daily treatment with Rapamycin (500 nM) for 7 days. Seven days of treatment with Arimoclomol (1 µM), Salubrinal (25 µM), STF-083010 (50 µM) and Trehalose (50 mM) showed no significant differences. DMSO or distilled water were used as vehicle controls. Cell nuclei were counterstained with Hoechst. Scale bars=20 µm. B) Western blot showing a decrease in the expression of S6, p-S6 RLBP1, HSPB1, and activation of LC3-II in Rapamycin-treated RP11S3-RPE cells compared to vehicle-treated RP11S3 RPE cells. Analysis performed 12 weeks post-plating of RPE cells in transwell inserts. Representative images from three independent experiments.

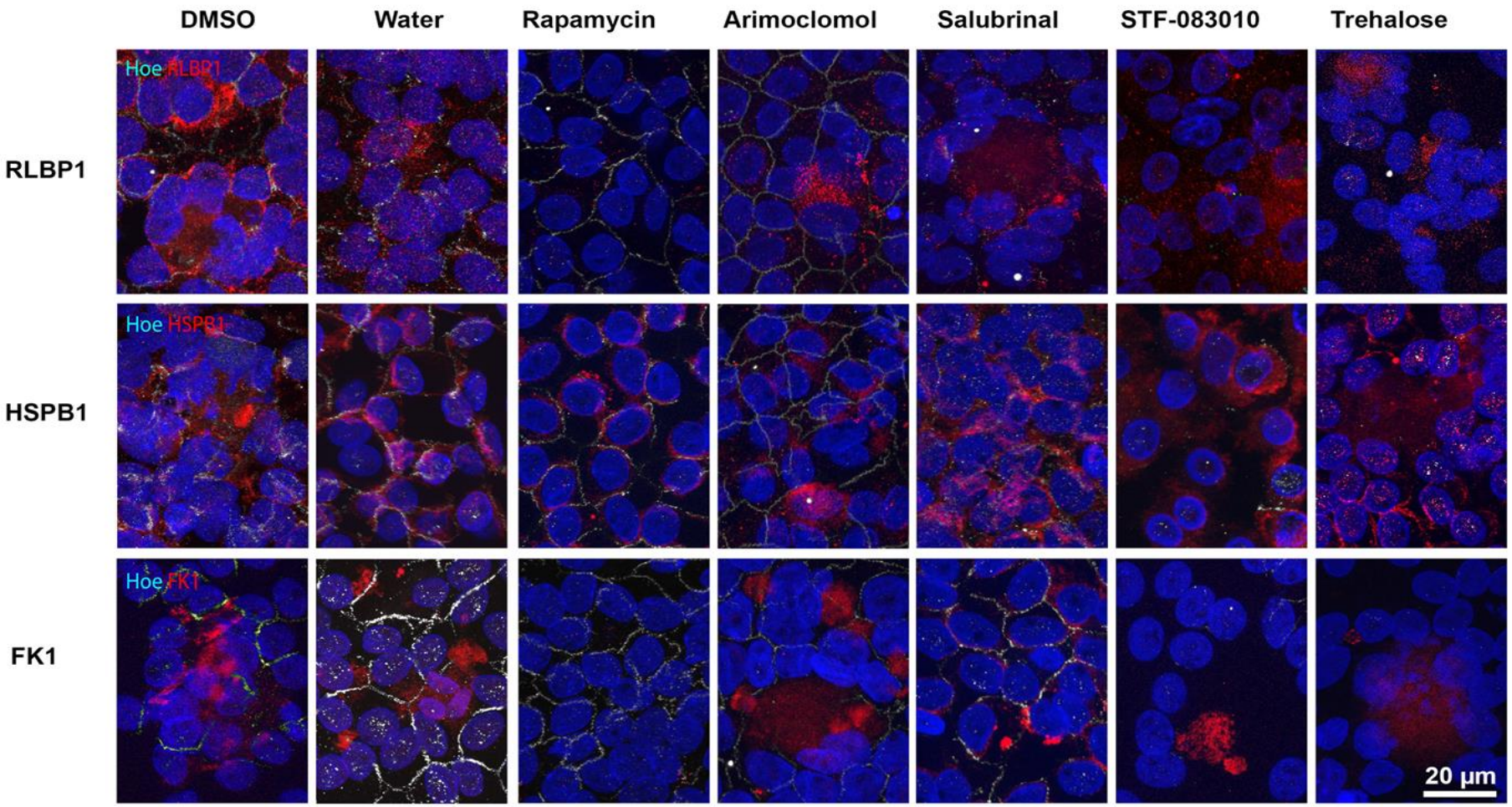

Figure 4-21: Elimination of aggregates in RP11-RPE cells by pharmacological interventions in RP11S3-RPE cells. Immunostaining of RP11S3-RPE cells showing a significant decrease of cytoplasmic aggregates containing RLBP1, HSPB1 and FK1 (red) upon daily treatment with Rapamycin (500 nM) for 7 days. No significant differences were detected after 7 days of treatment with Arimoclomol (1 µM), Salubrinal (25 µM), STF-083010 (50 µM) and Trehalose (50 mM). Cell nuclei were stained with Hoechst. Scale bars=20 µm. Analysis performed 12 weeks post-plating of RPE cells in transwell inserts. Representative images from three independent experiments.

4.4.14. Decreased activated Caspase-3 after treatment with Rapamycin

The previous results showed that cytoplasmic aggregates containing RLBP1, HSPB1 and FK1 in RP11-RPE cells could be eliminated after 7 days of treatment with Rapamycin. Therefore, the effects of Rapamycin on cell survival after 7 days treatment of RP11-RPE cells with vehicle or Rapamycin were assessed by IF analysis using an anti-cleaved Caspase-3 antibody as described in section 4.3.10.

The results showed that Rapamycin-treated RP11-RPE cells had reduced nuclear localization of Caspase-3 compared to vehicle-treated RP11-RPE cells, indicating a positive effect in cell survival (**Figure 4-22**). These results suggest that Rapamycin has a positive impact on the elimination of cytoplasmic aggregates, potentially leading to enhanced cell survival.

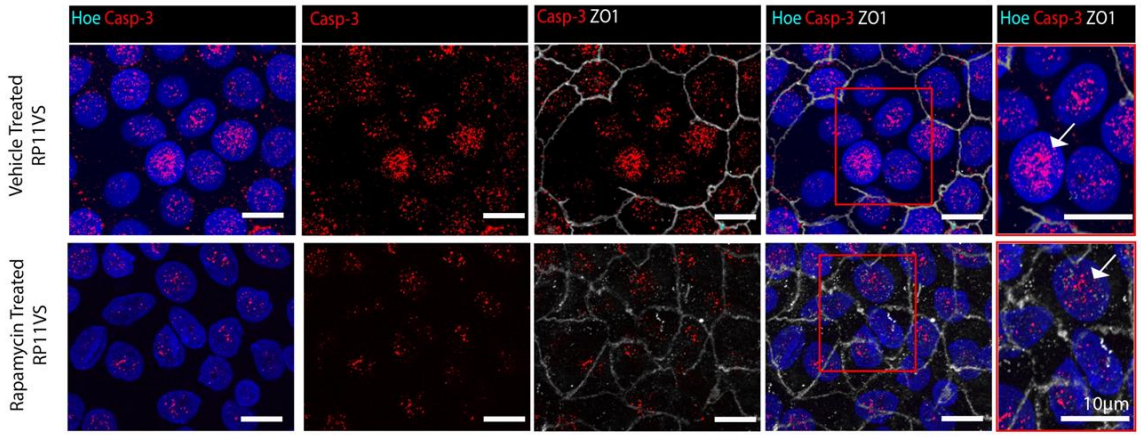

Figure 4-22: The effects of Rapamycin on RP11VS-RPE cell survival. Immunofluorescence images of Rapamycin and vehicle-treated RP11VS-RPE cells stained with Caspase-3 (red) and ZO1 (white) showing reduced nuclear levels of cleaved Caspase-3 in the nucleus of Rapamycin-treated RP11VS-RPE cells (shown by white arrow). Analysis performed 12 weeks post-plating of RPE cells in transwell inserts. Representative images from three independent experiments.

4.4.15. Phagocytosis

Phagocytosis of POSs is one of the most important functions of RPE cells. The RPE cells engulf shed POSs from PRs daily to maintain the PR cells. However, defects in this process could cause several retinal diseases.

To assess the ability of RPE cells to phagocytose, untreated and 7 days vehicle- or Rapamycin-treated control and RP11-RPE cells were fed with FITC-labelled POSs (**Figure 4-23 A**) and analyzed by Fluorescence-activated cell sorting (FACS) as mentioned in section 4.3.14. For the robustness of the data, a number of control experiments were used. RP11-RPE cells were fed with FITC-labelled POSs at 4°C to block their ability to phagocytose (**Figure 4-23 B**). Also, RPE cells were fed with unlabeled POSs to assess background fluorescence (**Figure 4-23 B**). Additionally, to prevent false-positive fluorescence signals from free or unbound POSs, Trypan blue was used to quench any extracellular fluorescence. Analysis of the results was performed by FCS Express 7.

The results were expressed as a percentage of FITC-positive cells, indicating the percentage of cells from the total population that have ingested POSs, and as median fluorescence intensity (MFI), indicating the amount of FITC-labelled POSs internalized by individual cells as an indication of cell-surface receptor density involved in phagocytosis.

The results indicated that there were no significant differences in the percentage of FITC-positive cells that internalized POSs between untreated and Rapamycin-treated RP11-RPE (**Figure 4-23 C**). Similarly, no significant differences were observed in MFI values between untreated and Rapamycin-treated RP11VS and RP11S1 RPE cells. However, a significant difference in MFI values was observed between untreated and Rapamycin-treated RP11S3 RPE cells (**Figure 4-23 C**), suggesting that probably Rapamycin improved phagocytosis of POSs only in RP11S3 RPE cells.

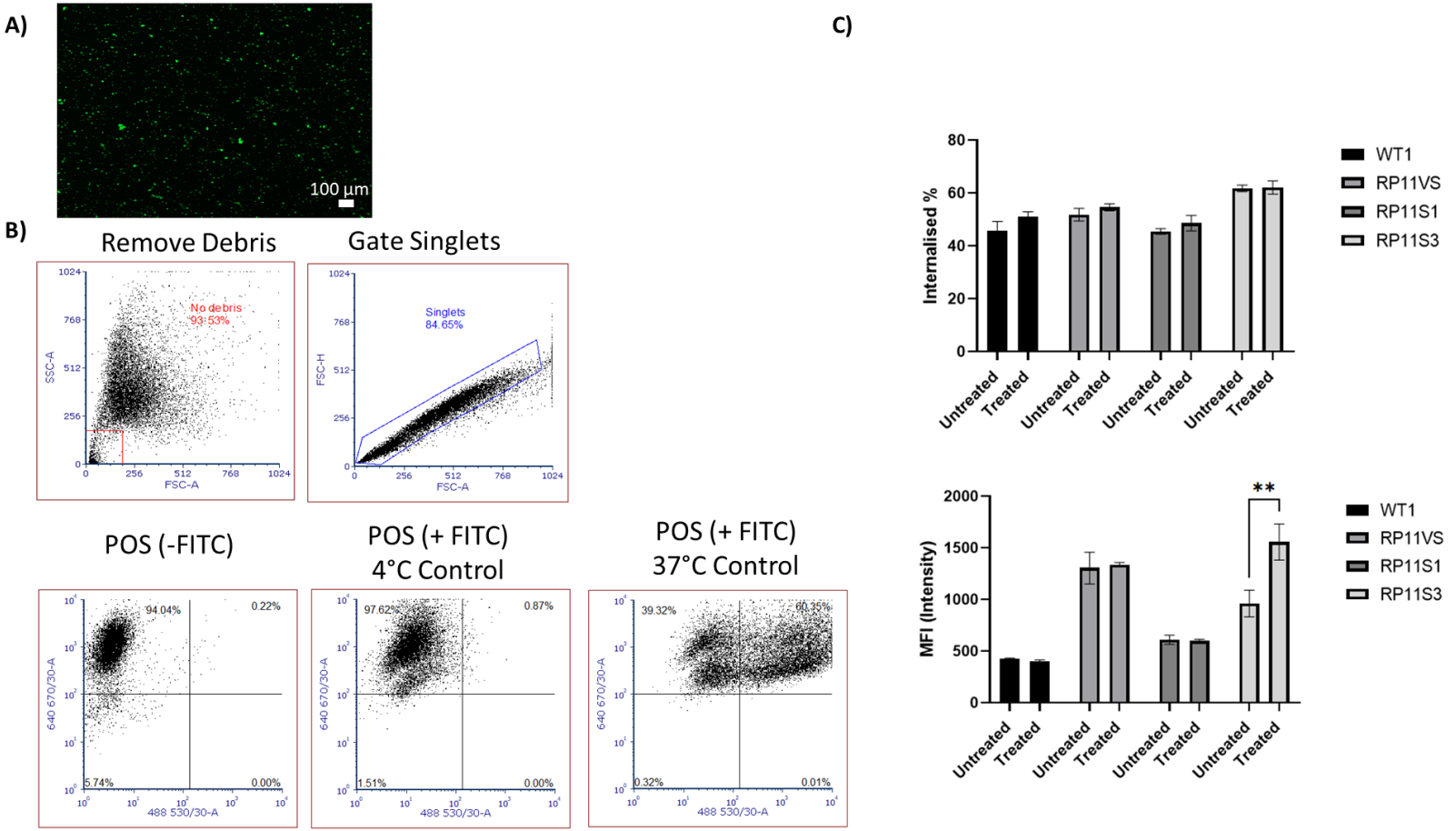

Figure 4-23: Phagocytosis of photoreceptor outer segments in hiPSC-derived RPE cells by flow cytometry. A) FITC-labelled POSs. B) Example of the results fed with unlabelled, 4°C FITC-labelled, and 37°C labelled POSs. C) The results show no significant differences in the percentage of internalised POSs between Rapamycin-treated and untreated RP11-RPE cells. No significant differences were detected in the number of POSs internalised by each cell in Rapamycin-treated and untreated RP11VS and RP11S1 RPE cells. However, an increase in the MFI value in Rapamycin RP11S3 RPE cells was seen compared to untreated RP11S3 RPE cells. All cells were age-matched with regards to the length of differentiation time (~5 months). Statistically significant differences are indicated by *t*-test (**p< 0.001). The data are shown as mean ± SEM, n=3.

4.4.16. The effects of Rapamycin treatment on tight-junction integrity in RP11-RPE cells

The findings of this study revealed that cytoplasmic aggregates disrupt the tight junctions in RP11-RPE cells; however, 7-day treatment of RP11-RPE cells with Rapamycin has shown to eliminate the presence of these cytoplasmic aggregates. Therefore, to investigate whether tight junction integrity can be improved, TER measurements were taken, as mentioned in section 4.3.4.2, before and after 7 days treatment of RP11-RPE cells with Rapamycin or with vehicle (DMSO).

The results indicated that Rapamycin-treated RP11-RPE cells have lower TER measurements compared to vehicle-treated RP11-RPE cells (**Figure 4-24**). These results suggest that despite the beneficial effects of Rapamycin in reducing cytoplasmic aggregates, the tight junction integrity of RP11-RPE cells cannot be restored upon treatment with Rapamycin at the selected dose and treatment duration.

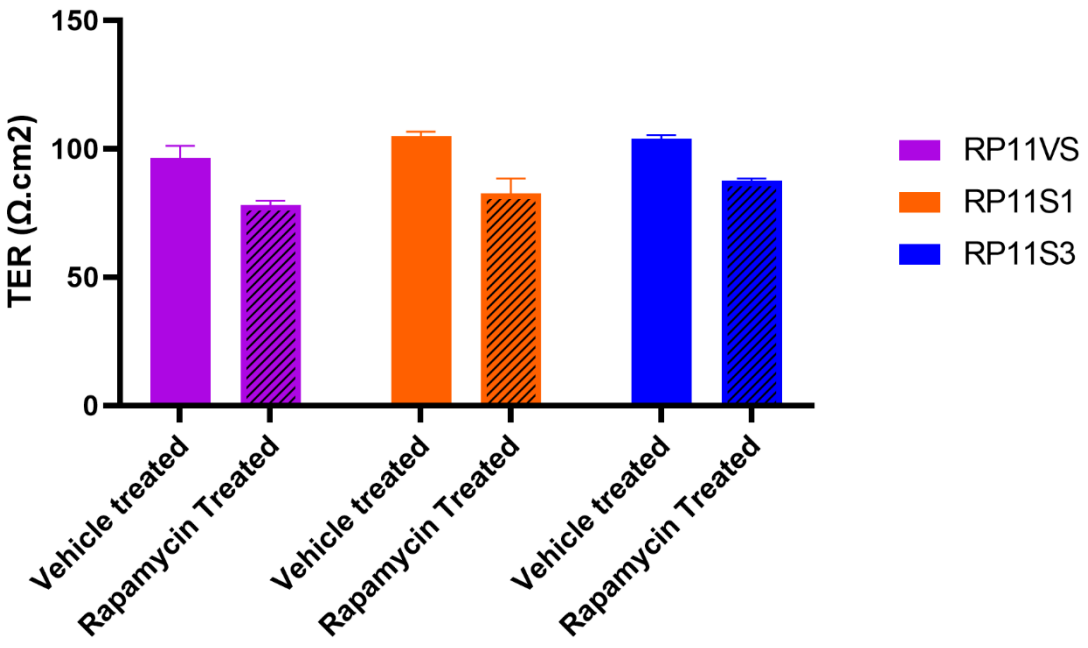

Figure 4-24: Trans-epithelial resistance of Rapamycin and vehicle-treated RP11-RPE cells. TER values of RP11-RPE cells decreased after 7 days of treatment with Rapamycin compared to RP11-RPE cells treated with vehicle. Data are shown as mean ± SEM, n=5.

4.5. Discussion

The generation of hiPSC-derived RP disease models provides a powerful tool to study and identify the mechanisms causing RP and investigate the impact of mutations on the proteome of retinal cells. *PRPF31* mutation accounts for approximately 15% of RP cases, and although PRPF31 is ubiquitously expressed and is involved in the formation and stability of U4/U6.U5 tri-snRNPs, mutations have been associated with retinal-specific phenotypes specifically.

In previous work, using a hiPSC-disease modelling approach, we have shown that mutations in the spliceosomal U4/U6 snRNP-specific protein PRPF31 result in global splicing changes, specifically in retinal cells and RPE (Buskin et al., 2018). To fully understand the impact of such global splicing dysregulation on the RPE cells, we have undertaken a detailed quantitative proteomic and immunofluorescence analysis of RPE cells harbouring *PRPF31* mutations. These new findings have shown the predominant accumulation of mutant PRPF31 protein as aggregates in the cytoplasm of RPE cells. This results in reduced nuclear levels of wild type isoform in RP11 patient RPE cells. Quantitative proteomics revealed that several key cellular processes in addition to mRNA splicing, namely waste disposal and UPR were significantly affected, resulting in progressive accumulation of insoluble aggregates containing key components of each of the aforementioned pathways within RPE cells, that affected cell survival. Aggregate formation also affected the expression and/or localization of key proteins of the retinoid metabolism and visual perception pathways, including RLBP, which accumulated in the PRPF31 cytoplasmic aggregates. Furthermore, proteomic analysis of insoluble aggregates in RP11-RPE cells identified the presence of other core components of the tri-snRNP including PRPF6, PRPF4 and PRPF8 (all of which are linked to adRP) together with chaperone proteins important for U4/U6 and U5 snRNPs assembly. Strikingly, activating autophagy via the application of Rapamycin resulted in the reduction of these cytoplasmic aggregates and improved cell survival (**Figure 4-25**).

Aggregation of PRPFs in retinal PRs and RPE cells has been reported previously and shown to be cell type specific. For example, the mutant PRPF3^{T494M} amasses in big aggregates in the nucleolus region (Comitato et al., 2007), causing mislocalisation of splicing factors that may be detrimental for PR cells. In contrast, the mutant PRPF31 protein forms insoluble aggregates in the cytoplasm of RPE cells of Prpf31$^{A216P/+}$ mice (Valdés-Sánchez et al., 2019), decreasing the protein levels of this splicing factor in the nucleus. Our data show reduced nuclear expression of the wild type PRPF31 and cytoplasmic localisation of mutant PRPF31 protein, corroborating the mouse RPE studies. Nonetheless, the impacts of *PRPF* mutations on tri-snRNPs formation,

the spliceosome activity and abundance directly on patient-specific RPE cells has not been reported previously.

In addition to splicing dysregulation, our proteomics data revealed an enrichment of proteins involved in the retinoid metabolic process and visual perception. Of particular interest in the retinoid metabolic and visual perception is the Retinaldehyde-binding protein (RLBP1), which is significantly overexpressed in RP11-RPE cells and found in the form of cytoplasmic aggregates. RLBP1 is a retinoid-binding protein expressed in RPE and Müller glial cells and involved in the conversion of 11-*trans*-retinal to the light-sensitive 11-*cis* retinal (Xue et al., 2015). Mutations in RLBP1 cause a range of retinopathies, including retinitis punctata albescens (RPA), Bothnia-type dystrophy (BD), Newfoundland rod-cone dystrophy (NFRCD), RP and fundus albipunctatus (FA) (Hipp et al., 2015). Based on our data, our hypothesis is that the accumulation of RLBP1 in the insoluble aggregates reduces the available RLBP1 protein needed for recycling of retinal, impacting directly on the visual cycle and the phototransduction pathway.

Studies performed in the RPE of Prpf31$^{A216P/+}$ mice have revealed overexpression of heat shock protein 70 (Hsp70) family and its co-localisation with mutant PRPF31 in the insoluble cytoplasmic aggregates. It is reasonable to assume that protein aggregation of mutant PRPF31 is responsible for activating the chaperone response. Corroborating these studies, our data also revealed significant changes in expression of several HSPs and overexpression of HSPA4L, HSPB1 and HSPA2, that accumulated in the form of aggregates in association with PRPF31 in RP11-RPE cells. HSPs facilitate protein homeostasis and cell protection against damaged proteins or aggregation of harmful denatured proteins. Their upregulation in RP11-RPE cells could be a direct response of global splicing deregulation, which is bound to result in misfolded or aggregated proteins, as shown in our study. Previous studies have reported that under stress conditions (e.g. hyperglycemia) or upon mutations, soluble HSPs are depleted, becoming unavailable to target other proteins, affecting further their functionality (Reddy et al., 2013) and leading to the accumulation of insoluble aggregates in the retina (Reddy et al., 2013). Our data demonstrate preferential HSP accumulation in the insoluble aggregates of RP11-RPE cells, suggesting a change in their solubility and function, which could be due to "overwhelming" of HSP response by a large amount of misfolded or aggregates proteins resulting from the global spliceosome dysfunction.

The formation of cytoplasmic aggregates is a common hallmark event of many neurodegenerative diseases and is associated with protein misfolding (Sweeney et al., 2017). Usually, in response to misfolded protein, cellular defence mechanisms like molecular

chaperones such as HSPs are activated. However, when quality control systems are incapable to restore the normal conformation of denature proteins and thus are overloaded with an excessive amount of denatured proteins, then it is possible that the solubility of HSPs can be transformed from a soluble state to an insoluble form, as shown in this study. When HSPs fail to restore misfolded proteins, denatured or aggregated proteins are tagged with ubiquitin (Ub) and are directed to the Ub-proteasome system (UPS) for proteolytic degradation (Ciechanover and Kwon, 2015). Our results revealed increased protein ubiquitination and reduced enzymatic activity (trypsin-like) of the proteasome degradation system in RP11-RPE compared to control RPE cells. The reduced proteasome activity revealed in our results is also a common characteristic feature of other NDs such as AD, PD, ALS, and HD (Ciechanover and Kwon, 2015). Particularly in AD disease, various studies have shown that tau aggregates can bind to the recognition site of the 19S catalytic particle of the proteasome, inducing protein congestion that further leads to impairment of protein degradation (Tai et al., 2012). Also, misfolded prion proteins (β-sheet-rich PrP) in Prion disease disrupt the opening of the 20S proteasome particle, thus inhibiting the function of the 26S proteasome (Andre and Tabrizi, 2012). This association of pathogenic protein aggregates and reduced or blocked proteasome activity has been reported by several studies focusing on the AD (Lindersson et al., 2004, Gregori et al., 1995). Our data mirror these findings, however, in the case of RP11-RPE cells, it is unknown whether the accumulation of misfolded/aggregated proteins is a result of decreased proteasome activity or whether the proteasome system is incapable of coping with the burden of misfolded, ubiquitinated and aggregated proteins resulting from global spliceosome dysregulation.

Under stress conditions when the chaperone and proteasome systems are overwhelmed, clearance of cytoplasmic aggregates is facilitated by autophagy, where cytoplasmic substrates are engulfed and degraded into amino acids (Ciechanover and Kwon, 2015). Although most proteins in the human genome can be successfully degraded from the cells, genetic defects can affect their conformation leading to the formation of aggregates. For example, mutations of huntingtin proteins inhibit the proteolytic machinery and induce the accumulation of cytoplasmic aggregates in patients with HD (Qi et al., 2012). This is characterised by an increase of key autophagic components such as p62, LC3 in HD mouse models due to the impairment of cargos to be directed to autophagic vacuoles for degradation (Martinez-Vicente et al., 2010). Likewise, our results demonstrate an upregulation of p62 and LC3 expression in RP11-RPE cells compared to control RPE cells suggesting an impairment of autophagy. We hypothesise that this combined dysfunction of proteasome and autophagy-mediated degradation together with accumulation of HSPs in the insoluble fractions leads to the accumulation and

growth of larger aggregated proteins, which may be cytotoxic to the cells. This is a characteristic of many NDs such as HD, AD, PD, and ALS, where mutant aggregated proteins become resistant to degradation, inducing cytotoxicity and neuronal cell death (Ciechanover and Kwon, 2015). To this end, it has been reported that neuronal cells of AD patients (Louneva et al., 2008) have increased levels of Caspase-3, associated with degeneration of synapses and a decrease in synaptic plasticity, suggesting that intracellular protein deposits might disrupt the normal function of neurons, inducing stress which in turn leads to the initiation of cell death. Similarly, our results have shown the progressive accumulation of large cytoplasmic aggregates containing the mutant PRPF31 itself as well as misfolded, ubiquitin conjugated, and visual cycle proteins found in areas with disrupted tight junctions and increased Caspase 3 activity. Tight junction disruption has been reported by other studies associating RPE remodeling with retinal degeneration (Falasconi et al., 2019). Collectively these results suggest that continuous accumulation of aggregates in patient-specific RP11-RPE cells impairs RPE cell survival.

One potential strategy to enhance the degradation of misfolded proteins is to induce the activation of autophagy. Many small molecules have been developed to activate autophagy and induce clearance of pathogenic proteins, and the most widely known is by inhibiting mTORC1 by Rapamycin. It has been shown that Rapamycin can effectively reduce cytoplasmic mutant proteins such as α-synuclein (Webb et al., 2003), huntingtin (Sarkar and Rubinsztein, 2008), or tau mutant proteins (Rodriguez-Navarro and Cuervo, 2010) from the brains of transgenic mouse models. Our study showed that treatment of RP11-RPE cells with Rapamycin for 7 days at a selected concentration can reduce cytoplasmic aggregates and can improve cell survival; however, the integrity of tight junctions as well as the ability of RP11-RPE cells to phagocytose have not been improved. Nevertheless, a significant increase in the number of POSs phagocytosed by RP11S3 Rapamycin-treated cells was observed compared to vehicle-treated RP11S3 cells. However, other pharmacological treatments targeting autophagy (Trehalose), ER stress (Salubrinal and STF-083010) or inducers of HSPs such as Arimoclomol had no beneficial effects in reducing the volume of cytoplasmic aggregates in RP11-RPE cells at the selected concentrations used. The improved aggregate clearance by activation of autophagy via Rapamycin administration indicates that it is the progressive aggregate accumulation that overburdens the waste disposal machinery rather than direct PRPF31 initiated misplicing. Hence therapeutic strategies aiming at waste disposal activation present an important approach that needs to be investigated in close conjunction with gene therapy studies. Work was published in Georgiou et al 2021. These data were published and can be found in the following link: https://www.biorxiv.org/content/10.1101/2021.10.11.463925v1.

4.6. Conclusion

Mutations in pre-mRNA processing factor 31 (*PRPF31*) result in autosomal-dominant retinitis pigmentosa (adRP), characterised by global dysregulation of spliceosome in retinal cells and the adjacent retinal pigment epithelium (RPE). Proteomic analysis of RPE cells from three patients with severe and very severe adRP revealed RNA splicing, protein folding (UPR) and visual cycle-related pathways to be significantly affected. The patient-derived RPE were characterised by the presence of insoluble aggregates containing the mutant PRPF31 and misfolded, ubiquitin-conjugated proteins, including key visual cycle protein, which accumulated progressively with time. The waste disposal mechanisms via autophagy and proteasome-mediated degradation were impaired, further exacerbating aggregate formation, which was closely linked with activation of cell death (**Figure 4-25**). Targeting the waste disposal mechanisms by activating the autophagy pathway using Rapamycin resulted in the reduction of these cytoplasmic aggregates in RP11-RPE cells, leading to improved cell survival (**Figure 4-25**). Together these data indicate a vicious circle initiated by mutations in *PRPF31*, which lead to spliceosome dysregulation and accumulation of misfolded proteins in the form of insoluble cytoplasmic aggregates that affect RPE cell survival. Relieving the RPE cells from the accumulation of these insoluble cytoplasmic aggregates presents a novel therapeutic strategy (**Figure 4-25**) that can be combined with gene therapy studies to fully restore RPE function in RP11 patients.

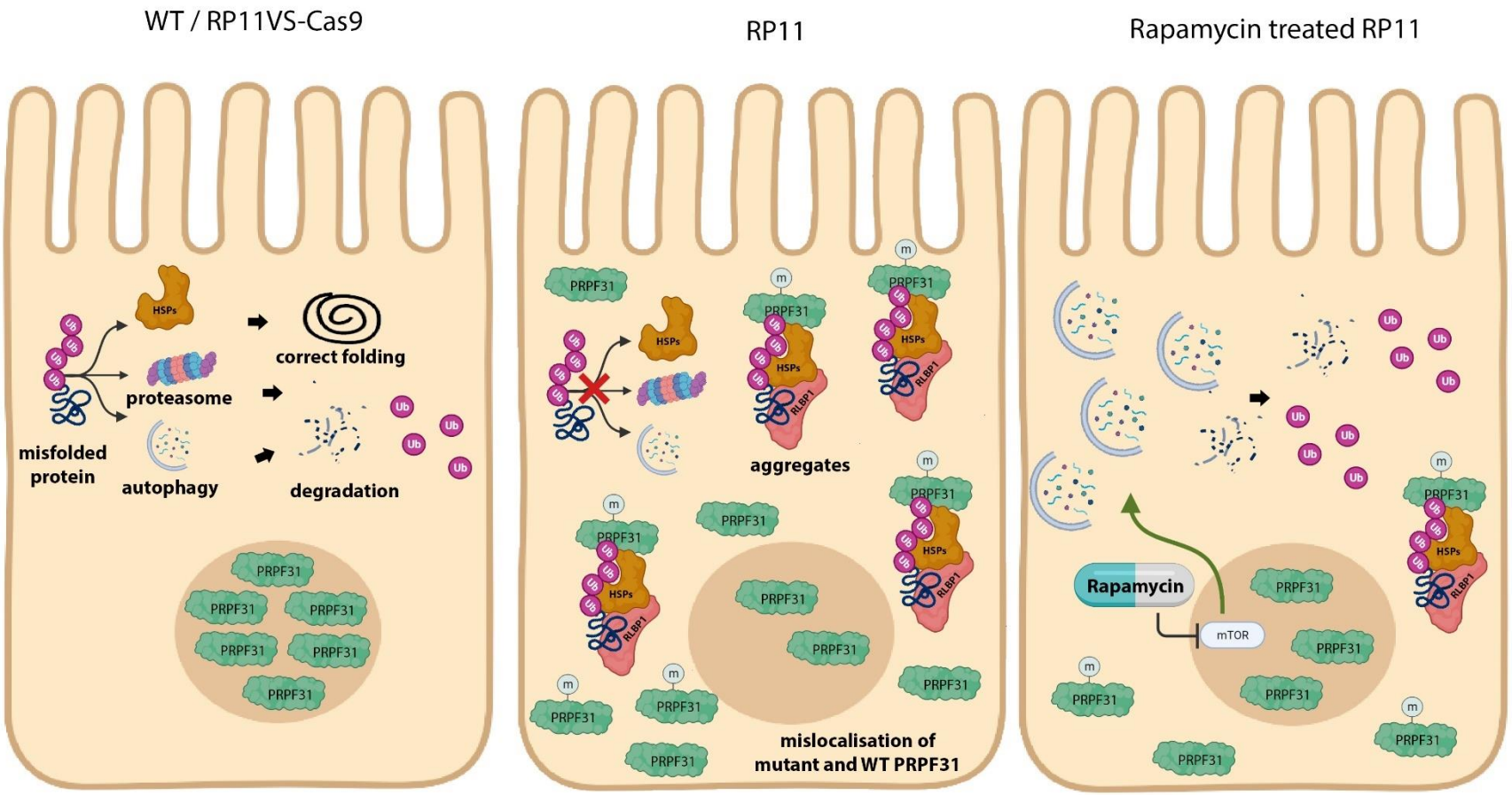

Figure 4-25: Schematic presentation showing the pathway in control, RP11 and Rapamycin-treated RP11-RPE cells. The diagram illustrates the localisation of mutant PRPF31 in the cytoplasm of RP11-RPE cells and the accumulation of aggregates containing HSPs, visual cycle and ubiquitin conjugated proteins, which were much reduced upon application of Rapamycin (autophagy activator). m=mutant PRPF31, WT= Wild type PRPF31, Ub-ubiquitin.

Chapter 5

Chapter 5. General Discussion and Future Work

Inherited retinal diseases (IRDs) are a diverse group of heterogeneous disorders leading to blindness. Approximately 1 in 3000 individuals (Olivares-Gonzalez et al., 2021) and more than 2 million people are affected worldwide. IRDs are characterised by the gradual degeneration of key retinal cells, including PRs and RPE cells. The loss of retinal cells leads to visual impairment and blindness in the working-age population, profoundly impacting individuals' quality of life (Jones et al., 2003). IRDs have some common pathological features; however, they are clinically and genotypically variable with a broad spectrum of symptoms such as loss of visual acuity, night vision problems, visual field defects and colour vision difficulties (Sahel et al., 2014). There are many different types of IRDs classified as syndromic and non-syndromic, with the most common to be Retinitis Pigmentosa (RP) with 1:4000 individuals affected worldwide (Cremers et al., 2018). Individuals with RP are characterised by progressive loss of peripheral retinal cells leading to blindness (Hamel, 2006).

Animal models such as mice, monkeys, primates and dogs have been used for disease modelling providing major insights into the pathogenesis of many diseases, including retinal dystrophies (Moshiri et al., 2019, Winkler et al., 2020). Despite the numerous advantages, animal models do not faithfully mimic key aspects of human pathophysiology due to the differences between human and animal species in terms of retinal architecture, cellular composition and longevity (Singh et al., 2015), preventing full understanding of the mechanisms or pathways causing retinal dystrophies. Despite the existing ethical issues, animal models are very expensive, and their response to drugs is not always similar to the human response (Doke and Dhawale, 2015). An alternative method to study retinal diseases is patients' primary cells; however, their availability is limited.

Instead, hiPSCs are an excellent choice for drug testing and disease modelling as they can be patient-specific, mimicking disease phenotypes and studying the pathogenesis of the diseases (Karagiannis et al., 2019). These advantages give the possibility to differentiate hiPSCs into retinal organoids (Nakano et al., 2012, Mellough et al., 2012) or RPE cells (Buchholz et al., 2009).

In this study, retinal-specific cells mimicking human retinal and RPE cells were generated from hiPSCs to study their applications in cryopreservation (Chapter 2), shipping (Chapter 3) and disease mechanisms causing RP (Chapter 4), which are discussed below:

5.1. Cryopreservation

The first aim of this thesis was to generate and establish a novel reproducible cryopreservation method to freeze retinal organoids (Chapter 2). Cryopreservation protocols were adopted from previous cryopreservation studies that reported the successful cryopreservation of complex tissues (Pichugin et al., 2006, Richards et al., 2004, Fayomi et al., 2019, de Vries et al., 2019). Building upon previously tested cryopreservation methodologies, key factors, such as the concentration of cryoprotectants (CPAs), the incubation time of organoids with CPAs, and the cooling and thawing rate, were modified according to the total freezing volume and the number of organoids used per cryovial. The cryopreserved retinal organoids were compared to control (non-cryopreserved) retinal organoids, and a brightfield microscope was used to assess their overall structural integrity and presence of the neuroepithelium. Cryopreserved organoids that maintained their overall structural integrity after 14-days post-thaw were collected and analyzed further by immunofluorescence analysis using retinal-cell specific markers to quantify the expression of retinal-related cells. I have tested several different cryopreservation protocols in this study, including slow and fast freezing and vitrification methodologies. Among all, the most effective cryopreservation protocol was the 'Master Liver Supercooling' protocol. Compared to all other protocols that were tested in this study, cryopreserved organoids using the 'Master Liver Supercooling' protocol retained their overall structural integrity and morphology and preserved PR cells in all experimental runs. However, not all retina cells survived, and their presence was variable within different experimental runs. This study enhances our knowledge and understanding of the most suitable conditions for cryopreserving retinal organoids and offers the foundations for building an optimal protocol. To the best of my knowledge, no previous studies have reported the cryopreservation of whole retinal organoids at day 80 or older after cryopreservation.

5.1.1. Strengths

Cryopreservation is vital for the long-term storage of tissues at cryogenic temperatures. In this study, attempts to cryopreserve and store mature retinal organoids were performed, aiming to provide retinal organoids to pharmacological companies and collaborating labs for drug and toxicological tests on demand supply.

The generation of retinal organoids is a labour-intensive method that requires skilled researchers. It is a very lengthy procedure and demands precision. Developing a cryopreservation method allows the storage of many retinal organoids, reducing the laborious

continuous generation of organoids without limiting their availability. Also, cryopreservation of a large number of organoids reduces batch to batch variability.

The ‘Master Liver Supercooling’ protocol, which has been the most promising protocol in this study for the cryopreservation of organoids, contains reagents and CPAs that are commonly used, relatively cheap, and easily accessible, allowing the application of the protocol by other researchers worldwide. In contrast, some cryopreservation studies use ready-made CPAs that are usually expensive, increasing the experiment's cost, especially when using a large number of samples. Usually, ready-made CPAs are provided by specific suppliers or companies, limiting their availability (Arai et al., 2020, Pichugin et al., 2006).

The ‘Master Liver Supercooling’ is relatively quick and easy protocol to follow without requiring specialized skills. A major advantage of this protocol is that no special equipment are needed, apart from the Via freeze machine, which can be substituted by any other automated freezing machinery, making this procedure applicable globally. In contrast, other cryopreservation protocols require special equipment such as thawing devices (Heger et al., 2017), limiting the protocol's application or replication in other laboratories.

In our study, retinal organoids derived from two control cell lines (WT2 and WT3) were cryopreserved using the ‘Master Liver Supercooling’ protocol with no significant variation in their overall survival. This implies that the differences observed between control and cryopreserved retinal organoids are not cell-line dependent, suggesting that probably retinal organoids derived from different control and probably patient cell lines can be cryopreserved using the same methodology.

In this study, several cryopreservation protocols, including vitrification and slow-cooling experiments, were tested. Additionally, several CPAs, cooling rates and freezing temperatures were assessed to define an optimal cryopreservation protocol. Despite the variable and negative results obtained from most cryopreservation experiments tested herein, including the loss of the bright phase neuroepithelium and the shrinkage of organoids, this study provides information about which reagents, CPAs, and freezing conditions may be more optimal for future cryopreservation studies in retinal organoids.

5.1.2. Limitations

The ‘Master Liver Supercooling’ protocol was the most promising approach for the cryopreservation of mature retinal organoids. Although this protocol preserves the structure and

morphology of retinal organoids to some extent, the overall survival needs to be further improved. Based on the IF results, cryopreserved organoids lost several key retinal cells compared to control sections, and the structure of cryopreserved organoids was not fully preserved. Interestingly variability between experimental repeats in the lamination and expression of retinal-related cells were observed. This could be due to the differences in cryotolerance, or permeability of the variable interconnected single cells that constitute multicellular systems like retinal organoids. In combination with the differences in the diffusion of water and CPAs that each cell or organoid is experienced, these factors lead to differences in the freezing environment (Baust et al., 2009). A better understanding of the biology and chemistry behind freezing and thawing will help to develop an effective cryopreservation method for retinal organoids (Jang et al., 2017).

In most cryopreservation experiments, the bright phase of the neuroepithelium and the structure of retinal organoids were damaged within 14 days post-thaw, suggesting cell death; however, the mechanisms causing cell death in retinal organoids are far from being clearly understood. To improve the survival of retinal organoids, modifications were applied to the 'Master Liver Supercooling' protocol by changing one parameter at a time. Changes included the pre-treatment of the organoids with CPAs, the extension of the incubation time of organoids with CPAs or the enrichment of the thawing solution with matrigel, glycerol, ROCK inhibitor or other CPAs. However, no improvements in the overall survival of organoids were observed, making the development of an effective protocol more challenging. To maximize the survival rate of retinal cells, several factors such as the cooling and thawing rate, storage temperature, concentration, and type of CPAs should be considered and optimized (Pegg, 2007).

It is challenging to define an optimal cryopreservation protocol suitable for all cell types or tissues due to the complexity and the different cell types that organoids are composed of (Baust et al., 2009). Each cell differs in sensitivity to stress responses and cell death processes between other cells. These differences could be due to uncontrol ice nucleation that is performed during cryopreservation (Morris and Acton, 2013). Due to these challenges, variability between runs is a significant limitation of the study.

In this study, we developed a protocol to cryopreserve retinal organoids with a final freezing temperature -60°C. Although lower freezing temperatures (-80°C) have been used for the storage of cells (red blood cells), showing good survival rates up to 10 years after cryopreservation (also such temperatures have been approved by FDA) (Lagerberg, 2015), for maximum stability of the samples, ultra-low temperatures (below −150°C) are recommended.

This is because, at very low temperatures, metabolic activities and chemical reactions are inhibited.

A disadvantage for this setup is that organoids were stored at -60˚C for 24 hours only without testing extended storage at such temperatures. At temperatures above -130˚C, the biological and metabolic reactions are not completely ceased leading to tissue degeneration (Paynter, 2008). Investigating the period of time that retinal organoids can be maintained at -60˚C will provide more insights into their storage and survival.

The cryopreservation methods have been tested using a relatively small scale (10-20) of organoids. Therefore, scaling up the number of organoids will be more representative in a real scenario of bulk cryopreservation experiments. Until this point, 10-20 retinal organoids were cryopreserved in 0.3 ml total volume, in 1.8 ml cryovials. However, on a larger scale, this will be impractical and probably the addition of more organoids in one vial will affect the results.

This study focused on the findings of previously tested cryopreservation methodologies (Pichugin et al., 2006, Richards et al., 2004, Fayomi et al., 2019, de Vries et al., 2019) which were modified and assessed on retinal organoids. Although this could provide some foundation in our study, for the best survival of retinal cells, the sample volume, cooling and thawing rate, and CPAs concentration should be optimized (Pegg, 2007).

5.1.3. Future directions

At the moment, the most promising cryopreservation approach is the 'Master Liver Supercooling' protocol. However, cell survival and recovery of organoids need to be improved as not all retinal-related cells were preserved by 14 days post-thaw, suggesting cell death. Either necrosis or apoptosis could induce cell death, but it is not clear yet which is the primary mechanism. In future studies, this could be assessed by Western blot and/or IF analysis using cellular markers such as Caspases which are hallmark characteristics of apoptosis (Krysko et al., 2008). Necrosis is an uncontrolled process, while apoptosis can be induced by variable factors, including environmental stress factors (Baust et al., 2017). Apoptosis of different cell types, including ESCs (Xu et al., 2010), liver cells (Vanhulle et al., 2006) or sperm (Khan et al., 2009), was reported after cryopreservation, suggesting that hypothermic temperatures can induce apoptosis. An approach to prevent this and improve cell recovery is the use of antioxidants that reduce ROS and have been shown positive results in rat hepatocytes (Vairetti et al., 2001). Although the addition of Trolox and Glutathione did not improve the survival of

retinal cells after cryopreservation, probably the use of other antioxidants such as N-acetyl-cysteine can be more beneficial. Also, other small molecules can be used to reduce apoptosis. For example, successful results were obtained following the addition of Caspase inhibitors upon cryopreservation of ovarian tissue (Matsushita et al., 2003) and liver cells (Zhang et al., 2009).

Several factors such as the sample size, shape, permeability and concentration of CPAs, and water diffusion are critical parameters for the cryopreservation procedures. To improve the survival of organoids, it is important to understand the freezing/thawing mechanisms. For this reason, further studies on the physicochemical and biophysical reactions of the organoids during cryopreservation are required. Also, future studies focusing on the mechanisms of crystallization, water and CPA diffusivity within the organoids, sample volume and viscosity are needed.

In the 'Master Liver Supercooling' protocol, commonly used CPAs were combined, providing promising results. Therefore, the addition of alternative CPAs or changes in the concentration of CPAs could improve the survival of retinal cells.

In future experiments, a larger scale of organoids should be used to mimic a real cryopreservation scenario. This experiment will provide more insights into the number of organoids that can be cryopreserved in the same vial and test whether adding more organoids would impact their survival. Additionally, cryopreservation of organoids could be tested in 96-well plates instead of using cryovials. This will minimise possible damage of organoids from their transfer from the 96-well plates to the cryovials and then back to the 96-well plates.

A cryopreservation protocol that maintains retinal organoids at -60°C was developed. However, it has not yet been tested for how long the organoids can survive at -60°C. Are the metabolic and biological reactions of retinal cells ceased at this temperature? And if yes, for how long can the organoids survive at -60°C? To investigate that, organoids need to be stored with different storage periods at -60°C and assessed for their survival.

In this thesis, 'Master Liver Supercooling' was the most promising protocol among all for the cryopreservation of retinal organoids. Storage of retinal organoids was performed at -60°C; however, studies have reported that for long-term storage, samples need to be cryopreserved at temperatures below -130°C where the metabolic activities and chemical reactions are completely ceased (Paynter, 2008, Jang et al., 2017). Additionally, some studies have reported that freezing samples at -80°C could preserve tissues such as rat hepatocytes for up to 90 days (Sugimachi et al., 2004). To enable long-term storage, freezing of retinal organoids at lower

temperatures is needed. Long-term storage will provide the samples with a shelf life and minimise possible epigenetic changes and genetic drift (Hunt, 2019).

5.2. Shipping

Using hiPSC-derived retinal organoids, I assessed the shipping of live hiPSC-derived organoids at room temperature (RT) using a commercially available container that maintains the environment at ambient temperature (Chapter 3). After shipping, retinal organoids retained their structural and functional characteristics, which were assessed by IF analysis and electrophysiology, respectively. Also, no differences in cell-type composition and position within the laminated retinal structure were observed. Analysis of neuroepithelial thickness revealed no differences between control, RT incubated and shipped organoids. This shipping method enables the transport of ready-made retinal organoids, increasing their availability to many research and pharma labs worldwide, facilitating thus cross-collaborative research.

5.2.1. Strengths

This study achieved an effective method to ship hiPSC-derived retinal organoids safely abroad at RT. The development of 3D retinal structures is a labour-intensive procedure that requires specialized labs and equipment to be carried out. Shipping retinal organoids abroad provides several advantages as it enhances collaboration between research centres and pharmaceutical companies. It also facilitates their availability worldwide by providing patient-specific disease models that could be used to understand better human retinal diseases, reveal unknown mechanisms of pathogenesis of the disease, and to provide new pathways for drug screening.

For the shipping of retinal organoids, low-cost ($50) commercially available shipping containers were used in our study to maintain the environment at ambient temperature. This method provides an easy and cost-effective way to ship retinal organoids abroad at RT without requiring special equipment that can be expensive, in contrast to other studies that have developed a portable shipping container to maintain the temperature at 37°C, which increases the cost of the delivery 4 times (£216) (Singh et al., 2020).

Additionally, our shipping method minimizes any variables that can affect the survival of the organoids, such as battery failure during transportation which could delay organoid's delivery. Shipping the organoids at RT conditions minimizes the need to cryopreserve them or ship them at cryogenic conditions (Simione and Sharp, 2017). This gives the possibility to the recipient of the parcel to process the samples without any specialized instructions for thawing. Also,

avoiding freezing of the organoids minimises the risk of structural and morphological damages caused by freezing/thawing cycles (Jang et al., 2017).

Additionally, the method established in this thesis has been tested on a large scale of organoids resembling a real scenario of shipping multiple plates of retinal organoids to the recipient.

Importantly, no variability was observed between shipped and control organoids, making the transportation of hiPSCs derived retinal organoids an effective method. This transportation method could provide a solution towards wide access and availability of organoids, making this technology ultimately accessible worldwide.

5.2.2. Limitations

In this study, we have generated hiPSC-derived retinal organoids on 96-well plates. For the shipping of organoids, 96-well plates were wrapped and sealed with parafilm and then were placed in the shipping container. Although instructions to maintain the container upright were provided, leakage of media was observed upon arrival. This could induce the degeneration of organoids or cause contamination. Probably, transferring the organoids in a falcon tube full of media will prevent any leakage in case of turbulences.

Other studies have tested the heat-insulating capacity of the shipping containers (Hori et al., 2019). In this study, temperature fluctuations were recorded between 23.8 and 18.8˚C, based on the temperature control. Probably exposing the shipping package to extreme temperatures such as 50°C or 0°C could provide better insights on whether the package is suitable for maintaining organoids at ambient temperatures without affecting the survival of organoids.

In this study, we investigated the impact of five-day storage and three-day shipment at RT on retinal organoids. This delivery period is ideal for domestic shipments as well as for shipments in European countries. However, it is essential to investigate whether retinal organoids can survive being kept at RT for a longer time mimicking shipping of the organoids to further destinations, or cases of delayed shipping, to provide more insights into the extent of storage of retinal organoids at RT.

The approaches described above to overcome the study's limitations could be considered the future directions of the project.

5.3. Retinitis Pigmentosa

Using hiPSC technology, control and patient-specific RP11-hiPSCs were differentiated into RPE monolayers using an established protocol (Regent et al., 2019) to investigate the disease mechanisms in Retinitis Pigmentosa caused by mutations in the *PRPF31* gene (Chapter 4). To assess the impact of *PRPF31* mutation on the proteome of RPE cells, proteomic analysis of control and RP11-RPE cells was performed. Gene ontology analysis showed RNA splicing, retinoid metabolism and visual perception, and protein folding (UPR) pathways to be affected in RP11-RPE cells. The patient-derived RPE cells were characterised by reduced levels of PRPF31 protein, which was predominantly located in the cytoplasm in an aggregate-like pattern. Cytoplasmic PRPF31 protein was associated with misfolded, ubiquitin conjugated and visual cycle proteins and accumulated progressively with time. Analysis of the waste disposal mechanisms showed impairment in proteasome and autophagy activity hence exacerbating aggregate formation, which was closely linked with activation of cell death. Reduction of cytoplasmic aggregates was tested using variable drugs that activate autophagy, HSP inducers and inhibitors of UPR. Rapamycin, an inducer of autophagy, has been shown to reduce these cytoplasmic aggregates in RP11-RPE cells and improved cell survival. Relieving the RPE cells from the accumulation of insoluble cytoplasmic aggregates presents a novel therapeutic strategy for RP11-patients.

5.3.1. Strengths

The ability of hiPSCs to develop into any type of cells has given us the possibility to generate RPE cells from patients harbouring *PRPF31* mutations to investigate the mechanisms causing Retinitis Pigmentosa. In this study, iPSCs from 3 patients with severe and very severe RP phenotypes (RP11VS, RP11S1, RP11S3) were differentiated into RPE cells to investigate the impact of *PRPF31* mutations on the formation and stability of the spliceosome and the proteome of RPE cells. Using hiPSC-derived RPE cells from patients harbouring different *PRPF31* mutations enabled us to understand the disease's complexity and reveal unknown mechanisms of pathogenesis.

RPE cells across all cell lines were plated at the same densities either on 12-well plates or 24-well transwell inserts. Additionally, RPE cells were collected at passage number 3 to minimise any possible differences that could arise from different passages. Differentiated RPE cells were pigmented, tightly packed and were characterised with a cobblestone morphology, which are all hallmark characteristics of RPE cells.

Our previous work, using a hiPSC-disease modelling approach, showed that mutations in the pre-mRNA processing factor, *PRPF31*, result in global spliceosome dysregulation specifically in retinal cells and RPE cells (Buskin et al., 2018). To fully understand the impact of such global splicing dysregulation on the RPE, we have undertaken a detailed proteomic analysis of RPE cells. Proteomic analysis is a powerful technique used in our study to quantify changes in the abundance of proteins among the samples. Several studies have used this high-throughput technique to reveal affected proteins within the cells and advance our understanding of RPE cell biology in health and disease (Buskin et al., 2018, Hongisto et al., 2017). Proteomic analysis revealed an enrichment of proteins involved in RNA splicing, retinoid metabolism and visual perception, and protein folding (UPR) pathways. Key candidates from each enriched pathway were selected and were validated by Western blot and IF analysis. Confirmability of the results was performed by three methods which enhances the outcome and strengthens the study's conclusions.

In our study, 3 RP11-RPE cell lines were derived from patients that harboured different *PRPF31* mutations and differed in the disease's severity. Our results revealed the presence of insoluble aggregates which contain the mutant PRPF31 protein, misfolded and ubiquitin-conjugated proteins in all RP11-RPE cell lines, which accumulate progressively over time. Confirming the same findings across different RP11 cell lines is a powerful method to confidently report a mechanism of pathogenesis in RP11-RPE cells. Our findings are in agreement with recent studies reporting the cytoplasmic accumulation and aggregation of wild-type and mutant PRPF31 protein in the insoluble fraction of mouse RPE cells with $Prpf31^{A216P/+}$ mutation (Valdés-Sánchez et al., 2019).

5.3.2. Limitations

In our previous study hiPSCs were differentiated to RPE cells using a stepwise protocol that includes small molecules (Buskin et al., 2018). In this study, we used a novel differentiation protocol to enhance RPE differentiation and produce large-scale hiPSC-RPE cells (Regent et al., 2019). Despite the disease severity or phenotypic differences, all hiPSCs were differentiated to RPE cells, suggesting that differentiation efficiency could be cell line dependent. In addition to the differences observed between RPE patches between different cell lines, differences within the same cell lines were observed between different experimental runs. This suggests that the efficacy of RPE differentiation is variable and can not be predicted until the differentiation is performed.

In this study, pharmacological agents were selected to assess whether cytoplasmic aggregate accumulation could be eliminated. The concentrations of the selected drugs were based on previously published studies. Ideally, a range of different drug concentrations should have been tested on RPE cells to investigate the optimum concentration and treatment period on RPE cells. This is because, between different cell lines, the efficacy of the drugs might change. For example, studies have shown that different concentrations of Rapamycin cause different effects across different cell types, and these vary by more than 1,000-fold (Foster and Toschi, 2009).

Our study assessed the presence of cytoplasmic aggregates by IF analysis, and the most promising results were confirmed by Western blot. Ideally, the efficacy of all drugs should have been tested by both IF and Western blot to observe which drug had the best effects.

5.3.3. Future directions:

The findings of this study have shown reduced nuclear expression of PRPF31 protein RP11-RPE cells compared to control cells and translocation of PRPF31 protein to the cytoplasm in an aggregate-like form. We have shown that Rapamycin can eliminate insoluble cytoplasmic aggregates, and in future studies, this strategy can be combined with gene therapy studies to restore RPE function and localisation of PRPF31 in RP11 patients.

Whilst this study assessed the localisation of WT and mutant PRPF31 protein in all control and RP11-RPE cells by IF analysis and evaluated further by Western blot the differences in expression levels of PRPF31 protein between PR11VS and Cas9-RP11VS cell lines, future studies should focus on the expression of mutant and WT PRPF31 protein in soluble and insoluble fractions of all patient and control cell lines. This will provide a better understanding of whether mutant PRPF31 protein is expressed in all patient RPE cells and whether its expression levels vary between patient cell lines that harbour different mutations.

In this thesis, we assessed the effects of pharmacological agents on the cytoplasmic aggregates in RP11-RPE cells. Mature RP11-RPE cells (with distinct hexagonal morphology and dark pigmentation) that have been seeded on transwell inserts for 12 weeks (unless otherwise indicated) were used. Assessing the effects of pharmacological agents on RP11-RPE cells at earlier stages of maturity (week 4 and 8) would provide deeper insights into which stages of the disease Rapamycin has optimum results.

Pharmacological agents were selected to eliminate cytoplasmic aggregates, and drug concentrations were chosen based on previously published studies. Although previous studies

have reported promising results, the efficacy of drugs can vary between different cell lines. Therefore, a wider range of doses could be used in future studies to assess whether different concentrations can have a better therapeutic effect.

Our results have shown that patient-derived RPE cells were characterised by reduced levels of active spliceosomes and the presence of insoluble aggregates containing the mutant PRPF31 together with misfolded, ubiquitin-conjugated proteins, which accumulated progressively with time. Additionally, we revealed that the waste disposal mechanisms via autophagy and proteasome-mediated degradation were impaired. However, it is unknown whether the accumulation of misfolded/aggregated proteins results from decreased proteasome/autophagy activity or whether the waste disposal mechanisms are incapable of coping with the burden of misfolded, ubiquitinated and aggregated proteins resulting from global spliceosome dysregulation. To investigate the exact mechanisms leading to protein aggregation, further experiments assessing the expression of cytoplasmic aggregates and the activity of proteasome and autophagy at different maturity stages are required.

Misfolded and aggregated proteins are a hallmark of many neurodegenerative diseases (NDs), and have been linked to neurodegeneration and cell death. Several studies have reported that NDs like AD have increased levels of Caspase-3. Specifically, in AD, accumulation of Caspase-3 induces degeneration of synapses and decreases synaptic plasticity (Snigdha et al., 2012). Our results have shown activation of Caspase-3 in RP11-RPE cells compared to control RPE cells, but the exact mechanism by which protein aggregates activate cell death is still unknown. Activation of Caspase-3 in RP11-RPE cells has been revealed by IF analysis. Therefore, other methods such as Western Blot analysis could be performed to confirm the activation of Caspase-3 on RPE cells.

Several molecules have been reported to activate autophagy and reduce cytoplasmic aggregates in NDs by activating waste disposal mechanisms. Specifically, a recent study has reported induction of autophagy using indirect inhibitors of mTOR, which are considered a promising therapeutic strategy in dry AMD. Flubendazole (FLBZ) has been approved by FDA and has been shown to promote degradation of indigested materials and alleviate tight junction disruption in RPE cells of AMD patients (Zhang et al., 2021). It will be interesting for future studies to assess the effects of indirect inhibitors such as FLBZ on RP11-RPE cells to explore whether they provide better results (reduce cytoplasmic aggregates, restore WT PRPF31, restore tight junctions and phagocytosis with the minimum toxicity) compared to the current findings from Rapamycin.

Despite the numerous advantages that hiPSC technology has provided in regenerative medicine, including disease modelling, drug discovery and cytotoxicity studies, the development of retinal models requires further improvements. For example, retinal organoids are physiologically, developmentally and anatomically similar to the retinal tissue in the human eye (Lancaster and Huch, 2019); however, the interaction of PRs and RPE cells needs further improvements to elucidate and improve our understanding of retinal diseases.

5.4. General Conclusions

Using hiPSCs technology has provided remarkable advantages in regenerative medicine, including disease modelling, drug screening and toxicological studies. hiPSC-derived retinal organoids and RPE cells recapitulate the morphology, composition and structure of cells found in human retina tissues. Modelling of retinal tissues enabled us to study their applications in cryopreservation, shipping and disease mechanisms. Cryopreservation of whole retinal organoids has been attempted with limited success, such as the survival of PR cells only; however, this study provides the foundations for building an optimal protocol for the cryopreservation of retinal organoids. Also, this study reported an economical method to ship retinal organoids at RT, facilitating transportation between research centres. This work was published (Georgiou et al., 2020). Furthermore, using hiPSCs-derived RPE cells, this study has elucidated potential pathological mechanisms causing Retinitis Pigmentosa and has provided insights about potential therapeutic agents that could alleviate the pathological mechanisms. This work is deposited in BioArchive (Georgiou et al., 2021), and the data are available at this link: https://www.biorxiv.org/content/10.1101/2021.10.11.463925v1.

Appendices

Appendix A: List of Publications

Georgiou M, Chichagova V, Hilgen G, Dorgau B, Sernagor E, Armstrong L, et al. (2020) Room temperature shipment does not affect the biological activity of pluripotent stem cell-derived retinal organoids. PLoS ONE 15(6): e0233860.

Chichagova V, Hilgen G, Ghareeb A, **Georgiou M**, Carter M, Sernagor E, Lako M, Armstrong L. Human iPSC differentiation to retinal organoids in response to IGF1 and BMP4 activation is line- and method-dependent. Stem Cells. 2020 Feb;38(2):195-201. doi: 10.1002/stem.3116. Epub 2019 Dec 30. Erratum in: Stem Cells. 2020 Oct 1;38(10):E4. PMID: 31721366; PMCID: PMC7383896.

Chichagova, V., Dorgau, B., Felemban, M., **Georgiou, M**., Armstrong, L., & Lako, M. (2019). Differentiation of retinal organoids from human pluripotent stem cells. *Current Protocols in Stem Cell Biology*, *50,* e95. doi: 10.1002/cpsc.95

Yang C, **Georgiou M**, Atkinson R, Collin J, Al-Aama J, Nagaraja-Grellscheid, Johnson C, Ali R, Armstrong L, Mozaffari-Jovin S*, Lako M*. Pre-mRNA processing factors and retinitis pigmentosa: RNA splicing and beyond. Front. Cell Dev. Biol. 9:700276. doi: 10.3389/fcell.2021.700276.

Collin, J., Queen, R., Zerti, D., Dorgau, B., **Georgiou, M.,** Djidrovski, I., Hussain, R., Coxhead, J. M., Joseph, A., Rooney, P., Lisgo, S., Figueiredo, F., Armstrong, L., & Lako, M. (2021). Co-expression of SARS-CoV-2 entry genes in the superficial adult human conjunctival, limbal and corneal epithelium suggests an additional route of entry via the ocular surface. Ocular Surface, 19. https://doi.org/10.1016/j.jtos.2020.05.013

Georgiou M, Yang C, Atkinson R, Pan KT, Buskin A, Molina MM, Collin j, Al-Aama J, Goertler F, Kudwig SEJ, Davey T, Lührmann R, Nagaraja-Grellscheid S, Johnson C, Ali R, Armstrong L, Korolchuk V, Urlaub H, Mozaffari-Jovin and Lako M. Progressive protein aggregation causes cytotoxicity in PRPF31 patient retinal pigment epithelium cells: the mechanism and its reversal through activation of autophagy. (Under review of CTM).

Djidrovski I, **Georgiou M**, Hughes GL, Patterson EI, Casas-Sanchez A, Pennington SH, Biagini GA, Moya-Molina M, van den Bor J, Smit MJ, Chung G, Lako M, Armstrong L. SARS-CoV-2 infects an upper airway model derived from induced pluripotent stem cells. Stem Cells. 2021 Jun 21. doi: 10.1002/stem.3422. Epub ahead of print. PMID: 34152044.

Valeria Chichagova, **Maria Georgiou**, Birthe Dorgau, Madeleine Carter, Git Chung, Evelyne Sernagor, Lyle Armstrong, Majlinda Lako. Enhancing human iPSC-derived retinal organoids by incorporating microglia-like cells. Investigative Ophthalmology & Visual Science. 2020; 61(7).

Bibliography

ABOKYI, S., SHAN, S. W., TO, C. H., CHAN, H. H. & TSE, D. Y. 2020. Autophagy Upregulation by the TFEB Inducer Trehalose Protects against Oxidative Damage and Cell Death Associated with NRF2 Inhibition in Human RPE Cells. *Oxid Med Cell Longev,* 2020**,** 5296341.

ACHBERGER, K., HADERSPECK, J. C., KLEGER, A. & LIEBAU, S. 2019. Stem cell-based retina models. *Adv Drug Deliv Rev,* 140**,** 33-50.

ACLAND, G. M., AGUIRRE, G. D., RAY, J., ZHANG, Q., ALEMAN, T. S., CIDECIYAN, A. V., PEARCE-KELLING, S. E., ANAND, V., ZENG, Y., MAGUIRE, A. M., JACOBSON, S. G., HAUSWIRTH, W. W. & BENNETT, J. 2001. Gene therapy restores vision in a canine model of childhood blindness. *Nat Genet,* 28**,** 92-5.

ADAMS, C. J., KOPP, M. C., LARBURU, N., NOWAK, P. R. & ALI, M. M. U. 2019. Structure and Molecular Mechanism of ER Stress Signaling by the Unfolded Protein Response Signal Activator IRE1. *Front Mol Biosci,* 6**,** 11.

ALEXANDRE, E., VIOLLON-ABADIE, C., DAVID, P., GANDILLET, A., COASSOLO, P., HEYD, B., MANTION, G., WOLF, P., BACHELLIER, P., JAECK, D. & RICHERT, L. 2002. Cryopreservation of adult human hepatocytes obtained from resected liver biopsies. *Cryobiology,* 44**,** 103-13.

AMIR, G., HOROWITZ, L., RUBINSKY, B., YOUSIF, B. S., LAVEE, J. & SMOLINSKY, A. K. 2004. Subzero nonfreezing cryopresevation of rat hearts using antifreeze protein I and antifreeze protein III. *Cryobiology,* 48**,** 273-82.

ANDRE, R. & TABRIZI, S. J. 2012. Misfolded PrP and a novel mechanism of proteasome inhibition. *Prion,* 6**,** 32-6.

ANTONENAS, V., GARVIN, F., WEBB, M., SARTOR, M., BRADSTOCK, K. F. & GOTTLIEB, D. 2006. Fresh PBSC harvests, but not BM, show temperature-related loss of CD34 viability during storage and transport. *Cytotherapy,* 8**,** 158-65.

ARAI, K., MURATA, D., TAKAO, S., VERISSIOMO, A. R. & NAKAYAMA, K. 2020. Cryopreservation method for spheroids and fabrication of scaffold-free tubular constructs. *PLoS One,* 15**,** e0230428.

AUDO, I., BUJAKOWSKA, K., MOHAND-SAÏD, S., LANCELOT, M. E., MOSKOVA-DOUMANOVA, V., WASEEM, N. H., ANTONIO, A., SAHEL, J. A., BHATTACHARYA, S. S. & ZEITZ, C. 2010. Prevalence and novelty of PRPF31 mutations in French autosomal dominant rod-cone dystrophy patients and a review of published reports. *BMC medical genetics,* 11.

BADRZADEH, H., NAJMABADI, S., PAYMANI, R., MACASO, T., AZADBADI, Z. & AHMADY, A. 2010. Super cool X-1000 and Super cool Z-1000, two ice blockers, and their effect on vitrification/warming of mouse embryos. *Eur J Obstet Gynecol Reprod Biol,* 151**,** 70-1.

BAEHR, W. & CHEN, C. K. 2001. RP11 and RP13: unexpected gene loci. *Trends Mol Med,* 7**,** 484-6.

BAERTSCHIGER, R. M., BERNEY, T. & MOREL, P. 2008. Organ preservation in pancreas and islet transplantation. *Curr Opin Organ Transplant,* 13**,** 59-66.

BAHARI, L., BEIN, A., YASHUNSKY, V. & BRASLAVSKY, I. 2018. Directional freezing for the cryopreservation of adherent mammalian cells on a substrate. *PLoS One,* 13**,** e0192265.

BAHRAMI, H., MELIA, M. & DAGNELIE, G. 2006. Lutein supplementation in retinitis pigmentosa: PC-based vision assessment in a randomized double-masked placebo-controlled clinical trial [NCT00029289]. *BMC Ophthalmol,* 6**,** 23.

BAKHACH, J. 2009. The cryopreservation of composite tissues: Principles and recent advancement on cryopreservation of different type of tissues. *Organogenesis,* 5**,** 119-26.

BAREZ, S. R., ATAR, A. M. & AGHAEI, M. 2020. Mechanism of inositol-requiring enzyme 1-alpha inhibition in endoplasmic reticulum stress and apoptosis in ovarian cancer cells. *J Cell Commun Signal,* 14**,** 403-415.

BAUST, J. G., GAO, D. & BAUST, J. M. 2009. Cryopreservation: An emerging paradigm change. *Organogenesis,* 5**,** 90-6.

BAUST, J. G., SNYDER, K. K., VAN BUSKIRK, R. & BAUST, J. M. 2017. Integrating Molecular Control to Improve Cryopreservation Outcome. *Biopreserv Biobank,* 15**,** 134-141.

BENATAR, M., WUU, J., ANDERSEN, P. M., ATASSI, N., DAVID, W., CUDKOWICZ, M. & SCHOENFELD, D. 2018. Randomized, double-blind, placebo-controlled trial of arimoclomol in rapidly progressive. *Neurology,* 90**,** e565-e574.

BERGER, Z., RAVIKUMAR, B., MENZIES, F. M., OROZ, L. G., UNDERWOOD, B. R., PANGALOS, M. N., SCHMITT, I., WULLNER, U., EVERT, B. O., O'KANE, C. J. & RUBINSZTEIN, D. C. 2006. Rapamycin alleviates toxicity of different aggregate-prone proteins. *Hum Mol Genet,* 15**,** 433-42.

BERNAL, S., AYUSO, C., ANTIÑOLO, G., GIMENEZ, A., BORREGO, S., TRUJILLO, M. J., MARCOS, I., CALAF, M., DEL RIO, E. & BAIGET, M. 2003. Mutations in USH2A in Spanish patients with autosomal recessive retinitis pigmentosa: high prevalence and phenotypic variation. *J Med Genet,* 40**,** e8.

BERSON, E. L., ROSNER, B., SANDBERG, M. A., WEIGEL-DIFRANCO, C., BROCKHURST, R. J., HAYES, K. C., JOHNSON, E. J., ANDERSON, E. J., JOHNSON, C. A., GAUDIO, A. R., WILLETT, W. C. & SCHAEFER, E. J. 2010. Clinical trial of lutein in patients with retinitis pigmentosa receiving vitamin A. *Arch Ophthalmol,* 128**,** 403-11.

BERSON, E. L., ROSNER, B., SANDBERG, M. A., WEIGEL-DIFRANCO, C., MOSER, A., BROCKHURST, R. J., HAYES, K. C., JOHNSON, C. A., ANDERSON, E. J., GAUDIO, A. R., WILLETT, W. C. & SCHAEFER, E. J. 2004a. Clinical trial of docosahexaenoic acid in patients with retinitis pigmentosa receiving vitamin A treatment. *Arch Ophthalmol,* 122**,** 1297-305.

BERSON, E. L., ROSNER, B., SANDBERG, M. A., WEIGEL-DIFRANCO, C., MOSER, A., BROCKHURST, R. J., HAYES, K. C., JOHNSON, C. A., ANDERSON, E. J., GAUDIO, A. R., WILLETT, W. C. & SCHAEFER, E. J. 2004b. Further evaluation of docosahexaenoic acid in patients with retinitis pigmentosa receiving vitamin A treatment: subgroup analyses. *Arch Ophthalmol,* 122**,** 1306-14.

BEST, B. P. 2015. Cryoprotectant Toxicity: Facts, Issues, and Questions. *Rejuvenation Res,* 18**,** 422-36.

BINDU A, H. & B, S. 2011. Potency of Various Types of Stem Cells and their Transplantation. *J Stem Cell Res Ther Journal of Stem Cell Research & Therapy,* 01.

BOESZE-BATTAGLIA, K. & GOLDBERG, A. F. 2002. Photoreceptor renewal: a role for peripherin/rds. *Int Rev Cytol,* 217**,** 183-225.

BOJIC, S., MURRAY, A., BENTLEY, B. L., SPINDLER, R., PAWLIK, P., CORDEIRO, J. L., BAUER, R. & DE MAGALHAES, J. P. 2021. Winter is coming: the future of cryopreservation. *BMC Biol,* 19**,** 56.

BOULTON, M. & DAYHAW-BARKER, P. 2001. The role of the retinal pigment epithelium: topographical variation and ageing changes. *Eye (Lond),* 15**,** 384-9.

BRAFMAN, D. A. 2013. Constructing stem cell microenvironments using bioengineering approaches. *Physiol Genomics,* 45**,** 1123-35.

BRYDON, E. M., BRONSTEIN, R., BUSKIN, A., LAKO, M., PIERCE, E. A. & FERNANDEZ-GODINO, R. 2019. AAV-Mediated Gene Augmentation Therapy Restores Critical Functions in Mutant PRPF31. *Mol Ther Methods Clin Dev,* 15**,** 392-402.

BUCHHOLZ, D. E., HIKITA, S. T., ROWLAND, T. J., FRIEDRICH, A. M., HINMAN, C. R., JOHNSON, L. V. & CLEGG, D. O. 2009. Derivation of functional retinal pigmented epithelium from induced pluripotent stem cells. *Stem Cells,* 27**,** 2427-34.

BUSKIN, A., ZHU, L., CHICHAGOVA, V., BASU, B., MOZAFFARI-JOVIN, S., DOLAN, D., DROOP, A., COLLIN, J., BRONSTEIN, R., MEHROTRA, S., FARKAS, M., HILGEN, G., WHITE, K., PAN, K. T., TREUMANN, A., HALLAM, D., BIALAS, K., CHUNG, G., MELLOUGH, C., DING, Y., KRASNOGOR, N., PRZYBORSKI, S., ZWOLINSKI, S., AL-AAMA, J., ALHARTHI, S., XU, Y., WHEWAY, G., SZYMANSKA, K., MCKIBBIN, M., INGLEHEARN, C. F., ELLIOTT, D. J., LINDSAY, S., ALI, R. R., STEEL, D. H., ARMSTRONG, L., SERNAGOR, E., URLAUB, H., PIERCE, E., LÜHRMANN, R., GRELLSCHEID, S. N., JOHNSON, C. A. & LAKO, M. 2018. Disrupted alternative splicing for genes implicated in splicing and ciliogenesis causes PRPF31 retinitis pigmentosa. *Nat Commun,* 9**,** 4234.

BUTLER, J. M., SUPHARATTANASITTHI, W., YANG, Y. C. & PARAOAN, L. 2021. RNA-seq analysis of ageing human retinal pigment epithelium: Unexpected up-regulation of visual cycle gene transcription. *J Cell Mol Med,* 25**,** 5572-5585.

CAMPBELL, M., HUMPHRIES, M., KENNAN, A., KENNA, P., HUMPHRIES, P. & BRANKIN, B. 2006. Aberrant retinal tight junction and adherens junction protein expression in an animal model of autosomal dominant Retinitis pigmentosa: the Rho(-/-) mouse. *Exp Eye Res,* 83**,** 484-92.

CARR, A. J., VUGLER, A. A., HIKITA, S. T., LAWRENCE, J. M., GIAS, C., CHEN, L. L., BUCHHOLZ, D. E., AHMADO, A., SEMO, M., SMART, M. J., HASAN, S., DA CRUZ, L., JOHNSON, L. V., CLEGG, D. O. & COFFEY, P. J. 2009. Protective effects of human iPS-derived retinal pigment epithelium cell transplantation in the retinal dystrophic rat. *PLoS One,* 4**,** e8152.

CERNIAUSKAS, E., KURZAWA-AKANBI, M., XIE, L., HALLAM, D., MOYA-MOLINA, M., WHITE, K., STEEL, D., DOHERTY, M., WHITFIELD, P., AL-AAMA, J., ARMSTRONG, L., KAVANAGH, D., LAMBRIS, J. D., KOROLCHUK, V. I., HARRIS, C. & LAKO, M. 2020. Complement modulation reverses pathology in Y402H-retinal pigment epithelium cell model of age-related macular degeneration by restoring lysosomal function. *Stem Cells Transl Med,* 9**,** 1585-1603.

CHEN, S. U., LIEN, Y. R., CHAO, K., LU, H. F., HO, H. N. & YANG, Y. S. 2000. Cryopreservation of mature human oocytes by vitrification with ethylene glycol in straws. *Fertil Steril,* 74**,** 804-8.

CHEN, X., LI, M., LI, L., XU, S., HUANG, D., JU, M., HUANG, J., CHEN, K. & GU, H. 2016. Trehalose, sucrose and raffinose are novel activators of autophagy in human keratinocytes through an mTOR-independent pathway. *Sci Rep,* 6**,** 28423.

CHESNE, C. & GUILLOUZO, A. 1988. Cryopreservation of isolated rat hepatocytes: a critical evaluation of freezing and thawing conditions. *Cryobiology,* 25**,** 323-30.

CHICHAGOVA, V., HALLAM, D., COLLIN, J., BUSKIN, A., SARETZKI, G., ARMSTRONG, L., YU-WAI-MAN, P., LAKO, M. & STEEL, D. H. 2017. Human iPSC disease modelling reveals functional and structural defects in retinal pigment epithelial cells harbouring the m.3243A > G mitochondrial DNA mutation. *Sci Rep,* 7**,** 12320.

CHICHAGOVA, V., HILGEN, G., GHAREEB, A., GEORGIOU, M., CARTER, M., SERNAGOR, E., LAKO, M. & ARMSTRONG, L. 2020. Human iPSC differentiation to retinal organoids in response to IGF1 and BMP4 activation is line- and method-dependent. *Stem Cells,* 38**,** 195-201.

CHUNG, K. K., DAWSON, V. L. & DAWSON, T. M. 2001. The role of the ubiquitin-proteasomal pathway in Parkinson's disease and other neurodegenerative disorders. *Trends Neurosci,* 24**,** S7-14.

CIDECIYAN, A. V., JACOBSON, S. G., BELTRAN, W. A., SUMAROKA, A., SWIDER, M., IWABE, S., ROMAN, A. J., OLIVARES, M. B., SCHWARTZ, S. B., KOMÁROMY, A. M., HAUSWIRTH, W. W. & AGUIRRE, G. D. 2013. Human retinal gene therapy for Leber congenital amaurosis shows advancing retinal degeneration despite enduring visual improvement. *Proc Natl Acad Sci U S A,* 110**,** E517-25.

CIECHANOVER, A. & KWON, Y. T. 2015. Degradation of misfolded proteins in neurodegenerative diseases: therapeutic targets and strategies. *Exp Mol Med,* 47**,** e147.

COHEN, R. I., THOMPSON, M. L., SCHRYVER, B. & EHRHARDT, R. O. 2014. Standardized cryopreservation of pluripotent stem cells. *Curr Protoc Stem Cell Biol,* 28**,** Unit 1C 14.

COMITATO, A., SPAMPANATO, C., CHAKAROVA, C., SANGES, D., BHATTACHARYA, S. S. & MARIGO, V. 2007. Mutations in splicing factor PRPF3, causing retinal degeneration, form detrimental aggregates in photoreceptor cells. *Hum Mol Genet,* 16**,** 1699-707.

CORIELL, L. L., GREENE, A. E. & SILVER, R. K. 1964. Histological Development of Cell and Tissue Culture Freezing. *Cryobiology,* 51**,** 72-9.

COX, D., WHITEN, D. R., BROWN, J. W. P., HORROCKS, M. H., SAN GIL, R., DOBSON, C. M., KLENERMAN, D., VAN OIJEN, A. M. & ECROYD, H. 2018. The small heat shock protein Hsp27 binds alpha-synuclein fibrils, preventing elongation and cytotoxicity. *J Biol Chem,* 293**,** 4486-4497.

CREMERS, F. P. M., BOON, C. J. F., BUJAKOWSKA, K. & ZEITZ, C. 2018. Special Issue Introduction: Inherited Retinal Disease: Novel Candidate Genes, Genotype-Phenotype Correlations, and Inheritance Models. *Genes (Basel),* 9.

DA CRUZ, L., FYNES, K., GEORGIADIS, O., KERBY, J., LUO, Y. H., AHMADO, A., VERNON, A., DANIELS, J. T., NOMMISTE, B., HASAN, S. M., GOOLJAR, S. B., CARR, A. F., VUGLER, A., RAMSDEN, C. M., BICTASH, M., FENSTER, M., STEER, J., HARBINSON, T., WILBREY, A., TUFAIL, A., FENG, G., WHITLOCK, M., ROBSON, A. G., HOLDER, G. E., SAGOO, M. S., LOUDON, P. T., WHITING, P. & COFFEY, P. J. 2018. Phase 1 clinical study of an embryonic stem cell-derived retinal pigment epithelium patch in age-related macular degeneration. *Nat Biotechnol,* 36**,** 328-337.

DAGNELIE, G., ZORGE, I. S. & MCDONALD, T. M. 2000. Lutein improves visual function in some patients with retinal degeneration: a pilot study via the Internet. *Optometry,* 71**,** 147-64.

DAIGER, S. P., BOWNE, S. J. & SULLIVAN, L. S. 2007. Perspective on genes and mutations causing retinitis pigmentosa. *Arch Ophthalmol,* 125**,** 151-8.

DE VRIES, R. J., TESSIER, S. N., BANIK, P. D., NAGPAL, S., CRONIN, S. E. J., OZER, S., HAFIZ, E. O. A., VAN GULIK, T. M., YARMUSH, M. L., MARKMANN, J. F., TONER, M., YEH, H. & UYGUN, K. 2019. Supercooling extends preservation time of human livers. *Nat Biotechnol,* 37**,** 1131-1136.

DECANINI, A., NORDGAARD, C. L., FENG, X., FERRINGTON, D. A. & OLSEN, T. W. 2007. Changes in select redox proteins of the retinal pigment epithelium in age-related macular degeneration. *Am J Ophthalmol,* 143**,** 607-15.

DEERY, E. C., VITHANA, E. N., NEWBOLD, R. J., GALLON, V. A., BHATTACHARYA, S. S., WARREN, M. J., HUNT, D. M. & WILKIE, S. E. 2002. Disease mechanism for retinitis pigmentosa (RP11) caused by mutations in the splicing factor gene PRPF31. *Hum Mol Genet,* 11**,** 3209-19.

DEJNEKA, N. S., SURACE, E. M., ALEMAN, T. S., CIDECIYAN, A. V., LYUBARSKY, A., SAVCHENKO, A., REDMOND, T. M., TANG, W., WEI, Z., REX, T. S., GLOVER, E., MAGUIRE, A. M., PUGH, E. N., JACOBSON, S. G. & BENNETT, J. 2004. In utero gene therapy rescues vision in a murine model of congenital blindness. *Mol Ther,* 9**,** 182-8.

DOKE, S. K. & DHAWALE, S. C. 2015. Alternatives to animal testing: A review. *Saudi Pharm J,* 23**,** 223-9.

DONNEZ, J., MARTINEZ-MADRID, B., JADOUL, P., VAN LANGENDONCKT, A., DEMYLLE, D. & DOLMANS, M. M. 2006. Ovarian tissue cryopreservation and transplantation: a review. *Hum Reprod Update,* 12**,** 519-35.

DORGAU, B., FELEMBAN, M., HILGEN, G., KIENING, M., ZERTI, D., HUNT, N. C., DOHERTY, M., WHITFIELD, P., HALLAM, D., WHITE, K., DING, Y., KRASNOGOR, N., AL-AAMA, J., ASFOUR, H. Z., SERNAGOR, E. & LAKO, M. 2019. Decellularised extracellular matrix-derived peptides from neural retina and retinal pigment epithelium enhance the expression of synaptic markers and light responsiveness of human pluripotent stem cell derived retinal organoids. *Biomaterials,* 199**,** 63-75.

DRYJA, T. P., HAHN, L. B., KAJIWARA, K. & BERSON, E. L. 1997. Dominant and digenic mutations in the peripherin/RDS and ROM1 genes in retinitis pigmentosa. *Invest Ophthalmol Vis Sci,* 38**,** 1972-82.

DRYJA, T. P., MCGEE, T. L., REICHEL, E., HAHN, L. B., COWLEY, G. S., YANDELL, D. W., SANDBERG, M. A. & BERSON, E. L. 1990. A point mutation of the rhodopsin gene in one form of retinitis pigmentosa. *Nature,* 343**,** 364-6.

DUTTA, D., HEO, I. & CLEVERS, H. 2017. Disease Modeling in Stem Cell-Derived 3D Organoid Systems. *Trends Mol Med,* 23**,** 393-410.

EHRHART, F., SCHULZ, J. C., KATSEN-GLOBA, A., SHIRLEY, S. G., REUTER, D., BACH, F., ZIMMERMANN, U. & ZIMMERMANN, H. 2009. A comparative study of freezing single cells and spheroids: towards a new model system for optimizing freezing protocols for cryobanking of human tumours. *Cryobiology,* 58**,** 119-27.

EIRAKU, M. & SASAI, Y. 2011. Mouse embryonic stem cell culture for generation of three-dimensional retinal and cortical tissues. *Nat Protoc,* 7**,** 69-79.

EIRAKU, M., TAKATA, N., ISHIBASHI, H., KAWADA, M., SAKAKURA, E., OKUDA, S., SEKIGUCHI, K., ADACHI, T. & SASAI, Y. 2011. Self-organizing optic-cup morphogenesis in three-dimensional culture. *Nature,* 472**,** 51-6.

EIRAKU, M., WATANABE, K., MATSUO-TAKASAKI, M., KAWADA, M., YONEMURA, S., MATSUMURA, M., WATAYA, T., NISHIYAMA, A., MUGURUMA, K. & SASAI, Y. 2008. Self-organized formation of polarized cortical tissues from ESCs and its active manipulation by extrinsic signals. *Cell Stem Cell,* 3**,** 519-32.

EISELE, Y. S., MONTEIRO, C., FEARNS, C., ENCALADA, S. E., WISEMAN, R. L., POWERS, E. T. & KELLY, J. W. 2015. Targeting protein aggregation for the treatment of degenerative diseases. *Nat Rev Drug Discov,* 14**,** 759-80.

ESKELINEN, E. L. & SAFTIG, P. 2009. Autophagy: a lysosomal degradation pathway with a central role in health and disease. *Biochim Biophys Acta,* 1793**,** 664-73.

FAHY, G. M. & ALI, S. E. 1997. Cryopreservation of the mammalian kidney. II. Demonstration of immediate ex vivo function after introduction and removal of 7.5 M cryoprotectant. *Cryobiology,* 35**,** 114-31.

FAHY, G. M., MACFARLANE, D. R., ANGELL, C. A. & MERYMAN, H. T. 1984. Vitrification as an approach to cryopreservation. *Cryobiology,* 21**,** 407-26.

FAHY, G. M. & WOWK, B. 2021. Principles of Ice-Free Cryopreservation by Vitrification. *Methods Mol Biol,* 2180**,** 27-97.

FAHY, G. M., WOWK, B., WU, J., PHAN, J., RASCH, C., CHANG, A. & ZENDEJAS, E. 2004. Cryopreservation of organs by vitrification: perspectives and recent advances. *Cryobiology,* 48**,** 157-78.

FALASCONI, A., BIAGIONI, M., NOVELLI, E., PIANO, I., GARGINI, C. & STRETTOI, E. 2019. Retinal Phenotype in the rd9 Mutant Mouse, a Model of X-Linked RP. *Front Neurosci,* 13**,** 991.

FARKAS, M. H., LEW, D. S., SOUSA, M. E., BUJAKOWSKA, K., CHATAGNON, J., BHATTACHARYA, S. S., PIERCE, E. A. & NANDROT, E. F. 2014. Mutations in pre-mRNA processing factors 3, 8, and 31 cause dysfunction of the retinal pigment epithelium. *Am J Pathol,* 184**,** 2641-52.

FAYOMI, A. P., PETERS, K., SUKHWANI, M., VALLI-PULASKI, H., SHETTY, G., MEISTRICH, M. L., HOUSER, L., ROBERTSON, N., ROBERTS, V., RAMSEY, C., HANNA, C., HENNEBOLD, J. D., DOBRINSKI, I. & ORWIG, K. E. 2019. Autologous grafting of cryopreserved prepubertal rhesus testis produces sperm and offspring. *Science,* 363**,** 1314-1319.

FERRARI, S., DI IORIO, E., BARBARO, V., PONZIN, D., SORRENTINO, F. S. & PARMEGGIANI, F. 2011. Retinitis pigmentosa: genes and disease mechanisms. *Curr Genomics,* 12**,** 238-49.

FERRER, M., CORNEO, B., DAVIS, J., WAN, Q., MIYAGISHIMA, K. J., KING, R., MAMINISHKIS, A., MARUGAN, J., SHARMA, R., SHURE, M., TEMPLE, S., MILLER, S. & BHARTI, K. 2014. A multiplex high-throughput gene expression assay to simultaneously detect disease and functional markers in induced pluripotent stem cell-derived retinal pigment epithelium. *Stem Cells Transl Med,* 3**,** 911-22.

FOSTER, D. A. & TOSCHI, A. 2009. Targeting mTOR with rapamycin: one dose does not fit all. *Cell Cycle,* 8**,** 1026-9.

FU, Y. & YAU, K. W. 2007. Phototransduction in mouse rods and cones. *Pflugers Arch,* 454**,** 805-19.

FUJIOKA, T., YASUCHIKA, K., NAKAMURA, Y., NAKATSUJI, N. & SUEMORI, H. 2004. A simple and efficient cryopreservation method for primate embryonic stem cells. *Int J Dev Biol,* 48**,** 1149-54.

GAST, C. E., SILK, A. D., ZAROUR, L., RIEGLER, L., BURKHART, J. G., GUSTAFSON, K. T., PARAPPILLY, M. S., ROH-JOHNSON, M., GOODMAN, J. R., OLSON, B., SCHMIDT, M., SWAIN, J. R., DAVIES, P. S., SHASTHRI, V., IIZUKA, S., FLYNN, P., WATSON, S., KORKOLA, J., COURTNEIDGE, S. A., FISCHER, J. M., JABOIN, J., BILLINGSLEY, K. G., LOPEZ, C. D., BURCHARD, J., GRAY, J., COUSSENS, L. M., SHEPPARD, B. C. & WONG, M. H. 2018. Cell fusion potentiates tumor heterogeneity and reveals circulating hybrid cells that correlate with stage and survival. *Sci Adv,* 4**,** eaat7828.

GENTIER, R. J. & VAN LEEUWEN, F. W. 2015. Misframed ubiquitin and impaired protein quality control: an early event in Alzheimer's disease. *Front Mol Neurosci,* 8**,** 47.

GEORGIOU, M., CHICHAGOVA, V., HILGEN, G., DORGAU, B., SERNAGOR, E., ARMSTRONG, L. & LAKO, M. 2020. Room temperature shipment does not affect the biological activity of pluripotent stem cell-derived retinal organoids. *PLoS One,* 15**,** e0233860.

GEORGIOU, M., YANG, C., ATKINSON, R., PAN, K.-T., BUSKIN, A., MOLINA, M. M., COLLIN, J., AL-AAMA, J., GOERTLER, F., LUDWIG, S. E. J., DAVEY, T., LÜHRMANN, R., NAGARAJA-GRELLSCHEID, S., JOHNSON, C., ALI, R., ARMSTRONG, L., KOROLCHUK, V., URLAUB, H., MOZAFFARI-JOVIN, S. & LAKO, M. 2021. Progressive protein aggregation in PRPF31 patient retinal pigment epithelium cells: the mechanism and its reversal through activation of autophagy. *bioRxiv***,** 2021.10.11.463925.

GIWA, S., LEWIS, J. K., ALVAREZ, L., LANGER, R., ROTH, A. E., CHURCH, G. M., MARKMANN, J. F., SACHS, D. H., CHANDRAKER, A., WERTHEIM, J. A., ROTHBLATT, M., BOYDEN, E. S., EIDBO, E., LEE, W. P. A., POMAHAC, B., BRANDACHER, G., WEINSTOCK, D. M., ELLIOTT, G., NELSON, D., ACKER, J. P., UYGUN, K., SCHMALZ, B., WEEGMAN, B. P., TOCCHIO, A., FAHY, G. M., STOREY, K. B., RUBINSKY, B., BISCHOF, J., ELLIOTT, J. A. W., WOODRUFF, T. K., MORRIS, G. J., DEMIRCI, U., BROCKBANK, K. G. M., WOODS, E. J., BEN, R. N., BAUST, J. G., GAO, D., FULLER, B., RABIN, Y.,

KRAVITZ, D. C., TAYLOR, M. J. & TONER, M. 2017. The promise of organ and tissue preservation to transform medicine. *Nat Biotechnol,* 35**,** 530-542.

GLICKMAN, M. H. & CIECHANOVER, A. 2002. The ubiquitin-proteasome proteolytic pathway: destruction for the sake of construction. *Physiol Rev,* 82**,** 373-428.

GOLDBERG, A. L. 2003. Protein degradation and protection against misfolded or damaged proteins. *Nature,* 426**,** 895-9.

GONZALEZ-CORDERO, A., KRUCZEK, K., NAEEM, A., FERNANDO, M., KLOC, M., RIBEIRO, J., GOH, D., DURAN, Y., BLACKFORD, S. J. I., ABELLEIRA-HERVAS, L., SAMPSON, R. D., SHUM, I. O., BRANCH, M. J., GARDNER, P. J., SOWDEN, J. C., BAINBRIDGE, J. W. B., SMITH, A. J., WEST, E. L., PEARSON, R. A. & ALI, R. R. 2017. Recapitulation of Human Retinal Development from Human Pluripotent Stem Cells Generates Transplantable Populations of Cone Photoreceptors. *Stem Cell Reports,* 9**,** 820-837.

GREGORI, L., FUCHS, C., FIGUEIREDO-PEREIRA, M. E., VAN NOSTRAND, W. E. & GOLDGABER, D. 1995. Amyloid beta-protein inhibits ubiquitin-dependent protein degradation in vitro. *J Biol Chem,* 270**,** 19702-8.

GREGORY-EVANS, K., PENNESI, M. E. & WELEBER, R. G. 2013. Retinitis Pigmentosa and Allied Disorders. 761-835.

GUO, Y., WANG, P., MA, J. H., CUI, Z., YU, Q., LIU, S., XUE, Y., ZHU, D., CAO, J., LI, Z., TANG, S. & CHEN, J. 2019. Modeling Retinitis Pigmentosa: Retinal Organoids Generated From the iPSCs of a Patient With the USH2A Mutation Show Early Developmental Abnormalities. *Frontiers in Cellular Neuroscience,* 13.

HALLAM, D., COLLIN, J., BOJIC, S., CHICHAGOVA, V., BUSKIN, A., XU, Y., LAFAGE, L., OTTEN, E. G., ANYFANTIS, G., MELLOUGH, C., PRZYBORSKI, S., ALHARTHI, S., KOROLCHUK, V., LOTERY, A., SARETZKI, G., MCKIBBIN, M., ARMSTRONG, L., STEEL, D., KAVANAGH, D. & LAKO, M. 2017. An Induced Pluripotent Stem Cell Patient Specific Model of Complement Factor H (Y402H) Polymorphism Displays Characteristic Features of Age-Related Macular Degeneration and Indicates a Beneficial Role for UV Light Exposure. *Stem Cells,* 35**,** 2305-2320.

HALLAM, D., HILGEN, G., DORGAU, B., ZHU, L., YU, M., BOJIC, S., HEWITT, P., SCHMITT, M., UTENG, M., KUSTERMANN, S., STEEL, D., NICHOLDS, M., THOMAS, R., TREUMANN, A., PORTER, A., SERNAGOR, E., ARMSTRONG, L. & LAKO, M. 2018a. Human-Induced Pluripotent Stem Cells Generate Light Responsive Retinal Organoids with Variable and Nutrient-Dependent Efficiency. *Stem Cells,* 36**,** 1535-1551.

HALLAM, D., RAWLINGS, D., STEEL, D., ARMSTRONG, L. & LAKO, M. 2018b. In Reply to the Letter to the Editor from Anderson et al.: An Induced Pluripotent Stem Cell Patient Specific Model of Complement Factor H (Y402H) Polymorphism Displays Characteristic Features of Age-Related Macular Degeneration and Indicates a Beneficial Role for UV Light Exposure. *Stem Cells,* 36**,** 627-629.

HAMEL, C. 2006. Retinitis pigmentosa. *Orphanet J Rare Dis,* 1**,** 40.

HAN, J. W. & YOON, Y. S. 2011. Induced pluripotent stem cells: emerging techniques for nuclear reprogramming. *Antioxid Redox Signal,* 15**,** 1799-820.

HARTL, F. U. 1996. Molecular chaperones in cellular protein folding. *Nature,* 381**,** 571-9.

HARTONG, D. T., BERSON, E. L. & DRYJA, T. P. 2006. Retinitis pigmentosa. *Lancet,* 368**,** 1795-809.

HEAVNER, W. & PEVNY, L. 2012. Eye development and retinogenesis. *Cold Spring Harb Perspect Biol,* 4.

HENDRICKSON, A. & ZHANG, C. 2019. Development of cone photoreceptors and their synapses in the human and monkey fovea. *The Journal of comparative neurology,* 527**,** 38-51.

HERRERO, L., MARTÍNEZ, M. & GARCIA-VELASCO, J. A. 2011. Current status of human oocyte and embryo cryopreservation. *Curr Opin Obstet Gynecol,* 23**,** 245-50.

HIPP, S., ZOBOR, G., GLOCKLE, N., MOHR, J., KOHL, S., ZRENNER, E., WEISSCHUH, N. & ZOBOR, D. 2015. Phenotype variations of retinal dystrophies caused by mutations in the RLBP1 gene. *Acta Ophthalmol,* 93**,** e281-6.

HOFFMAN, D. R., LOCKE, K. G., WHEATON, D. H., FISH, G. E., SPENCER, R. & BIRCH, D. G. 2004. A randomized, placebo-controlled clinical trial of docosahexaenoic acid supplementation for X-linked retinitis pigmentosa. *Am J Ophthalmol,* 137**,** 704-18.

HONGISTO, H., JYLHA, A., NATTINEN, J., RIECK, J., ILMARINEN, T., VEREB, Z., AAPOLA, U., BEUERMAN, R., PETROVSKI, G., UUSITALO, H. & SKOTTMAN, H. 2017. Comparative proteomic analysis of human embryonic stem cell-derived and primary human retinal pigment epithelium. *Sci Rep,* 7**,** 6016.

HORI, K., KUWABARA, J., TANAKA, Y., NISHIDA, M., KOIDE, N. & TAKAHASHI, M. 2019. A simple and static preservation system for shipping retinal pigment epithelium cell sheets. *J Tissue Eng Regen Med,* 13**,** 459-468.

HUANG, C. Y., LIU, C. L., TING, C. Y., CHIU, Y. T., CHENG, Y. C., NICHOLSON, M. W. & HSIEH, P. C. H. 2019. Human iPSC banking: barriers and opportunities. *J Biomed Sci,* 26**,** 87.

HUANG, X., CHEN, Y., ZHANG, H., MA, Q., ZHANG, Y. W. & XU, H. 2012. Salubrinal attenuates β-amyloid-induced neuronal death and microglial activation by inhibition of the NF-κB pathway. *Neurobiol Aging,* 33**,** 1007.e9-17.

HUNT, C. J. 2011. Cryopreservation of Human Stem Cells for Clinical Application: A Review. *Transfus Med Hemother,* 38**,** 107-123.

HUNT, C. J. 2019. Technical Considerations in the Freezing, Low-Temperature Storage and Thawing of Stem Cells for Cellular Therapies. *Transfus Med Hemother,* 46**,** 134-150.

HYTTINEN, J. M., AMADIO, M., VIIRI, J., PASCALE, A., SALMINEN, A. & KAARNIRANTA, K. 2014. Clearance of misfolded and aggregated proteins by aggrephagy and implications for aggregation diseases. *Ageing Res Rev,* 18**,** 16-28.

IKELLE, L., AL-UBAIDI, M. R. & NAASH, M. I. 2020. Pluripotent Stem Cells for the Treatment of Retinal Degeneration: Current Strategies and Future Directions. *Front Cell Dev Biol,* 8**,** 743.

ILLING, M. E., RAJAN, R. S., BENCE, N. F. & KOPITO, R. R. 2002. A rhodopsin mutant linked to autosomal dominant retinitis pigmentosa is prone to aggregate and interacts with the ubiquitin proteasome system. *J Biol Chem,* 277**,** 34150-60.

ISACHENKO, E., ISACHENKO, V., KATKOV, I. I., RAHIMI, G., SCHÖNDORF, T., MALLMANN, P., DESSOLE, S. & NAWROTH, F. 2004. DNA integrity and motility of human spermatozoa after standard slow freezing versus cryoprotectant-free vitrification. *Hum Reprod,* 19**,** 932-9.

JANG, T. H., PARK, S. C., YANG, J. H., KIM, J. Y., SEOK, J. H., PARK, U. S., CHOI, C. W., LEE, S. R. & HAN, J. 2017. Cryopreservation and its clinical applications. *Integr Med Res,* 6**,** 12-18.

JEONG, Y. H., KIM, U., LEE, S. G., RYU, B., KIM, J., IGOR, A., KIM, J. S., JUNG, C. R., PARK, J. H. & KIM, C. Y. 2020. Vitrification for cryopreservation of 2D and 3D stem cells culture using high concentration of cryoprotective agents. *BMC Biotechnol,* 20**,** 45.

JI, L., DE PABLO, J. J. & PALECEK, S. P. 2004. Cryopreservation of adherent human embryonic stem cells. *Biotechnol Bioeng,* 88**,** 299-312.

JONES, B. W., KONDO, M., TERASAKI, H., LIN, Y., MCCALL, M. & MARC, R. E. 2012. Retinal remodeling. *Jpn J Ophthalmol,* 56**,** 289-306.

JONES, B. W., WATT, C. B., FREDERICK, J. M., BAEHR, W., CHEN, C. K., LEVINE, E. M., MILAM, A. H., LAVAIL, M. M. & MARC, R. E. 2003. Retinal remodeling triggered by photoreceptor degenerations. *J Comp Neurol,* 464**,** 1-16.

KAMADA, S., KIKKAWA, U., TSUJIMOTO, Y. & HUNTER, T. 2005. Nuclear translocation of caspase-3 is dependent on its proteolytic activation and recognition of a substrate-like protein(s). *J Biol Chem,* 280**,** 857-60.

KANAI, Y., DOHMAE, N. & HIROKAWA, N. 2004. Kinesin transports RNA: isolation and characterization of an RNA-transporting granule. *Neuron,* 43**,** 513-25.

KANG, X., YU, Q., HUANG, Y., SONG, B., CHEN, Y., GAO, X., HE, W., SUN, X. & FAN, Y. 2015. Effects of Integrating and Non-Integrating Reprogramming Methods on Copy Number Variation and Genomic Stability of Human Induced Pluripotent Stem Cells. *PLoS One,* 10**,** e0131128.

KARAGIANNIS, P., TAKAHASHI, K., SAITO, M., YOSHIDA, Y., OKITA, K., WATANABE, A., INOUE, H., YAMASHITA, J. K., TODANI, M., NAKAGAWA, M., OSAWA, M., YASHIRO, Y., YAMANAKA, S. &

OSAFUNE, K. 2019. Induced Pluripotent Stem Cells and Their Use in Human Models of Disease and Development. *Physiol Rev,* 99**,** 79-114.
KEFALOV, V., FU, Y., MARSH-ARMSTRONG, N. & YAU, K. W. 2003. Role of visual pigment properties in rod and cone phototransduction. *Nature,* 425**,** 526-31.
KHAN, D. R., AHMAD, N., ANZAR, M. & CHANNA, A. A. 2009. Apoptosis in fresh and cryopreserved buffalo sperm. *Theriogenology,* 71**,** 872-6.
KIERAN, D., KALMAR, B., DICK, J. R., RIDDOCH-CONTRERAS, J., BURNSTOCK, G. & GREENSMITH, L. 2004. Treatment with arimoclomol, a coinducer of heat shock proteins, delays disease progression in ALS mice. *Nat Med,* 10**,** 402-5.
KIM, J., KOO, B. K. & KNOBLICH, J. A. 2020. Human organoids: model systems for human biology and medicine. *Nat Rev Mol Cell Biol,* 21**,** 571-584.
KIM, J. H., KI, S. M., JOUNG, J. G., SCOTT, E., HEYNEN-GENEL, S., AZA-BLANC, P., KWON, C. H., KIM, J., GLEESON, J. G. & LEE, J. E. 2016. Genome-wide screen identifies novel machineries required for both ciliogenesis and cell cycle arrest upon serum starvation. *Biochim Biophys Acta,* 1863**,** 1307-18.
KIM, S. J., PARK, J. H., LEE, J. E., KIM, J. M., LEE, J. B., MOON, S. Y., ROH, S. I., KIM, C. G. & YOON, H. S. 2004. Effects of type IV collagen and laminin on the cryopreservation of human embryonic stem cells. *Stem Cells,* 22**,** 950-61.
KIM, Y. C. & GUAN, K. L. 2015. mTOR: a pharmacologic target for autophagy regulation. *J Clin Invest,* 125**,** 25-32.
KISER, P. D., GOLCZAK, M. & PALCZEWSKI, K. 2014. Chemistry of the retinoid (visual) cycle. *Chem Rev,* 114**,** 194-232.
KLEINSMITH, L. J. & PIERCE, G. B., JR. 1964. Multipotentiality of Single Embryonal Carcinoma Cells. *Cancer Res,* 24**,** 1544-51.
KLIMANSKAYA, I., HIPP, J., REZAI, K. A., WEST, M., ATALA, A. & LANZA, R. 2004. Derivation and comparative assessment of retinal pigment epithelium from human embryonic stem cells using transcriptomics. *Cloning Stem Cells,* 6**,** 217-45.
KOCATURK, N. M. & GOZUACIK, D. 2018. Crosstalk Between Mammalian Autophagy and the Ubiquitin-Proteasome System. *Frontiers in Cell and Developmental Biology,* 6.
KOLB H, F. E. N. R. E. 1995. Webvision : the Organization of the Retina and Visual System.
KROEMER, G., MARIÑO, G. & LEVINE, B. 2010. Autophagy and the integrated stress response. *Mol Cell,* 40**,** 280-93.
KRYSKO, D. V., VANDEN BERGHE, T., PARTHOENS, E., D'HERDE, K. & VANDENABEELE, P. 2008. Methods for distinguishing apoptotic from necrotic cells and measuring their clearance. *Programmed Cell Death, General Principles for Studying Cell Death, Pt A,* 442**,** 307-341.
KULESHOVA, L. L., TAN, F. C. K., MAGALHÃES, R., GOUK, S. S., LEE, K. H. & DAWE, G. S. 2009. Effective Cryopreservation of Neural Stem or Progenitor Cells without Serum or Proteins by Vitrification. *Cell Transplant,* 18**,** 135-144.
KULESHOVA, L. L., WANG, X. W., WU, Y. N., ZHOU, Y. & YU, H. 2004. Vitrification of encapsulated hepatocytes with reduced cooling and warming rates. *Cryo Letters,* 25**,** 241-54.
KUWAHARA, A., OZONE, C., NAKANO, T., SAITO, K., EIRAKU, M. & SASAI, Y. 2015. Generation of a ciliary margin-like stem cell niche from self-organizing human retinal tissue. *Nat Commun,* 6**,** 6286.
KWAN, K. M., OTSUNA, H., KIDOKORO, H., CARNEY, K. R., SAIJOH, Y. & CHIEN, C. B. 2012. A complex choreography of cell movements shapes the vertebrate eye. *Development,* 139**,** 359-72.
LAGERBERG, J. W. 2015. Cryopreservation of red blood cells. *Methods Mol Biol,* 1257**,** 353-67.
LAKOWSKI, J., BARON, M., BAINBRIDGE, J., BARBER, A. C., PEARSON, R. A., ALI, R. R. & SOWDEN, J. C. 2010. Cone and rod photoreceptor transplantation in models of the childhood retinopathy Leber congenital amaurosis using flow-sorted Crx-positive donor cells. *Hum Mol Genet,* 19**,** 4545-59.
LANCASTER, M. A. & HUCH, M. 2019. Disease modelling in human organoids. *Dis Model Mech,* 12.
LEE, C. Y. & BASTACKY, J. 1995. Comparative mathematical analyses of freezing in lung and solid tissue. *Cryobiology,* 32**,** 299-305.

LEIST, M., BREMER, S., BRUNDIN, P., HESCHELER, J., KIRKEBY, A., KRAUSE, K. H., POERZGEN, P., PUCEAT, M., SCHMIDT, M., SCHRATTENHOLZ, A., ZAK, N. B. & HENTZE, H. 2008. The biological and ethical basis of the use of human embryonic stem cells for in vitro test systems or cell therapy. *ALTEX,* 25**,** 163-90.

LEN, J. S., KOH, W. S. D. & TAN, S. X. 2019. The roles of reactive oxygen species and antioxidants in cryopreservation. *Biosci Rep,* 39.

LI, T., LEWALLEN, M., CHEN, S., YU, W., ZHANG, N. & XIE, T. 2013. Multipotent stem cells isolated from the adult mouse retina are capable of producing functional photoreceptor cells. *Cell Res,* 23**,** 788-802.

LILIENBAUM, A. 2013. Relationship between the proteasomal system and autophagy. *Int J Biochem Mol Biol,* 4**,** 1-26.

LIN, B., MASLAND, R. H. & STRETTOI, E. 2009. Remodeling of cone photoreceptor cells after rod degeneration in rd mice. *Exp Eye Res,* 88**,** 589-99.

LINDER, B., DILL, H., HIRMER, A., BROCHER, J., LEE, G. P., MATHAVAN, S., BOLZ, H. J., WINKLER, C., LAGGERBAUER, B. & FISCHER, U. 2011. Systemic splicing factor deficiency causes tissue-specific defects: a zebrafish model for retinitis pigmentosa. *Hum Mol Genet,* 20**,** 368-77.

LINDERSSON, E., BEEDHOLM, R., HOJRUP, P., MOOS, T., GAI, W., HENDIL, K. B. & JENSEN, P. H. 2004. Proteasomal inhibition by alpha-synuclein filaments and oligomers. *J Biol Chem,* 279**,** 12924-34.

LIU, C., OIKONOMOPOULOS, A., SAYED, N. & WU, J. C. 2018a. Modeling human diseases with induced pluripotent stem cells: from 2D to 3D and beyond. *Development,* 145.

LIU, L., XU, L., ZHANG, S., WANG, D., DONG, G., CHEN, H., LI, X., SHU, C. & WANG, R. 2018b. STF-083010, an inhibitor of XBP1 splicing, attenuates acute renal failure in rats by suppressing endoplasmic reticulum stress-induced apoptosis and inflammation. *Exp Anim,* 67**,** 373-382.

LIU, Y., XU, H. W., WANG, L., LI, S. Y., ZHAO, C. J., HAO, J., LI, Q. Y., ZHAO, T. T., WU, W., WANG, Y., ZHOU, Q., QIAN, C. & YIN, Z. Q. 2018c. Human embryonic stem cell-derived retinal pigment epithelium transplants as a potential treatment for wet age-related macular degeneration. *Cell Discov,* 4**,** 50.

LLONCH, S., CARIDO, M. & ADER, M. 2018. Organoid technology for retinal repair. *Dev Biol,* 433**,** 132-143.

LOU, J. J., MIRSADRAEI, L., SANCHEZ, D. E., WILSON, R. W., SHABIHKHANI, M., LUCEY, G. M., WEI, B., SINGER, E. J., MARENINOV, S. & YONG, W. H. 2014. A review of room temperature storage of biospecimen tissue and nucleic acids for anatomic pathology laboratories and biorepositories. *Clinical Biochemistry Clinical Biochemistry,* 47**,** 267-273.

LOUNEVA, N., COHEN, J. W., HAN, L. Y., TALBOT, K., WILSON, R. S., BENNETT, D. A., TROJANOWSKI, J. Q. & ARNOLD, S. E. 2008. Caspase-3 is enriched in postsynaptic densities and increased in Alzheimer's disease. *Am J Pathol,* 173**,** 1488-95.

LOVE, R. 2009. Chillin' at the Symposium with Plato: Refrigeration in the Ancient World. *Ashrae Transactions 2009, Vol 115, Pt 1,* 115**,** 106-110.

LOWE, A., HARRIS, R., BHANSALI, P., CVEKL, A. & LIU, W. 2016. Intercellular Adhesion-Dependent Cell Survival and ROCK-Regulated Actomyosin-Driven Forces Mediate Self-Formation of a Retinal Organoid. *Stem Cell Reports,* 6**,** 743-756.

LUND, R. D., WANG, S., KLIMANSKAYA, I., HOLMES, T., RAMOS-KELSEY, R., LU, B., GIRMAN, S., BISCHOFF, N., SAUVÉ, Y. & LANZA, R. 2006. Human embryonic stem cell-derived cells rescue visual function in dystrophic RCS rats. *Cloning Stem Cells,* 8**,** 189-99.

LUO, M., LU, Z., SUN, H., YUAN, K., ZHANG, Q., MENG, S., WANG, F., GUO, H., JU, X., LIU, Y., YE, T. & ZHAI, Z. 2010. Nuclear entry of active caspase-3 is facilitated by its p3-recognition-based specific cleavage activity. *Cell Res,* 20**,** 211-22.

LUYET, B. J. & GEHENIO, M. P. 1940. *Life and death at low temperatures,* Normandy, Mo.,, Biodynamica.

MACLAREN, R. E., PEARSON, R. A., MACNEIL, A., DOUGLAS, R. H., SALT, T. E., AKIMOTO, M., SWAROOP, A., SOWDEN, J. C. & ALI, R. R. 2006. Retinal repair by transplantation of photoreceptor precursors. *Nature,* 444**,** 203-7.

MALINOVA, A., CVACKOVA, Z., MATEJU, D., HOREJSI, Z., ABEZA, C., VANDERMOERE, F., BERTRAND, E., STANEK, D. & VERHEGGEN, C. 2017. Assembly of the U5 snRNP component PRPF8 is controlled by the HSP90/R2TP chaperones. *J Cell Biol,* 216**,** 1579-1596.

MANDAI, M., WATANABE, A., KURIMOTO, Y., HIRAMI, Y., MORINAGA, C., DAIMON, T., FUJIHARA, M., AKIMARU, H., SAKAI, N., SHIBATA, Y., TERADA, M., NOMIYA, Y., TANISHIMA, S., NAKAMURA, M., KAMAO, H., SUGITA, S., ONISHI, A., ITO, T., FUJITA, K., KAWAMATA, S., GO, M. J., SHINOHARA, C., HATA, K. I., SAWADA, M., YAMAMOTO, M., OHTA, S., OHARA, Y., YOSHIDA, K., KUWAHARA, J., KITANO, Y., AMANO, N., UMEKAGE, M., KITAOKA, F., TANAKA, A., OKADA, C., TAKASU, N., OGAWA, S., YAMANAKA, S. & TAKAHASHI, M. 2017. Autologous Induced Stem-Cell-Derived Retinal Cells for Macular Degeneration. *N Engl J Med,* 376**,** 1038-1046.

MANDRIOLI, J., D'AMICO, R., ZUCCHI, E., GESSANI, A., FINI, N., FASANO, A., CAPONNETTO, C., CHIÒ, A., DALLA BELLA, E., LUNETTA, C., MAZZINI, L., MARINOU, K., SORARÙ, G., DE BIASI, S., LO TARTARO, D., PINTI, M., COSSARIZZA, A. & GROUP, R.-A. I. 2018. Rapamycin treatment for amyotrophic lateral sclerosis: Protocol for a phase II randomized, double-blind, placebo-controlled, multicenter, clinical trial (RAP-ALS trial). *Medicine (Baltimore),* 97**,** e11119.

MANNU, G. S. 2014. Retinal phototransduction. *Neurosciences (Riyadh),* 19**,** 275-80.

MARC, R. E., JONES, B. W., WATT, C. B. & STRETTOI, E. 2003. Neural remodeling in retinal degeneration. *Prog Retin Eye Res,* 22**,** 607-55.

MARTIN-IBANEZ, R., UNGER, C., STROMBERG, A., BAKER, D., CANALS, J. M. & HOVATTA, O. 2008. Novel cryopreservation method for dissociated human embryonic stem cells in the presence of a ROCK inhibitor. *Hum Reprod,* 23**,** 2744-54.

MARTIN, G. R. 1981. Isolation of a pluripotent cell line from early mouse embryos cultured in medium conditioned by teratocarcinoma stem cells. *Proc Natl Acad Sci U S A,* 78**,** 7634-8.

MARTINEZ-VICENTE, M., TALLOCZY, Z., WONG, E., TANG, G., KOGA, H., KAUSHIK, S., DE VRIES, R., ARIAS, E., HARRIS, S., SULZER, D. & CUERVO, A. M. 2010. Cargo recognition failure is responsible for inefficient autophagy in Huntington's disease. *Nat Neurosci,* 13**,** 567-76.

MATHEW, A. J., BAUST, J. M., VAN BUSKIRK, R. G. & BAUST, J. G. 2004. Cell preservation in reparative and regenerative medicine: evolution of individualized solution composition. *Tissue Eng,* 10**,** 1662-71.

MATSUOKA, M. & KOMOIKE, Y. 2015. Experimental Evidence Shows Salubrinal, an eIF2alpha Dephosphorylation Inhibitor, Reduces Xenotoxicant-Induced Cellular Damage. *Int J Mol Sci,* 16**,** 16275-87.

MATSUSHITA, T., YAGI, T., HARDIN, J. A., CRAGUN, J. D., CROW, F. W., BERGEN, H. R., 3RD, GORES, G. J. & NYBERG, S. L. 2003. Apoptotic cell death and function of cryopreserved porcine hepatocytes in a bioartificial liver. *Cell Transplant,* 12**,** 109-21.

MAZUR, P. 1960. Physical factors implicated in the death of microorganisms at subzero temperatures. *Ann N Y Acad Sci,* 85**,** 610-29.

MAZUR, P. 1965. The role of cell membranes in the freezing of yeast and other single cells. *Ann N Y Acad Sci,* 125**,** 658-76.

MAZUR, P., RALL, W. F. & RIGOPOULOS, N. 1981. Relative contributions of the fraction of unfrozen water and of salt concentration to the survival of slowly frozen human erythrocytes. *Biophys J,* 36**,** 653-75.

MCKIE, A. B., MCHALE, J. C., KEEN, T. J., TARTTELIN, E. E., GOLIATH, R., VAN LITH-VERHOEVEN, J. J., GREENBERG, J., RAMESAR, R. S., HOYNG, C. B., CREMERS, F. P., MACKEY, D. A., BHATTACHARYA, S. S., BIRD, A. C., MARKHAM, A. F. & INGLEHEARN, C. F. 2001. Mutations in the pre-mRNA splicing factor gene PRPC8 in autosomal dominant retinitis pigmentosa (RP13). *Hum Mol Genet,* 10**,** 1555-62.

MELGUIZO-SANCHIS, D., XU, Y., TAHEEM, D., YU, M., TILGNER, K., BARTA, T., GASSNER, K., ANYFANTIS, G., WAN, T., ELANGO, R., ALHARTHI, S., EL-HAROUNI, A. A., PRZYBORSKI, S., ADAM, S., SARETZKI, G., SAMARASINGHE, S., ARMSTRONG, L. & LAKO, M. 2018. iPSC modeling of severe aplastic anemia reveals impaired differentiation and telomere shortening in blood progenitors. *Cell Death Dis,* 9**,** 128.

MELLOUGH, C. B., BAUER, R., COLLIN, J., DORGAU, B., ZERTI, D., DOLAN, D. W. P., JONES, C. M., IZUOGU, O. G., YU, M., HALLAM, D., STEYN, J. S., WHITE, K., STEEL, D. H., SANTIBANEZ-KOREF, M., ELLIOTT, D. J., JACKSON, M. S., LINDSAY, S., GRELLSCHEID, S. & LAKO, M. 2019a. An integrated transcriptional analysis of the developing human retina. *Development,* 146.

MELLOUGH, C. B., COLLIN, J., KHAZIM, M., WHITE, K., SERNAGOR, E., STEEL, D. H. & LAKO, M. 2015. IGF-1 Signaling Plays an Important Role in the Formation of Three-Dimensional Laminated Neural Retina and Other Ocular Structures From Human Embryonic Stem Cells. *Stem Cells,* 33**,** 2416-30.

MELLOUGH, C. B., COLLIN, J., QUEEN, R., HILGEN, G., DORGAU, B., ZERTI, D., FELEMBAN, M., WHITE, K., SERNAGOR, E. & LAKO, M. 2019b. Systematic Comparison of Retinal Organoid Differentiation from Human Pluripotent Stem Cells Reveals Stage Specific, Cell Line, and Methodological Differences. *Stem Cells Transl Med,* 8**,** 694-706.

MELLOUGH, C. B., COLLIN, J., SERNAGOR, E., WRIDE, N. K., STEEL, D. H. & LAKO, M. 2014. Lab generated retina: realizing the dream. *Vis Neurosci,* 31**,** 317-32.

MELLOUGH, C. B., SERNAGOR, E., MORENO-GIMENO, I., STEEL, D. H. & LAKO, M. 2012. Efficient stage-specific differentiation of human pluripotent stem cells toward retinal photoreceptor cells. *Stem Cells,* 30**,** 673-86.

MERYMAN, H. T. 2007. Cryopreservation of living cells: principles and practice. *Transfusion,* 47**,** 935-45.

METCALF, D. J., GARCÍA-ARENCIBIA, M., HOCHFELD, W. E. & RUBINSZTEIN, D. C. 2012. Autophagy and misfolded proteins in neurodegeneration. *Exp Neurol,* 238**,** 22-8.

MEYER, J. S., HOWDEN, S. E., WALLACE, K. A., VERHOEVEN, A. D., WRIGHT, L. S., CAPOWSKI, E. E., PINILLA, I., MARTIN, J. M., TIAN, S., STEWART, R., PATTNAIK, B., THOMSON, J. A. & GAMM, D. M. 2011. Optic vesicle-like structures derived from human pluripotent stem cells facilitate a customized approach to retinal disease treatment. *Stem Cells,* 29**,** 1206-18.

MEYER, J. S., SHEARER, R. L., CAPOWSKI, E. E., WRIGHT, L. S., WALLACE, K. A., MCMILLAN, E. L., ZHANG, S. C. & GAMM, D. M. 2009. Modeling early retinal development with human embryonic and induced pluripotent stem cells. *Proc Natl Acad Sci U S A,* 106**,** 16698-703.

MILLER, T. D., MAXWELL, A. J., LINDQUIST, T. D. & REQUARD, J. 2013. Validation of cooling effect of insulated containers for the shipment of corneal tissue and recommendations for transport. *Cornea,* 32**,** 63-9.

MIYAZAKI, T. & SUEMORI, H. 2016. Slow Cooling Cryopreservation Optimized to Human Pluripotent Stem Cells. *Adv Exp Med Biol,* 951**,** 57-65.

MIZUSHIMA, N. & KOMATSU, M. 2011. Autophagy: renovation of cells and tissues. *Cell,* 147**,** 728-41.

MONAHAN, Z., RYAN, V. H., JANKE, A. M., BURKE, K. A., RHOADS, S. N., ZERZE, G. H., O'MEALLY, R., DIGNON, G. L., CONICELLA, A. E., ZHENG, W., BEST, R. B., COLE, R. N., MITTAL, J., SHEWMAKER, F. & FAWZI, N. L. 2017. Phosphorylation of the FUS low-complexity domain disrupts phase separation, aggregation, and toxicity. *EMBO J,* 36**,** 2951-2967.

MORRIS, G. J. & ACTON, E. 2013. Controlled ice nucleation in cryopreservation--a review. *Cryobiology,* 66**,** 85-92.

MOSHIRI, A., CHEN, R., KIM, S., HARRIS, R. A., LI, Y., RAVEENDRAN, M., DAVIS, S., LIANG, Q., POMERANTZ, O., WANG, J., GARZEL, L., CAMERON, A., YIU, G., STOUT, J. T., HUANG, Y., MURPHY, C. J., ROBERTS, J., GOPALAKRISHNA, K. N., BOYD, K., ARTEMYEV, N. O., ROGERS, J. & THOMASY, S. M. 2019. A nonhuman primate model of inherited retinal disease. *J Clin Invest,* 129**,** 863-874.

MOTTA, F. L., MARTIN, R. P., FILIPPELLI-SILVA, R., SALLES, M. V. & SALLUM, J. M. F. 2018. Relative frequency of inherited retinal dystrophies in Brazil. *Sci Rep,* 8**,** 15939.

MURPHY, D., CIEPLY, B., CARSTENS, R., RAMAMURTHY, V. & STOILOV, P. 2016. The Musashi 1 Controls the Splicing of Photoreceptor-Specific Exons in the Vertebrate Retina. *PLoS Genet,* 12**,** e1006256.

NAG, T. C. & WADHWA, S. 2006a. Morphological and Neurochemical Development of the Human Neural Retina. *Neuroembryology and Aging,* 4**,** 19-30.

NAG, T. C. & WADHWA, S. 2006b. Vascular changes of the retina and choroid in systemic lupus erythematosus: pathology and pathogenesis. *Curr Neurovasc Res,* 3**,** 159-68.

NAKANO, T., ANDO, S., TAKATA, N., KAWADA, M., MUGURUMA, K., SEKIGUCHI, K., SAITO, K., YONEMURA, S., EIRAKU, M. & SASAI, Y. 2012. Self-formation of optic cups and storable stratified neural retina from human ESCs. *Cell Stem Cell,* 10**,** 771-785.

NARFSTRÖM, K., KATZ, M. L., BRAGADOTTIR, R., SEELIGER, M., BOULANGER, A., REDMOND, T. M., CARO, L., LAI, C. M. & RAKOCZY, P. E. 2003. Functional and structural recovery of the retina after gene therapy in the RPE65 null mutation dog. *Invest Ophthalmol Vis Sci,* 44**,** 1663-72.

NASH, B. M., WRIGHT, D. C., GRIGG, J. R., BENNETTS, B. & JAMIESON, R. V. 2015. Retinal dystrophies, genomic applications in diagnosis and prospects for therapy. *Transl Pediatr,* 4**,** 139-63.

NCT04339764. 2020. *Autologous Transplantation of Induced Pluripotent Stem Cell-Derived Retinal Pigment Epithelium for Geographic Atrophy Associated With Age-Related Macular Degeneration* [Online]. Available: https://ClinicalTrials.gov/show/NCT04339764 [Accessed].

NIKOLAEV, N. I., LIU, Y., HUSSEIN, H. & WILLIAMS, D. J. 2012. The sensitivity of human mesenchymal stem cells to vibration and cold storage conditions representative of cold transportation. *J R Soc Interface,* 9**,** 2503-15.

NOBUSAWA, S., YOKOO, H., HIRATO, J., KAKITA, A., TAKAHASHI, H., SUGINO, T., TASAKI, K., ITOH, H., HATORI, T., SHIMOYAMA, Y., NAKAZAWA, A., NISHIZAWA, S., KISHIMOTO, H., MATSUOKA, K., NAKAYAMA, M., OKURA, N. & NAKAZATO, Y. 2012. Analysis of chromosome 19q13.42 amplification in embryonal brain tumors with ependymoblastic multilayered rosettes. *Brain Pathol,* 22**,** 689-97.

O'RAHILLY, R. & GARDNER, E. 1975. The timing and sequence of events in the development of the limbs in the human embryo. *Anat Embryol (Berl),* 148**,** 1-23.

OH, S. I., LEE, C. K., CHO, K. J., LEE, K. O., CHO, S. G. & HONG, S. 2012. Technological progress in generation of induced pluripotent stem cells for clinical applications. *ScientificWorldJournal,* 2012**,** 417809.

OLIVARES-GONZALEZ, L., VELASCO, S., CAMPILLO, I. & RODRIGO, R. 2021. Retinal Inflammation, Cell Death and Inherited Retinal Dystrophies. *Int J Mol Sci,* 22.

OSAKADA, F., IKEDA, H., MANDAI, M., WATAYA, T., WATANABE, K., YOSHIMURA, N., AKAIKE, A., SASAI, Y. & TAKAHASHI, M. 2008. Toward the generation of rod and cone photoreceptors from mouse, monkey and human embryonic stem cells. *Nat Biotechnol,* 26**,** 215-24.

PAMPHILON, D. H., SELOGIE, E., SZCZEPIORKOWSKI, Z. M. & TEAM, B. C. C. T. 2010. Transportation of cellular therapy products: report of a survey by the cellular therapies team of the Biomedical Excellence for Safer Transfusion (BEST) collaborative. *Vox Sang,* 99**,** 168-73.

PARFITT, D. A., AGUILA, M., MCCULLEY, C. H., BEVILACQUA, D., MENDES, H. F., ATHANASIOU, D., NOVOSELOV, S. S., KANUGA, N., MUNRO, P. M., COFFEY, P. J., KALMAR, B., GREENSMITH, L. & CHEETHAM, M. E. 2014. The heat-shock response co-inducer arimoclomol protects against retinal degeneration in rhodopsin retinitis pigmentosa. *Cell Death Dis,* 5**,** e1236.

PARMEGGIANI, F., SATO, G., DE NADAI, K., ROMANO, M. R., BINOTTO, A. & COSTAGLIOLA, C. 2011. Clinical and Rehabilitative Management of Retinitis Pigmentosa: Up-to-Date. *Curr Genomics,* 12**,** 250-9.

PAYNTER, S. J. 2008. Principles and practical issues for cryopreservation of nerve cells. *Brain Res Bull,* 75**,** 1-14.

PEARSON, R. A., GONZALEZ-CORDERO, A., WEST, E. L., RIBEIRO, J. R., AGHAIZU, N., GOH, D., SAMPSON, R. D., GEORGIADIS, A., WALDRON, P. V., DURAN, Y., NAEEM, A., KLOC, M., CRISTANTE, E., KRUCZEK, K., WARRE-CORNISH, K., SOWDEN, J. C., SMITH, A. J. & ALI, R. R. 2016. Donor and host photoreceptors engage in material transfer following transplantation of post-mitotic photoreceptor precursors. *Nat Commun,* 7**,** 13029.

PEGG, D. E. 2007. Principles of cryopreservation. *Methods Mol Biol,* 368**,** 39-57.

PEGG, D. E., WANG, L. & VAUGHAN, D. 2006. Cryopreservation of articular cartilage. Part 3: The liquidus-tracking method. *YCRYO Cryobiology,* 52**,** 360-368.

PERA, M. F., REUBINOFF, B. & TROUNSON, A. 2000. Human embryonic stem cells. *J Cell Sci,* 113 (Pt 1)**,** 5-10.

PHILLIPS, M. J., PEREZ, E. T., MARTIN, J. M., RESHEL, S. T., WALLACE, K. A., CAPOWSKI, E. E., SINGH, R., WRIGHT, L. S., CLARK, E. M., BARNEY, P. M., STEWART, R., DICKERSON, S. J., MILLER, M. J., PERCIN, E. F., THOMSON, J. A. & GAMM, D. M. 2014. Modeling human retinal development with patient-specific induced pluripotent stem cells reveals multiple roles for visual system homeobox 2. *Stem Cells,* 32**,** 1480-92.

PICHUGIN, Y., FAHY, G. M. & MORIN, R. 2006. Cryopreservation of rat hippocampal slices by vitrification. *Cryobiology,* 52**,** 228-40.

POLGE, C., SMITH, A. U. & PARKES, A. S. 1949. Revival of spermatozoa after vitrification and dehydration at low temperatures. *Nature,* 164**,** 666.

PRENDINI, L., HANNER, R. & DESALLE, R. 2002. Obtaining, Storing and Archiving Specimens and Tissue Samples for Use in Molecular Studies. 176-248.

QI, L., ZHANG, X. D., WU, J. C., LIN, F., WANG, J., DIFIGLIA, M. & QIN, Z. H. 2012. The role of chaperone-mediated autophagy in huntingtin degradation. *PLoS One,* 7**,** e46834.

QUINN, P. M. J. & WIJNHOLDS, J. 2019. Retinogenesis of the Human Fetal Retina: An Apical Polarity Perspective. *Genes (Basel),* 10.

RAJU, R., BRYANT, S. J., WILKINSON, B. L. & BRYANT, G. 2021. The need for novel cryoprotectants and cryopreservation protocols: Insights into the importance of biophysical investigation and cell permeability. *Biochim Biophys Acta Gen Subj,* 1865**,** 129749.

RAO, R. V. & BREDESEN, D. E. 2004. Misfolded proteins, endoplasmic reticulum stress and neurodegeneration. *Curr Opin Cell Biol,* 16**,** 653-62.

RAVIKUMAR, B., VACHER, C., BERGER, Z., DAVIES, J. E., LUO, S., OROZ, L. G., SCARAVILLI, F., EASTON, D. F., DUDEN, R., O'KANE, C. J. & RUBINSZTEIN, D. C. 2004. Inhibition of mTOR induces autophagy and reduces toxicity of polyglutamine expansions in fly and mouse models of Huntington disease. *Nat Genet,* 36**,** 585-95.

RAY, P., LUO, X. Y., RAO, E. J., BASHA, A., WOODRUFF, E. A. & WU, J. Y. 2010. The splicing factor Prp31 is essential for photoreceptor development in Drosophila. *Protein & Cell,* 1**,** 267-274.

REDDY, V. S., RAGHU, G., REDDY, S. S., PASUPULATI, A. K., SURYANARAYANA, P. & REDDY, G. B. 2013. Response of small heat shock proteins in diabetic rat retina. *Invest Ophthalmol Vis Sci,* 54**,** 7674-82.

REGENT, F., MORIZUR, L., LESUEUR, L., HABELER, W., PLANCHERON, A., BEN M'BAREK, K. & MONVILLE, C. 2019. Automation of human pluripotent stem cell differentiation toward retinal pigment epithelial cells for large-scale productions. *Sci Rep,* 9**,** 10646.

REICHENBACH, A. & BRINGMANN, A. 2013. New functions of Müller cells. *Glia,* 61**,** 651-78.

REICHMAN, S., SLEMBROUCK, A., GAGLIARDI, G., CHAFFIOL, A., TERRAY, A., NANTEAU, C., POTEY, A., BELLE, M., RABESANDRATANA, O., DUEBEL, J., ORIEUX, G., NANDROT, E. F., SAHEL, J. A. & GOUREAU, O. 2017. Generation of Storable Retinal Organoids and Retinal Pigmented Epithelium from Adherent Human iPS Cells in Xeno-Free and Feeder-Free Conditions. *Stem Cells,* 35**,** 1176-1188.

REUBINOFF, B. E., PERA, M. F., VAJTA, G. & TROUNSON, A. O. 2001. Effective cryopreservation of human embryonic stem cells by the open pulled straw vitrification method. *Hum Reprod,* 16**,** 2187-94.

REZAZADEH VALOJERDI, M., EFTEKHARI-YAZDI, P., KARIMIAN, L., HASSANI, F. & MOVAGHAR, B. 2009. Vitrification versus slow freezing gives excellent survival, post warming embryo morphology and pregnancy outcomes for human cleaved embryos. *J Assist Reprod Genet,* 26**,** 347-54.

RIBEIRO, J., PROCYK, C. A., WEST, E. L., O'HARA-WRIGHT, M., MARTINS, M. F., KHORASANI, M. M., HARE, A., BASCHE, M., FERNANDO, M., GOH, D., JUMBO, N., RIZZI, M., POWELL, K., TARIQ, M., MICHAELIDES, M., BAINBRIDGE, J. W. B., SMITH, A. J., PEARSON, R. A., GONZALEZ-CORDERO, A. & ALI, R. R. 2021. Restoration of visual function in advanced disease after transplantation of purified human pluripotent stem cell-derived cone photoreceptors. *Cell Rep,* 35**,** 109022.

RICHARDS, M., FONG, C. Y., TAN, S., CHAN, W. K. & BONGSO, A. 2004. An efficient and safe xeno-free cryopreservation method for the storage of human embryonic stem cells. *Stem Cells,* 22**,** 779-89.

RIVOLTA, C., MCGEE, T. L., RIO FRIO, T., JENSEN, R. V., BERSON, E. L. & DRYJA, T. P. 2006. Variation in retinitis pigmentosa-11 (PRPF31 or RP11) gene expression between symptomatic and asymptomatic patients with dominant RP11 mutations. *Hum Mutat,* 27**,** 644-53.

ROBINTON, D. A. & DALEY, G. Q. 2012. The promise of induced pluripotent stem cells in research and therapy. *Nature,* 481**,** 295-305.

RODRIGUEZ-NAVARRO, J. A. & CUERVO, A. M. 2010. Autophagy and lipids: tightening the knot. *Semin Immunopathol,* 32**,** 343-53.

ROWE, R. G. & DALEY, G. Q. 2019. Induced pluripotent stem cells in disease modelling and drug discovery. *Nat Rev Genet,* 20**,** 377-388.

RUSSELL, S., BENNETT, J., WELLMAN, J. A., CHUNG, D. C., YU, Z. F., TILLMAN, A., WITTES, J., PAPPAS, J., ELCI, O., MCCAGUE, S., CROSS, D., MARSHALL, K. A., WALSHIRE, J., KEHOE, T. L., REICHERT, H., DAVIS, M., RAFFINI, L., GEORGE, L. A., HUDSON, F. P., DINGFIELD, L., ZHU, X., HALLER, J. A., SOHN, E. H., MAHAJAN, V. B., PFEIFER, W., WECKMANN, M., JOHNSON, C., GEWAILY, D., DRACK, A., STONE, E., WACHTEL, K., SIMONELLI, F., LEROY, B. P., WRIGHT, J. F., HIGH, K. A. & MAGUIRE, A. M. 2017. Efficacy and safety of voretigene neparvovec (AAV2-hRPE65v2) in patients with RPE65-mediated inherited retinal dystrophy: a randomised, controlled, open-label, phase 3 trial. *Lancet,* 390**,** 849-860.

RŮŽIČKOVÁ, Š. & STANĚK, D. 2017. Mutations in spliceosomal proteins and retina degeneration. *RNA Biol,* 14**,** 544-552.

RYHANEN, T., HYTTINEN, J. M., KOPITZ, J., RILLA, K., KUUSISTO, E., MANNERMAA, E., VIIRI, J., HOLMBERG, C. I., IMMONEN, I., MERI, S., PARKKINEN, J., ESKELINEN, E. L., UUSITALO, H., SALMINEN, A. & KAARNIRANTA, K. 2009. Crosstalk between Hsp70 molecular chaperone, lysosomes and proteasomes in autophagy-mediated proteolysis in human retinal pigment epithelial cells. *J Cell Mol Med,* 13**,** 3616-31.

SAHEL, J. A., MARAZOVA, K. & AUDO, I. 2014. Clinical characteristics and current therapies for inherited retinal degenerations. *Cold Spring Harb Perspect Med,* 5**,** a017111.

SALIBA, R. S., MUNRO, P. M., LUTHERT, P. J. & CHEETHAM, M. E. 2002. The cellular fate of mutant rhodopsin: quality control, degradation and aggresome formation. *J Cell Sci,* 115**,** 2907-18.

SANO, R. & REED, J. C. 2013. ER stress-induced cell death mechanisms. *Biochim Biophys Acta,* 1833**,** 3460-3470.

SANTOS-FERREIRA, T., LLONCH, S., BORSCH, O., POSTEL, K., HAAS, J. & ADER, M. 2016. Retinal transplantation of photoreceptors results in donor-host cytoplasmic exchange. *Nat Commun,* 7**,** 13028.

SANTOS, L. E. & FERREIRA, S. T. 2018. Crosstalk between endoplasmic reticulum stress and brain inflammation in Alzheimer's disease. *Neuropharmacology,* 136**,** 350-360.

SANTOS, N. C., FIGUEIRA-COELHO, J., MARTINS-SILVA, J. & SALDANHA, C. 2003. Multidisciplinary utilization of dimethyl sulfoxide: pharmacological, cellular, and molecular aspects. *Biochem Pharmacol,* 65**,** 1035-41.

SARKAR, S. & RUBINSZTEIN, D. C. 2008. Huntington's disease: degradation of mutant huntingtin by autophagy. *FEBS J,* 275**,** 4263-70.

SAXENA, S., CABUY, E. & CARONI, P. 2009. A role for motoneuron subtype-selective ER stress in disease manifestations of FALS mice. *Nat Neurosci,* 12**,** 627-36.

SCHALLENBERGER, M., LOVICK, H., LOCKE, J., MEYER, T. & JUDA, G. 2016. The effect of temperature exposure during shipment on a commercially available demineralized bone matrix putty. *Cell Tissue Bank,* 17**,** 677-687.

SCHRÖDER, M. & KAUFMAN, R. J. 2005. The mammalian unfolded protein response. *Annu Rev Biochem,* 74**,** 739-89.

SEILER, M. J. & ARAMANT, R. B. 2012. Cell replacement and visual restoration by retinal sheet transplants. *Prog Retin Eye Res,* 31**,** 661-87.

SHAMSI, T. N., ATHAR, T., PARVEEN, R. & FATIMA, S. 2017. A review on protein misfolding, aggregation and strategies to prevent related ailments. *Int J Biol Macromol,* 105**,** 993-1000.

SHI, X., HU, H., JI, G., ZHANG, J., LIU, R., ZHANG, H. & LI, M. 2018. Protective Effect of Sucrose and Antioxidants on Cryopreservation of Sperm Motility and DNA Integrity in C57BL/6 Mice. *Biopreserv Biobank,* 16**,** 444-450.

SHI, Y., INOUE, H., WU, J. C. & YAMANAKA, S. 2017. Induced pluripotent stem cell technology: a decade of progress. *Nat Rev Drug Discov,* 16**,** 115-130.

SHIARLI, A. M., JENNINGS, R., SHI, J., BAILEY, K., DAVIDSON, Y., TIAN, J., BIGIO, E. H., GHETTI, B., MURRELL, J. R., DELISLE, M. B., MIRRA, S., CRAIN, B., ZOLO, P., ARIMA, K., ISEKI, E., MURAYAMA, S., KRETZSCHMAR, H., NEUMANN, M., LIPPA, C., HALLIDAY, G., MACKENZIE, J., KHAN, N., RAVID, R., DICKSON, D., WSZOLEK, Z., IWATSUBO, T., PICKERING-BROWN, S. M. & MANN, D. M. 2006. Comparison of extent of tau pathology in patients with frontotemporal dementia with Parkinsonism linked to chromosome 17 (FTDP-17), frontotemporal lobar degeneration with Pick bodies and early onset Alzheimer's disease. *Neuropathol Appl Neurobiol,* 32**,** 374-87.

SILLER, R., GREENHOUGH, S., PARK, I. H. & SULLIVAN, G. J. 2013. Modelling human disease with pluripotent stem cells. *Curr Gene Ther,* 13**,** 99-110.

SIMIONE, F. & SHARP, T. 2017. Best practices for storing and shipping cryopreserved cells. *In Vitro Cell Dev Biol Anim,* 53**,** 888-895.

SINGH, M. S., CHARBEL ISSA, P., BUTLER, R., MARTIN, C., LIPINSKI, D. M., SEKARAN, S., BARNARD, A. R. & MACLAREN, R. E. 2013. Reversal of end-stage retinal degeneration and restoration of visual function by photoreceptor transplantation. *Proc Natl Acad Sci U S A,* 110**,** 1101-6.

SINGH, R., CUZZANI, O., BINETTE, F., STERNBERG, H., WEST, M. D. & NASONKIN, I. O. 2018. Pluripotent Stem Cells for Retinal Tissue Engineering: Current Status and Future Prospects. *Stem Cell Rev Rep,* 14**,** 463-483.

SINGH, R. K., WINKLER, P., BINETTE, F., GLICKMAN, R. D., SEILER, M., PETERSEN-JONES, S. M. & NASONKIN, I. O. 2020. Development of a protocol for maintaining viability while shipping organoid-derived retinal tissue. *J Tissue Eng Regen Med,* 14**,** 388-394.

SINGH, V. K., KALSAN, M., KUMAR, N., SAINI, A. & CHANDRA, R. 2015. Induced pluripotent stem cells: applications in regenerative medicine, disease modeling, and drug discovery. *Front Cell Dev Biol,* 3**,** 2.

SNIGDHA, S., SMITH, E. D., PRIETO, G. A. & COTMAN, C. W. 2012. Caspase-3 activation as a bifurcation point between plasticity and cell death. *Neurosci Bull,* 28**,** 14-24.

SON, W. Y. & TAN, S. L. 2009. Comparison between slow freezing and vitrification for human embryos. *Expert Rev Med Devices,* 6**,** 1-7.

SOTO, C. & PRITZKOW, S. 2018. Protein misfolding, aggregation, and conformational strains in neurodegenerative diseases. *Nat Neurosci,* 21**,** 1332-1340.

STEFAN, M. M., GORLIN, J., ILLES, M. & WALLACE, M. 2001. Shipping frozen components: The dry ice alternative. *Transfusion,* 41**,** 136s-136s.

STRAUSS, O. 2005. The retinal pigment epithelium in visual function. *Physiol Rev,* 85**,** 845-81.

SUGIMACHI, K., SOSEF, M. N., BAUST, J. M., FOWLER, A., TOMPKINS, R. G. & TONER, M. 2004. Long-term function of cryopreserved rat hepatocytes in a coculture system. *Cell Transplant,* 13**,** 187-95.

SUNG, C. H. & CHUANG, J. Z. 2010. The cell biology of vision. *J Cell Biol,* 190**,** 953-63.

SURGUCHEVA, I., NINKINA, N., BUCHMAN, V. L., GRASING, K. & SURGUCHOV, A. 2005. Protein aggregation in retinal cells and approaches to cell protection. *Cell Mol Neurobiol,* 25**,** 1051-66.

SWAROOP, A., KIM, D. & FORREST, D. 2010. Transcriptional regulation of photoreceptor development and homeostasis in the mammalian retina. *Nat Rev Neurosci,* 11**,** 563-76.

SWEENEY, P., PARK, H., BAUMANN, M., DUNLOP, J., FRYDMAN, J., KOPITO, R., MCCAMPBELL, A., LEBLANC, G., VENKATESWARAN, A., NURMI, A. & HODGSON, R. 2017. Protein misfolding in neurodegenerative diseases: implications and strategies. *Transl Neurodegener,* 6**,** 6.

SYME, R., BEWICK, M., STEWART, D., PORTER, K., CHADDERTON, T. & GLUCK, S. 2004. The role of depletion of dimethyl sulfoxide before autografting: on hematologic recovery, side effects, and toxicity. *Biol Blood Marrow Transplant,* 10**,** 135-41.

TAI, H. C., SERRANO-POZO, A., HASHIMOTO, T., FROSCH, M. P., SPIRES-JONES, T. L. & HYMAN, B. T. 2012. The Synaptic Accumulation of Hyperphosphorylated Tau Oligomers in Alzheimer Disease Is Associated With Dysfunction of the Ubiquitin-Proteasome System. *American Journal of Pathology,* 181**,** 1426-1435.

TAKAHASHI, K., TANABE, K., OHNUKI, M., NARITA, M., ICHISAKA, T., TOMODA, K. & YAMANAKA, S. 2007. Induction of pluripotent stem cells from adult human fibroblasts by defined factors. *Cell,* 131**,** 861-72.

TAKAHASHI, K. & YAMANAKA, S. 2006. Induction of pluripotent stem cells from mouse embryonic and adult fibroblast cultures by defined factors. *Cell,* 126**,** 663-76.

TAKALO, M., SALMINEN, A., SOININEN, H., HILTUNEN, M. & HAAPASALO, A. 2013. Protein aggregation and degradation mechanisms in neurodegenerative diseases. *Am J Neurodegener Dis,* 2**,** 1-14.

TANACKOVIC, G., RANSIJN, A., AYUSO, C., HARPER, S., BERSON, E. L. & RIVOLTA, C. 2011. A missense mutation in PRPF6 causes impairment of pre-mRNA splicing and autosomal-dominant retinitis pigmentosa. *Am J Hum Genet,* 88**,** 643-9.

TANACKOVIC, G. & RIVOLTA, C. 2009. PRPF31 alternative splicing and expression in human retina. *Ophthalmic Genet,* 30**,** 76-83.

TANAKA, K. 2009. The proteasome: overview of structure and functions. *Proc Jpn Acad Ser B Phys Biol Sci,* 85**,** 12-36.

TAYLOR, M. J., WEEGMAN, B. P., BAICU, S. C. & GIWA, S. E. 2019. New Approaches to Cryopreservation of Cells, Tissues, and Organs. *Transfus Med Hemother,* 46**,** 197-215.

TERRY, C., DHAWAN, A., MITRY, R. R., LEHEC, S. C. & HUGHES, R. D. 2006. Preincubation of rat and human hepatocytes with cytoprotectants prior to cryopreservation can improve viability and function upon thawing. *Liver Transpl,* 12**,** 165-77.

TERSKIKH, V. V., VOROTELYAK, Y. A. & VASILIEV, A. V. 2009. Self-renewal of stem cells. *Acta Naturae,* 1**,** 61-5.

THOMSON, J. A., ITSKOVITZ-ELDOR, J., SHAPIRO, S. S., WAKNITZ, M. A., SWIERGIEL, J. J., MARSHALL, V. S. & JONES, J. M. 1998. Embryonic stem cell lines derived from human blastocysts. *Science,* 282**,** 1145-7.

TIRKKONEN, L., HALONEN, H., HYTTINEN, J., KUOKKANEN, H., SIEVANEN, H., KOIVISTO, A. M., MANNERSTROM, B., SANDOR, G. K., SUURONEN, R., MIETTINEN, S. & HAIMI, S. 2011. The effects of vibration loading on adipose stem cell number, viability and differentiation towards bone-forming cells. *J R Soc Interface,* 8**,** 1736-47.

TRAVIS, G. H., GOLCZAK, M., MOISE, A. R. & PALCZEWSKI, K. 2007. Diseases caused by defects in the visual cycle: retinoids as potential therapeutic agents. *Annu Rev Pharmacol Toxicol,* 47**,** 469-512.

TSIN, A., BETTS-OBREGON, B. & GRIGSBY, J. 2018. Visual cycle proteins: Structure, function, and roles in human retinal disease. *J Biol Chem,* 293**,** 13016-13021.

TUCKER, B. A., MULLINS, R. F., STREB, L. M., ANFINSON, K., EYESTONE, M. E., KAALBERG, E., RIKER, M. J., DRACK, A. V., BRAUN, T. A. & STONE, E. M. 2013. Patient-specific iPSC-derived photoreceptor precursor cells as a means to investigate retinitis pigmentosa. *Elife,* 2**,** e00824.

TYANOVA, S., TEMU, T., SINITCYN, P., CARLSON, A., HEIN, M. Y., GEIGER, T., MANN, M. & COX, J. 2016. The Perseus computational platform for comprehensive analysis of (prote)omics data. *Nat Methods,* 13**,** 731-40.

TYZACK, G. E., LUISIER, R., TAHA, D. M., NEEVES, J., MODIC, M., MITCHELL, J. S., MEYER, I., GREENSMITH, L., NEWCOMBE, J., ULE, J., LUSCOMBE, N. M. & PATANI, R. 2019. Widespread FUS mislocalization is a molecular hallmark of amyotrophic lateral sclerosis. *Brain,* 142**,** 2572-2580.

UDAGAWA, T., FUJIOKA, Y., TANAKA, M., HONDA, D., YOKOI, S., RIKU, Y., IBI, D., NAGAI, T., YAMADA, K., WATANABE, H., KATSUNO, M., INADA, T., OHNO, K., SOKABE, M., OKADO, H., ISHIGAKI, S. & SOBUE, G. 2015. FUS regulates AMPA receptor function and FTLD/ALS-associated behaviour via GluA1 mRNA stabilization. *Nat Commun,* 6**,** 7098.

URBANI, L., MAGHSOUDLOU, P., MILAN, A., MENIKOU, M., HAGEN, C. K., TOTONELLI, G., CAMILLI, C., EATON, S., BURNS, A., OLIVO, A. & DE COPPI, P. 2017. Long-term cryopreservation of decellularised oesophagi for tissue engineering clinical application. *PLoS One,* 12**,** e0179341.

UTZ, V. M., BEIGHT, C. D., MARINO, M. J., HAGSTROM, S. A. & TRABOULSI, E. I. 2013. Autosomal dominant retinitis pigmentosa secondary to pre-mRNA splicing-factor gene PRPF31 (RP11): review of disease mechanism and report of a family with a novel 3-base pair insertion. *Ophthalmic Genet,* 34**,** 183-8.

VAIRETTI, M., GRIFFINI, P., PIETROCOLA, G., RICHELMI, P. & FREITAS, I. 2001. Cold-induced apoptosis in isolated rat hepatocytes: protective role of glutathione. *Free Radic Biol Med,* 31**,** 954-61.

VALDÉS-SÁNCHEZ, L., CALADO, S. M., DE LA CERDA, B., ARAMBURU, A., GARCÍA-DELGADO, A. B., MASSALINI, S., MONTERO-SÁNCHEZ, A., BHATIA, V., RODRÍGUEZ-BOCANEGRA, E., DIEZ-LLORET, A., RODRÍGUEZ-MARTÍNEZ, D., CHAKAROVA, C., BHATTACHARYA, S. S. & DÍAZ-CORRALES, F. J. 2019. Retinal pigment epithelium degeneration caused by aggregation of PRPF31 and the role of HSP70 family of proteins. *Mol Med,* 26**,** 1.

VALDEZ, C. A., ABAS MAZNI, O., TAKAHASHI, Y., FUJIKAWA, S. & KANAGAWA, H. 1992. Successful cryopreservation of mouse blastocysts using a new vitrification solution. *J Reprod Fertil,* 96**,** 793-802.

VANHULLE, V. P., NEYRINCK, A. M., PYCKE, J. M., HORSMANS, Y. & DELZENNE, N. M. 2006. Role of apoptotic signaling pathway in metabolic disturbances occurring in liver tissue after cryopreservation: Study on rat precision-cut liver slices. *Life Sci,* 78**,** 1570-7.

VERBAKEL, S. K., VAN HUET, R. A. C., BOON, C. J. F., DEN HOLLANDER, A. I., COLLIN, R. W. J., KLAVER, C. C. W., HOYNG, C. B., ROEPMAN, R. & KLEVERING, B. J. 2018. Non-syndromic retinitis pigmentosa. *Prog Retin Eye Res,* 66**,** 157-186.

VÍGH, L., LITERÁTI, P. N., HORVÁTH, I., TÖRÖK, Z., BALOGH, G., GLATZ, A., KOVÁCS, E., BOROS, I., FERDINÁNDY, P., FARKAS, B., JASZLITS, L., JEDNÁKOVITS, A., KORÁNYI, L. & MARESCA, B. 1997. Bimoclomol: a nontoxic, hydroxylamine derivative with stress protein-inducing activity and cytoprotective effects. *Nat Med,* 3**,** 1150-4.

VILLANUEVA, A., WILLER, J. R., BRYOIS, J., DERMITZAKIS, E. T., KATSANIS, N. & DAVIS, E. E. 2014. Whole exome sequencing of a dominant retinitis pigmentosa family identifies a novel deletion in PRPF31. *Invest Ophthalmol Vis Sci,* 55**,** 2121-9.

VITHANA, E. N., ABU-SAFIEH, L., PELOSINI, L., WINCHESTER, E., HORNAN, D., BIRD, A. C., HUNT, D. M., BUSTIN, S. A. & BHATTACHARYA, S. S. 2003. Expression of PRPF31 mRNA in patients with autosomal dominant retinitis pigmentosa: a molecular clue for incomplete penetrance? *Invest Ophthalmol Vis Sci,* 44**,** 4204-9.

VÖLKNER, M., ZSCHÄTZSCH, M., ROSTOVSKAYA, M., OVERALL, R. W., BUSSKAMP, V., ANASTASSIADIS, K. & KARL, M. O. 2016. Retinal Organoids from Pluripotent Stem Cells Efficiently Recapitulate Retinogenesis. *Stem Cell Reports,* 6**,** 525-538.

WAHL, M. C., WILL, C. L. & LÜHRMANN, R. 2009. The spliceosome: design principles of a dynamic RNP machine. *Cell,* 136**,** 701-18.

WALGENBACH, S., ROSNIATOWSKI, R., BITTINGER, F., SCHICKETANZ, K. H., HAFNER, F., HENGSTLER, J. & JUNGINGER, T. 1999. Modified cryopreservation and xenotransplantation of human parathyroid tissue. *Langenbecks Arch Surg,* 384**,** 277-83.

WANG, L., PEGG, D. E., LORRISON, J., VAUGHAN, D. & ROONEY, P. 2007. Further work on the cryopreservation of articular cartilage with particular reference to the liquidus tracking (LT) method. *Cryobiology,* 55**,** 138-47.

WANG, S. & KAUFMAN, R. J. 2012. The impact of the unfolded protein response on human disease. *J Cell Biol,* 197**,** 857-67.

WANG, X., YU, Q., YUE, H., ZHANG, J., ZENG, S. & CUI, F. 2018. Corrigendum to "Circulating Endocannabinoids and Insulin Resistance in Patients with Obstructive Sleep Apnea". *Biomed Res Int,* 2018**,** 5080563.

WANG, Z. F., GAO, C., CHEN, W., GAO, Y., WANG, H. C., MENG, Y., LUO, C. L., ZHANG, M. Y., CHEN, G., CHEN, X. P., WANG, T. & TAO, L. Y. 2019. Salubrinal offers neuroprotection through

suppressing endoplasmic reticulum stress, autophagy and apoptosis in a mouse traumatic brain injury model. *Neurobiol Learn Mem,* 161**,** 12-25.

WASEEM, N. H., VACLAVIK, V., WEBSTER, A., JENKINS, S. A., BIRD, A. C. & BHATTACHARYA, S. S. 2007. Mutations in the gene coding for the pre-mRNA splicing factor, PRPF31, in patients with autosomal dominant retinitis pigmentosa. *Invest Ophthalmol Vis Sci,* 48**,** 1330-4.

WEBB, J. L., RAVIKUMAR, B., ATKINS, J., SKEPPER, J. N. & RUBINSZTEIN, D. C. 2003. Alpha-Synuclein is degraded by both autophagy and the proteasome. *J Biol Chem,* 278**,** 25009-13.

WHEWAY, G., DOUGLAS, A., BARALLE, D. & GUILLOT, E. 2020. Mutation spectrum of PRPF31, genotype-phenotype correlation in retinitis pigmentosa, and opportunities for therapy. *Exp Eye Res,* 192**,** 107950.

WHEWAY, G., SCHMIDTS, M., MANS, D. A., SZYMANSKA, K., NGUYEN, T. T., RACHER, H., PHELPS, I. G., TOEDT, G., KENNEDY, J., WUNDERLICH, K. A., SORUSCH, N., ABDELHAMED, Z. A., NATARAJAN, S., HERRIDGE, W., VAN REEUWIJK, J., HORN, N., BOLDT, K., PARRY, D. A., LETTEBOER, S. J. F., ROOSING, S., ADAMS, M., BELL, S. M., BOND, J., HIGGINS, J., MORRISON, E. E., TOMLINSON, D. C., SLAATS, G. G., VAN DAM, T. J. P., HUANG, L., KESSLER, K., GIESSL, A., LOGAN, C. V., BOYLE, E. A., SHENDURE, J., ANAZI, S., ALDAHMESH, M., AL HAZZAA, S., HEGELE, R. A., OBER, C., FROSK, P., MHANNI, A. A., CHODIRKER, B. N., CHUDLEY, A. E., LAMONT, R., BERNIER, F. P., BEAULIEU, C. L., GORDON, P., PON, R. T., DONAHUE, C., BARKOVICH, A. J., WOLF, L., TOOMES, C., THIEL, C. T., BOYCOTT, K. M., MCKIBBIN, M., INGLEHEARN, C. F., STEWART, F., OMRAN, H., HUYNEN, M. A., SERGOUNIOTIS, P. I., ALKURAYA, F. S., PARBOOSINGH, J. S., INNES, A. M., WILLOUGHBY, C. E., GILES, R. H., WEBSTER, A. R., UEFFING, M., BLACQUE, O., GLEESON, J. G., WOLFRUM, U., BEALES, P. L., GIBSON, T., DOHERTY, D., MITCHISON, H. M., ROEPMAN, R., JOHNSON, C. A., CONSORTIUM, U. K. & GENOMICS, U. O. W. C. F. M. 2015. An siRNA-based functional genomics screen for the identification of regulators of ciliogenesis and ciliopathy genes. *Nat Cell Biol,* 17**,** 1074-1087.

WILKIE, S. E., MORRIS, K. J., BHATTACHARYA, S. S., WARREN, M. J. & HUNT, D. M. 2006. A study of the nuclear trafficking of the splicing factor protein PRPF31 linked to autosomal dominant retinitis pigmentosa (ADRP). *Biochim Biophys Acta,* 1762**,** 304-11.

WINKLER, P. A., OCCELLI, L. M. & PETERSEN-JONES, S. M. 2020. Large Animal Models of Inherited Retinal Degenerations: A Review. *Cells,* 9.

WOLF, D. H. & HILT, W. 2004. The proteasome: a proteolytic nanomachine of cell regulation and waste disposal. *Biochim Biophys Acta,* 1695**,** 19-31.

WRIGHT, A. F., CHAKAROVA, C. F., ABD EL-AZIZ, M. M. & BHATTACHARYA, S. S. 2010. Photoreceptor degeneration: genetic and mechanistic dissection of a complex trait. *Nat Rev Genet,* 11**,** 273-84.

WU, Y., YU, H., CHANG, S., MAGALHÃES, R. & KULESHOVA, L. L. 2007. Vitreous cryopreservation of cell-biomaterial constructs involving encapsulated hepatocytes. *Tissue Eng,* 13**,** 649-58.

XU, X., COWLEY, S., FLAIM, C. J., JAMES, W., SEYMOUR, L. & CUI, Z. 2010. The roles of apoptotic pathways in the low recovery rate after cryopreservation of dissociated human embryonic stem cells. *Biotechnol Prog,* 26**,** 827-37.

XUE, Y., SHEN, S. Q., JUI, J., RUPP, A. C., BYRNE, L. C., HATTAR, S., FLANNERY, J. G., CORBO, J. C. & KEFALOV, V. J. 2015. CRALBP supports the mammalian retinal visual cycle and cone vision. *J Clin Invest,* 125**,** 727-38.

YAMANAKA, S. 2012. Induced pluripotent stem cells: past, present, and future. *Cell Stem Cell,* 10**,** 678-684.

YAMASHITA, Y. M., YUAN, H., CHENG, J. & HUNT, A. J. 2010. Polarity in stem cell division: asymmetric stem cell division in tissue homeostasis. *Cold Spring Harb Perspect Biol,* 2**,** a001313.

YANG, J. J., XU, X. X., MIN, L. F., LIN, P. & QIAN, G. S. 2012. [The negative enrichment by immunomagnetic beads for tumor cells from malignant pleural effusions]. *Zhonghua Jie He He Hu Xi Za Zhi,* 35**,** 673-8.

YANG, L., GAL, J., CHEN, J. & ZHU, H. 2014. Self-assembled FUS binds active chromatin and regulates gene transcription. *Proc Natl Acad Sci U S A,* 111**,** 17809-14.

YANG, L., LI, C., CHEN, L. & LI, Z. 2009. An agarose-gel based method for transporting cell lines. *Curr Chem Genomics,* 3**,** 50-3.

YAVIN, S. & ARAV, A. 2007. Measurement of essential physical properties of vitrification solutions. *Theriogenology,* 67**,** 81-9.

YOKOMISE, H., INUI, K., WADA, H., UEDA, M. & HITOMI, S. 1996. Reliable long-term cryopreservation of trachea for tissue banks. *Transplant Proc,* 28**,** 1119-20.

YOSHIDA, T., OZAWA, Y., SUZUKI, K., YUKI, K., OHYAMA, M., AKAMATSU, W., MATSUZAKI, Y., SHIMMURA, S., MITANI, K., TSUBOTA, K. & OKANO, H. 2014. The use of induced pluripotent stem cells to reveal pathogenic gene mutations and explore treatments for retinitis pigmentosa. *Mol Brain,* 7**,** 45.

YOSHIHARA, M., HAYASHIZAKI, Y. & MURAKAWA, Y. 2017. Genomic Instability of iPSCs: Challenges Towards Their Clinical Applications. *Stem Cell Rev Rep,* 13**,** 7-16.

YOU, M., RONG, R., ZENG, Z., LI, H., XIA, X. & JI, D. 2021. Single-cell RNA sequencing: A new opportunity for retinal research. *Wiley Interdiscip Rev RNA***,** e1652.

YU, J., VODYANIK, M. A., SMUGA-OTTO, K., ANTOSIEWICZ-BOURGET, J., FRANE, J. L., TIAN, S., NIE, J., JONSDOTTIR, G. A., RUOTTI, V., STEWART, R., SLUKVIN, I. I. & THOMSON, J. A. 2007. Induced pluripotent stem cell lines derived from human somatic cells. *Science,* 318**,** 1917-20.

ZERTI, D., HILGEN, G., DORGAU, B., COLLIN, J., ADER, M., ARMSTRONG, L., SERNAGOR, E. & LAKO, M. 2021. Transplanted pluripotent stem cell-derived photoreceptor precursors elicit conventional and unusual light responses in mice with advanced retinal degeneration. *Stem Cells,* 39**,** 882-896.

ZHANG, J. M., LI, L. X., YANG, Y. X., LIU, X. L. & WAN, X. P. 2009. Is caspase inhibition a valid therapeutic strategy in cryopreservation of ovarian tissue? *J Assist Reprod Genet,* 26**,** 415-20.

ZHANG, Q. T., PRESSWALLA, F., ALI, R. R., ZACKS, D. N., THOMPSON, D. A. & MILLER, J. M. L. 2021. Pharmacologic activation of autophagy without direct mTOR inhibition as a therapeutic strategy for treating dry macular degeneration. *Aging-Us,* 13**,** 10866-10890.

ZHANG, X., CATALANO, P. N., GURKAN, U. A., KHIMJI, I. & DEMIRCI, U. 2011. Emerging technologies in medical applications of minimum volume vitrification. *Nanomedicine (Lond),* 6**,** 1115-29.

ZHONG, X., GUTIERREZ, C., XUE, T., HAMPTON, C., VERGARA, M. N., CAO, L. H., PETERS, A., PARK, T. S., ZAMBIDIS, E. T., MEYER, J. S., GAMM, D. M., YAU, K. W. & CANTO-SOLER, M. V. 2014. Generation of three-dimensional retinal tissue with functional photoreceptors from human iPSCs. *Nat Commun,* 5**,** 4047.

ZHOU, C. Q., MAI, Q. Y., LI, T. & ZHUANG, G. L. 2004. Cryopreservation of human embryonic stem cells by vitrification. *Chin Med J (Engl),* 117**,** 1050-5.

ZHOU, Y., LIU, S., LIU, G., OZTÜRK, A. & HICKS, G. G. 2013. ALS-associated FUS mutations result in compromised FUS alternative splicing and autoregulation. *PLoS Genet,* 9**,** e1003895.

ZHOU, Y., ZHOU, B., PACHE, L., CHANG, M., KHODABAKHSHI, A. H., TANASEICHUK, O., BENNER, C. & CHANDA, S. K. 2019. Metascape provides a biologist-oriented resource for the analysis of systems-level datasets. *Nat Commun,* 10**,** 1523.